PARAMETRIC AND NONPARAMETRIC BAYESIAN MIXTURE MODELS FOR BRIDGE CONDITION ASSESSMENT

RAN CHEN

PhD

The Hong Kong Polytechnic University

2020

The Hong Kong Polytechnic University

Department of Civil and Environmental Engineering

Parametric and Nonparametric Bayesian Mixture Models for Bridge Condition Assessment

Ran Chen

A thesis submitted in partial fulfilment of the requirements for the degree of Doctor of Philosophy

August 2019

To my parents, wife and son

CERTIFICATE OF ORIGINALITY

I hereby declare that this thesis is my own work and that, to the best of my knowledge and belief, it reproduces no material previously published or written, nor material that has been accepted for the award of any other degree or diploma, except where due acknowledgement has been made in the text.

____________________________(Signed)

Ran Chen (Name of student)

ABSTRACT

Long-span bridges are vital components in the public transportation network, while ensuring the serviceability and integrity of these assets are of great significance to a modern sustainable city. Bridge condition diagnosis based on the long-term structural health monitoring (SHM) technology has been recognised as a promising approach for achieving the condition-based preventive maintenance. In the real situation, in-service long-span bridges are normally subject to combined execution of multiple stochastic loads such as highway traffic, railway traffic, wind and temperature, which cause heterogeneous structural responses with multimodality. Conventional probabilistic assumptions for modelling the monitoring data could be quite restrictive and unverifiable, leading to high bias in characterisation of structural behaviours. More importantly, multiple sources of uncertainties are inevitably encountered in the process of data interpretation, including the intrinsic randomness, uncertain model parameter, uncertain model order, and among others. Prediction of structural performance under severe uncertainties remains as the most challenging task in the monitoring-based bridge condition assessment. The present Ph.D. thesis dedicates to develop two classes of Bayesian mixture models for condition assessment of long-span bridges that are able to better address the above scientific issues. The suspension Tsing Ma Bridge serves as the testbed for this research.

A parametric Bayesian mixture model is first established to accommodate the multimodal structural responses with consideration of parametric uncertainty. Efficient Markov chain Monte Carlo (MCMC) simulation based Gibbs sampler is devised to pursue the joint posterior

of the mixture parameters. Convergence of the MCMC simulation is ensured through a quantitative procedure. A Bayes factor based method is employed to find the optimal model order of the mixture model. The parametric Bayesian mixture model is utilised to identify neutral axis positions of the Tsing Ma Bridge under stochastic traffic loads. A novel neutral axis position based damage identification method is proposed for real-time alert of abnormal bridge condition. Single and multiple damages of the bridge deck are confidently detected by the proposed damage indexes based on neutral axis change. Subsequently, a nonparametric Bayesian mixture model is further developed to allow the model complexity automatically adapts to the monitoring data with the joint consideration of the parametric and model order uncertainties. A collapsed Gibbs sampler is devised to pursue the nonparametric estimation of the mixture density samples. Convergence diagnosis of the MCMC simulation is achieved based on a quantitative procedure. Both the parametric and nonparametric Bayesian mixture models are used to characterise the live load effects of the bridge under multi-load condition. An updatable conditional reliability index is formulated based on the first-order reliability method (FORM) that is able to account for both the aleatory and epistemic uncertainties arising from load effect characterisation. Bayesian updating of the reliability for the bridge deck is carried out based on the accumulation of monitoring data. A clear vision on the safety risk can be learnt by bridge authorities through reporting not only the average structural reliability but also its associated uncertain range.

LIST OF PUBLICATIONS

Refereed Journal Papers

Ni, Y. Q., and Chen, R. (2019). Uncertainty quantification in mixture modelling of stress response using Bayesian approach. *Journal of Computing in Civil Engineering*. (submitted)

Conference Papers

Ni, Y. Q., and Chen, R. (2016). Bayesian approach for mixture modelling of stress response data. *Proceedings of the 2016 International Conference on Advances in Structural Monitoring and Maintenance*, Jeju, Korea.

Chen, R., and Ni, Y. Q. (2019). SHM-based bridge reliability assessment with inherent modelling uncertainties: a nonparametric Bayesian approach. *Proceedings of the 17th International Probabilistic Workshop*, Edinburgh, U.K.

Ni, Y. Q., and Chen, R. (2019). Bayesian framework for SHM-based bridge reliability assessment: parametric and nonparametric approaches. *Proceedings of the 16th East Asia-Pacific Conference on Structural Engineering & Construction (EASEC16)*, Brisbane, Australia.

ACKNOWLEDGEMENTS

I would like to express deepest gratitude to my supervisor, Prof. Yi-Qing Ni, Chair Professor of the Department of Civil and Environmental Engineering in The Hong Kong Polytechnic University, for offering me with the excellent opportunity to pursue my Ph.D. study and the generous support throughout my research and life in Hong Kong. His wisdom, passion, diligence, and vision have constantly motivated me in research and writing of this thesis. I feel really honour to have studied and worked under his supervision. I wish to take this chance to express profound appreciation to my former supervisor, Prof. Cheng Su, Professor of the School of Civil Engineering and Transportation at the South China University of Technology, for his expert guidance and continuous support.

I would like to acknowledge the financial support from the Research Grants Council of the HKSAR, The Hong Kong Polytechnic University and the National Rail Transit Electrification and Automation Engineering Technology Research Center (Hong Kong Branch) (Project No. PolyU 152241/15E; Project No. 1-ZVNF). My acknowledgements also go to the Highways Department of the HKSAR Government for providing the long-term structural health monitoring data of the Tsing Ma Bridge.

My heartfelt thanks go to the professors and colleagues that I have met over the past years. I would like to thank Prof. Y. Xia, Dr. S. Y. Zhu, Dr. S. K. Lai and Dr. Y. Dong from PolyU, Prof. Z. G. Ying and Dr. H. P. Wan from ZJU, Dr. J. Li and Dr. H. Q. Mu from SCUT, who gave me valuable suggestions and help for my research. Sincere thanks go to my colleagues Dr. L. Zhou, Dr. Y. W. Wang, Dr. X. Z. Liu, Mr. T. T. Wai, Ms. A. Lin, Mr. W. H. Kwan, Mr. C. Zhang, Mr. Q. H. Zhang, Mr. C. Xu, Mr. S. Q. Ding, and Mr. S. X. Chen from the National Rail Transit Electrification and Automation Engineering Technology Research Center (Hong Kong Branch) for their useful comments and discussions. I would also like to thank my dearest friends Dr. W. Liao, Mr. L. B. Li, Mr. Q. L. Cai, Dr. Y. S. Wang, Dr. Y. F. Hu, Dr. J. Y. Zhu, and Dr. J. K. Zhou for their help and support in both study and living. The adventure would not be so fascinating without you fellows.

I am deeply grateful to my parents and wife, who always stand behind me, understand me and give me encouragement along the way. I am in debt to my wife and my son for not being able to accompany them during every joy and sorrow in the past years. This thesis is dedicated to them, my most beloved family.

Ran Chen

August of 2019

PolyU Campus

CONTENTS

LIST OF FIGURES

LIST OF TABLES

LIST OF SYMBOLS

B	number of burn-in samples
Dir	Dirichlet distribution
$D_{KL}(P\|Q)$	Kullback-Leibler divergence
D_n	Kolmogorov-Smirnov statistic
E	elastic module
$f_j(\cdot\,\|\theta)$	the jth component density indexed by parameter θ
G	number of samples after burn-in period
G_0	base measure for Dirichlet process
$g(\cdot)$	performance function
H	depth of cross section
$H_{n,k}$	vertical load associated with the kth axle of the nth vehicle
$InvC$	scaled inverse-chi-squared distribution
J	total number of mixture components
$K(\cdot\,\|\theta)$	kernel density indexed by parameter θ
K_H	number of axles of a vehicle
K_R	number of bogies of a train
M_i	candidate models
$Mult$	multinomial distribution
N	normal distribution
NIC	normal-inverse-chi-squared distribution
N_H	number of vehicles
N_R	number of trains

n	total number of observations
n_j	number of observations in the jth component
$\Pr(\cdot)$	probability of an event
$p(\cdot)$	probability density function
$P_f(\cdot)$	failure probability
p_R	probability distribution for structural resistance
p_S	probability distribution for load effect
$p^{(t)}(y)$	mixture density samples
$p(\tilde{y}\|\boldsymbol{y})$	predictive mixture density
Q	number of parallel Markov chains
R	structural resistance
R_0	potential scale reduction factor
R_{tot}	potential scale reduction factors of total variance
R_W	potential scale reduction factors of within-model variance
R_B	potential scale reduction factors of between-model variance
$R_{n,k}$	vertical load associated with the kth bogie of the nth train
S	load effect
T	total number of iterations
V_b	between-sequence variance
V_w	within-sequence variance
$\boldsymbol{y}$	observation set
y_i	the ith observation
y_O	distance from bottom chord to neutral axis
$\boldsymbol{Z}_i$	component indicator

α	concentration parameter for Dirichlet process
α_j	hyperparameter for Dirichlet distribution
$\beta(\boldsymbol{\Theta})$	conditional reliability index
β_{pred}	predictive reliability index
β_j	reliability estimate associated with the jth mixture component
$\Gamma(\cdot)$	gamma function
$\boldsymbol{\delta}$	neutral axis change ratio
δ_{θ_i}	Dirac measure located at atom θ_i
ε	relative error of estimation
ε_B	absolute strain values from bottom chord
ε_T	absolute strain values from top chord
$\varepsilon(y)$	longitudinal strain
η	cumulative neutral axis change ratio
$\boldsymbol{\Theta}$	vector of unknown mixture parameters
$\boldsymbol{\Theta}^{\star}$	vector of most plausible mixture parameters
θ_i	Gaussian parameters associated with y_i
θ_j	Gaussian parameters associated with the jth component
$\boldsymbol{\theta}_R$	model parameters associated with structural resistance
$\boldsymbol{\theta}_S$	model parameters associated with load effect
$\boldsymbol{\mu}$	vector of component means
μ_j	the jth component mean
$\{\nu, s^2\}$	hyperparameters for scaled inverse-chi-squared distribution
$\{\xi, \kappa\}$	hyperparameters for normal distribution
ρ	curvature radius of the neutral axis

$\mathbf{\Sigma}$	vector of component variance
σ_j^2	the jth component variance
$\sigma(y)$	normal stress
σ_B	absolute stress values from bottom chord
σ_B^{max}	absolute peak stress values of bottom chord induced by moving vehicle
σ_T	absolute stress values from top chord
σ_T^{max}	absolute peak stress values of top chord induced by moving vehicle
$\sigma(t)$	traffic-induced dynamic stress response at time t
$\sigma_H(t)$	dynamic stress response due to highway traffic at time t
$\sigma_R(t)$	dynamic stress response due to railway traffic at time t
Φ^{-1}	inverse cumulative probability density
$\Phi_{n,k}^l(t)$	highway stress influence coefficient
$\boldsymbol{\varphi}$	sample of neutral axis positions
$\bar{\boldsymbol{\varphi}}$	mean value of neutral axis positions
ϕ	model deviance
$\mathbf{\Omega}$	vector of mixing weights
$\Omega_{n,k}^l(t)$	railway stress influence coefficient
ω_j	the jth mixing weight

LIST OF ABBREVIATIONS

AASHTO	American Association of State Highway and Transportation Officials
AIC	Akaike Information Criterion
ASCE	American Society of Civil Engineers
BF	Bayes factor
BIC	Bayesian Information Criterion
CI	Credible interval
CRP	Chinese restaurant process
DP	Dirichlet process
DPM	Dirichlet process mixture (model)
FBG	Fibre Bragg grating
FEM	Finite element model
FGM	Finite Gaussian mixture (model)
FORM	First-order reliability method
GVW	Gross vehicle weight
ICE	Institutions of Civil Engineers
IS	Importance sampling
LML	Log marginal likelihood
MCMC	Markov chain Monte Carlo
NA	Neutral axis
NLML	Negative log marginal likelihood
PDF	Probability density function
PMF	Probability mass function

PSRF	Potential scale reduction factor
SD	Standard deviation
SHM	Structural health monitoring
SIL	Stress influence line
SS	Subset simulation
UIL	Unit influence line
WIM	Weigh-in-motion

CHAPTER 1
INTRODUCTION

1.1 BACKGROUD AND MOTIVATION

Civil infrastructures such as highways, bridges, railways, pipelines and dams are huge capital investment that play a significant role in functioning modern sustainable city. Any malfunction of these structural or mechanical systems can cause possible interruption of public transit, energy supply and industrial production, resulting in civic chaos. Recently, several reported accidents in Hong Kong have raised considerable public concern. On October 2015, an unexpected tugboat collision at the Kap Shui Mun Bridge caused emergency closure of all traffic lanes to the Hong Kong International Airport, leading to approximately ten thousand travellers stranded at different locations (Lau et al., 2015; Legislative Council of the HKSAR, 2015). On March 2019, two subway trains collided at the crossover section near the Central station, one of the busiest stations in Hong Kong, during testing of a new signal system in the early morning. Train service between Central and Admiralty stations was suspended for two days, leading to approximately one billion financial loss (China Daily, 2019; Tsang et al., 2019). These accidents highlight the urgency of infrastructure maintenance.

Long-span bridges are vital components to the infrastructure system. As time goes, in-service bridge structures suffer from inevitable deterioration due to material aging, harsh operational environment, increasing traffic demands as well as extreme events such as earthquake, typhoon or collision. The continuous deterioration, if not mitigated, cumulates into damage and affects the structural performance to various degrees, from non-optimal operation to catastrophic failure, resulting in large economic loss or even casualties. According to the 2017 Infrastructure Report Card released by the American Society of Civil Engineers (ASCE), 9.1% of the bridges in the U.S. were rated structurally deficient in 2016 with a need of $123 billion USD to rehabilitate the nation-wide bridge condition (ASCE, 2017). While in the U.K., the Institution of Civil Engineers (ICE) reported that 24,000 miles of local roads are in need of essential maintenance, which will cost at least £5 billion GBP over 10 years to repair (ICE, 2018). Together with rapid urbanisation, the issue of bridge maintenance increasingly becomes a crucial concern among authorities, researchers and practitioners throughout the world.

To ensure the serviceability and integrity of long-span bridges in their service periods, efficient and innovative maintenance strategies need to be planned and implemented in an optimal sense that making best use of limited budget available. Integration of long-term structural health monitoring (SHM) technology to bridge surveillance and assessment offers an ideal solution to condition-based preventive maintenance of these significant assets (Bhattacharya et al., 2005; Catbas et al., 2008; Frangopol et al., 2008). By embedding multiple types of permanent sensing devices on the bridge, a long-term SHM system is generally designed to consecutively acquire on-site authentic measurements of structural responses, external loadings and environmental effects in an automatic manner. Local and global structural behaviours under operational environment can be fully characterised by the great amount of monitoring data, with which early warning of anomalies in responses and loads can be signalled prior to any possible negative consequences (Ko and Ni, 2005). Current bridge status of concern such as deterioration or damages can be reasonably inferred through the investigation of long-term structural behaviours. Monitoring-based condition assessment is expected to realise objective and quantitative health index of the bridge, which will further facilitate the preventive and condition-based life-cycle maintenance scheme. Over the past three decades, with the rapid development in advanced sensing, signal processing, data management and structural identification techniques, impressive SHM practices on large-scale bridges appear across different countries with typical examples such as the Great Belt Bridge (1600 m, 1998)[a] in Denmark (Andersen and Pedersen, 1994), the Tamar Bridge (335 m, 2006) in the U.K. (Koo et al., 2013), the Commodore Barry Bridge (501 m, 1998) in the U.S. (Barrish et al., 2000), the Tsing Ma Bridge (1377 m, 1997) in Hong Kong (Wong, 2004), the Runyang Bridge (1490 m, 2005) in China (Wang et al., 2014), and the Akashi Kaikyo Bridge (1991 m, 1998) in Japan (Kashima et al., 2001).

Although the merits and achievements of SHM technology have now been acknowledged by the bridge management authorities, there are yet challenging scientific issues that need to be addressed for successful monitoring-based long-span bridge condition assessment. A key task here is how to perceive in-service structural condition by taking full advantage of various types of field measurement data in order to make efficient maintenance decisions. The mapping

[a] The numbers in the parenthesis are the main span of the bridge and the year of instrumentation of permanent monitoring system, respectively.

between structural behaviours characterised by monitoring data and the safety or reliability of the bridge components/system is usually difficult to establish (Catbas and Aktan, 2002). In recognition that the presence of multiple sources of uncertainties in the process, learning of monitoring data by making use of statistical models stands as an essential step.

Long-span bridges are normally subject to multiple types of loads and environmental stressors such as highway traffic, railway traffic, wind effect and temperature effect during their service life. The stochastic nature of these live loads is time-varying with different frequencies and amplitudes. Structural responses under the combined effect of multi-load condition will exhibit considerable variation both locally and globally, resulting to heterogeneous data structure with multimodality (Ni et al., 2011b; Ni et al., 2011c; Ni and Chen, 2016). Standard unimodal distribution models, e.g. the Gaussian distribution, are often inadequate to characterise the multimodal structural responses, yielding bias model estimation. Furthermore, multiple levels of uncertainties arising from the interpretation of the response data, e.g., intrinsic variability, uncertain model parameters, uncertain model orders and measurement noise, have not been sufficiently considered in existing approaches. In order to make robust prediction of the structural behaviours by using the monitoring data, it is of necessity to develop advanced statistical tools, e.g. the Bayesian models, that can be performed in the presence of serve uncertainty.

Real-time identification of damage/abnormality of the in-service long-span bridge under the varying operational environment is regarded as one of the most challenging topics in the SHM community. Existing approaches like the vibration-based techniques may suffer substantial limitations for detecting damage of large-scale complex structure in real-world scenarios (Fan and Qiao, 2011). It is often difficult to capture minor local damage by means of change in dynamic measurements such as natural frequency and mode shape, which are global properties of a complex structure (Doebling et al., 1998). Furthermore, the environmental and operational variability of in-service bridge, other than real damage, could affect the dynamic characteristics to various degree, leading to ambiguous detection results (Farrar et al., 1994; Peeters and De Roeck, 2001; Sohn, 2006; Deraemaeker et al., 2008; Xia et al., 2012c). In contrast, in-situ strain measurement, served as structural static response, affords a more intuitional measure of the local stiffness and strength of a structure than the dynamic counterparts. The advancement of strain monitoring techniques such as the long-gauge fibre Bragg grating (FBG) sensor enable to achieve long-term reliable strain measurement within a large region of a complex structure in an economical way (Chen et al., 2019). Developing efficient damage identification methods based on strain monitoring data that are comparable to the widely used vibration-based methods has its practical significance.

Reliability principles play a guiding role in probabilistic structural design, with which the safety, serviceability and durability of a new bridge in design service life can be guaranteed given its capacity and demand (Melchers and Beck, 2017). Reliability-based methods have recently been extended to the condition assessment of existing bridge in view of the ability to account for the inherent randomness associated with loads and material properties (Bhattacharya et al., 2005; Catbas et al., 2008; Frangopol et al., 2008). The reliability index or failure probability serves as a quantitative measure of healthy condition for in-service bridge. As soon as the new bridge is opened to public, the loading scenarios or material constitution are somewhat determined, and the degradation begins. By means of the SHM system, the site-specific structural and loading information, such as strain, acceleration, displacement, wind velocity and traffic loads, can be incorporated into reliability-based approaches to alleviate the substantial uncertainty in live loads and resistance, leading to a more rational condition assessment of the existing bridge. Nonetheless, classic reliability theory is built upon conventional probability distribution models that only considers the aleatory uncertainty in capacity and demand. The modelling uncertainties, which are of epistemic type, have not yet been taken into consideration (Zhang and Mahadevan, 2000; Der Kiureghian, 2008; Der Kiureghian and Ditlevsen, 2009). Examples are the use of imprecise distribution models for basic random variables and the statistical uncertainty stemming from parameter estimation. In contrast to the fundamental randomness in current reliability analysis, influence of the modelling uncertainties on estimation of failure probability or reliability index is yet a less explored area.

1.2 RESEARCH OBJECTIVES

In view of the above research needs, the present Ph.D. thesis aims to develop two class of Bayesian mixture models for condition assessment of long-span bridge instrumented with SHM system, which are able to (1) accommodate heterogeneous structural responses under multi-load condition, and (2) deal with modelling uncertainties arising from characterisation of monitoring data. The suspension Tsing Ma Bridge along with its long-term monitoring data are taken as the ideal testbed for this research. The proposed damage detection and reliability-based assessment procedure based on the Bayesian mixture models are purely data-driven methods with no need of physical models (e.g. bridge finite element model (FEM)). The Ph.D. study intends to provide some technical solutions for the current practice of monitoring-based bridge condition assessment.

To achieve the research objectives described above, the thesis is focus on the following specific topics.

(1) To develop a parametric Bayesian mixture model that is capable of accommodating multimodal structural response with consideration of parametric uncertainty. The conjugate priors are selected for the mixture parameters in order to derive analytical form of the full conditional posteriors. Approximation techniques such as the Markov chain Monte Carlo (MCMC) simulation methods are pursued to realise the joint posterior of the mixture parameters. The optimal model order (number of mixture components) is determined based on the Bayes factor based method. Convergence check of the Markov chains is carried out to ensure the efficiency of the model estimation.

(2) To propose a damage identification method based on tracking the neutral axis (NA) position for detecting damage of the in-service Tsing Ma Bridge. Neutral axis position derived from strain measurement is deemed as a cross-sectional property related physical parameter that can be utilised as a promising damage indicator. A sensitivity analysis is conducted to first investigate the variation of neutral axis position due to moving loads on

multiple traffic lanes. Neutral axis positions under multi-lane stochastic traffic condition based on monitoring and simulated stress responses are identified using the parametric Bayesian mixture model respectively. Damage indexes based on change of neutral axis position are proposed. Detection of damage cases postulated on the bridge deck is carried out under stochastic traffic condition by use of the proposed damage indexes.

(3) To develop a nonparametric Bayesian mixture model that allows the model complexity automatically adapts to the multimodal structural response with the capability to joint consideration of parametric and model order uncertainties. The nonparametric approach stands as an improvement over the parametric counterpart. Dirichlet process prior is adopted in this nonparametric mixture model. Inference on infinite-dimensional parameter space is pursued by using the MCMC techniques. Convergence diagnosis is needed to check the convergence of simulations within chains and model orders.

(4) To conduct long-term reliability-based assessment of the in-service Tsing Ma Bridge by using two Bayesian mixture models respectively with consideration of parametric and model order uncertainties. Temperature-induced stress response is eliminated from the raw signal to obtain the live load effect due to vehicle, train and normal wind. Probability density functions (PDF) of the live load effect are established using the Bayesian mixture models. A conditional reliability index is formulated to not only account for aleatory uncertainty but also epistemic uncertainty arsing from multimodal stress response. The conditional reliability index can be updated with the availability of consecutive monitoring data.

1.3 THESIS LAYOUT

A systematic and coherent research is conducted in this thesis with two important topics being covered, i.e. damage detection and reliability assessment, which fall within the engineering practice of the condition assessment of long-span bridges. Innovative Bayesian mixture models are developed for probabilistic modelling of multimodal structural responses under modelling uncertainties. Seven chapters are included in the thesis with the content layout being as follows.

Chapter 1 serves as an introduction with research motivation and objectives being claimed.

Chapter 2 presents a comprehensive literature review on key issues studied in this thesis. First, topics on structural condition assessment are widely reviewed. General concepts are introduced together with current technical trends. Damage detection methods, from vibration- to static-based approaches, are critically discussed. Reliability assessment of existing structures is then reviewed with emphasis on making use of health monitoring data. Second, the Bayesian methods applied in civil engineering are briefly discussed, including model updating, damage identification, uncertainty quantification and reliability analysis. Lastly, theory and application of mixture models are reviewed ranging from non-Bayesian to Bayesian perspective.

Chapter 3 proposes the parametric Bayesian mixture model, specifically the finite Gaussian mixture model, to deal with the multimodal structural response with consideration of parametric uncertainty. In this parametric model, the conjugate priors are adopted with the analytical form of full conditional posteriors being derived for the mixture parameters. A class of Markov chain Monte Carlo based simulation techniques, namely the Gibbs sampler, is used to realise the joint posterior of the mixture parameters. A quantitative convergence diagnosis strategy is proposed to ensure the global convergence of the simulation. A Bayes factor based approach is developed to optimally determined the model order. Effectiveness of the parametric Bayesian mixture model is validated based on artificial mixture data sets.

Chapter 4 presents the damage detection of the in-service Tsing Ma Bridge by using the neutral axis position based method. A sensitivity analysis based on FEM is conducted to first gain insight into the variation of neutral axis position due to moving loads on multiple traffic lanes in a deterministic sense. Neutral axis positions of bridge deck under multi-lane stochastic traffic flow are predicted based on monitoring and simulated stress responses using the parametric Bayesian mixture model respectively. Two damage indexes, i.e. the NA change ratio and cumulative NA change ratio, are proposed for online damage detection using monitoring stress responses. Postulated single- and multiple-damage cases on the bridge deck are studied to testify the feasibility of the new method.

Chapter 5 proposes the nonparametric Bayesian mixture model, specifically the Dirichlet process mixture model, which allows the model complexity to automatically fit the multimodal structural response with the capability to joint consideration of parametric and model order uncertainties. In this nonparametric model, the clustering property of the Dirichlet process along with the mechanism of inference on infinite-dimensional parameter space are briefly introduced. The sampling form of the Dirichlet process mixture model is derived based on the stick-breaking construction. To avoid low efficiency of direct sampling from the conditional posteriors, the collapsed Gibbs sampler is devised to pursue the posterior mixture density samples. An extended version of the quantitative convergence diagnosis strategy is proposed to assess the convergence of simulations within both chains and model orders. Effectiveness of the DPM model is verified through the demonstration on the modelling of the trimodal data set. A comprehensive comparison study is given to investigate the performance of two Bayesian models in terms of model complexity, goodness-of-fit, uncertainty characterisation and computational demands.

Chapter 6 presents the long-term reliability assessment of the in-service Tsing Ma Bridge using two Bayesian mixture models respectively with consideration of parametric and model order uncertainties. Statistical analysis of the monitoring stress responses on the bridge deck is conducted with the live load effect being extracted after the elimination of temperature-induced strain. PDFs of the live load effect with multimodality are estimated by means of the mixture models. A new concept of conditional reliability index based on first-order reliability method is proposed to not only account for aleatory uncertainty but also epistemic uncertainty arsing from multimodal stress response. Influence of uncertain mixture parameters on the reliability estimate is investigated. Bayesian updating of one-year reliability of the bridge deck is carried out based on the accumulation of monitoring data to render a more persuasive assessment result.

Chapter 7 summarises the key findings of the Ph.D. study and offers some views on SHM-based condition assessment of long-span bridge. Limitations and future research directions are highlighted in the meantime.

CHAPTER 2
LITERATURE REVIEW

2.1 STRUCTURAL CONDITION ASSESSMENT

2.1.1 General Concepts

Condition assessment is a process of measuring and evaluating the healthy status of in-service civil infrastructure with the ultimate goal to predict the life-cycle structural performance (Aktan et al., 1996; Aktan et al., 1997). Through the process of condition assessment, (1) structural deterioration or damage signs such as cracks, corrosion, voids and de-bonding, can be collected to evaluate the current structural integrity in a direct manner; and (2) structural behaviours such as strain, displacement, acceleration and settlement, can be measured to reflect the safety reserve in an indirect way (Catbas and Aktan, 2002). Immediate remedial actions are triggered if severe damages or aging of the structure are observed. Popular and practical means engaged in infrastructure assessment include but not limited to (1) visual inspection; (2) non-destructive testing; (3) controlled load testing; and (4) instrumented long-term structural health monitoring (SHM) system.

Visual inspection, standing as a simple and direct tool, is commonly accepted in national standards and regulations of bridge inspection and evaluation among many countries (AASHTO, 2011; Ministry of Transport of the People's Republic of China, 2011; FHWA, 2012;

The Highways Agency, 2017). Combined with predetermined ranking system, visible bridge components are classified into different grades of condition according to their physical appearance. Rating of global bridge system is conducted based on the grades of substructures. Obviously, the conventional visual inspection unavoidable contains subjective descriptions of the bridge status by individual inspectors, leading to possible difference in assessment results. Meanwhile, it is a time-consuming and labour-intensive work especially for network-wide bridges. Some invisible defects, such as voids and de-bonding embedded in the concrete, can hardly be found and recorded in this way.

Non-destructive testing such as ultrasonic guided waves, infrared thermography, X-ray, and eddy current techniques are rapidly developed over the past several decades and have reached to a mature stage for commercial application (Auld and Moulder, 1999; McCann and Forde, 2001; Drinkwater and Wilcox, 2006; Bagavathiappan et al., 2013). These techniques serve as efficient tools for local damage characterisation with the extent and severity of damage can be satisfactorily measured. However, it is required the prior knowledge of the existence and precise location of damage which cannot be guaranteed for most scenarios in civil structures. Implementation of non-destructive test is still time-consuming and expensive.

Controlled load testing is another standard procedure for carrying-capacity evaluation. By assigning prescribed loadings on the structure, typically a series of trucks with known weights, the static and dynamic responses of a bridge can be ideally captured by field measurements. Loading and response information are together used to infer the bridge performance. A barrier to apply this method is the requirement of temporary suspension of the traffic operation on the bridge during the test, which is usually unacceptable for management authorities. Take the Kap Shui Mun Bridge as an example, the unexpected close of the bridge for nearly two hours in 2015 leads to chaos of transportation between the Hong Kong International Airport and city centre (Lau et al., 2015). Time-consuming and high cost are drawbacks of the controlled load test as well.

The SHM technology has been witnessed a great progress for the past two decades with the advancement in sensing, signal processing, pattern recognition and machine learning techniques. There are a surge of research on SHM technology for civil infrastructure across different countries, indicating remarkable achievements of such technique (Pines and Aktan, 2002; Yun et al., 2003; Ko and Ni, 2005; Brownjohn, 2007; Ni et al., 2009; Ou and Li, 2010; Fujino and Siringoringo, 2011; Li and Hao, 2016). By deploying permanent sensing devices on critical parts of a bridge, the long-term SHM system is capable of acquiring abundant amount of information about the external loadings, structural responses and environmental effects of the in-service bridge in an automatic manner. Local and global structural behaviours under operational environment are well characterised by the historical monitoring data. Early warning of anomalies in loads/responses and possible detection of damage/deterioration can be achieved through an efficient and timely way (Ko and Ni, 2005).

Apparently, instrumentation with automatic SHM system acts as a beneficial complement to the bridge inspection that one does not necessary to cease transportation service. A strategy of integrating long-term SHM data into condition assessment is expected to achieve objective and quantitative health index of the structure and facilitate preventive and condition-based life-cycle maintenance scheme. Hence, the SHM-based condition diagnosis and prognosis are recognized as a promising method amongst aforementioned conventional approaches. In view of this, the studies described in this thesis fall within the context of SHM.

2.1.2 Vibration-based Methods

Structural identification using dynamic properties for the purpose of condition evaluation became popular since the 1990s because of the rapid development of vibration test techniques (Aktan et al., 1997). The fundamental principle behind vibration-based methods is that the damage-induced changes in the physical properties, i.e. mass, damping and stiffness, will cause detectable changes in modal parameters, i.e. natural frequencies, modal damping and mode shapes. Therefore, damage or condition of a structure can be inferred by the changes in dynamic properties. Well-known damage signatures derived from dynamic characteristics include flexibility matrix (Pandey and Biswas, 1994), modal assurance criterion (Heylen et al., 1997), coordinate modal assurance criterion (Heylen et al., 1997), modal strain energy (Shi et al., 1998), and frequency response function (Maia et al., 2003). A significant amount of literature has been published in the scope of damage identification using vibration characteristics (Salawu, 1997; Doebling et al., 1998; Farrar et al., 2001; Sohn et al., 2003; Carden and Fanning, 2004; Alvandi and Cremona, 2006; Fan and Qiao, 2011).

Although vibration-based methods are prevailing in existing literature, damage identification of a long-span bridge by means of dynamic characteristics faces substantial difficulties. First, natural frequencies and mode shapes are global properties of a structure, which may be insensitive to local minor damage or degradation. From a practitioner's point of view, higher structural modes associated with local responses are often difficult to measure in field test (Doebling et al., 1998). Second, previous studies have acknowledged that structural dynamic properties can be significantly influenced by the ambient environment variability (Farrar et al., 1994; Peeters and De Roeck, 2001; Sohn, 2006; Deraemaeker et al., 2008; Xia et al., 2012c). Temperature and traffic volume can give rise to 5 to 10% variation in average of bridge's modal parameters (Figueiredo et al., 2014). Changes in vibration characteristics caused by the environmental and operational variability might mask subtle changes caused by the damage, leading to invalid of the vibration-based detection techniques. Figueiredo et al. (2014) points out that separation of damage-induced structural responses from the varying environmental condition is the main challenge to transfer SHM technology from research to practice.

2.1.3 Static-based Methods

In contrast to vibration-based approach, the static-based methods receive rare attention among the research community so far. In fact, it is believed that structural static responses such as displacement, tilt, strain and their representative derivatives offer a more intuitional measure on the local stiffness or strength of a structure than the dynamic counterparts. Early research recognised that the static test data are suitable for damage detection (Sanayei and Onipede, 1991; Hjelmstad and Shin, 1997). However, it is costly and impractical to implement static test on an existing complex structure. Some researchers suggested the damage-induced dead load redistribution in structural elements, which is essential static feature, can be measured to indicate damage location and severity (Zhao and Shenton III, 2005; Hua et al., 2009). It is often required to deploy strain sensors in the erection stage to capture the dead load redistribution and the strain measurements are also vulnerable to uncertainties arising from thermal effect. Recently, Li and Hao (2015) investigated the use of relative displacement measurements to detect damage of shear connectors by using the continuous wavelet transform and Hilbert-Huang transform. He et al. (2017) proposed a two-stage method to quantify damages by use of quasi-static moving load induced displacement response. Although these studies demonstrate certain degree of success in damage identification in laboratory setting, further research efforts are still needed on damage detection of long-span bridge using static response especially under daily normal traffic condition.

A unit influence line (UIL) represents the variation of a particular response at a given location when a unit concentrated force moves along the bridge (Zaurin and Catbas, 2009). Because the influence line itself is an intrinsic static characteristic of a structure, it is proposed to be a condition index when measured responses can be retrieved from passing vehicles if the weigh-in-motion (WIM) device is available (Catbas and Aktan, 2002). Chen et al. (2014) proposed a mathematical regularization method to extract the stress influence lines (SIL) of bridge components based on measured train information and train-induced stress responses. They demonstrated the identified SILs offer a promising real-time technique for damage localization of in-service suspension bridge instrumented with SHM system. Later, Chen et al. (2016)

developed the SIL identification method by integrating the least squares solution and weighted moving average technique. Recently, an influence line based damage detection method using the long-gauge fibre Bragg grating sensor was proposed by Chen et al. (2019), in which the identification of damage location and extent of a bridge are achieved under stochastic traffic flow. Although the concept of UIL is straightforward, identification of UIL based on field measurements of structural responses and corresponding axle weights and axle positions is an ill-conditioned inverse equation that one inevitably faces numerical instability and non-unique solution problems.

The neutral axis of beam-like structure passes across the geometrical centroid of the cross section under pure bending, leading itself to be a cross-sectional property related physical parameter. Questionable movement of the neutral axis position can be a sign of abnormal change of cross-sectional property, i.e., damage. The neutral axis position can be served as damage indictor for flexural behaviour dominated structural members. DeWolf and his co-workers evaluated the composite action of a steel-concrete simply supported girder bridge by tracking the neutral axis position during the passage of normal truck traffic (Chakraborty and DeWolf, 2006; Cardini and DeWolf, 2009). Although no change of composite action was found in their study, they point out that monitoring of neutral axis position can provide valuable information to condition assessment of the bridge deck. Ni and his co-workers proposed a Kalman filter estimator to locate the neutral axis position using strain measurement data (Ni et al., 2012; Xia et al., 2012b). The capability of the Kalman filter estimator for consistently locating the neutral axis position was verified under varying traffic load patterns. Crack detection of a scaled bridge deck model was successfully detected using the neutral axis position as the damage index. Sigurdardottir and Glisic (2013, 2014) investigated the uncertain factors other than damage that would adversely affect the estimation of neutral axis location of a girder. They recognise that neutral axis position can act as a damage indicator only if the uncertainties associated with its localization can be well quantified. Recently, the neutral axis position was also used to diagnose the condition of wind-turbine towers (Soman et al., 2016) and concrete box girder bridges (Xia et al., 2018). A state-of-the-art review on neutral axis position for structural health monitoring can be found in Sigurdardottir and Glisic (2015).

2.1.4 Reliability-based Approach

Reliability-based structural condition assessment has attracted plenty of attention during the past two decades due to the capability of accommodating stochastic nature in both load- and resistance-related parameters. Inspired by the concept of reliability principles for design, Ellingwood and his co-workers conducted pioneer works on implementing assessment for existing structures in the reliability framework (Mori and Ellingwood, 1993; Ellingwood, 1996; Zheng and Ellingwood, 1998). The inherent uncertainty in loading condition, structural strength and deterioration was highlighted, and time-dependent reliability analysis was proposed to determine the condition of ageing concrete structures. Almost the same time, Enright and Frangopol (1998, 1999b) proposed the time-variant series system reliability approach to investigate the reliability of reinforced concrete girder bridges subject to environmental attack. Several system reliability models were considered, and the corresponding reliability estimates were compared. Later, Imai and Frangopol (2001) conducted reliability assessment of a suspension bridge in Japan with considering geometrical nonlinearity. Practical implementation of reliability-based assessment on European road and rail bridges was introduced by Enevoldsen (2011). In contrast with deterministic methods, the reliability approach could provide more accurate assessment with which rehabilitation cost could be minimized.

2.1.5 Integration with SHM Data

Site-specific observational data of load- and resistance-related parameters can help to improve the accuracy of reliability assessment since these parameters are both time- and spatial-variant. Measurement data acquired from SHM system, which represents the authentic measure of structural response and ambient factors, are ideal information for aiding reliability-based assessment. Bhattacharya et al. (2005) used site-specific in-service strain response data to reliability evaluation of bridges with the consideration of measurement noise and modelling uncertainty. Catbas et al. (2008) presented the reliability analysis for the main truss components as well as the entire structural system of a long span truss bridge in the U.S. by using monitoring data. A key finding was that the system reliability was significantly affected by the temperature-induced strain variation. Hosser et al. (2008) developed a framework for reliability-based system assessment using data from SHM system. A substitute structure, which could be deemed as large-scale model, was used to verify the proposed framework. Frangopol and his colleagues contributed a number of papers on the topic of monitoring-based condition assessment (Frangopol et al., 2008; Liu et al., 2009a, 2009b; Messervey et al., 2011; Okasha et al., 2012; Saydam and Frangopol, 2013). The efficient utilization of structural monitoring data in reliability assessment process as well as the development of prediction models was discussed in Frangopol et al. (2008), and the Lehigh River Bridge was taken as the illustrative example. Liu et al. (2009a) developed the limited state equation associated with structural component strain measurements with the consideration of condition variations. Later, the approach of bridge component reliability analysis was extended to bridge system reliability level with a comprehensive sensitivity study carried out (Liu et al., 2009b). Messervey et al. (2011) applied extreme value distribution to enhance the assessment and performance prediction of bridges by using monitoring live load data. Okasha et al. (2012) evaluated lifetime reliability of ageing bridges with automated finite element model updating techniques. The resistance parameters of the structure were updated by using monitoring strain data acquired from crawl tests. Saydam and Frangopol (2013) investigated the error in system reliability index calculated by first-order second-moment method when load effect and structural resistance were not normal or lognormal distributions.

Taking the Tsing Ma Bridge in Hong Kong as the testbed, Ni and his co-workers conducted pioneer works on reliability assessment of in-service long suspension bridge using long-term monitoring data (Ni et al., 2010; Ni et al., 2011b; Ni et al., 2011c; Xia et al., 2012a). Analytical models of stress spectrum under multi-load condition were derived by use of finite mixture distributions in conjunction with a hybrid mixture parameter estimation algorithm (Ni et al., 2011c). Based on long-term strain monitoring data, the fatigue life and reliability assessment at fatigue-susceptible locations were carried out by using the formulated probabilistic model of the hot spot stress (Ni et al., 2010). A wavelet multiresolution decomposition method is proposed to extract live-load effects from the raw strain measurements with the recognition that temperature-induced strain has been mostly released by the deck movement at the expansion joint (Ni et al., 2011b). Due to the multiple types of loads acting on the bridge, including railway traffic, highway traffic and wind, the in-service monitoring stress responses exhibit significant multimodality, which cannot be adequately captured by conventional unimodal distribution models. Xia et al. (2012a) used the Weibull mixture distribution model to characterize the multimodal stress, in which the expectation maximization algorithm in conjunction with the Akaike information criterion is designed to pursue the optimal model selection and mixture parameter estimation. Estimated probability density functions (PDF) are further utilised to derive reliability indexes of truss members of the Tsing Ma Bridge.

2.2 BAYESIAN METHODS IN CIVIL ENGINEERING

2.2.1 Bayesian Perspective

In the scope of statistics, there exists two schools of thought, namely the Frequentist and the Bayesian perspectives. Incessant debate on these two philosophies is ongoing. The fundamental difference between the Frequentist and the Bayesian approaches starts from the definition on probability of an event. The Frequentist approach treats probability as the limit of frequency of an event when large number of trials are conducted. On the contrary, the

Bayesian approach allows to define probability of an event in which random experiment cannot be designed (Yuen, 2010). It extends the applicability of probability to a more general degree, in which people often refer to plausibility. The building block of the Bayesian statistics is the well-known Bayes' Theorem

$$p(\theta|y) = \frac{p(\theta)p(y|\theta)}{p(y)} \tag{2.1}$$

where $p(\theta|y)$ is the posterior distribution of the unknown parameter θ, $p(\theta)$ is the prior distribution of θ before any new data are observed, y are the new observations of variable of interest, $p(y|\theta)$ is the likelihood function, and $p(y) = \int p(\theta)p(y|\theta)\,\mathrm{d}\theta$ is the normalized constant which does not depend on θ. The Bayesian statistical conclusion about a parameter θ is made in terms of probability statement, namely assigning probability distribution for θ, and the probability statement is conditional on the observed values of y. Consequently, model parameters are usually treated as random variables in Bayesian inference rather than fixed quantities in classical statistics. On the basis of statistical data analysis, the intrinsic characteristic of Bayesian methods is the explicit adoption of probability for quantification of uncertainty in inference (Gelman et al., 2014). It is recognised that the modelling and parametric uncertainties widely encountered in civil engineering can be explicitly quantified by using the Bayesian probability statements.

2.2.2 Model Updating, Damage Identification and Uncertainty Quantification

In the late 1990s, Beck and Katafygiotis (1998) proposed a general Bayesian statistical framework for updating structural model and associated uncertainties using dynamic test data. In their approach, both accurate response predictions and the assessment of this accuracy were given within a Bayesian approach. The issue of identifiability of the model parameters was investigated by Katafygiotis and Beck (1998). Later, Katafygiotis et al. (1998) discussed the treatment of unidentifiable case and proposed an efficient approximate representation for the posterior PDF of the model parameters. The feasibility of applying Bayesian probabilistic approach to SHM was investigated in Vanik et al. (2000) with introducing a novel damage measure considering time variation.

Sohn and Law (1997) proposed a Bayesian probabilistic damage detection approach to identify the most likely damage location and its extent by using a branch-and-bound search scheme. The measurement noise and modelling error between the structure and the analytical model were explicitly considered within the Bayesian framework. The approach was further applied to predict the location of plastic hinge deformation using the experimental data obtained from the vibration tests of a reinforced-concrete bridge column (Sohn and Law, 2000). Nichols et al. (2010) used the Bayesian approach to identify both linear and nonlinear parameters of a structural system with free-decay vibrations and later to detect the delamination of a composite beam. Figueiredo et al. (2014) proposed a Bayesian-based algorithm to identify structural condition and damage by using daily response data from a real bridge in Switzerland.

Igusa et al. (2002) investigated the effects of aleatory and epistemic uncertainty on design and analysis of structure system using the Bayesian techniques. The influence of multi model uncertainties was explored by the Bayesian hierarchical analysis. Goller and Schueller (2011) investigated the role of model uncertainties, i.e. the discrepancy between finite element model and real structure, within the Bayesian updating procedure. Zhang et al. (2011) presents a comprehensive Bayesian approach for structural model updating with consideration of errors from different sources including measurement noise, linearization error, and modelling errors due to limited predictability.

Au (2011) developed a fast Bayesian FFT method for ambient modal identification with separated modes, in which the efficient computation of the posterior most probable modal parameters and their covariance matrix is achieved. Lam et al. (2014) proposed a step-by-step modification technique for the selection of a representative model class within the Bayesian model updating framework. Yuen and Mu (2015) proposed a Bayesian real-time system identification algorithm using response measurement, in which the model class selection and parametric identification can be simultaneously implemented. It can be seen that the studies on Bayesian methods in civil engineering during the past twenty years are enthusiastic, ranging from model updating, damage identification to uncertainty quantification. A comprehensive study on the Bayesian methods and applications can be referred to the book of Yuen (2010).

2.2.3 Bayesian-based Reliability

Incorporating Bayesian analysis with reliability-based condition assessment for uncertain structural and statistical models was first introduced by Der Kiureghian (1989, 1991), in which a new reliability index was proposed to account for model uncertainty due to formulation inexactness, measurement error and insufficient data. To evaluate the new measure of structural safety, first-order reliability methods and their derivations were proposed to compute the probability distribution or variance of the safety measure. Later, the measure of reliability that incorporated parameter uncertainty was termed the 'predictive reliability index', which was a similar concept with the Bayesian predictive distribution (Der Kiureghian, 2008). The proposed Bayesian approach provided measure of the uncertainty inherent in the estimate of reliability index and the failure probability, which arise from parameter uncertainty. Two types of uncertainty, i.e. aleatory or epistemic uncertainty, in modelling and their different effects for risk and reliability analysis were discussed in Der Kiureghian and Ditlevsen (2009). A concept of robust reliability with the consideration of uncertainties from structural modelling was discussed in Papadimitriou et al. (2001). Assessment of the robust reliability is updated based on dynamic test data by the use of a Bayesian system identification methodology integrated with probabilistic structural analysis tools. Zhang and Mahadevan (2000) proposed a Bayesian procedure to assess the modelling uncertainty including the uncertainty in mechanical and statistical model selection and the uncertainty in distribution parameters with an application in fatigue reliability analysis.

Computation of small failure probability encountered in reliability analysis of structural system has been widely investigated during the past decades. Based on the Markov simulation algorithm, Au and Beck (1999) proposed an adaptive importance sampling (IS) scheme to compute the multi-dimensional integrals in reliability analysis. A subset simulation (SS) approach was introduced by Au and Beck (2001), in which the failure probability is replaced by larger conditional failure probabilities with the aid of introducing intermediate failure events. The conditional probabilities can be estimated efficiently by the Markov chain Monte Carlo (MCMC) simulation technique. In order to evaluate the probability centred in a small region with high dimension parameter space, Beck and Au (2002) utilized an adaptive MCMC simulation approach with a sequence of intermediate probability densities to gradually portray the desired high dimension probability region.

Combination of prior knowledge or expert judgement in engineering decision are desired and it can be rationally realized by the Bayesian manner. Enright and Frangopol (1999a) used information from inspection results as the prior knowledge to better predict future bridge conditions through Bayesian updating. The approach allowed accounting for inspection results in the quantitative assessment of bridge condition and showed how to incorporate quantitative information into bridge system and component condition prediction. Later, the incorporation of historical monitoring extreme data in the reliability assessment of an existing bridge in the U.S. with Bayesian method was again illustrated in Strauss et al. (2008). Recently, Zhu and Frangopol (2013) presented an approach for reducing the uncertainty in the performance assessment of ship structures by updating the wave-induced load effects with the monitoring data. Bayesian updating was performed to estimate the parameters in the Rayleigh and Type I extreme value distributions which were used to model wave-induced responses. Garbatov and Soares (2002) adopted a Bayesian approach to update parameters of probability distribution governing the reliability assessment of maintained floating structures, where the information from inspections was used.

A number of researches on the Bayesian network for structural reliability analysis were emerged recently, where the Bayesian network is efficient in representing and evaluating complex probabilistic dependence broadly existed in infrastructure system. Mahadevan et al. (2001) applied Bayesian networks to system reliability reassessment considering multi failure sequences and correlations between component-level limit states. A framed structure was analysed to verify the proposed method. Straub and Der Kiureghian (2010a, 2010b) proposed the enhanced Bayesian network method combined with reliability methods to efficiently compute the probabilities of rare events in complex systems in which information evolved in time. The application included the assessment of the life-cycle reliability of a structural system, the optimization of a decision on performing measurements, and the risk assessment subject to natural hazards and deterioration. Rafiq et al. (2015) developed a condition-based time-dependent deterioration modelling method at bridge group level using Bayesian network.

2.3 MIXTURE MODELS

2.3.1 Non-Bayesian Mixture Model

Generally, the standard distribution models such as the normal, lognormal, Weibull and Gumbel distribution models are widely used in describing the statistical characteristics of load- and resistance-related parameters (Catbas et al., 2008; Frangopol et al., 2008; Liu et al., 2009a). These unimodal distribution models, however, may fail to depict some complicated distributional shapes such as multimodality, skewness, or asymmetry arising from real-world

SHM data. For example, Enright and OBrien (2013) reported that the gross vehicle weights (GVW) and wheelbase data derived from WIM system in European bridges tended to display two peaks, leading to bimodal distributional curves. It indicates two classes of vehicles are predominant in the traffic volume. Similar multimodal features are also found in the vehicle speed data (Park et al., 2010). In recognising that heterogeneous populations exist in monitoring data, it is desirable to find an analytical distribution model to characterise such underlying statistical nature.

Mixture modelling technique is deemed as an ideal solution with which aforementioned random phenomena can be favourably captured. The PDF of a finite mixture distribution model can be expressed as

$$p(y|\theta) = \sum_{j=1}^{J} \omega_j f_j(y|\theta) \tag{2.2}$$

where y is the random variable arising from the finite mixture distribution, $f_j(y|\theta)$ is the jth component density indexed by parameter θ, ω_j denotes the mixing weight associated with the jth component ($0 \leq \omega_j \leq 1$ and $\sum_j \omega_j = 1$) and J is the number of components (mixture model order). Through a finite number of weighted standard component densities (e.g. Gaussian component), mixture distribution models can approach various irregular density shapes. Over the past decade, the successful applications of mixture models in statistical analysis of astronomy, biology, economics and sociology have proven its effectiveness (McLachlan and Peel, 2000; Frühwirth-Schnatter, 2006). In the context of SHM, researchers have made attempts to utilise the finite mixture distributions to model the real data sets with heterogeneity. Nair and Kiremidjian (2006) applied the Gaussian mixture distribution to model the group-shaped vibration signals for damage identification of a benchmark structure. This work showed that the change of number of mixture groups could be regarded as an indicator for damage occurrence, while damage extent could be measured by the Mahalanobis Distance between the questionable mixture and the baseline mixture. A similar study by Qiu et al. (2014) showed that Gaussian mixture distribution was able to describe the dispersed Lamb wave feature vectors. By adding new monitoring signals, damage progress of an aircraft wing spar could be evaluated through the cumulative shifting trend of the mixture contours. Farhidzadeh et al. (2013) modelled two bunch of acoustic emission parameters by a two-component Gaussian mixture distribution for performing crack mode classification. The experiment showed that the mixture model was able to detect different stages of crack growth by observing the change of mixture distribution shapes. Recently, an adaptive guided-wave Gaussian mixture model-based damage monitoring method is proposed for health monitoring of aircraft structures under time-varying conditions (Qiu et al., 2017). These meaningful researches broaden the potential values of the finite mixture models in the data-driven SHM methodology.

2.3.2 Parametric Bayesian Mixture Model

Regarding to parameter estimation and model order selection, the main task of finite mixture modelling, the existing literature mainly relies on the frequentist statistic theory (Nair and Kiremidjian, 2006; Farhidzadeh et al., 2013; Qiu et al., 2014). Based on the available training data, the mixture parameters are inferred through the maximum likelihood path (e.g. the expectation maximization algorithm) with the single optimal parameters given. Nevertheless, the drawback of the conventional frequentist approach is that the parametric uncertainty arising from limited observational data cannot be explicitly considered under such circumstances.

The Bayesian approach for mixture modelling has some unique merits in both theoretical and practical aspects. As being an incomplete data problem, the heterogeneous data are usually allocated with different component indicators so as to specify the mixture component from which each particular observation is drawn, say giving an "identity" to each observation (Dempster et al., 1977). Thus, the mixture model becomes a conditional-probability-based structure which can be best tackled in a Bayesian manner (Gelman et al., 2014). An intuitive formulation of the parametric Bayesian mixture model consisting of J components is as follows

$$
\begin{array}{ll}
\omega|\alpha \sim Dir(\alpha/J, \cdots, \alpha/J) & \theta_j^*|H \sim H \\
z_i|\omega \sim Mult(\omega) & y_i\big|z_i, \theta_j^* \sim f_j(\theta_{z_i}^*)
\end{array}
\tag{2.3}
$$

where ω is the mixing weight, α is the hyperparameter of the Dirichlet prior, H is the prior distribtion over component parameters θ_j^*, z_i is the component assignment indicator, and $f_j(\theta)$ is the component density parametrised by θ. Graphical illustration of the finite mixture model is given in Figure 2.1.

An apperant distinction from frequentist counterpart is that the Bayesian inference views the unkown mixture parameters as random variables rather than fixed quantities. By selecting appropriate conjugate prior for the mixture parameters, the joint posterior can always be approximated by the MCMC simulation techniques, with which not only the most plausible mixture parameters but also the associated uncertain bounds can be obtained (Lavine and West, 1992; Diebolt and Robert, 1994; Richardson and Green, 1997). In this sense, the Bayesian analysis of mixture model can be routinely imitated and repeated with the aid of MCMC, avioding complex high-demesional intergrals. Figueiredo et al. (2014) recently proposed a Bayesian-based procedure making use of the Markov chain Monte Carlo algorithm to cluster structural responses of bridges by accounting for eventual multimodality and heterogeneity of SHM data distribution. As compared to the widely accepted frequentist approach, there are still few demonstrations of Bayesian treatment for the SHM-based mixture modelling to date.

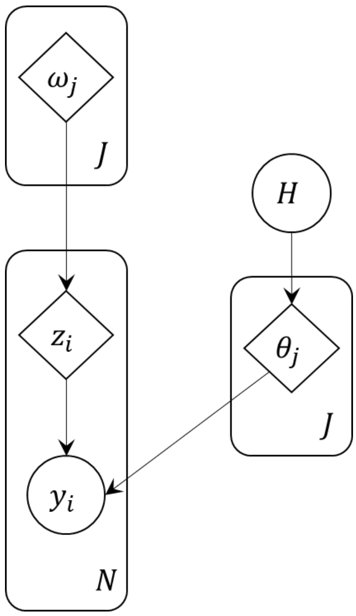

Figure 2.1 Graphical illustration of parametric Bayesian mixture model

2.3.3 Nonparametric Bayesian Mixture Model

When interpreting the training data via parametric models, certain assumptions have been made about the underlying data-generating mechanism. For example, one may raise the hypothesis that samples are drawn from a distribution family indexed with a set of finite-dimensional parameters. These probabilistic assumptions, however, are often hard to validate based on the observational data such as in-situ measurements. The nonparametric (or semiparametric) approach has long been discussed in both theoretical and practical aspects as it offers a way that one can avoid arbitrary and possibly unverifiable assumptions in the parametric approach (Ghosal and Van der Vaart, 2017). The nonparametric approach generally interprets training data over an infinite-dimensional parameter space with no need of specific parametric assumptions. A simple demonstration of the nonparametric approach can be the Parzen window method to density estimation, in which Gaussian density is placed at each observation.

Motivating by the coherent and unified framework of the Bayesian theory, the nonparametric Bayesian approach arose in the 1970s and it paves a way to consider nonparametric models under the Bayesian framework. The Bayesian approach to nonparametric problems was introduced in the pioneer work of Ferguson (1973) and further refined by the works including Antoniak (1974), Ferguson (1983) and Lo (1984). The Dirichlet process mixture (DPM) model is the representative amongst Bayesian nonparametric methods, which has been widely used in clustering. The DPM model can be written in a mixture perspective as follows

$$\begin{aligned} &\omega|\alpha \sim GEM(\alpha) && \theta_j^*|H \sim H \\ &z_i|\omega \sim Mult(\omega) && y_i\big|z_i, \theta_j^* \sim f_j(\theta_{z_i}^*) \end{aligned} \tag{2.4}$$

where GEM is the stick-breaking construction over mixing weight ω. Graphical illustration of the DPM model is given in Figure 2.2.

The DPM model is a Bayesian nonparametric model that defined on an infinite-dimensional parameter space (infinite number of components) and uses only a finite subset of the available parameters (effective components) to represent the model. Hence, the model order as measured by the effective number of components can freely adapt to the observational data. In this way, the number of components in mixture model is no longer a deterministic value but a random variable that can be directly inferred from the data. One can bypass the model order selection issue, which is usually fraught with technical difficulties. More importantly, the model order uncertainty in the mixture model can be assessed in the meantime. Quantification of both model order and parametric uncertainties of multimodal data can then be pursued. These advantages are desirable in data-driven SHM practice where different levels of uncertainties are of great concerned (Der Kiureghian, 2008; Der Kiureghian and Ditlevsen, 2009; Yuen, 2010).

In the past decade, the Bayesian nonparametric models have been successfully demonstrated in a variety of research fields (Orbanz and Teh, 2010). Orbanz and Buhmann (2008) proposed a nonparametric Bayesian model for image segmentation, in which the number of segments is automatically determined. In this work, the level of resolution is controlled by the Dirichlet process prior, which corresponds to the number of clusters in data. Huang et al. (2012) used the DPM model to discover the latent cluster structure in document clustering with feature partition. A variational inference algorithm is adopted in the DPM modelling. Mokhtarian et al. (2013) investigated the reliability estimation of railway system in component level by using the DPM model under the situation of a lack of failure data and unknown lifetime distributions. Liu et al. (2017) demonstrated the application of DPM model for anomaly detection based on numerical data as well as vibration data collected from the chemical mechanical planarization testbed. Rogers et al. (2019) proposed a Bayesian nonparametric clustering based online feature extraction technique to learn cluster of data without a training phase.

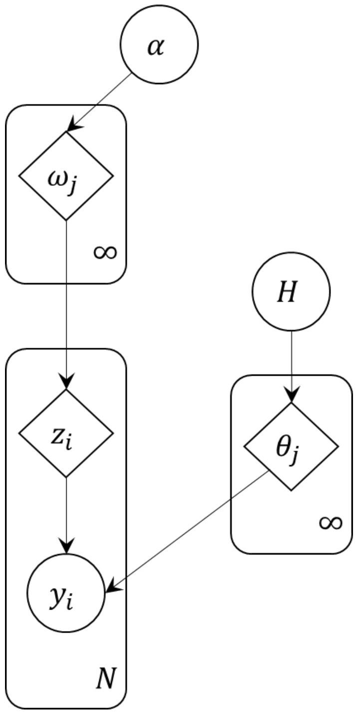

Figure 2.2 Graphical illustration of nonparametric Bayesian mixture model

CHAPTER 3
PARAMETRIC BAYESIAN MIXTURE MODEL

3.1 INTRODUCTION

As stated in Chapter 2, in-service large-scale bridges are normally subject to multiple types of live loads such as highway vehicle, railway vehicle and wind loading. These multiple types of loads are naturally time-varying with different load frequencies and amplitudes. Structural responses under the combined effect of multi-load will exhibit considerable variation both locally and globally, resulting to heterogeneous and multimodal data characteristics (Ni et al., 2011b; Ni et al., 2011c; Xu and Xia, 2011). The complex data structure imposes challenges for response interpretation and further bridge condition assessment. This chapter presents the parametric Bayesian mixture model to accommodate multimodal structural responses with considering of parametric uncertainty.

The parametric finite mixture models are ideal to capture the multimodal data structure. Through a finite number of weighted standard component densities (e.g. Gaussian component), the mixture distribution models can approach various irregular density shapes. Parameter estimation and model selection are the main tasks to finite mixture modelling. Under the conventional frequentist framework, the mixture (model) parameters are usually inferred through maximum likelihood path (e.g. the Expectation Maximization algorithm) with point estimation given (McLachlan and Peel, 2000). Nevertheless, modelling complicated data structure with only single optimal parameters could be sometimes untenable especially with limited amount of monitoring data. People tend to believe in phenomena that supported by large number of evidences. From the perspective of decision making, it is expected that the accuracy of mixture parameter estimation is reported as well (in terms of variability or a probable interval for the location of the parameter value). Thus, one of the limitations of the conventional frequentist approach is that the parametric uncertainty of mixture model cannot be explicitly treated under such circumstances.

Recently, the Bayesian perspective for mixture modelling is found of some unique advantages in both theoretical and practical ways. First, as being an incomplete data problem, the heterogeneous observations are usually allocated with different component indicators so as to specify the mixture component from which each particular observation is drawn, say giving an "identity" to each observation (Dempster et al., 1977). Thus, the mixture modelling becomes a conditional-probability-based model issue which can be best tackled in the Bayesian manner (Gelman et al., 2014). Second, by selecting appropriate conjugate prior distributions for the mixture parameters, the corresponding joint posterior distributions can always be approximated by Markov chain Monte Carlo (MCMC) simulation methods, with which not only the most plausible mixture parameters but also the associated uncertain bounds can be obtained (Lavine and West, 1992; Diebolt and Robert, 1994; Richardson and Green, 1997). In this sense, the Bayesian analysis of mixture can be routinely imitated and repeated with the aid of MCMC, avoiding complex high-dimensional integrals. Third, an apparent distinction from frequentist counterpart is that the Bayesian inference views the unknown mixture parameters (e.g.

Gaussian component mean and variance) as random variables rather than fixed quantities. More importantly, the well-recognized parametric uncertainty can be explicitly quantified, and much richer model information can be available. These advantages are desirable in SHM data analysis where different levels of uncertainties are of great concerned (Diebolt and Robert, 1994; Der Kiureghian, 2008; Der Kiureghian and Ditlevsen, 2009; Yuen, 2010).

This chapter presents the theoretical framework of parametric Bayesian mixture model, aiming at providing a new perspective for uncertainty quantification of the heterogeneous data acquired from SHM system. The content of this chapter is organized as follows. Section 3.2 gives the mathematical framework of the parametric Bayesian mixture model. A MCMC-based algorithm is proposed to progressively reach the posterior distributions of mixture parameter. Section 3.3 discusses the model selection issue. The optimal number of components is determined by comparing the Bayes factors among the candidate models. Section 3.4 investigates the effectiveness of the proposed method through numerical studies. The statistical performance of Bayesian approach is verified based on artificial mixture data sets.

3.2 MODEL FRAMEWORK

3.2.1 Finite Mixture Model

The general finite mixture distribution model has a parametric probability density function which is the form of weighted sum of J component densities. Let $p(\cdot)$ denotes the probability density function of a random variable and $\Pr(\cdot)$ denotes the probability of an event. Consider an independent random variable Y arises from the finite mixture distribution, the probability density function can be expressed as

$$p(y) = \sum_{j=1}^{J} \omega_j f_j(y) \tag{3.1}$$

where $f_j(y)$ is the jth component density and ω_j denotes the mixing weight of the jth component, satisfying $0 \leq \omega_j \leq 1$ and $\sum \omega_j = 1$. Specifically, Equation (3.1) implies that an observation comes from the jth mixture component with a probability of ω_j. In this study, the Gaussian (normal) distribution is adopted as component density, hence it becomes a finite Gaussian mixture model which can be expressed as

$$p(y; \mathbf{\Theta}) = \sum_{j=1}^{J} \omega_j N_j(y; \mu_j, \sigma_j^2) \tag{3.2}$$

where $\mathbf{\Theta}$ denotes the unknown mixture parameters comprising of the vector of mixing weights $\mathbf{\Omega} = \{\omega_1, \cdots, \omega_J\}$, vector of component means $\boldsymbol{\mu} = \{\mu_1, \cdots, \mu_J\}$ and vector of component variances $\mathbf{\Sigma} = \{\sigma_1^2, \cdots, \sigma_J^2\}$. The elements in the vector of unknown mixture parameters $\mathbf{\Theta} = \{\mu_1, \cdots, \mu_J, \sigma_1^2, \cdots, \sigma_J^2, \omega_1, \cdots, \omega_J\}$ are treated as independent random variables in the Bayesian context that needed to be estimated.

The difficulty in estimating the mixture model is the uncertainty of allocating observations to each component, say the data is incomplete as mentioned above. Therefore, the component indicator $\boldsymbol{Z}_i = (Z_{i1}, \cdots, Z_{iJ})$ is introduced for each observation y_i $(i = 1, \cdots, N)$, where Z_{ij} is defined to be one or zero depending on whether y_i comes from the jth component or not

$$Z_{ij} = \begin{cases} 1, \text{if the } i\text{th observation belongs to the } j\text{th component} \\ 0, \text{otherwise} \end{cases} \tag{3.3}$$

A graphical illustration of the component indicator is depicted in Figure 3.1. Thus $\mathbf{Z}_i$ follows a multinomial distribution

$$\mathbf{Z}_i \sim Mult(1, \boldsymbol{\Omega}) \tag{3.4}$$

and its probability mass function (PMF) can be fully expressed as

$$p(Z_{i1}, \cdots, Z_{iJ}) = \frac{1!}{0!\,1!} \omega_1^{Z_{i1}} \cdots \omega_J^{Z_{iJ}} = \omega_1^{Z_{i1}} \cdots \omega_J^{Z_{iJ}} \tag{3.5}$$

Once $\mathbf{Z}_i$ is sampled from the multinomial distribution, the allocation of each observation can be determined, therefore the Gaussian parameters of each component can be estimated accordingly. The overall unknown parameters in the finite Gaussian mixture model are

$$\begin{gathered} \boldsymbol{\Theta} = \{\boldsymbol{\mu}, \boldsymbol{\Sigma}, \boldsymbol{\Omega}\} = \{\mu_1, \cdots, \mu_J, \sigma_1^2, \cdots, \sigma_J^2, \omega_1, \cdots, \omega_J\} \text{ and} \\ \mathbf{Z} = \{\mathbf{Z}_1, \cdots, \mathbf{Z}_N\} \end{gathered} \tag{3.6}$$

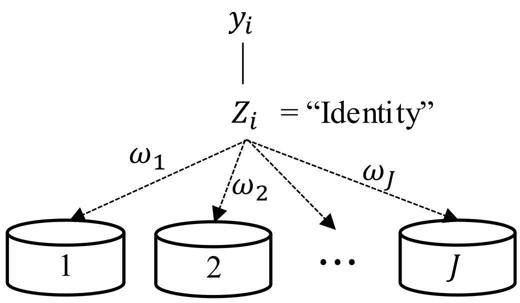

Figure 3.1 Allocating observations to each component

3.2.2 Prior Selection

The Bayes estimation for the mixture model can be well defined when the prior distributions are properly selected (McLachlan and Peel, 2000). In this study, the conjugate priors on the mixture parameters $\boldsymbol{\mu}$, $\boldsymbol{\Sigma}$ and $\boldsymbol{\Omega}$ are adopted. The use of conjugate priors allows the same distributional types for the posteriors of model parameters. Integrals in posterior inference can be sidestepped by modifying the parameters of prior distribution (so-called hyperparameters). For mixture models, the full conditional posteriors can be explicitly derived if the conjugate priors are used.

Providing that component means and variances are mutually independent over the components, the normal-inverse-chi-squared prior can be used for μ_j and σ_j^2 (Diebolt and Robert, 1994; Gelman et al., 2014)

$$\sigma_j^2 \sim InvC(\nu_j, s_j^2) \tag{3.7}$$

$$\mu_j | \sigma_j^2 \sim N(\xi_j, \sigma_j^2/\kappa_j) \tag{3.8}$$

where $\{\nu_j, s_j^2\}$ and $\{\xi_j, \kappa_j\}$ are hyperparameters of scaled inverse-chi-squared density and normal density for σ_j^2 and μ_j, respectively. The product of Equations (3.7) and (3.8) yields the joint prior distribution for (μ_j, σ_j^2)

$$\begin{aligned} p(\mu_j, \sigma_j^2) &= p(\mu_j|\sigma_j^2)p(\sigma_j^2) \\ &\propto \sigma_j^{-1}(\sigma_j^2)^{-(\nu_j/2+1)}\exp\left(-\frac{\nu_j s_j^2 + \kappa_j(\mu_j - \xi_j)^2}{2\sigma_j^2}\right) \end{aligned} \tag{3.9}$$

The mixing weights are assumed to be independent of component means and variances. Hence, a suitable conjugate prior for $\boldsymbol{\Omega}$ is the Dirichlet distribution (McLachlan and Peel, 2000)

$$\boldsymbol{\Omega} \sim Dir(\alpha_1, \cdots, \alpha_J) \tag{3.10}$$

and can be fully expressed as

$$p(\omega_1, \cdots, \omega_J) = \frac{\Gamma(\alpha_1 + \cdots + \alpha_J)}{\Gamma(\alpha_1) \cdots \Gamma(\alpha_J)} \omega_1^{\alpha_1 - 1} \cdots \omega_J^{\alpha_J - 1} \tag{3.11}$$

where α_j's are the hyperparameters for the Dirichlet distribution and $\Gamma(\cdot)$ denotes the gamma function.

3.2.3 Posterior Simulation Using Gibbs Sampler

3.2.3.1 Joint posterior distribution

After the proper selection of prior distributions, the joint posterior distribution for the mixture parameters can be derived using the Bayes' theorem

$$p(\boldsymbol{\mu}, \boldsymbol{\Sigma}, \boldsymbol{\Omega} | y) = \frac{p(y | \boldsymbol{\mu}, \boldsymbol{\Sigma}, \boldsymbol{\Omega}) p(\boldsymbol{\mu}, \boldsymbol{\Sigma}, \boldsymbol{\Omega})}{\int p(y | \boldsymbol{\mu}, \boldsymbol{\Sigma}, \boldsymbol{\Omega}) p(\boldsymbol{\mu}, \boldsymbol{\Sigma}, \boldsymbol{\Omega}) \mathrm{d}\boldsymbol{\mu} \mathrm{d}\boldsymbol{\Sigma} \mathrm{d}\boldsymbol{\Omega}} \tag{3.12}$$

where $p(\boldsymbol{\mu}, \boldsymbol{\Sigma}, \boldsymbol{\Omega})$ is the joint prior distribution, $p(y | \boldsymbol{\mu}, \boldsymbol{\Sigma}, \boldsymbol{\Omega})$ is the likelihood function of the Gaussian mixture model with the formulation of

$$p(y | \boldsymbol{\mu}, \boldsymbol{\Sigma}, \boldsymbol{\Omega}) = \prod_{i=1}^{N} \sum_{j=1}^{J} \omega_j N_j(y_i; \mu_j, \sigma_j^2) \tag{3.13}$$

and $\int p(y | \boldsymbol{\mu}, \boldsymbol{\Sigma}, \boldsymbol{\Omega}) p(\boldsymbol{\mu}, \boldsymbol{\Sigma}, \boldsymbol{\Omega}) \mathrm{d}\boldsymbol{\mu} \mathrm{d}\boldsymbol{\Sigma} \mathrm{d}\boldsymbol{\Omega}$ is the normalizing constant which is the integral over all possible values of mixture parameters.

The direct inference of the joint posterior distribution using Equation (3.12), however, is computationally intractable especially when component number is large. A feasible alternative towards the Markov chain Monte Carlo (MCMC) methods which are devised for simulation and approximation of arbitrary distributions. The basic idea behind MCMC is to generate a series of Markov chains from approximate distributions and then corrects the samples so that the limiting distributions will approach the target distributions (Robert and Casella, 1999; Frühwirth-Schnatter, 2006; Gelman et al., 2014).

3.2.3.2 Full conditional posterior distribution

The Gibbs sampler is one of the frequently used MCMC algorithm based on full conditional sampling. Note that the introduction of $\mathbf{Z}$ makes the mixture model a hierarchical conditional probability structure, therefore, one can effectively implement the Gibbs sampler as long as the full conditional posteriors can be obtained. Thus, the Gibbs sampler is chosen here to approximate the posterior distributions for mixture parameters. The implementation of the Gibbs sampler contains two major steps (Gelman et al., 2014).

- Sampling from the full conditional posterior distributions of mixture parameters $\mathbf{\Theta}$ given current component indicators $\mathbf{Z}$; and
- Sampling from the full conditional posterior distribution of the component indicators $\mathbf{Z}$ given current mixture parameters $\mathbf{\Theta}$.

The full conditional posterior distributions of the unknown parameters are derived using the Bayes' theorem as follows.

Given the component indicator $\mathbf{Z}$, say the allocation of observations are known at the moment, the Gaussian mixture model reduces to J independent Gaussian components in which each pair of Gaussian parameters μ_j and σ_j^2 can be estimated separately and straightforward. For

jth component, multiplying the joint prior distribution of Equation (3.9) by the normal likelihood function yields the joint posterior distribution for (μ_j, σ_j^2)

$$\begin{aligned} p(\mu_j, \sigma_j^2 | y_{i\in j}, \mathbf{Z}) &\propto \sigma_j^{-1}(\sigma_j^2)^{-(\nu_j/2+1)} \exp\left(-\frac{\nu_j s_j^2 + \kappa_j(\mu_j - \xi_j)^2}{2\sigma_j^2}\right) \\ &\times (\sigma_j^2)^{-n_j/2} \exp\left(-\frac{1}{2\sigma_j^2}\left(\sum_{i\in j}(y_i - \bar{y}_j)^2 + n_j(\bar{y}_j - \mu_j)^2\right)\right) \end{aligned} \tag{3.14}$$

where $y_{i\in j}$ represents the observations that has been assigned to the jth component, n_j is the number of $y_{i\in j}$ and $\bar{y}_j$ is the sample mean of $y_{i\in j}$. Again Equation (3.14) is the normal-inverse-chi-squared distribution because of the conjugacy. The conditional posterior distribution of μ_j given σ_j^2 is proportional to the joint posterior distribution with σ_j^2 holding constant, which is the normal density

$$\begin{gathered} \mu_j | \sigma_j^2, y_{i\in j}, \mathbf{Z} \sim N(\xi_j^*, \sigma_j^2/\kappa_j^*) \\ \text{with } \xi_j^* = \frac{\kappa_j \xi_j + n_j \bar{y}_j}{\kappa_j + n_j} \text{ and} \\ \kappa_j^* = \kappa_j + n_j \end{gathered} \tag{3.15}$$

Then the marginal posterior distribution of σ_j^2 can be derived by integrating the joint posterior distribution over μ_j, which is the scaled inverse-chi-squared density

$$\begin{gathered} \sigma_j^2 | y_{i\in j}, \mathbf{Z} \sim InvC(\nu_j^*, s_j^{2*}) \\ \text{with } \nu_j^* = \nu_j + n_j \text{ and} \end{gathered} \tag{3.16}$$

$$s_j^{2*} = \frac{1}{\nu_j + n_j}\left(\nu_j s_j^2 + \sum_{i\in j}(y_i - \bar{y}_j)^2 + \frac{\kappa_j n_j}{\kappa_j + n_j}(\bar{y}_j - \xi_j)^2\right)$$

The posterior distribution of mixing weights $\mathbf{\Omega}$ are derived by use of the Bayes' theorem

$$\begin{aligned} p(\mathbf{\Omega}|y,\mathbf{Z}) &\propto p(y,\mathbf{Z}|\mathbf{\Omega})p(\mathbf{\Omega}) \\ &= \omega_1^{\sum Z_{i1}} \cdots \omega_J^{\sum Z_{iJ}} \times \omega_1^{\alpha_1 - 1} \cdots \omega_J^{\alpha_J - 1} \\ &= \omega_1^{n_1} \cdots \omega_J^{n_J} \times \omega_1^{\alpha_1 - 1} \cdots \omega_J^{\alpha_J - 1} \\ &= \prod_{j=1}^{J} \omega_j^{\alpha_j + n_j - 1} \end{aligned} \tag{3.17}$$

which has exactly the form of the Dirichlet distribution. Hence, it can be expressed as

$$\mathbf{\Omega}\big|y,\mathbf{Z} \sim Dir(\alpha_1 + n_1, \cdots, \alpha_J + n_J) \tag{3.18}$$

Comparing the algebraic forms of the posterior distributions to the prior distributions on $\boldsymbol{\mu}$, $\mathbf{\Sigma}$ and $\mathbf{\Omega}$, it is observed that the hyperparameters of posteriors contain both the information from priors and the observations.

Now we focus on the posterior distribution of the component indicator $\mathbf{Z}$ given the mixture parameters $\mathbf{\Theta}$. Equation (3.4) indicates that the distribution of $\mathbf{Z}_i$ relies on the mixing weights which shall be updated when mixture parameters are given. Thus, posterior distribution of $\mathbf{Z}_i$ for observation y_i can be expressed as

$$\mathbf{Z}_i \sim Mult(1, \boldsymbol{\tau}_i) \tag{3.19}$$

where $\boldsymbol{\tau}_i = (\tau_{i1}, \cdots, \tau_{iJ})$ is the updated mixing weight vector. The jth element in updated mixing weight vector τ_{ij} represents the posterior probability that y_i belongs to the jth component with y_i having been observed on it. By the Bayes' theorem, τ_{ij} can be calculated as

$$\begin{aligned}\tau_{ij} = \Pr(Z_{ij} = 1 | y_i) &= \frac{\Pr(y_i | Z_{ij} = 1) \Pr(Z_{ij} = 1)}{\sum_{j=1}^{J} \Pr(y_i | Z_{ij} = 1) \Pr(Z_{ij} = 1)} \\ &= \frac{N_j(y_i; \mu_j, \sigma_j^2)\omega_j}{\sum_{j=1}^{J} N_j(y_i; \mu_j, \sigma_j^2)\omega_j}\end{aligned} \tag{3.20}$$

Note that ω_j is viewed as the prior probability that y_i belongs to the jth component.

3.2.3.3 Gibbs sampler

After obtaining the above full conditional posterior distributions for all unknown parameters, the procedures of Gibbs sampler for the Gaussian mixture model can be summarized as the flow chart of Figure 3.2. Repeating the process, say $t = 1, \cdots, T$, the Gibbs sampler proceeds by generating random samples successively from the full conditional posterior distributions and replacing the conditioning parameters. Early draws of the Gibbs sampler, however, may still reflect the starting approximation rather than the target distributions. Convergence of the Gibbs sampler should be paid more attention, which is discussed in Section 3.2.4.

After discarding a number of early draws, here refer to burn-in samples B, the $G = T - B$ random samples can be regarded as the samples from the joint posterior distribution of mixture parameters. With the collection of posterior samples, the posterior distributions can be summarised and the moments, quantiles and other statistic metrics of interest can be obtained. In this study, the most plausible mixture parameters can be estimated by the posterior sample means

$$\mathbf{\Theta}^{\star} = G^{-1} \sum_{g=1}^{G} \mathbf{\Theta}^{(g)} \tag{3.21}$$

where $\mathbf{\Theta}^{(g)}$ are the Gibbs outputs. The parametric uncertainty can then be characterized by standard deviations (SD) or credible intervals (CI) of the posterior samples. It should be noted that, to start the Gibbs sampler, crude estimates for mixture parameters and relative proportions of observations in each component are needed (e.g. n_j, $\mathbf{Z}$ and ω_j). Hence, the K-means algorithm (Bishop, 2006) for parameter initialization is adopted here with which the parameter guesses will be closer to target values and the Markov chains can converge faster.

3.2.4 Quantitative Convergence Diagnosis

The nature of MCMC implies that the convergence on the Markov chain is of first concerned. Once the chains are converged, the samples can then be representative of the target distributions, in our case, the posterior distributions of the parameters. Two practical tools are widely used to check the convergence issue. With the display of iteration plots of the simulated Markov chain, one can perform visual inspection on the chain to determine the convergence. It is commonly acceptable that convergence is reached when the chain fluctuates within a certain region. Thus, longer iterations are needed to examine the stationarity of the chain. Although the direct visual inspection is easy to implement, it can be sometimes unreliable as subjective monitoring of the convergence is still a puzzling task. Moreover, it fails to distinguish local and global convergence in some cases (Gelman et al., 2014).

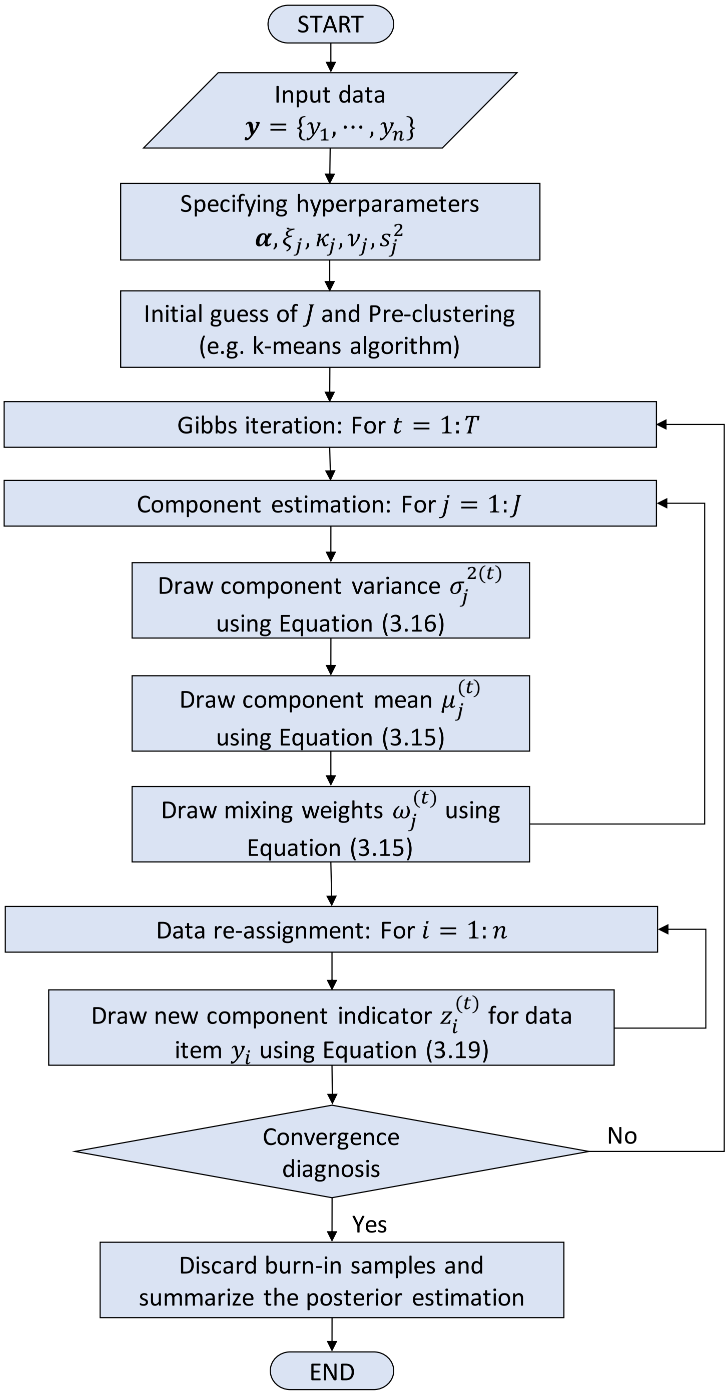

Figure 3.2 Flow chart of Gibbs sampler for mixture model

Another way to diagnose convergence is based on quantitative criteria. Based on the posterior sequences, the quantitative indicators tend to stabilize as the Markov chain convergence. Gelman et al. (2014) proposed the potential scale reduction factor R_0, which is a good indicator for convergence diagnosis by comparing between- and within-sequence variances. It works with simultaneously running several parallel chains from dispersed starting points. Suppose the Gibbs outputs of mixture parameter θ are being examined with the simulations labelled as θ_{tq} $(t = 1, \cdots, T; q = 1, \cdots, Q)$ where T is total number of iterations and Q is the number of parallel chains. The potential scale reduction factor is calculated as

$$R_0 = \sqrt{\frac{T-1}{T} + \frac{V_b}{TV_w}} \tag{3.22}$$

where V_b is the between-sequence variance

$$V_b = \frac{T}{Q-1}\sum\nolimits_{q=1}^{Q}\left(\bar{\theta}_q - \bar{\theta}\right)^2$$
$$\text{with } \bar{\theta}_q = T^{-1}\textstyle\sum_{t=1}^{T}\theta_{tq} \text{ and } \bar{\theta} = Q^{-1}\sum_{q=1}^{Q}\bar{\theta}_q \tag{3.23}$$

and V_w is the within-sequence variance

$$V_w = Q^{-1}\sum_{q=1}^{Q} s_q^2$$
$$\text{with } s_q^2 = \tfrac{1}{T-1}\textstyle\sum_{t=1}^{T}(\theta_{tq} - \bar{\theta}_q)^2 \tag{3.24}$$

After sufficient iterations, the parallel chains from dispersed starting points will properly mix together, indicating the convergence of chains to the same target distribution. Meanwhile, the factor of R_0 declines to 1 as $T \to \infty$. In this study, the convergence monitoring is performed by running two chains for each mixture parameter and convergence is reached when R_0 for all parameters drop to below 1.001.

3.3 MODEL SELECTION USING BAYES FACTOR

3.3.1 Bayes Factor

The determination of component number J in mixture model is a model selection problem, which can be addressed by the various model selection criteria. In Bayesian analysis, model comparison can be implemented by Bayes factor (Chib, 1995; Frühwirth-Schnatter, 2006; Gelman et al., 2014). Suppose two competing models M_1 and M_2 are interested, the Bayes factor (BF) is defined as

$$\mathrm{BF}(M_1; M_2) = \frac{p(y|M_1)}{p(y|M_2)} = \frac{\int p(y|\boldsymbol{\theta}_1, M_1)p(\boldsymbol{\theta}_1|M_1)\mathrm{d}\boldsymbol{\theta}_1}{\int p(y|\boldsymbol{\theta}_2, M_2)p(\boldsymbol{\theta}_2|M_2)\mathrm{d}\boldsymbol{\theta}_2} \tag{3.25}$$

where $p(y|M_i) = \int p(y|\boldsymbol{\theta}_i, M_i)p(\boldsymbol{\theta}_i|M_i)\mathrm{d}\boldsymbol{\theta}_i$ is the marginal likelihood (same as normalizing constant) of model M_i $(i = 1,2)$, $p(y|\boldsymbol{\theta}_i, M_i)$ and $p(\boldsymbol{\theta}_i|M_i)$ are the likelihood function and prior density under model M_i $(i = 1,2)$, respectively. If the observations y are more likely come from model M_i, then the associated marginal likelihood $p(y|M_i)$ will be large, and vice versa. Thus, a Bayes factor $\mathrm{BF}(M_1; M_2) > 1$ implies that model M_1 is more plausible than M_2 in predicting observation data. For multiple candidate model case, e.g. the selection of optimal component number in mixture model, it is usually more convenient to compare the logarithm of the marginal likelihood $\ln p(y|M_i)$ (LML) of each model, then optimal model is the one with maximum LML value.

3.3.2 Marginal Likelihood Based on Chib's Method

The calculation of the marginal likelihood $p(y|M_i)$ which involves integration over high dimensional parameter space and is usually analytical untraceable for complex models. Many numerical approximations have been developed for solving the marginal likelihood as introduced in Frühwirth-Schnatter (2006). In this mixture model selection problem, the marginal likelihood is estimated using the Chib's method (Chib, 1995) which is based on the Gibbs outputs and Monte Carlo estimate.

Recall from Equation (3.12), the marginal likelihood can be rewritten as

$$p(y|M) = \frac{p(y|\mathbf{\Theta})p(\mathbf{\Theta})}{p(\mathbf{\Theta}|y)} \tag{3.26}$$

where the numerator is the product of likelihood and the prior density, and the denominator is the posterior density under model M. Note that this identity holds for any $\mathbf{\Theta}$ and an efficient choice is to select the posterior mean values $\mathbf{\Theta}^\star$ to estimate marginal likelihood since the density functions have more accurate estimation at the high density points. Then the log marginal likelihood (LML) evaluated at $\mathbf{\Theta}^\star$ is given as

$$\ln p(y|M) = \ln p(y|\mathbf{\Theta}^\star) + \ln p(\mathbf{\Theta}^\star) - \ln p(\mathbf{\Theta}^\star|y) \tag{3.27}$$

The first two terms on the right hand side of Equation (3.27), i.e. the log likelihood and the log prior density, can be readily evaluated by using Equations(3.28) and (3.29)

$$\ln p(y|\mathbf{\Theta}^\star) = \sum_{i=1}^{N}\left(\ln\sum_{j=1}^{J}\omega_j^\star N_j(y_i;\mu_j^\star,\sigma_j^{2\star})\right) \tag{3.28}$$

$$\begin{aligned}\ln p(\mathbf{\Theta}^\star) &= \ln p(\mathbf{\Sigma}^\star) + \ln p(\boldsymbol{\mu}^\star|\mathbf{\Sigma}^\star) + \ln p(\mathbf{\Omega}^\star)\\ &= \sum_{j=1}^{J}\ln p(\sigma_j^{2\star}) + \sum_{j=1}^{J}\ln p(\mu_j^\star|\sigma_j^{2\star}) + \ln p\left(\omega_1^\star,\cdots,\omega_J^\star\right)\end{aligned} \tag{3.29}$$

The third term is the log posterior density which has implicit and high dimensional form, thus it cannot be directly calculated. As suggested by Chib (1995), the joint posterior density can be partitioned into the following three terms

$$\begin{aligned}\ln p(\boldsymbol{\Theta}^{\star}|y) &= \ln p(\boldsymbol{\mu}^{*}, \boldsymbol{\Sigma}^{*}, \boldsymbol{\Omega}^{*}|y) \\ &= \ln p(\boldsymbol{\Sigma}^{*}|y) + \ln p(\boldsymbol{\mu}^{*}|y, \boldsymbol{\Sigma}^{*}) + \ln p(\boldsymbol{\Omega}^{*}|y, \boldsymbol{\mu}^{*}, \boldsymbol{\Sigma}^{*})\end{aligned} \tag{3.30}$$

where each of these terms can be approximated by the Gibbs outputs. Detailed expressions and procedure are described as follows. Run Gibbs sampler for current mixture model M with J components. The approximate Monte Carlo estimate of the first term $p(\boldsymbol{\Sigma}^{\star}|y)$ is

$$\begin{aligned}p(\boldsymbol{\Sigma}^{\star}|y) &\approx G^{-1}\sum_{g=1}^{G} p\left(\boldsymbol{\Sigma}^{\star}|y, \mathbf{Z}^{(g)}\right) \\ &\approx G^{-1}\sum_{g=1}^{G}\left(\prod_{j=1}^{J} InvC(\sigma_j^{2\star}; v_j^{*(g)}, s_j^{2*(g)})\right)\end{aligned} \tag{3.31}$$

where $\mathbf{Z}^{(g)}$ is the initial G Gibbs outputs after discarding the burn-in samples. Then set $\boldsymbol{\Sigma} = \boldsymbol{\Sigma}^{\star}$ and continue to run additional G iterations of the Gibbs sampler in which the full conditional densities are

$$p(\boldsymbol{\mu}|y, \boldsymbol{\Sigma}^{\star}, \mathbf{Z}),\ p(\boldsymbol{\Omega}|y, \mathbf{Z}) \text{ and } p(\mathbf{Z}|y, \boldsymbol{\mu}, \boldsymbol{\Sigma}^{\star}, \boldsymbol{\Omega}) \tag{3.32}$$

The Gibbs output of the second stage can be used to estimate the second term $p(\boldsymbol{\mu}^{\star}|y, \boldsymbol{\Sigma}^{\star})$:

$$\begin{aligned}p(\boldsymbol{\mu}^{\star}|y, \boldsymbol{\Sigma}^{\star}) &\approx G^{-1}\sum_{g=1}^{G} p\left(\boldsymbol{\mu}^{\star}|y, \boldsymbol{\Sigma}^{\star}, \mathbf{Z}^{(g)}\right) \\ &\approx G^{-1}\sum_{g=1}^{G}\left(\prod_{j=1}^{J} N(\mu_j^{\star}; \xi_j^{*(g)}, \sigma_j^{2\star}/\kappa_j^{*(g)})\right)\end{aligned} \tag{3.33}$$

Let $\boldsymbol{\Sigma} = \boldsymbol{\Sigma}^{\star}$ and $\boldsymbol{\mu} = \boldsymbol{\mu}^{\star}$, continue again to run additional G iterations of the Gibbs sampler with the full conditional densities

$$p(\mathbf{\Omega}|y, \mathbf{Z}) \text{ and } p(\mathbf{Z}|y, \boldsymbol{\mu}^\star, \boldsymbol{\Sigma}^\star, \mathbf{\Omega}) \tag{3.34}$$

The Gibbs outputs of the third stage can be used to estimate the third term $p(\mathbf{\Omega}^\star|y, \boldsymbol{\mu}^\star, \boldsymbol{\Sigma}^\star)$:

$$\begin{aligned} p(\mathbf{\Omega}^\star|y, \boldsymbol{\mu}^\star, \boldsymbol{\Sigma}^\star) &\approx G^{-1}\sum_{g=1}^{G} p\left(\mathbf{\Omega}^\star|y, \boldsymbol{\mu}^\star, \boldsymbol{\Sigma}^\star, \mathbf{Z}^{(g)}\right) \\ &\approx G^{-1}\sum_{g=1}^{G} D(\mathbf{\Omega}^*; \alpha_1 + n_1^{(g)}, \cdots, \alpha_J + n_J^{(g)}) \end{aligned} \tag{3.35}$$

Substituting the estimates of Equations (3.31), (3.33) and (3.35) into Equation (3.30) gives the joint posterior density evaluated at $\mathbf{\Theta}^\star$. Together with Equations (3.28) and (3.29), the log marginal likelihood of model M can be calculated by using Equation (3.27).

3.4 NUMERICAL VERIFICATION

3.4.1 Generation of Data Sets

The effectiveness of the proposed Bayesian mixture modelling approach is verified through numerical studies. The verification is based on the artificial data sets generated from predefined mixture distributions with given model parameters. Two scenarios are considered in this study as illustrated in Table 3.1.

Table 3.1 Artificial mixture data sets with predefined model parameters

Comp.	Parameter μ	Parameter σ^2	Parameter ω	Sample size	Scenario
No. 1	1.000	0.200	0.600	2000	No. 1
No. 2	5.000	2.000	0.200		
No. 3	10.000	1.000	0.200		
		Case 2-1		1000	No. 2
No. 1	1.000	1.500	0.500		
No. 2	1.000	1.500	0.500		
		Case 2-2			
No. 1	1.000	1.500	0.500		
No. 2	2.000	1.500	0.500		
		Case 2-3			
No. 1	1.000	1.500	0.500		
No. 2	3.000	1.500	0.500		
		Case 2-4			
No. 1	1.000	1.500	0.500		
No. 2	4.000	1.500	0.500		
		Case 2-5			
No. 1	1.000	1.500	0.500		
No. 2	5.000	1.500	0.500		
		Case 2-6			
No. 1	1.000	1.500	0.500		
No. 2	6.000	1.500	0.500		
		Case 2-7			
No. 1	1.000	1.500	0.500		
No. 2	7.000	1.500	0.500		
		Case 2-8			
No. 1	1.000	1.500	0.500		
No. 2	8.000	1.500	0.500		

In Scenario 1, a trimodal data set is generated and the Bayesian estimation of this mixture model is testified. In Scenario 2, eight sets of bimodal data with shifted second component mean are generated to investigate the performance of the Bayesian approach in terms of estimation error. Note that the component number of the mixture model is assumed to be known in all numerical studies. Thus, model selection is not included in this chapter. In Chapter 6, the model selection procedure is demonstrated to identify component number of multimodal stress data.

3.4.2 Estimation of Trimodal Data Set

The trimodal data set with the sample size of 2000 is generated according to the PDF as follows

$$p(y;\mathbf{\Theta}) = 0.6N_1(y;1,0.2) + 0.2N_2(y;5,2) + 0.2N_3(y;10,1) \tag{3.36}$$

The diffuse prior densities are selected since no prior information is available for the unknown mixture parameters. Herein, the hyperparameters are set to $\nu_j = 2$, $s_j^2 = var(y) \times \nu_j$, $\xi_j = mean(y)$, $\kappa_j = 1$ and $\alpha_j = 5$ for all components.

The Gibbs sampler is set to run for $T = 10000$ iterations for each mixture parameter with two parallel chains. Figure 3.3 plots the Gibbs run for component means in the first 1000 iterations as initial stage. It is clear to see each pair of chains with dispersed starting points mix together quickly and reach stationary afterwards. Simulations of other parameters have similar behaviour. To check the convergence of simulations, the potential scale reduction factor R is monitored through the Gibbs run as illustrated in Figure 3.4. Quick drops of R for all mixture parameters can be observed, indicating the simulations are converged globally. Table 3.2 reveals that convergence of component means is the fastest with about only 150 iterations needed, following by component variance with about 200 iterations needed, while convergence of mixing weights is the slowest with about 700 iterations needed.

Based on the convergence results, the burn-in sequence for Gibbs iterations for this trimodal mixture model is determined as $B = 1000$. Then the rest of $G = T - B = 9000$ Gibbs outputs are deemed as samples from target distributions and can be used as posterior samples for parameter estimation. Note that samples from any single chain are enough for posterior summary and parameter estimation. Figure 3.5 plots the full Gibbs run with the initial burn-in samples and the remaining posterior samples.

The posterior sample means and associated 95% credible intervals for all mixture parameters are summarized in Table 3.3. The 'true' (predefined) parameter values are also listed in the table as the reference values. It is first observed that all the posterior sample means are very close to the 'true' values. The estimates of component means and mixing weights have better accuracy than the estimates of component variances. The 95% CIs quantify the variation of the parameter estimations, giving the extent of uncertainty on mixture parameters. Note that the 1st component means and variances (blue plots) are less uncertain than that of the 2nd and 3rd component (green and red plots) as the 95% CIs are relatively smaller, and recall that the 1st component has larger mixing weights than the other two components, thus it is reasonable to infer that increasing sample size helps to reduce the parametric uncertainty of component means and variances. The mixing weights, however, are less sensitive to sample size. Besides, component variances have the overall larger CIs (much more fluctuating of the chain plots) than component means and mixing weights.

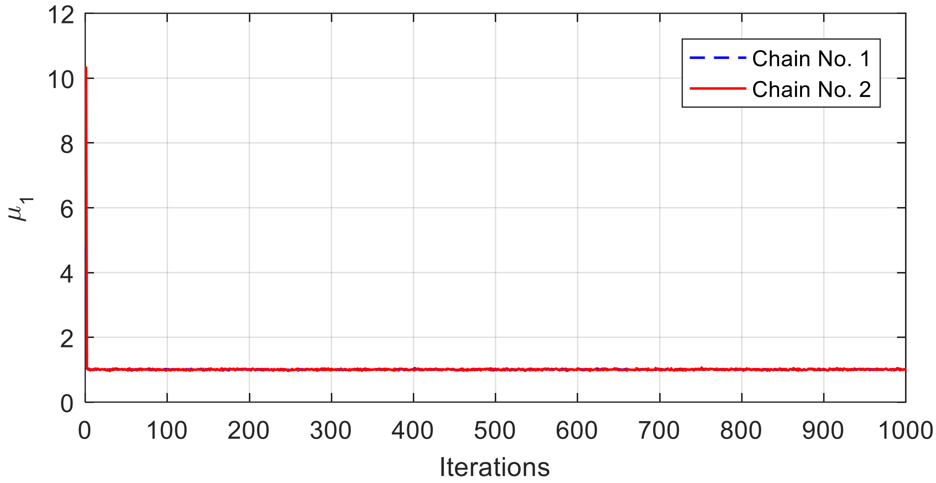

a) Parallel chains for μ_1

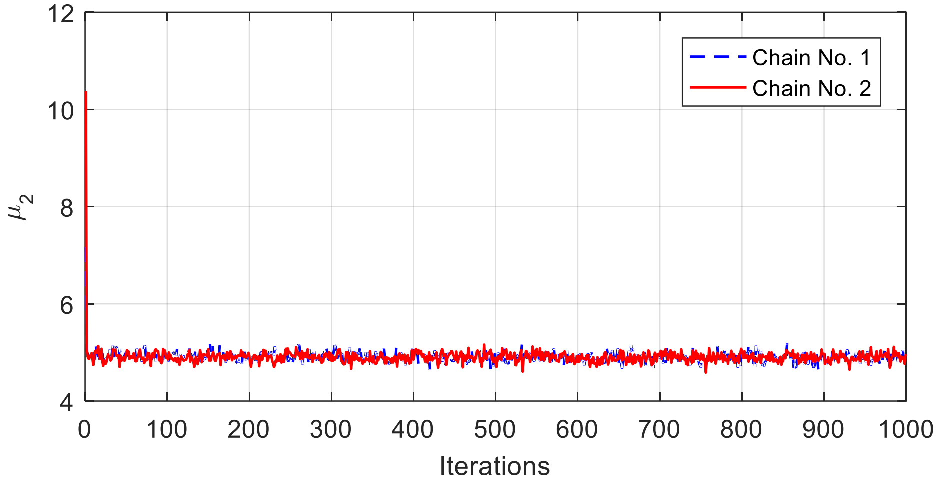

b) Parallel chains for μ_2

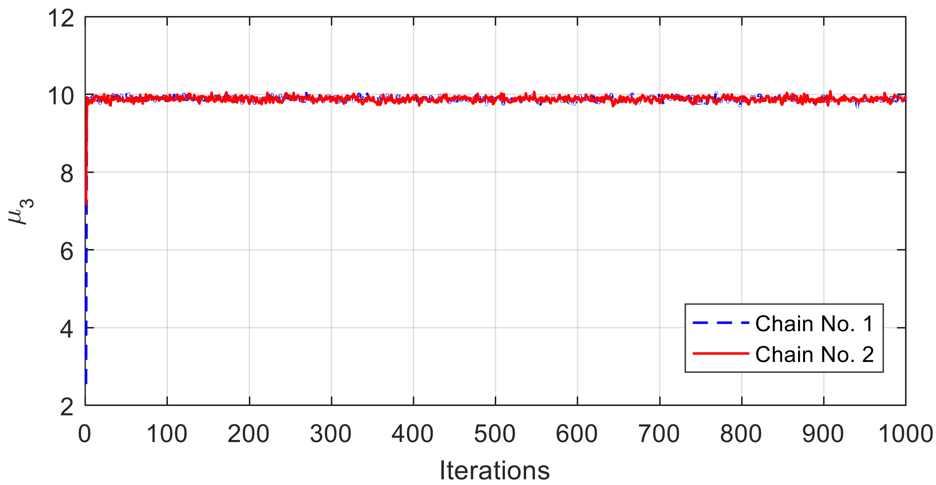

c) Parallel chains for μ_3

Figure 3.3 Initial Gibbs iterations for convergence diagnosis

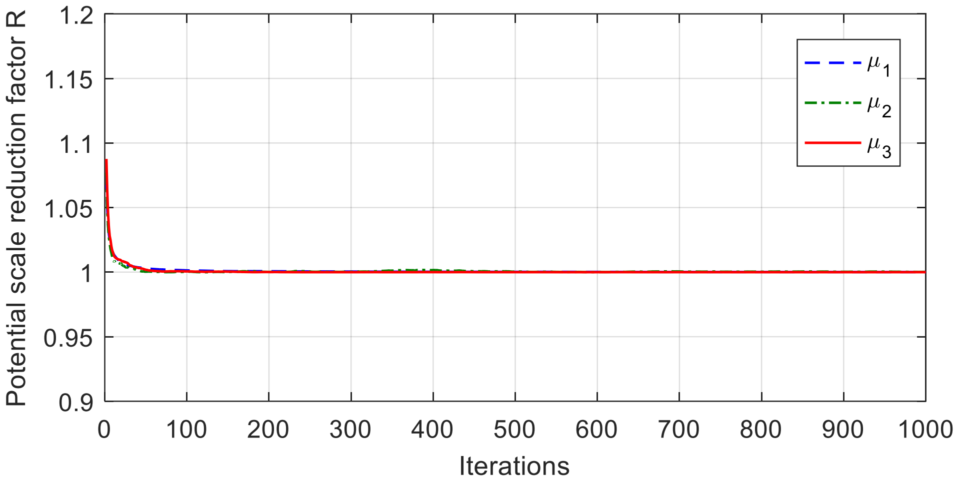

a) convergence of component means

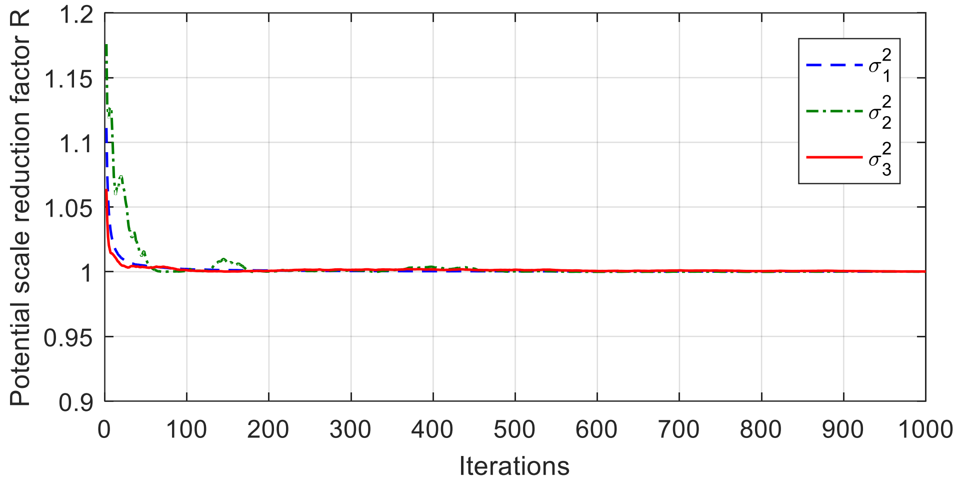

b) convergence of component variance

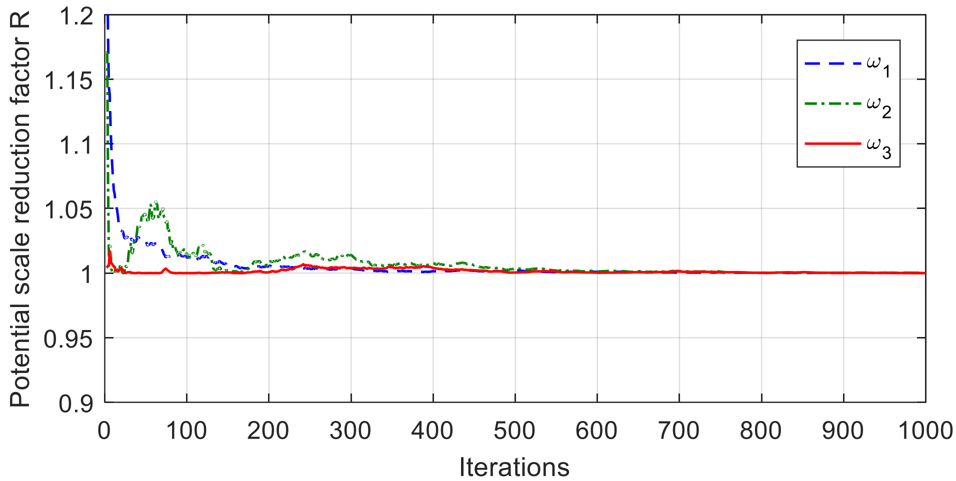

c) convergence of component weights

Figure 3.4 Convergence diagnosis based on potential scale reduction factor

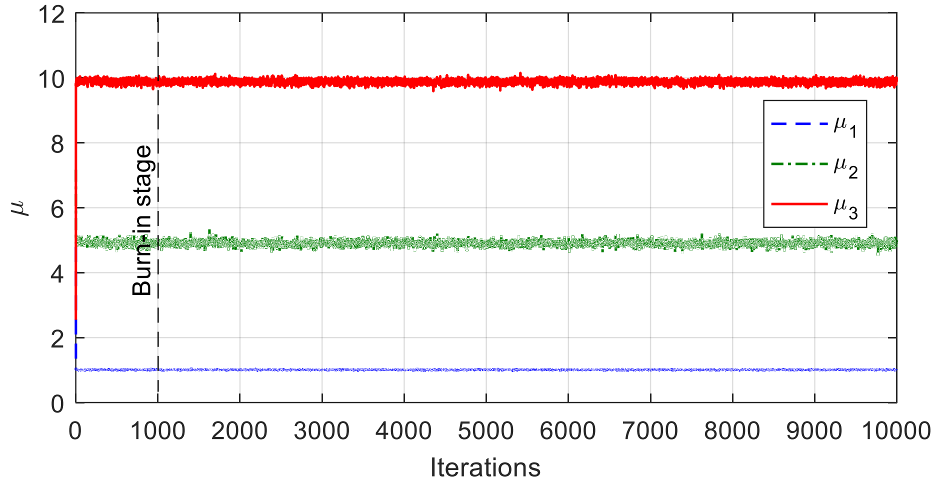

a) iterations of component means

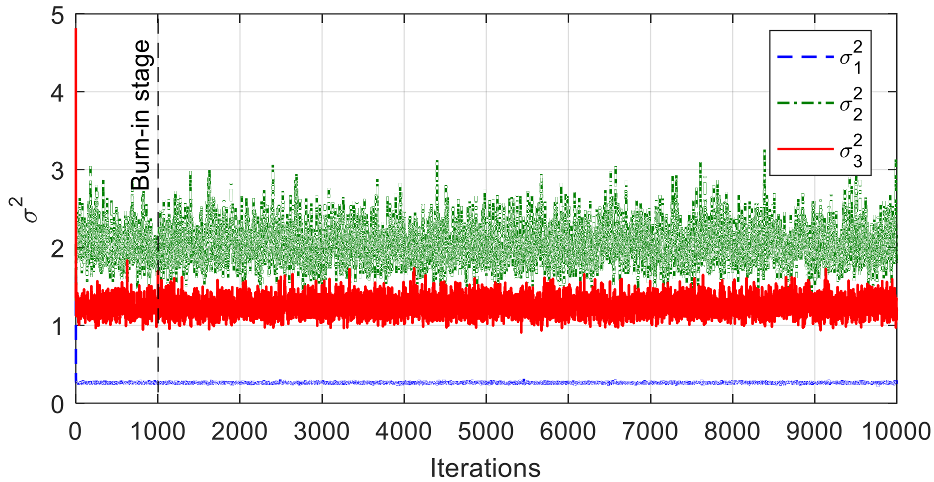

b) iterations of component variance

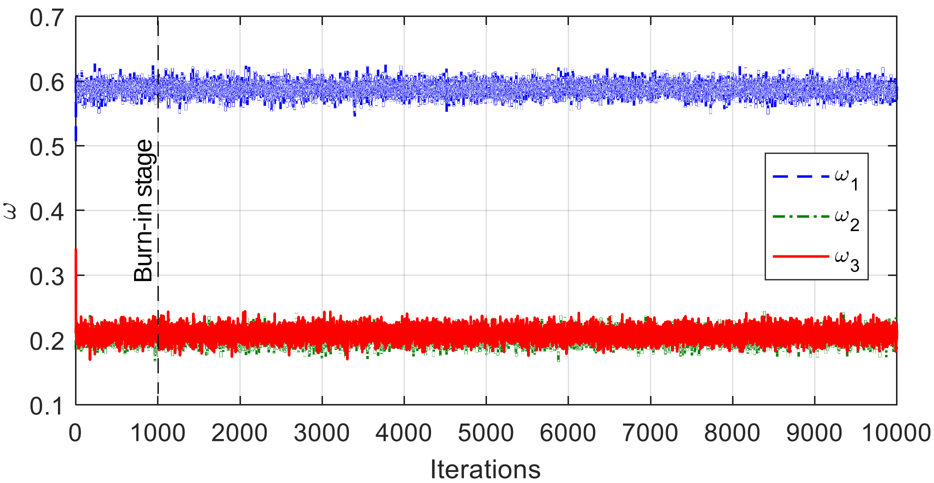

c) iterations of component weights

Figure 3.5 Gibbs run for posterior distributions of mixture parameters

Table 3.2 Convergence statistics for trimodal mixture model

Comp.	Parameter μ	Parameter σ^2	Parameter ω
	Gibbs iterations needed to reach convergence ($R < 1.001$)		
No. 1	128	185	382
No. 2	42	175	641
No. 3	59	102	486

Table 3.3 Bayesian estimation of the trimodal mixture model

Comp.	Parameter μ			Parameter σ^2			Parameter ω		
	5%	Mean	95%	5%	Mean	95%	5%	Mean	95%
					Bayesian estimation				
No. 1	0.982	1.007	1.033	0.243	0.262	0.282	0.569	0.588	0.606
No. 2	4.752	4.902	5.504	1.661	2.033	2.486	0.187	0.203	0.221
No. 3	9.774	9.880	9.986	1.073	1.244	1.436	0.193	0.209	0.225
					Given model parameters				
No. 1		1.000			0.200			0.600	
No. 2		5.000			2.000			0.200	
No. 3		10.000			1.000			0.200	

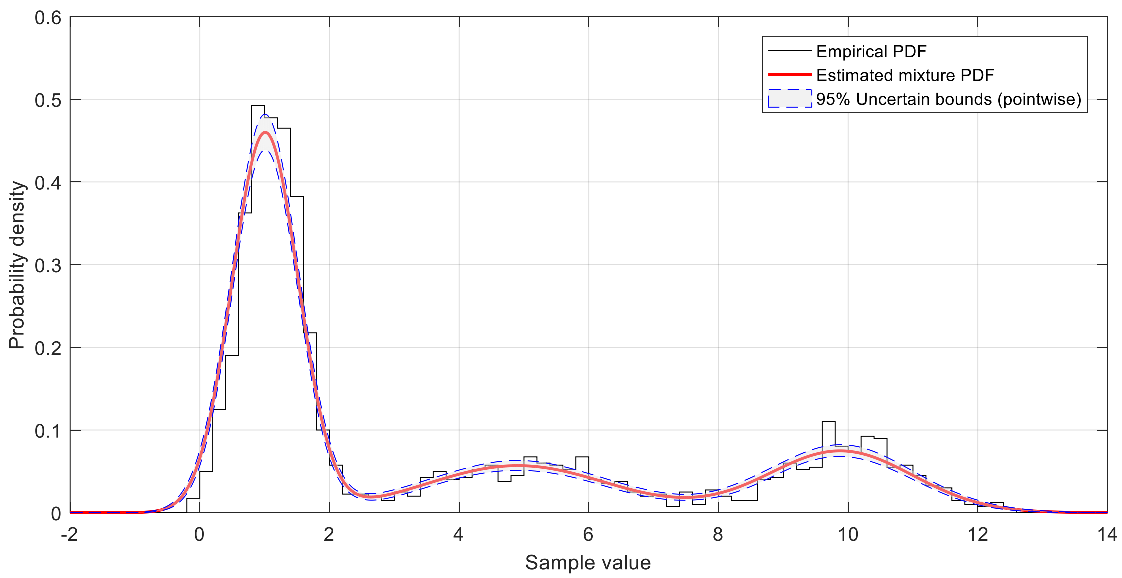

Figure 3.6 Estimated mixture PDF and associated uncertain bounds for trimodal data set

The estimated trimodal mixture PDF can be constructed based on the posterior sample means of the mixture parameters. Using the results in Table 3.3, the estimated PDF curve has a good fitting with the trimodal data set as shown in Figure 3.6. The pointwise uncertain bounds for the mixture PDF are also provided based on the posterior samples of mixture parameters. The uncertain bounds characterize the variability of PDF due to parametric uncertainty.

3.4.3 Performance of Bayesian Approach

The bimodal data sets with each sample size of 1000 are generated according to the PDFs as follows

$$p(y;\mathbf{\Theta}) = 0.5N_1(y;1,1.5) + 0.5N_2(y;\mu_2,1.5) \tag{3.37}$$

where μ_2 is predefined to vary from 1.0 to 8.0 with the step of 1.0. A total of eight sample sets are then used to investigate the performance of the Bayesian approach, where the bimodal distributions range from completely overlapped to completely separated with the shift of μ_2. The prior specification follows the same in Scenario number 1 and the Gibbs sampler is setting with $T = 10000$ and $B = 1000$ after checking the convergence. All eight sets of model parameters are uniquely identified by the Bayesian approach. The relative errors between the Bayesian estimates (posterior means) and the 'true' (predefined) parameter values are used as a measure of performance for the proposed Bayesian approach

$$\varepsilon = \frac{|\theta^{\star} - \theta|}{\theta} \times 100\% \tag{3.38}$$

Noted that as the sample size approaches to infinite, the Bayesian posterior mean converge to the given 'true' parameter value based on the law of large numbers, thus the relative error ε goes to zero.

The relative errors of parameter estimations are calculated as shown in Figure 3.7. The relative errors for most cases are acceptable except for two largely overlapped cases $\mu_2 = 2.0$ and $\mu_2 = 3.0$, where the errors of component means and component variances are around 30% to 50%. Checking with the Gibbs outputs indicates that the label switching occurs in these two cases along with the case of $\mu_2 = 1.0$ rather than others during the iterations. Label switching is a common issue in Bayesian mixture analysis where the labels of components can interchange frequently, leading to difficulties in summarizing the posterior samples. It arises because of the invariance of the mixture likelihood to component permutations (Gelman et al., 2014). Note that the case of $\mu_2 = 1.0$ stands as a special one with low relative errors. The reason is that although label switching is existed, the switching happens between two identical labels ($\mu_1 = \mu_2 = 1.0$), leading to no adverse influence on posterior summaries. Therefore, the numerical study indicates that label switching can be avoided when two components are well separated, but tends to occur when two components largely overlap with each other. Apart from that, the trends of the relative errors with respect to the shift of μ_2 give some new insights into the performance of the proposed Bayesian approach. With the increase of μ_2, say two component centroids become apart, better estimates of the component means, component variances and mixing weights can be obtained as the relative errors decrease gradually. Similar to the trimodal example, the component means and mixing weights have the overall better estimation accuracy than the component variances.

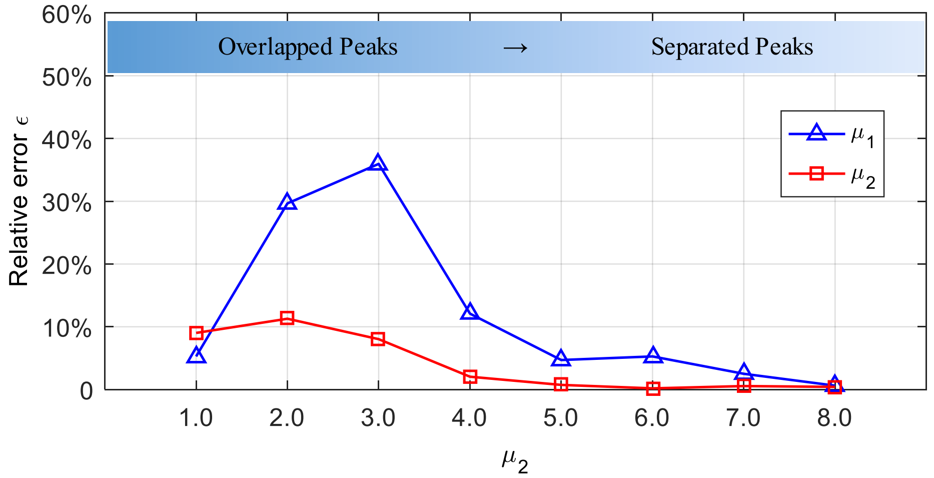

a) relative errors of component means

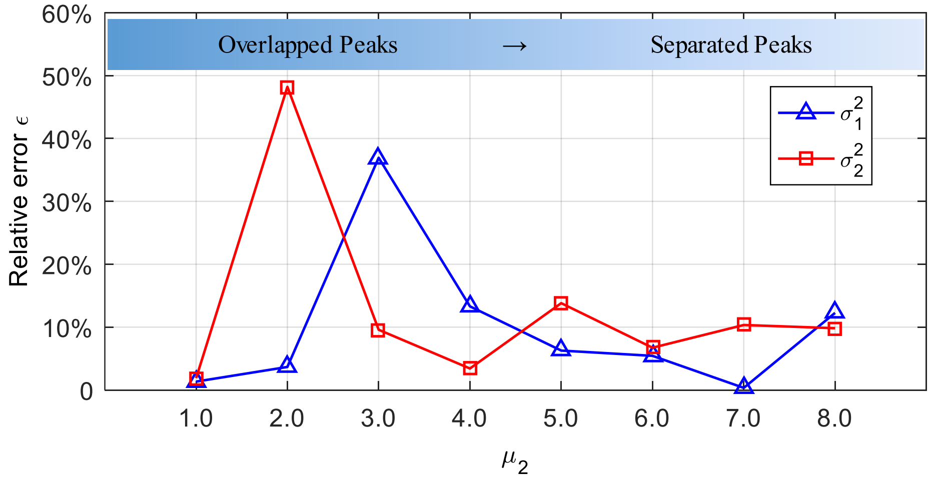

b) relative errors of component variances

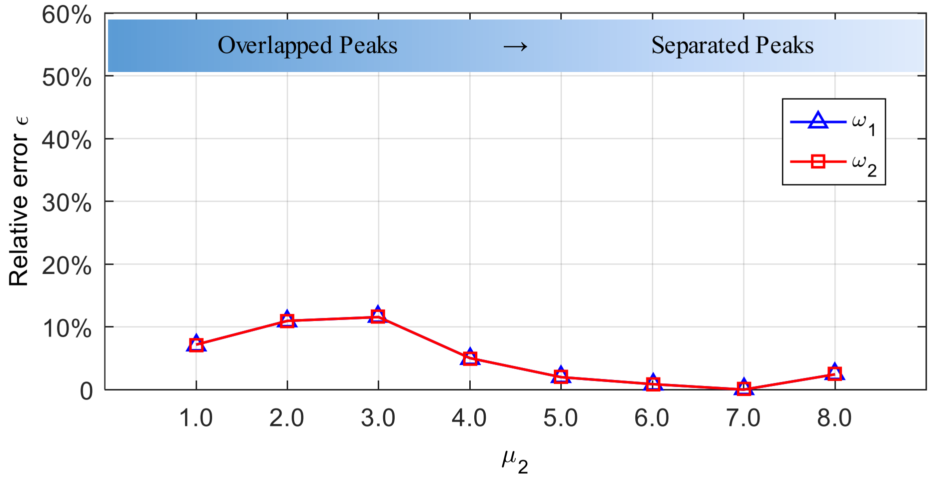

c) relative errors of mixing weights

Figure 3.7 Relative errors of the Bayesian approach

From the above numerical studies, it can be inferred that the proposed Bayesian approach is able to identify mixture parameters with good accuracy when the samples exhibit obvious multimodality. Besides, the parametric uncertainty can be simultaneously quantified, providing much richer model information.

3.5 SUMMARY

A parametric Bayesian mixture model is proposed in this chapter to characterise multimodal monitoring data with considering of parametric uncertainty. The conjugate normal-inverse-chi-squared priors are adopted for mixture parameters and the full conditional posteriors are derived under the Bayesian framework. To eschew inference on high dimensional joint posterior, the Gibbs sampler is devised to simulate posterior samples for mixture parameter estimation. Convergence diagnosis based on the potential scale reduction factor is proposed to check the stationarity of each chain and to ensure the global convergence. A model selection procedure based on the Bayes factor is proposed to determine the optimal number of components. Numerical examples using artificial mixture data sets are designed to first verify the effectiveness of the Bayesian mixture model. Estimation of a trimodal mixture model is demonstrated, including convergence diagnosis, parameter estimation and parametric uncertainty quantification. The performance of the Bayesian approach is investigated through a sets of bimodal mixture models range from completely overlapped to completely separated. To further demonstrate the validity of the proposed modelling framework, the multilevel stress responses acquired from instrumented Tsing Ma Bridge are estimated by the parametric

Bayesian mixture model in Chapter 4 for identification of the neutral axis position.

CHAPTER 4
NEUTRAL AXIS BASED DAMAGE DETECTION OF BRIDGE DECK UNDER STOCHASTIC TRAFFIC CONDITION

4.1 INTRODUCTION

As mentioned in Chapter 3, a parametric Bayesian mixture model, specifically the finite Gaussian mixture (FGM) model, is established to characterise the multimodal data structure in the presence of parametric uncertainty. This chapter demonstrates the application of parametric Bayesian mixture model to identify the neutral axis position of the Tsing Ma Bridge under multi-lane stochastic traffic condition. The neutral axis position based information is further used as damage sensitive feature to identify the postulated damage cases introduced to the bridge deck.

In the past decades, there has been encouraging progress on damage detection methodologies and their demonstrations in aerospace, mechanical, and civil engineering, ranging from laboratory tests to real-world scenarios. An ideal damage index is expected to possess the following characters: (1) sensitive to damage yet insensitive to varying operational condition; (2) convenient to measure with high fidelity; (3) directly derived from measurement with minimal assumptions or computational cost; and (4) conceptual and thus open to evaluation (Turer et al., 1998). Among a broad categories of damage identification techniques, the vibration-based approaches have been mostly highlighted and extensively studied by scholars. The premise behind the vibration-based methods is that the damage-induced changes in the physical properties of a structure (e.g., the stiffness, mass, and damping) will cause measurable changes in structural dynamic characteristics (e.g., natural frequencies, mode shapes, and modal damping). Monitoring of vibration signals thus provides an opportunity to damage detection of a structure. Nonetheless, diagnosis of a real-world large-scale structure by means of vibration-based methods suffers from several obstacles, one of which is the low sensitivity to local damage as the higher structural modes associated with local responses are often difficult to capture in field monitoring. Besides, previous studies have acknowledged that structural vibration characteristics can be significantly affected by the ambient condition as well. Changes in vibration characteristics caused by the environmental and operational variability might mask subtle changes caused by the damage, which fails the damage detection process. Pursuing practical damage identification of a large-scale complex structure, especially under varying operational and environmental conditions, still stands as one of the most challenging activities.

Structural static responses, such as displacement and strain, reflect the local stiffness or strength of a structure in a more intuitional way. However, a hindrance to direct use of these static measurements as damage sensitive feature is that they are proportional to external loadings as well. Elimination or normalization of the effects generated by external loadings rather than damage becomes a must before the implementation of damage detection using static responses. Theoretically, the neutral axis of beam-like structure passes across the geometrical centroid of the cross section under pure bending, leading itself to be a cross-sectional property related physical parameter that is immune to external loading condition. Questionable movement of the neutral axis position can be a sign of abnormal change of cross-sectional property, i.e., damage. Therefore, the neutral axis position has the potential to be the damage signature for flexural behaviour dominated structural members.

DeWolf and his co-workers evaluated the composite action of a steel-concrete simply supported girder bridge by tracking the neutral axis position during the passage of normal truck traffic (Chakraborty and DeWolf, 2006; Cardini and DeWolf, 2009). Although no change of composite action was found in their study, they point out that monitoring of neutral axis position can provide valuable information to condition assessment of the bridge deck. Ni and his co-workers proposed a Kalman filter estimator to locate the neutral axis position of bridge deck using strain measurement data (Ni et al., 2012; Xia et al., 2012b). The capability of the Kalman filter estimator for consistently locating the neutral axis position was verified under varying traffic load patterns. Crack detection of a scaled bridge deck model was successfully detected using the neutral axis position as the damage index. Sigurdardottir and Glisic (2013, 2014) investigated the uncertain factors other than damage that would adversely affect the estimation of neutral axis location of a girder. They recognise that neutral axis position can act as a damage indicator only if the uncertainties associated with its localization can be well quantified. Recently, the neutral axis position was also used to diagnose the condition of wind-turbine towers (Soman et al., 2016) and concrete box girder bridges (Xia et al., 2018). A state-of-the-art review on neutral axis position for structural health monitoring can be found in

Sigurdardottir and Glisic (2015).

Although the neutral axis position based information has been demonstrated to achieve satisfactory damage detection of typical structures under convenient chosen loads, it is yet a less explored but attractive topic that using neutral axis position as a performance indicator to health monitoring long-span bridges under stochastic traffic flow. This chapter investigates the feasibility of utilizing neutral axis position to detect local damage of the in-service Tsing Ma Bridge using monitoring stress response. A key issue here is accurate tracking of neutral axis position of the bridge deck under in-service condition since the pure bending hypothesis is nearly invalid and the loading combination changes from time to time. To quantify severe uncertainties due to the stochastic load, the parametric Bayesian mixture model is used to predict neutral axis positions of the deck truss under multi-lane stochastic traffic condition.

The layout of this chapter is organised as follows. The bridge FEM and neutral axis definition are first introduced in Section 4.2. A sensitivity analysis is carried out to investigate the variation of neutral axis position under moving point loads on multiple traffic lanes. Sections 4.3 and 4.4 present the identification of neutral axis positions based on monitoring and simulated stress response respectively by use of the parametric Bayesian mixture model. Two neutral axis based damage indexes are developed in Section 4.5. Damage detection of the bridge deck is demonstrated with single- and multiple-damage cases.

4.2 NEUTRAL AXIS POSITION OF TSING MA BRIDGE

This section first introduces the finite element model (FEM) of the suspension Tsing Ma Bridge. The definition and property of the neutral axis position is described based on a simplified beam model and it is further derived for the bridge deck of the Tsing Ma Bridge. A sensitivity analysis is carried out to investigate the variation of neutral axis position under moving vehicle loads on multiple traffic lanes by means of the FEM.

4.2.1 FEM of Tsing Ma Bridge

The Tsing Ma Bridge is a long suspension bridge located in Hong Kong with a main span of 1377 m and an overall length of 2.2 km. By carrying both highway and railway traffic, the bridge connects the Hong Kong International Airport in Lantau Island with the urban area of Kowloon. The structural configuration of the bridge can be referred to Chapter 6.

The Tsing Ma Bridge comprises nearly 20,000 structural members that belongs to several categories, including truss elements, deck plates, bracing, main cables, hangers, saddles, bearings, tower beams and legs, piers, and anchorages. To accurately predict the static and dynamic characteristics of the as-built bridge, a detailed three-dimensional global FEM with a total of 17,677 elements and 7,375 nodes was established by means of the commercial software package ABAQUS as shown in Figure 4.1(a). The modelling principles concerned for the FEM involve the following: (1) one critical real member is modelled by one analytical member with precise geometry shape; (2) the spatial arrangement of real bridge remains in the model; (3) the mass and stiffness contribution of each members are independently described in the model;

(4) the geometric stiffness of cables and hangers stemming from the large deflection is accurately considered in the model by a nonlinear static iteration analysis. Numerical convergence study was conducted to determine the proper element size, number of elements and mesh size so that a refined FEM can be achieved to minimize the deviance between the numerical model and real structure.

The FEM of a typical 18-m suspended bridge deck module is depicted in Figure 4.1(b). It is a double-level truss-stiffening box-shape steel deck that consists of cross frames, longitudinal trusses, deck plates and railway beams. A six-lane highway is laid on the upper deck while two railway lines and two emergency lanes are arranged within the sheltered lower deck. In this FEM module, the chord members of the cross frames, longitudinal trusses as well as railway beams are modelled as the B31 beam element (2-node linear beam element in space with 6-DOF in each node); and the deck plates are modelled as M3D4 membrane element (4-node quadrilateral membrane element in space with 3-DOF in each node). Parameters for modulus of elasticity, Poisson ratio, shear modulus, and density for the decking system are assigned as $E = 200\ \mathrm{kN/mm^2}$, $\rho = 0.3$, $G = 76.92\ \mathrm{kN/mm^2}$, and $\gamma = 7800\ \mathrm{kg/m^3}$ ($\gamma = 11500\ \mathrm{kg/m^3}$ for deck plate).

A validation of the developed FEM was carried out by comparing the analytical with measured modal properties of the bridge after opening to public (Wang et al., 2000). As shown in Table 4.1, the relative differences between the analytical and measured natural frequencies for the first four lateral, vertical, and torsional modes are quit small, indicating a satisfactory agreement of the FEM with the real bridge structure. Therefore, the developed FEM is suitable for performing numerical studies.

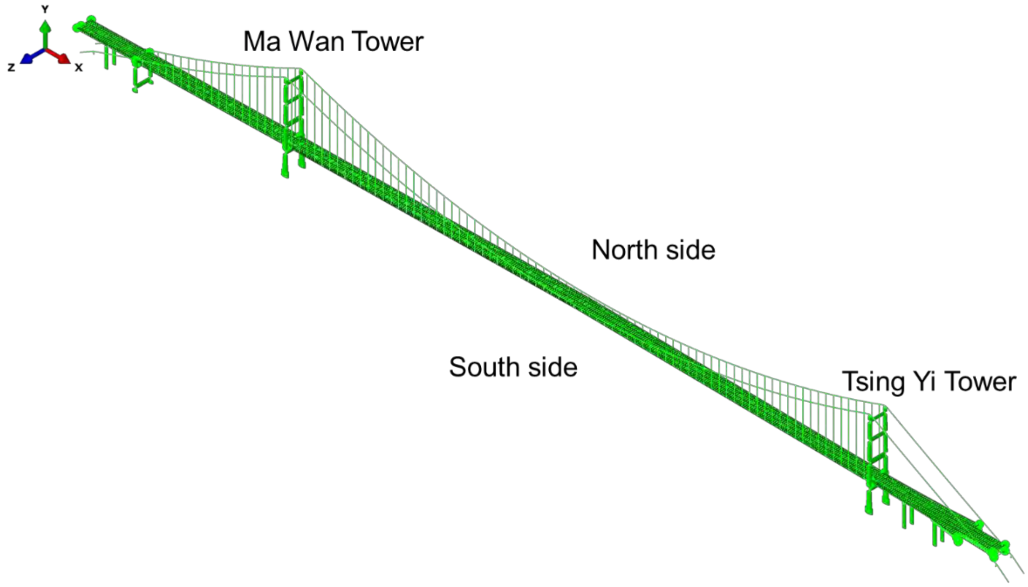

a) global FEM of the bridge

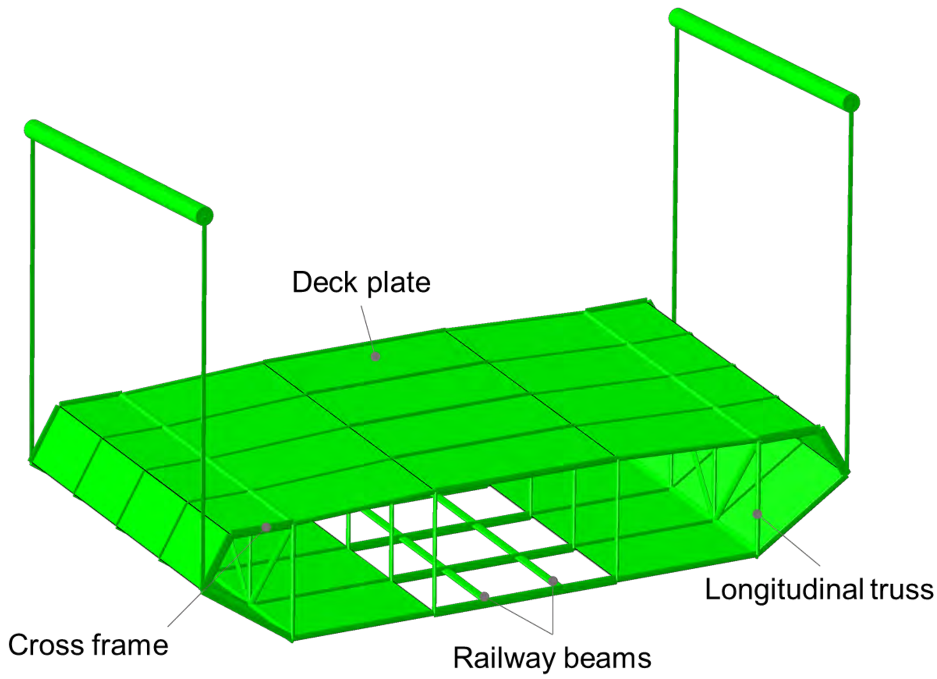

b) FEM of a typical bridge deck module

Figure 4.1 Three-dimensional finite element model of the Tsing Ma Bridge

Table 4.1 Comparison of measured and computed frequencies of Tsing Ma Bridge (Wang et al., 2000)

Mode type and order	Measured (Hz)	Computed (Hz)	Difference (%)
Predominantly lateral mode			
1st	0.070	0.0686	-2.00
2nd	0.170	0.1611	-5.24
3rd	0.254	0.2546	0.24
4th	0.301	0.2820	-6.34
Predominantly vertical mode			
1st	0.114	0.1154	1.23
2nd	0.133	0.1420	6.75
3rd	0.187	0.1836	-1.82
4th	0.249	0.2350	-5.62
Predominantly torsional mode			
1st	0.270	0.2584	-4.30
2nd	0.324	0.3014	-6.97
3rd	0.486	0.4942	1.69
4th	0.587	0.5660	-3.58

4.2.2 Definition of Neutral Axis Position

Based on the Euler-Bernoulli beam theory, the neutral axis within the cross section of a beam is a collection of points at which normal stress or strain vanishes under applied loads. Suppose a simply supported beam subject to vertical static point loads as shown in Figure 4.2. Segment CD undergoes pure bending as the bending moment applied on CD remains unchanged and no shear force acts there in the meantime. Given the plane cross-section assumption, the longitudinal strain distributed over the depth of the cross section can be determined according to the geometrical relationship as

$$\varepsilon(y) = \lim_{\Delta x \to 0} \frac{\Delta x' - \Delta x}{\Delta x} = \lim_{\Delta x \to 0} \frac{(\rho + y)\mathrm{d}\theta - \rho \mathrm{d}\theta}{\rho \mathrm{d}\theta} = \frac{y}{\rho} \tag{4.1}$$

where y is the distance from the neutral axis to a fibre of interest, Δx and $\Delta x'$ are the lengths of the fibre before and after deformation, ρ is the curvature radius of the neutral axis, and $\mathrm{d}\theta$ is the rotational angle of the cross section. With the Hooke's law, the normal stress at any point of the cross section is

$$\sigma(y) = E\varepsilon = E\frac{y}{\rho} \tag{4.2}$$

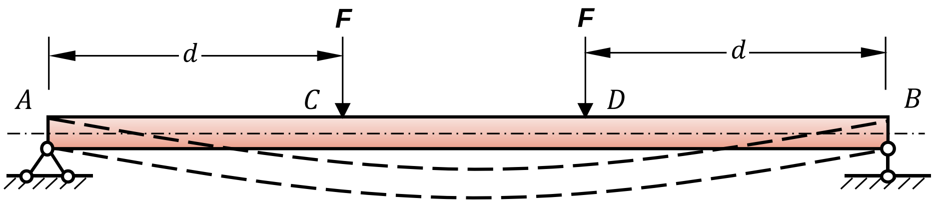

a) CD segment under pure bending

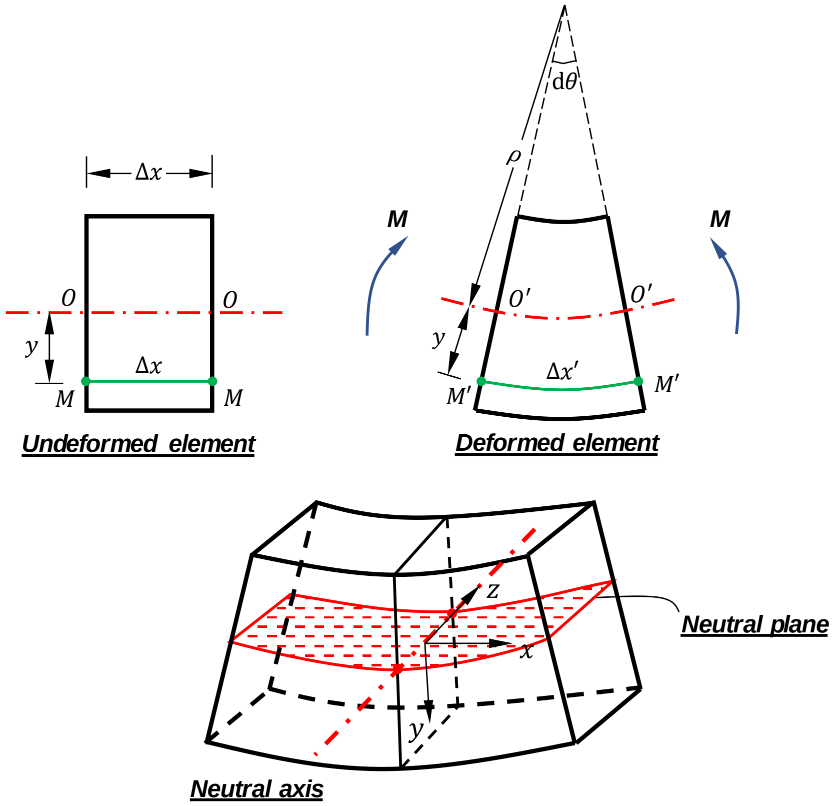

b) definition of the neutral axis

Figure 4.2 Neutral axis position of a simply supported beam

Equations (4.1) and (4.2) indicate the longitudinal strain as well as normal stress are linear distributed along the cross section with respect to the distance from neutral axis. Thus, pure bending of the beam will cause zero stress at the neutral axis, maximum tensile stress at top surface of the beam, and maximum compressive stress at bottom surface of the beam. According to the force equilibrium in x-direction, we have

$$F_N = \int_A \sigma \mathrm{d}A = \int_A E\frac{y}{\rho}\mathrm{d}A = 0 \tag{4.3}$$

Note that the elastic module E and curvature radius ρ are non-zero constants given the cross section, the following equality holds

$$\int_A y\mathrm{d}A = S_z = 0 \tag{4.4}$$

where S_z is moment of area with respect to neutral axis (z-axis). Theoretically, Equation (4.4) proves the neutral axis should strictly pass across the geometrical centroid of the cross section under pure bending since the moment of area with respect to neutral axis is zero. Therefore, the neutral axis position keeps stable as the centroid remains unchanged given the cross section. When the cross section is subject to both bending moment and shear force, Equation (4.4) still holds for beams with length-to-depth ratio $l/h > 5$, which are common types among bridge structures. However, when additional axial force (such as prestressing force) is applied on the cross section, the bending stress will be superimposed with axially applied stress, causing a shift of the neutral axis from the centroid.

Essentially, the location of neutral axis is highly correlated with the geometrical centroid of the cross section. Potential damage of the cross section, i.e., cracking and corrosion, will alter the position of the centroid, resulting a movement of the neutral axis. Thus, the neutral axis position can be utilised as a damage sensitive feature for flexural behaviour dominated structural members.

In general, the bridge deck of the Tsing Ma Bridge behaves like a flexural beam under railway and highway traffic loads. This structural behaviour has been observed by the time histories of monitoring stress response on the longitudinal truss as detailed in Chapter 6. Consequently, it is appropriate to utilise the neutral axis position of the longitudinal truss as a promising damage indicator for continuously monitoring of the bridge deck. As shown in Figure 4.3, with the sensor readings acquired from strain gauges deployed on the top and bottom chords of the longitudinal truss, the monitoring-based neutral axis position of the longitudinal truss is defined as

$$y_O = \frac{\varepsilon_B}{\varepsilon_T + \varepsilon_B} H \tag{4.5}$$

where y_O is the distance from the strain gauge at bottom chord to the neutral axis, ε_T and ε_B are absolute values of strain from top and bottom chords, respectively, and H is the depth of cross section of the longitudinal truss. According to the design documents, $H = 6.125\ m$ is adopted for calculating the cross section of the main span. Without loss of generality, the neutral axis position can be also calculated in terms of stress values

$$y_O = \frac{\sigma_B}{\sigma_T + \sigma_B} H \tag{4.6}$$

where $\sigma_T = E\varepsilon_T$ and $\sigma_B = E\varepsilon_B$ are the absolute stress values from top and bottom chords, respectively. Equations (4.5) or (4.6) can be used interchangeably upon the format of measurement data.

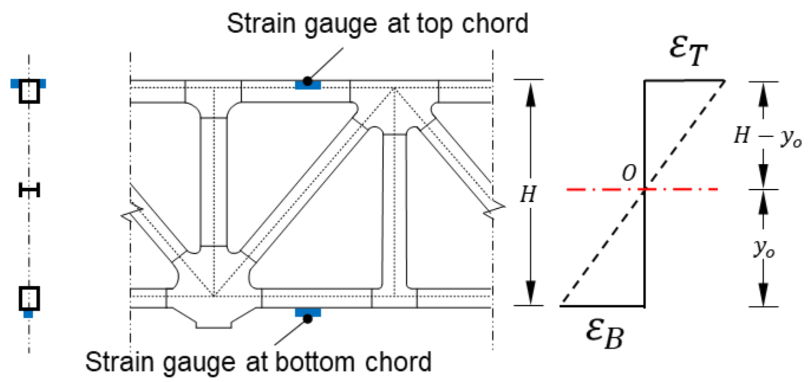

Figure 4.3 Monitoring-based neutral axis position estimation of the longitudinal truss

Although the definition of the neutral axis position is theoretical straightforward, it comes to substantial difficulties when applies to damage detection of the in-service Tsing Ma Bridge using monitoring stress response. The flexural behaviour of the bridge deck is far more complicated than the case of simply supported beam, which makes some premises for locating the neutral axis invalid. Firstly, either the highway or railway traffic caused bridge deck to bend is moving load on different lanes whose location is uncertain at any point in time. Previous studies have pointed out that the neutral axis of a girder cross section of a bridge is dependent on loading position in terms of both the distance to the measurement point and the lane in use (Elhelbawey et al., 1999; Cardini and DeWolf, 2009; Xia et al., 2018). Secondly, the longitudinal truss may suffer from out-of-plane bending when heavy truck vehicles run through the traffic lanes a distance away from the longitudinal truss. It could generate an inclined neutral axis, making the location of neutral axis based on two measurement points inadequate

(Sigurdardottir and Glisic, 2013). Lastly, the monitoring stress response of the in-service Tsing Ma Bridge is a superposition of multiple load effects, including those from vehicles, trains, wind and temperature. Whereas the identification of neutral axis position is critically dependent on traffic loads which cause the deck to bend other than the wind and temperature effects. The aforementioned issues, other than damage, will adversely deviate the neutral axis position, making it an uncertain variable under operational condition. It is impossible to implement the bridge damage detection unless the variation of neutral axis position due to operational environment has been fully understood.

To investigate the variation of neutral axis position under moving vehicle loadings, the sensitivity analysis with respect to change of loading distance, change of loading magnitude, and change of traffic lane is first carried out by means of the FEM of the Tsing Ma Bridge.

4.2.3 Sensitivity Analysis of Neutral Axis Position

4.2.3.1 Change of loading distance

To simulate the vehicles and trains running pass the bridge, the directions and positions of the traffic lanes on the deck model are determined based on the centre line of lanes and tracks in real bridge as shown in Figure 4.4, where N1 to N3 are highway lanes towards Kowloon (Tsing Yi direction) on north side; S1 to S3 are highway lanes towards airport (Ma Wan direction) on south side; and NT and ST are bi-directional railway lines for operation of the airport express. Note that the two emergency carriageways laid on the lower deck are not considered in this study. The neutral axis of monitoring cross section of CH24662.50 near 3/4 of the main span is investigated where strain gauges are mounted on top and bottom chords of the longitudinal truss. Hence, results from FEM analysis and field measurement data can be compared directly.

To analyse the effect of loading distance to the estimation of neutral axis position, a moving unit vertical force (1 MN) is applied on nodes of the designated traffic lane and runs through the monitoring cross section. Element outputs of stress from top and bottom chords are calculated by FEM static analysis. The neutral axis position is evaluated based on stress output in each load step by using Equation (4.6).

Figure 4.5 plots the neutral axis positions of north truss as well as the stress responses at top and bottom chords when the unit force moves along the rail track NT with the x-axis being the distance of the unit force from Ma Wan pier M1, the right y-axis being the stress values, and the left y-axis being the estimation of neutral axis position. It finds that stress responses reach the peak values when unit force acts on the nodes of NT at the cross section. A considerable movement of the neutral axis position is observed as it arises when the unit force approaches the cross section while it drops with the unit force moving far away. This coincides with the findings in previous studies that neutral axis position depends on the longitudinal location of loading. In general, the direct use of stress output of each load step, such as the continuous stress measurements induced by a moving vehicle, may render non-unique estimation of the neutral axis position. It is not a concern when the unit force is far from the cross section and the stress output is of vary small value. The definition of neutral axis position is invalid for this case.

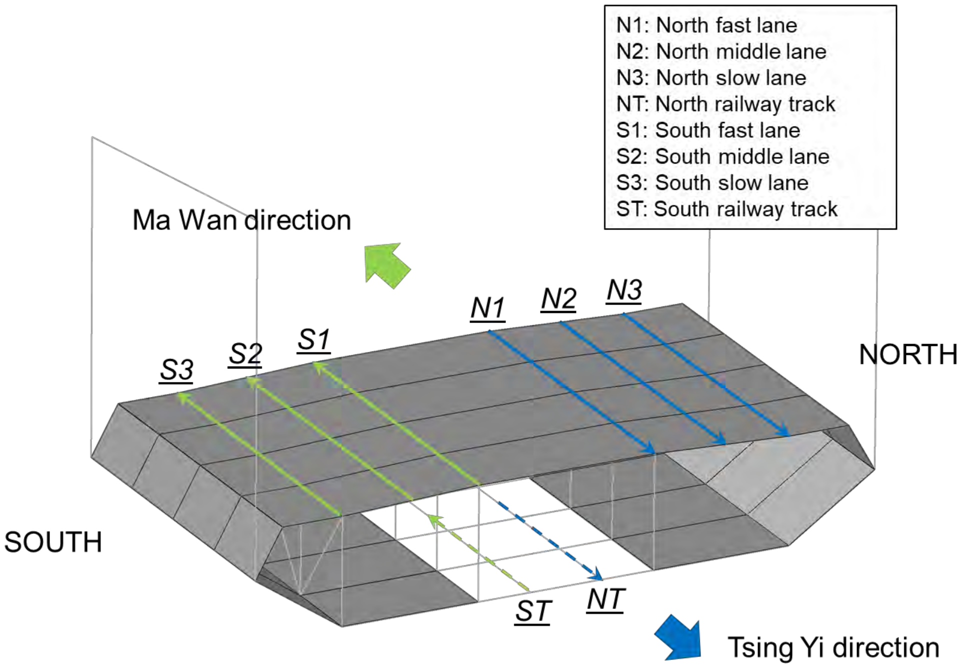

Figure 4.4 Layout of traffic lanes on the bridge deck

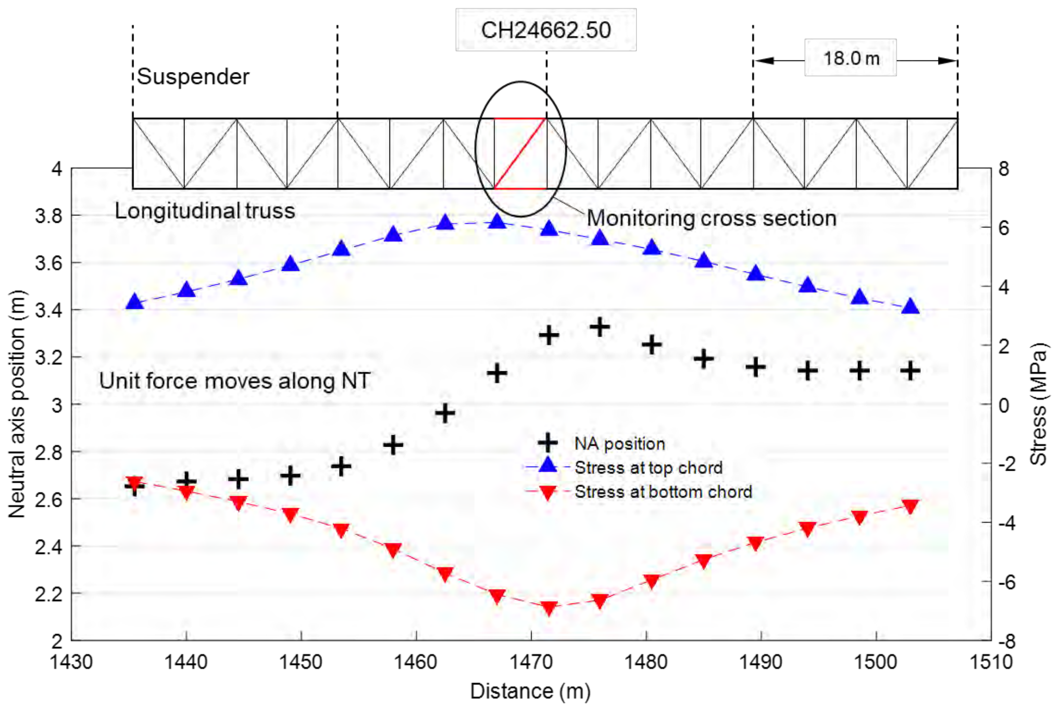

Figure 4.5 Neutral axis positions of north truss with respect to change of loading distance

4.2.3.2 Change of loading magnitude

To investigate the effect of loading magnitude to the estimation of neutral axis position, the unit force is first multiplied by scale factors to generate different magnitudes of loadings. These scaled moving loads are then applied on nodes of the designated traffic lane and run pass the monitoring cross section. Figure 4.6 presents the neutral axis positions of north truss when moving loads with different magnitudes act on NT. Despite the deviation of neutral axis position due to the moving loads, the consistent estimations of neutral axis positions are observed under different loading magnitudes for each loading location. It indicates that the estimation of neutral axis position is independent of the loading magnitude. A reasonable inference is that either heavy or light vehicle running on the bridge would generate same neutral axis value for the monitoring cross section.

Based on the discussion above, a consistent estimation of neutral axis position due to a specific moving vehicle that passes through the cross section can be defined as

$$y_O = \frac{\sigma_B^{max}}{\sigma_T^{max} + \sigma_B^{max}} H \tag{4.7}$$

where σ_T^{max} and σ_B^{max} are absolute peak stress values of top and bottom chords induced by the moving vehicle, respectively. Take the case in Figure 4.5 as an example, the peak value of compressive stress for top chord is $\sigma_T^{max} = 6.158$ MPa at location $d = 1467.0$ m; while the peak value of tensile stress for bottom chord is $\sigma_B^{max} = 6.871$ MPa at location $d = 1471.5$ m. The neutral axis position for the loading event is calculated as $y_O = \frac{6.158}{6.871+6.158} \times 6.125 = 3.230$ m. Table 4.2 lists the neutral axis positions of north truss calculated by the peak values, where a stable estimation of neutral axis under different loading magnitudes is achieved.

Recommendation of use of Equation (4.7) for monitoring-based neutral axis estimation is twofold: (1) the peak stress values caused by a passing vehicle can be measured with sufficient accuracy, which would produce more reliable estimation of neutral axis; (2) it is technically feasible to collect peak stress values from a continuously monitoring system, thus the long-term trend of neutral axis can be obtained.

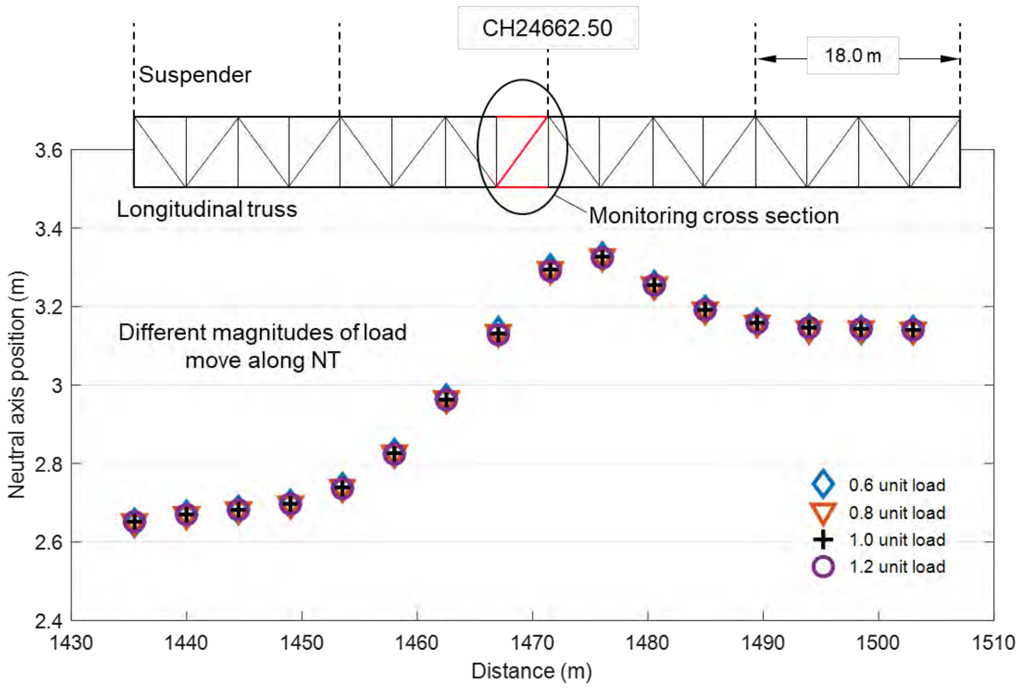

Figure 4.6 Neutral axis positions of north truss with respect to change of loading magnitude

Table 4.2 Neutral axis position under different loading magnitudes

	Loading magnitude (× 1 MN)			
	0.6	0.8	1.0	1.2
Neutral axis position (m)	3.235	3.232	3.230	3.228

Note: NA positions are calculated based on peak stress values.

4.2.3.3 Change of traffic lane

To analyse the effect of change of traffic lane to the estimation of neutral axis position, the moving unit force is applied on nodes of each traffic lane and runs through the monitoring cross section respectively. The neutral axis position is evaluated based on peak stress values by using Equation (4.7). Figure 4.7 shows the neutral axis positions of north truss as well as the peak stress responses at top and bottom chords with respect to unit force running on eight different traffic lanes. As expected, the unit force on traffic lanes further away from the truss generates lower level of stress responses on top and bottom chords. However, the neutral axis positions as calculated by the pair-wise peak stress values have a significant change with the highest position when S3 being loaded and the lowest position when N3 being loaded. The range of neutral axis values are from 2.860 m to 3.284 m as given in Table 4.3. It implies the neutral axis position is critically dependent on transverse location of the loading. An identical truck with known weight would induce change of neutral axis position when it runs on different traffic lanes.

The sensitivity analysis by means of FEM model concludes that (1) the neutral axis position is immune to loading magnitude; (2) the inconsistent neutral axis position due to moving load can be sidestepped by making use of peak stress responses; and (3) the moving load on different traffic lanes would create different neutral axis positions. Consequently, when it applies to monitoring stress responses acquired from the in-service Tsing Ma Bridge, the stochastic highway and railway traffic loads on multiple lanes could generate varying neutral axis position for a designated cross section over a given time period. The neutral axis position can only be adopted as a damage sensitive feature when the associated uncertainty is properly quantified. In view of this, a neutral axis position identification method based on the parametric Bayesian mixture model is developed to address the uncertainty issue under daily operation of the Tsing Ma Bridge.

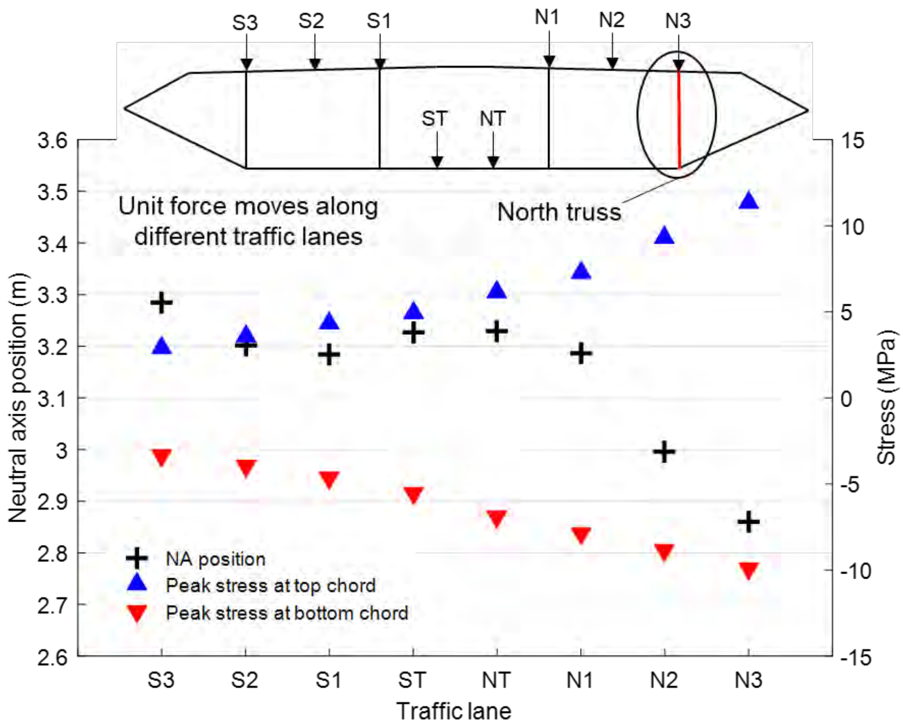

Figure 4.7 Neutral axis positions of north truss with respect to change of traffic lane

Table 4.3 Neutral axis position of longitudinal truss due to change of traffic lanes

	Traffic lanes							
	S3	S2	S1	ST	NT	N1	N2	N3
Neutral axis position (m)	3.284	3.201	3.185	3.226	3.230	3.186	2.995	2.860

Note: NA positions are calculated based on peak stress values.

4.3 IDENTIFICATION OF NEUTRAL AXIS POSITION BASED ON MONITORING STRESS RESPONSE

This section presents the identification of neutral axis position based on the monitoring stress response acquired from the instrumented Tsing Ma Bridge. Wind and thermal effects in the measured total strain are first eliminated because they do not contribute to the bending behaviour of the bridge deck. In-service multilevel stress responses due to stochastic traffic condition are estimated by using the parametric Bayesian mixture model. Identification of neutral axis positions of the longitudinal truss is carried out based on the estimation of component means.

4.3.1 Estimation of Multilevel Stress Response

The highway traffic on dual three-lane of the upper deck and railway traffic on two tracks of the lower deck are the main carrying loads for the in-service Tsing Ma Bridge. Daily passage of vehicles and trains induces the bending behaviour of the bridge deck. Identification of neutral axis position based on traffic-induced stress response is straightforward and it is expected to keep constant if no damage of the cross section has occurred. However, the wind load and thermal effect are another two sources acting on the bridge. The dynamic wind buffeting on the bridge usually causes stochastic vibration of the bridge deck. The temperature variation could generate thermal deformation of the steel deck, resulting in additional axial strain on structural members. Direct use of the total strain acquired from sensors is misleading because the wind- and temperature-induced responses could significantly deviate the neutral axis position. In Figure 6.8, 24-hour raw strain signals of top and bottom chord on the north truss acquired from sensors SPTLN01 and SSTLN03 are depicted, in which a mixed multi-component strain response is observed. Hence, the wind and temperature effects should be properly isolated from the total strain so that only traffic-induced stress response is employed to form the neutral axis position.

The static response due to mean winds and dynamic response due to fluctuating winds are two major wind effects on a long suspension bridge. Note that wind effects are also coupled with mode shapes of a bridge in vertical or lateral direction. An apparent difference to the traffic load is that either static wind force or buffeting force would trigger the vibration of bridge deck in a three-dimensional manner rather than the plane bending behaviour. The consistency of the neutral axis position does not apply to such a case. Feasibility of the proposed damage detection method may be in question especially under strong wind condition. Application scope of the proposed method will be extended if successful separation of wind-induced response from the monitoring signals can be achieved. In the present research, to minimise the influence of wind effect on the estimation of neutral axis position, only the monitoring data during weak wind days (daily mean wind speed lower than 3 m/s) are selected. A future study on the determination of a threshold for maximum wind speed to the success of damage detection is needed.

The 24-hour ambient temperature cycle due to solar radiation would considerably affect the deformation of the steel deck, especially along the bridge longitudinal direction. The low-frequency strain cycle with large amplitude as shown in Figure 6.8 reveals the longitudinal truss behaves expansion and compression in a daily manner. Hence, the temperature-induced axial deformation of the truss contributes to the axial strain on the cross section, which superposes with the bending strain due to traffic loads and eventually shifts the neutral axis position. To minimise the influence of temperature effect on the estimation of neutral axis position, the wavelet-based decomposition method as introduced in Chapter 6 is employed here to isolate the temperature-induced strain from the measured total strain (Ni et al., 2011b).

The monitoring data acquired from the north truss from November 1 to 10, 2005 are analysed. Figure 4.8(a) shows the time histories of traffic-induced stress responses at top and bottom chords on November 1 after eliminating the temperature effect. Vehicles or trains on different traffic lanes create stress pulses when they run across the monitoring location consecutively. High-frequency stress pulses with different amplitudes are observed during the whole day. When the airport railway stops its service from 2:00 to 5:00 a.m., the stress response maintains the low amplitude since only road vehicles are running on the deck. It is clear that response amplitude is related to loading magnitude and the traffic lane in use. As plotted in Figure 4.8(b), the occurrences of pair-wise peak stresses on the top and bottom chords coincide well with each other, indicating the monitoring cross section is subject to an identical load event at the same instant. The neutral axis position under a deterministic load event such as passing of vehicle or train on a known traffic lane can be readily calculated by using the peak stress values at top and bottom chords. However, as stated in sensitivity analysis, the neutral axis position is highly dependent on the transverse location of the load. Identification of neutral axis position with respect to individual load event would exhibit considerable variation due to the fact that traffic loads are of random appearance on multiple traffic lanes. The intrinsic variability of the neutral axis position needs to be quantified so that the abnormal movement due to damage can be ascertained.

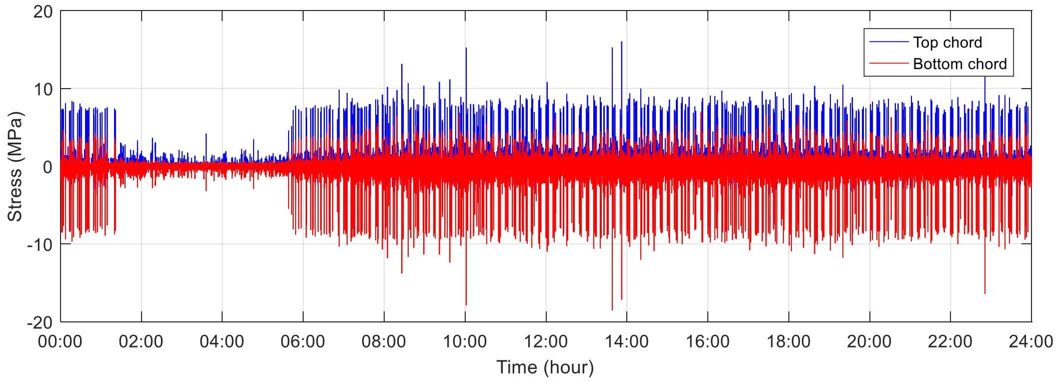

a) 24-hour stress responses

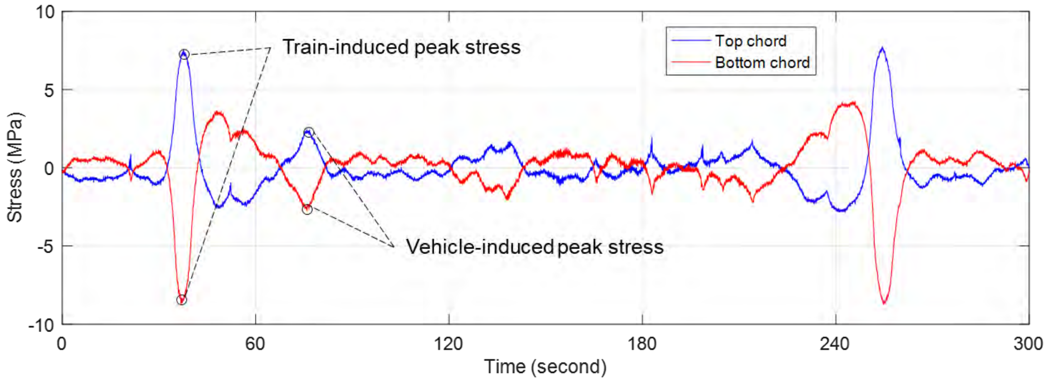

b) a zoom view of stress responses

Figure 4.8 Traffic-induced stress responses of top and bottom chords

Given a long time period, the collection of peak stresses can be regarded as the combined effect of numerous load events on randomly selected traffic lanes. Figure 4.9 shows the peak stresses extracted from the daily time histories of top and bottom chords respectively. Several clusters of the peak stresses are found in each of the scatter plots, which correspond to different load events of highway and railway traffic. A multimodal data structure is observed for the histograms, in which the peak stresses are randomly distributed but centralised to multiple stress levels. The multilevel stress serves as the representative of various load events and quantifies the effects due to change of traffic lanes. Hence, it is beneficial to make use of the multilevel stress responses for the estimation of neutral axis position.

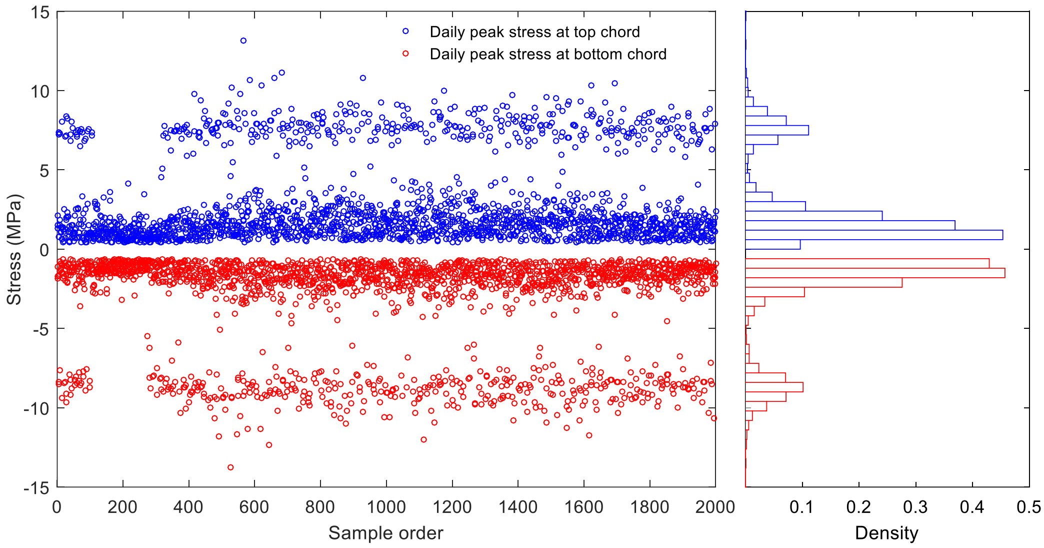

Figure 4.9 Daily peak stress responses based on monitoring

The parametric Bayesian mixture model, specifically the FGM model as introduced in Chapter 3, is utilised to estimate the multilevel stress responses of top and bottom chords. The optimal number of components is determined through the Bayes factor-based model order selection method. Results of model selection show that both NLMLs (negative log marginal likelihood) for top and bottom chords reach minimum value at $J = 4$, which implies the mixture model with optimal model order of four is adequate to characterise the multilevel stress responses. The posterior samples of mixture parameters are sought by using the Gibbs sampler. A satisfactory convergence of the Gibbs iteration is achieved for all parameters. Table 4.4 lists the sample mean and 5-95 credible interval of the posterior mixture parameters estimated for top and bottom chords.

Multiple stress levels are identified for the north truss: (1) the 1st and 2nd mixture components with lower component means represent the first stress level (level I) which can be interpreted as the load effect of highway traffic; (2) the 3rd component with greater component mean acts as the second stress level (level II) that accounts for the load effect due to railway traffic; and (3) the 4th component with the largest component variance represents the third stress level (level III) that can be interpreted as the combined effect due to highway and railway traffic. Taking advantage of the Bayesian approach, the multilevel stress as measured by the component means (parameter μ) is uniquely identified in terms of the mean values and associated uncertain bounds. Estimations of component means of the FGM model are employed to determine the neutral axis positions.

Table 4.4 FGM estimation of multilevel stress for north truss based on monitoring (November 3, 2005)

Comp.	Parameter μ			Parameter σ^2			Parameter ω			Stress level
	5%	Mean	95%	5%	Mean	95%	5%	Mean	95%	
Top chord										
No.1	1.054	1.100	1.154	0.169	0.194	0.226	0.453	0.500	0.553	I
No.2	1.902	1.999	2.105	0.439	0.515	0.603	0.259	0.310	0.356	
No.3	7.631	7.718	7.805	0.681	0.807	0.953	0.144	0.158	0.173	II
No.4	6.013	6.937	7.876	6.911	10.119	14.596	0.020	0.032	0.045	III
Bottom chord										
No.1	1.330	1.369	1.410	0.222	0.248	0.276	0.608	0.654	0.700	I
No.2	2.133	2.298	2.492	0.604	0.748	0.938	0.107	0.151	0.196	
No.3	8.717	8.811	8.908	0.913	1.069	1.249	0.157	0.172	0.187	II
No.4	7.149	8.499	9.907	9.253	15.538	24.077	0.013	0.022	0.033	III

Note: The order of components is ranked according to (1) the ascending order of μ; and (2) the 4th component with the maximum σ^2.

4.3.2 Identification of Neutral Axis Positions

Due to the parametric uncertainty of the component means, the predictions of neutral axis positions are random variables in the context of Bayesian approach. The posterior samples of component means from the Gibbs output play two roles here: (1) represent the time-average estimation of the multilevel stress; and (2) take into account the effect of multiple traffic lanes through the probabilistic clustering process. Consequently, the samples of neutral axis positions $\boldsymbol{\varphi}^{(g)} = \{\varphi_1^{(g)}, \cdots, \varphi_J^{(g)}\}$ based on component means can be determined as

$$\varphi_j^{(g)} = \frac{\mu_j^{B(g)}}{\mu_j^{T(g)} + \mu_j^{B(g)}} H \quad (j = 1, \cdots, J; g = 1, \cdots, G) \tag{4.8}$$

where $\varphi_j^{(g)}$ are samples of the jth neutral axis position, $\mu_j^{T(g)}$ and $\mu_j^{B(g)}$ are posterior samples of the jth component means of top and bottom chords respectively, and G is number of samples after burn-in period of the Gibbs iteration. The mean values of neutral axis positions $\bar{\boldsymbol{\varphi}} = \{\bar{\varphi}_1, \cdots, \bar{\varphi}_J\}$ can be obtained by averaging the samples of $\boldsymbol{\varphi}^{(g)}$

$$\bar{\varphi}_j = G^{-1} \sum_{g=1}^{G} \varphi_j^{(g)} \quad (j = 1, \cdots, J) \tag{4.9}$$

where $\bar{\varphi}_j$ is the mean value of the jth neutral axis position. The standard deviation (SD) and 5-95 credible interval (CI) of neutral axis positions can be calculated based on the samples of $\boldsymbol{\varphi}^{(g)}$ accordingly. Identification of neutral axis positions for north truss on November 3, 2005 is demonstrated in Table 4.5, in which they are classified to three categories according to the stress levels. In this day, the vehicle-induced 1st neutral axis has the highest position, whereas the train-induced 3rd neutral axis position is the lowest among four neutral axes. Note that the 4^{th} neutral axis position owns overall the greatest uncertainty than the other three neutral axes.

Table 4.5 Identification of neutral axis positions for north truss based on monitoring (November 3, 2005)

Comp.	Neutral axis position (m)			
	Mean	SD	5-95 CI	Category
No.1	3.397	0.050	[3.312, 3.476]	Highway traffic-induced
No.2	3.274	0.086	[3.140, 3.421]	
No.3	3.265	0.014	[3.242, 3.289]	Railway traffic-induced
No.4	3.369	0.201	[3.044, 3.697]	Jointly induced by highway and railway

Figure 4.10 plots the identified neutral axis positions and associated uncertain ranges for the north truss during ten consecutive days from November 1 to 10, 2005 based on monitoring. The multilevel stresses of top and bottom chords as inferred by the FGM model are also given for reference. The trend of daily pair-wise component means have symmetric pattern, i.e. μ^T and μ^B increase or decrease simultaneously at the same day. It finds the variation of component means for either top or bottom chords is rather small as well. Although the average neutral axis positions rise and fall slightly during the period, the change is quite small that beneath the tolerance level. The uncertain ranges quantify the intrinsic variation of the neutral axis under the normal operation of the Tsing Ma Bridge. Noted that the railway-induced uncertain range of the neutral axis is the narrowest. Based on the parametric Bayesian mixture model, the proposed neutral axis position identification method is applicable and efficient to track the neutral axis positions under multi-lane stochastic traffic condition.

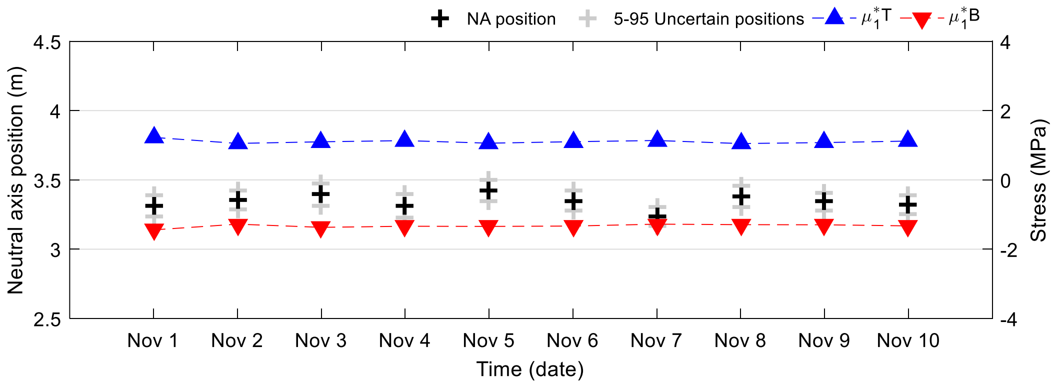

a) the 1st neutral axis position induced by highway traffic

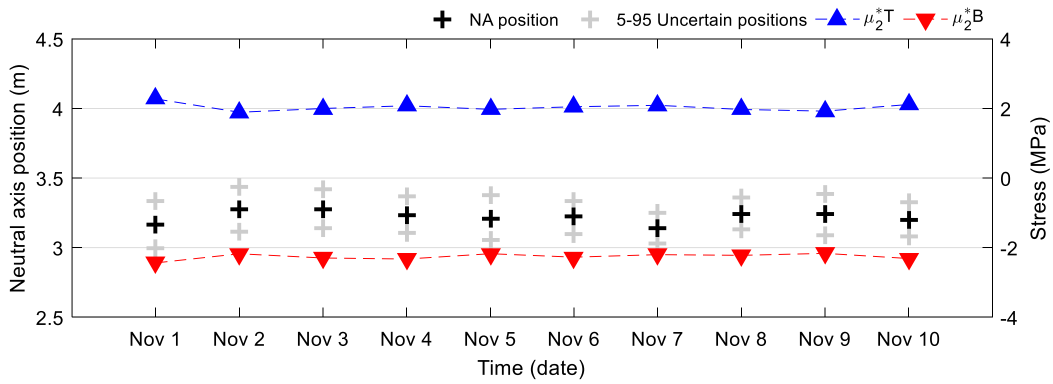

b) the 2nd neutral axis position induced by highway traffic

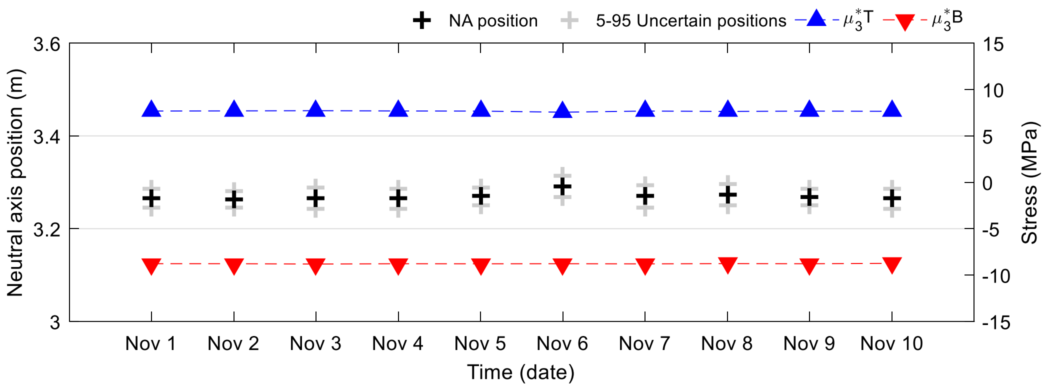

c) the 3rd neutral axis position induced by railway traffic

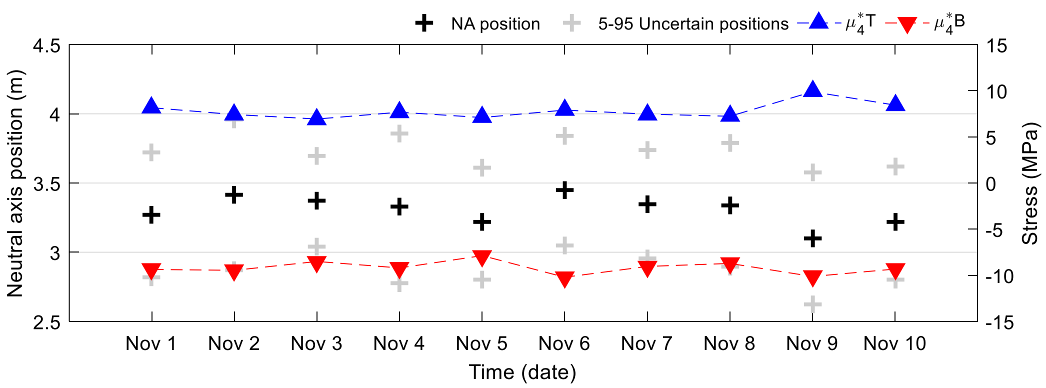

d) the 4th neutral axis position jointly induced by highway and railway

Figure 4.10 Daily neutral axis positions for north truss based on monitoring

4.4 IDENTIFICATION OF NEUTRAL AXIS POSITION BASED ON SIMULATED STRESS RESPONSE

Damage scenarios of the Tsing Ma Bridge are postulated with the aid of FEM. To verify the feasibility of the neutral axis based damage detection method, this section presents the identification of neutral axis position under stochastic traffic condition using the bridge FEM. Traffic-induced stress time histories are constructed by means of the bridge influence line method in conjunction with on-site traffic load data. The parametric Bayesian mixture model is employed to estimate the multilevel stress responses. Neutral axis positions of the longitudinal truss are identified using the estimation of component means.

4.4.1 Simulation of Traffic-Induced Stress Time History

4.4.1.1 Establishment of stress influence line

To derive the traffic-induced stress time history, the stress influence line method in conjunction with on-site traffic load data is first developed based on the bridge FEM. The influence line is a static property that characterise the variation of structural response such as reaction, deflection, and internal force of a specific member when a unit vertical force moves on the bridge under linear assumption. Note that the influence line method is invalid when nonlinear behaviour of bridge component is presented. Generally, an influence line is formulated as a function of the response amplitude of a given point and the location of unit force. Given the traffic layout of the Tsing Ma Bridge as shown in Figure 4.4, the stress influence lines of a designated truss member such as top chord or bottom chord induced by each traffic lane can be established based on the FEM. To achieve this aim, a moving unit vertical force of 1 MN is applied on nodes of beam elements along each traffic lane and runs through the bridge from one end to another end. Element stress outputs associated with each load step (node-to-node distance is 4.5 m) are computed by the static FEM analysis. The computed stress values are referred to the stress influence coefficients. Note that there are two railway stress influence lines and six highway stress influence lines for a given truss member.

Railway stress influence lines for top and bottom chords of the north truss at the monitoring cross section (distance of 1471.5 m) are given in Figure 4.11 with the x-axis being the distance of unit force from the Ma Wan pier M1, and the y-axis being the stress influence coefficient. Note that positive values denote the compression stress, whereas negative values denote the tension stress. Typical features of the railway stress influence lines are summarised as follows: (1) the influence lines are nearly at zero when the unit force is far away from the monitoring cross section, especially for the side spans; (2) the influence coefficients for top chord first become negative and reach to maximum values at the location where the unit force is placed at the node of monitoring cross section, whereas the asymmetry trends are observed for the influence lines of bottom chord; (3) the unit force generates greater influence coefficients on north track that is near to the north truss being monitored; and (4) the amplitudes of influence lines of bottom chord are larger than those of top chord.

Highway stress influence lines for top and bottom chords of the north truss at the monitoring cross section (distance of 1471.5 m) are plotted in Figure 4.12. Shapes of highway influence lines are similar to those of railway influence lines. Apparently, the maximum or minimum stress influence coefficient is proportional to the transverse distance between the lane and the north truss being monitored. However, as compared to the influence lines of north lanes, those of south lanes (S1 to S3) reach at maximums or minimums when the unit force is placed at the node of adjacent cross section rather than the exact monitoring cross section. The amplitudes of influence lines of bottom chord are greater than those of top chord except for N2 and N3.

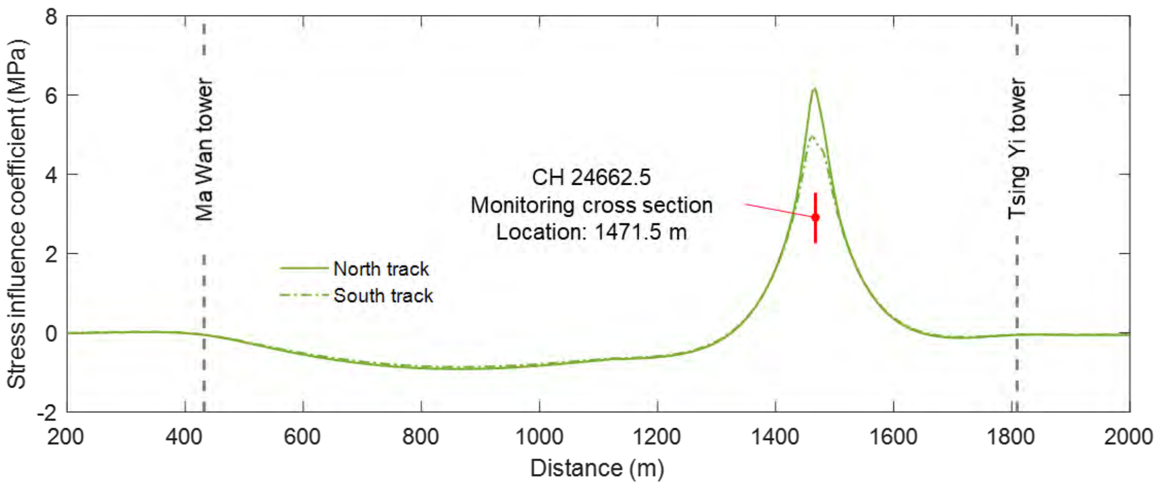

a) top chord

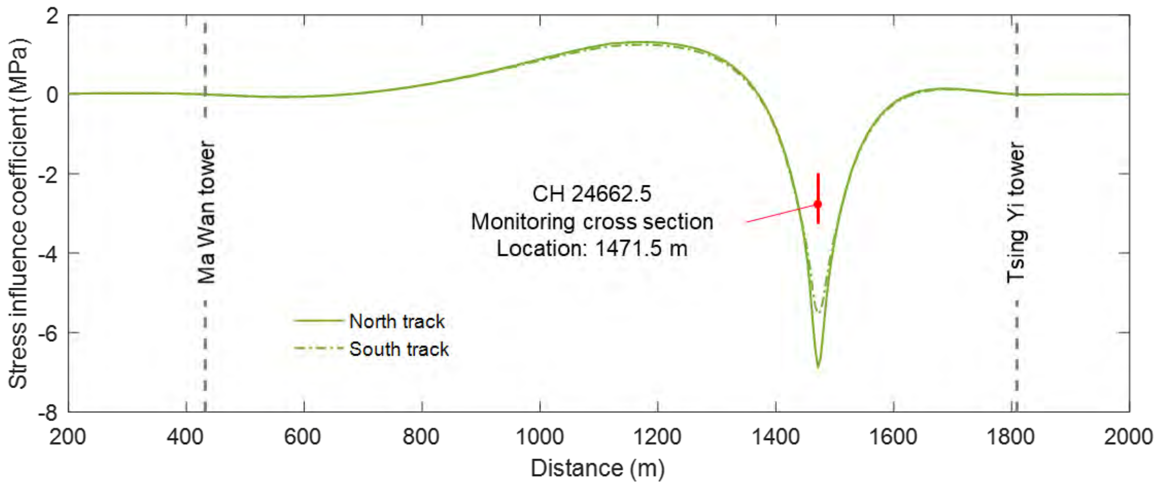

b) bottom chord

Figure 4.11 Railway stress influence lines for north truss

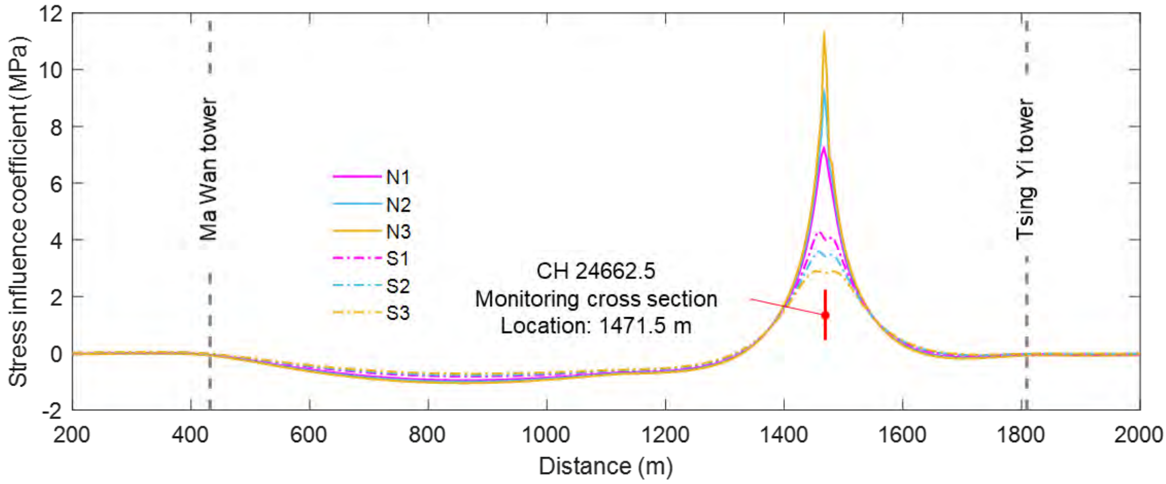

a) top chord

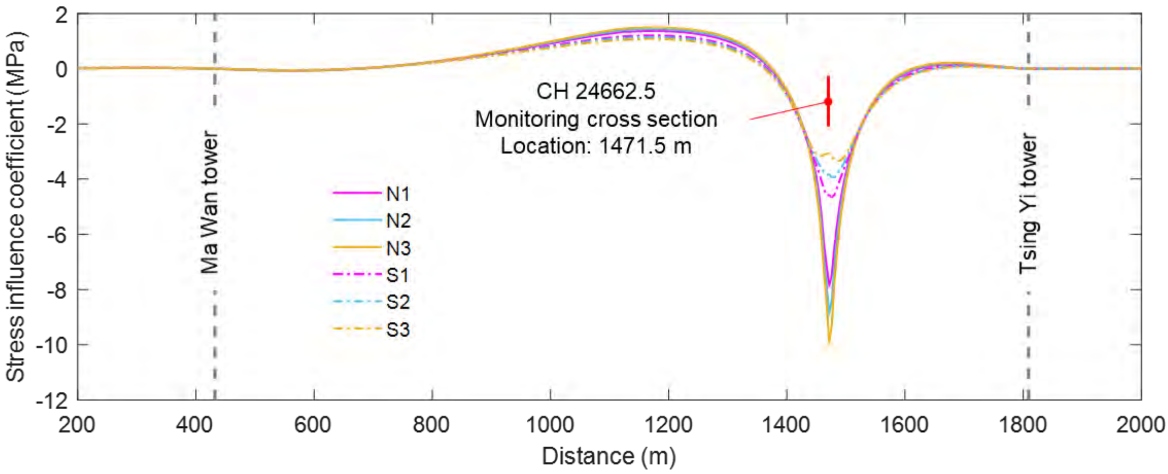

b) bottom chord

Figure 4.12 Highway stress influence lines for north truss

4.4.1.2 On-site traffic load monitoring data

Monitoring of railway and vehicle loads has been engaged in the structural health monitoring system of the Tsing Ma Bridge. The train load information is measured by a set of strain gauges attached on the inner waybeam of each pair of waybeams under the two rail tracks at CH 24664.75. Through a proper calibration, the signals of strain gauges can be converted to bogie load information. Data pre-processing is first requested to delete the abnormal train data due to malfunction of the sensors. Notice that the event of two trains meeting from opposite directions are currently unidentifiable by the strain-based conversion technique. Recorded train loads of such a meeting event are of large measurement error. Hence, such train records are also remove from the database. Table 4.6 gives a measured train sample during 10:00 to 11:00 a.m. on November 3, 2005, in which the time of arrival, running direction, speed, total number of bogies, bogie weight, and bogie spacing are provided. For example, the number 5 train is an eight-car train with 16 bogies, which is running on south track towards the airport at the speed of 35 m/s.

Table 4.6 A train sample (November 3, 2005)

Train number	1	2	3	4	5
Time of arrival	10:16:53	10:17:54	10:23:35	10:26:10	10:26:25
Bound	2	1	1	1	2
Speed (m/s)	34	29	30	30	35
Total number of bogies	16	16	16	14	16
Bogie 1 weight (kg)	24570	25526	24382	25824	25918
Bogie 1 spacing (m)	0	0	0	0	0
Bogie 2 weight (kg)	17049	22658	22314	23113	19258
Bogie 2 spacing (m)	14	15	16	16	14
Bogie 3 weight (kg)	20606	21405	20762	19869	23520
Bogie 3 spacing (m)	8	5	5	5	8
……					
Bogie 14 weight (kg)	19258	16296	18396	24272	20950
Bogie 14 spacing (m)	14	15	16	16	16
Bogie 15 weight (kg)	23473	22423	22376		22204
Bogie 15 spacing (m)	8	7	7		6
Bogie 16 weight (kg)	24570	21311	23426		19305
Bogie 16 spacing (m)	14	15	16		14

Note: Bound: 1-Kowloon; 2-Airport.

Table 4.7 A vehicle sample (November 3, 2005)

Vehicle number	1	2	3	4	5
Time of arrival	10:00:17	10:02:15	10:02:46	10:03:36	10:30:24
Bound	1	1	1	2	2
Lane	1	3	1	1	1
Speed (km/h)	74	91	60	76	56
Class	7	2	7	9	9
Total number of axles	3	2	3	3	5
Axle 1 weight (kg)	4850	450	5850	5260	5440
Axle 1 spacing (cm)	0	0	0	0	0
Axle 2 weight (kg)	6550	450	6760	10460	4170
Axle 2 spacing (cm)	584	249	557	408	335
Axle 3 weight (kg)	4760		5450	6700	3840
Axle 3 spacing (cm)	147		142	141	139
Axle 4 weight (kg)					4240
Axle 4 spacing (cm)					756
Axle 5 weight (kg)					4670
Axle 5 spacing (cm)					139

Note: Bound: 1-Kowloon; 2-Airport.
Lane: 1-slow lane; 2-middle lane; 3-fast lane.
Class: eight vehicle categories.

To monitor the road vehicle flow, a dynamic weigh-in-motion (WIM) system has been installed at the approach to Lantau Toll Plaza which is a distance away from bridge site. At the Plaza, a total of seven carriageways, including three lanes heading to airport and four lanes heading to Kowloon, were instrumented with the WIM sensors. The bending plate-type WIM sensor enables capturing of the vehicle information including the time of arrival, driven direction, lane, speed, class, total number of axles, axle weight, and axle spacing. The WIM data is first pre-processed to eliminate the abnormal vehicle data due to malfunction of the sensors. The upper limits of the maximum axle load and gross vehicle weight for each vehicle class are adopted according to the Hong Kong road traffic regulations and overloaded cases. Recorded vehicle data with axle load or gross vehicle weight exceeding the upper limits are thus removed. Noted that the vehicle data on two middle lanes heading to Kowloon are merged and assigned to the N2 lane on the bridge. A sample of WIM data during 10:00 to 11:00 a.m. of November 3, 2005 is given in Table 4.7. For example, the number 4 vehicle is a rigid heavy goods vehicle (Class-6) with four axles, which is running on N3 lane towards Kowloon at the speed of 70 km/h. One-month traffic load monitoring data of November 2005 are collected and pre-processed to serve as the database for subsequent analysis.

4.4.1.3 Simulation of traffic-induced stress response

Given the recorded on-site traffic information, each traffic load event is first discretised into a series of vertical point loads and assigned to corresponding traffic lanes. For instance, the number 5 train is represented by 16 vertical point loads at the locations of bogies and assigned to the south track; and the number 4 vehicle is represented by 3 vertical point loads at the locations of axles and applied to the N3 lane. With the arrival time and running speed, the coordinates of a vehicle or train on the bridge at any given time can be determined. First, the dynamic stress response due to railway traffic σ_R at time t is computed based on the railway stress influence lines

$$\sigma_R(t) = \sum_{n=1}^{N_R} \sum_{k=1}^{K_R} \Omega_{n,k}^{l}(t) R_{n,k} \tag{4.10}$$

where $R_{n,k}$ is the vertical load associated with the kth bogie of the nth train; $\Omega_{n,k}^{l}(t)$ is the railway stress influence coefficient due to the kth bogie of the nth train on the lth track at time t; N_R and K_R are the number of trains and the number of bogies of each train respectively. Similarly, the highway traffic induced dynamic stress response σ_H at time t can be computed using the highway stress influence lines

$$\sigma_H(t) = \sum_{n=1}^{N_H} \sum_{k=1}^{K_H} \Phi_{n,k}^{l}(t) H_{n,k} \tag{4.11}$$

where $H_{n,k}$ is the vertical load associated with the kth axle of the nth vehicle; $\Phi_{n,k}^{l}(t)$ is the highway stress influence coefficient due to the kth axle of the nth vehicle on the lth lane at time t; N_H and K_H are the number of vehicles and the number of axles of each vehicle respectively. Hence, the combined effect of railway and highway traffic is obtained by the superposition principle

$$\sigma(t) = \sigma_R(t) + \sigma_H(t) \tag{4.12}$$

where $\sigma(t)$ is the traffic-induced dynamic stress response at time t. A time step of $\Delta t = \frac{1}{51.2}$ s is adopted in the simulation of the stress time history which matches the sampling frequency of the strain sensor.

Traffic-induced stress time histories of top and bottom chords at the monitoring cross section from November 1 to 10, 2005 are generated by using Equations (4.10) to (4.12). As portrayed in Figure 4.13, the simulated stress responses have a close pattern with monitoring stress responses acquired from the strain gauge. Occurrences of either the vehicle- or train-induced peak stresses along the time axis are well coincided between two signals. Although the amplitudes of peak stresses of simulated time history are slightly greater than that of monitoring time history, the daily stress responses as constructed by the stress influence line method well reflect the flexural behaviour of the bridge deck. Hence, they are of satisfactory accuracy for the neutral axis identification.

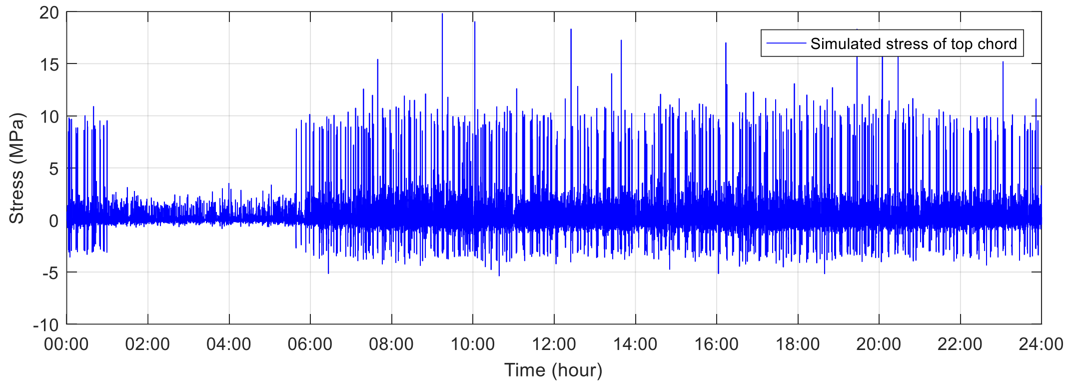

a) Simulated stress response

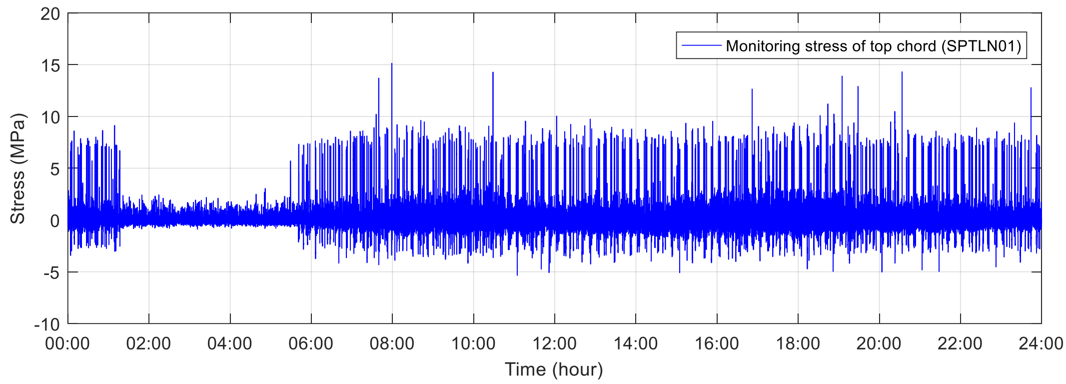

b) Monitoring stress response

Figure 4.13 Comparison of simulated and monitoring stress time histories (November 3, 2005)

4.4.2 Identification of Neutral Axis Positions

The traffic-induced peak stresses of top and bottom chords are extracted from the simulated stress time histories for the neutral axis position identification. In Figure 4.14, several stress clusters are observed in the extracted peak stresses, in which the histograms are of multimodality due to the presence of multiple types of traffic loads. The multilevel stress responses are inferred through the parametric Bayesian approach by use of the FGM model.

FGM estimations of the multilevel stress responses for top and bottom chords are given in Table 4.8 with the optimal number of components being inferred as four by the Bayes factor-based model selection method. The mean values and associated uncertain bounds of the component means (parameter μ) characterise the multilevel stress due to the multi-lane stochastic traffic condition.

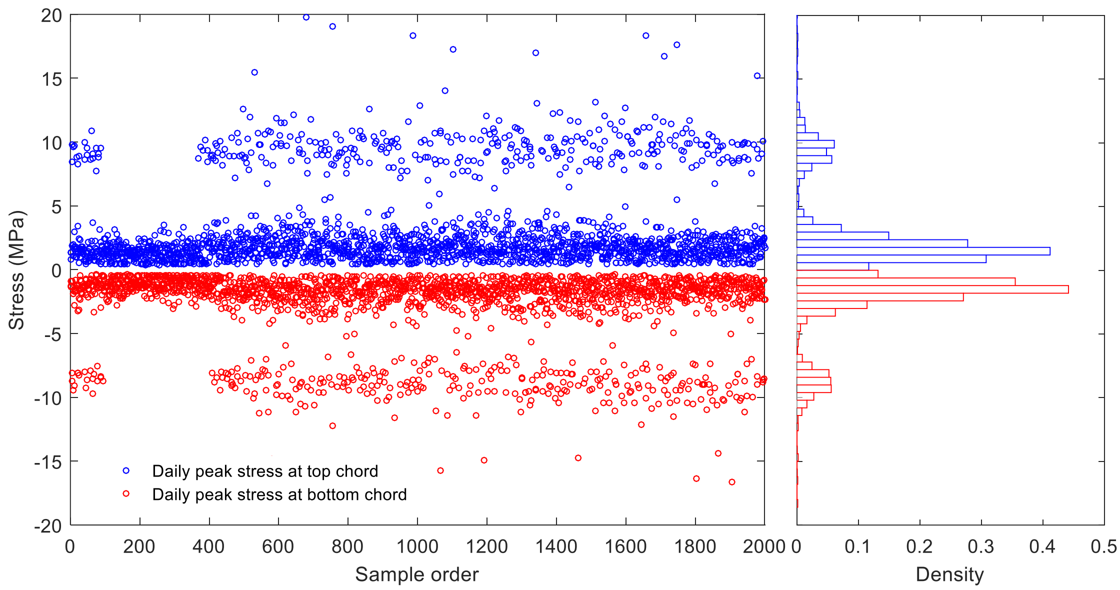

Figure 4.14 Daily peak stress responses based on simulation

Given the posterior samples of component means from the Gibbs iteration, the neutral axis positions $\boldsymbol{\varphi}$ are identified by using the Equation (4.8). The mean values, SD, and 5-95 CI of neutral axis positions can be obtained accordingly based on the samples of $\boldsymbol{\varphi}$. Identification of neutral axis positions for north truss of November 3, 2005 is shown in Table 4.9, in which they are classified into three categories according to the stress levels. On this day, the vehicle-induced 2nd neutral axis position is the highest, whereas the 4th neutral axis jointly induced by highway and railway has the lowest position among four neutral axes. Note that the 4th neutral axis position owns overall the greatest uncertainty than the other three neutral axes.

Table 4.8 FGM estimation of multilevel stress for north truss based on simulation (November 3, 2005)

Comp.	Parameter μ			Parameter σ^2			Parameter ω			Stress level
	5%	Mean	95%	5%	Mean	95%	5%	Mean	95%	
Top chord										
No.1	1.366	1.426	1.486	0.365	0.412	0.463	0.555	0.614	0.671	I
No.2	2.306	2.495	2.704	0.839	1.010	1.208	0.152	0.207	0.265	I
No.3	9.338	9.461	9.585	1.316	1.547	1.795	0.145	0.160	0.174	II
No.4	9.418	11.518	13.862	14.878	25.486	41.219	0.011	0.019	0.029	III
Bottom chord										
No.1	1.277	1.328	1.378	0.304	0.341	0.379	0.577	0.632	0.686	I
No.2	2.196	2.365	2.561	0.721	0.866	1.029	0.152	0.203	0.257	I
No.3	8.694	8.803	8.914	1.076	1.259	1.458	0.133	0.147	0.161	II
No.4	8.306	10.210	12.383	12.731	21.764	35.299	0.010	0.017	0.027	III

Note: The order of components is ranked according to (1) the ascending order of μ; and (2) the 4th component with the maximum σ^2.

Table 4.9 Identification of neutral axis positions for north truss based on simulation (November 3, 2005)

Comp.	Neutral axis position (m)			
	Mean	SD	5-95 CI	Category
No.1	2.954	0.052	[2.871, 3.043]	Highway-induced
No.2	2.980	0.102	[2.816, 3.151]	Highway-induced
No.3	2.952	0.017	[2.925, 2.980]	Railway-induced
No.4	2.879	0.263	[2.444, 3.307]	Jointly induced by highway and railway

Figure 4.15 plots the identified neutral axis positions and associated uncertain ranges for the north truss during ten consecutive days from November 1 to 10, 2005 based on simulation. The multilevel stresses of top and bottom chords as inferred through the FGM model are given for reference. It is observed that the trend of daily pair-wise component means have symmetric pattern, i.e. μ^T and μ^B increase or decrease at the same day. The neutral axis positions keep relatively stable within the period. Notice that the simulation-based neutral axis positions are of high similarity to the results based on monitoring in terms of the trend and uncertain range.

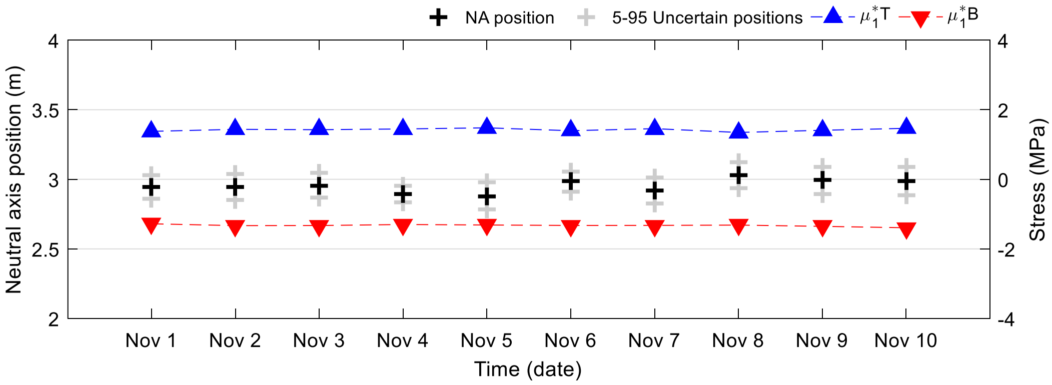

a) the 1st neutral axis position induced by highway traffic

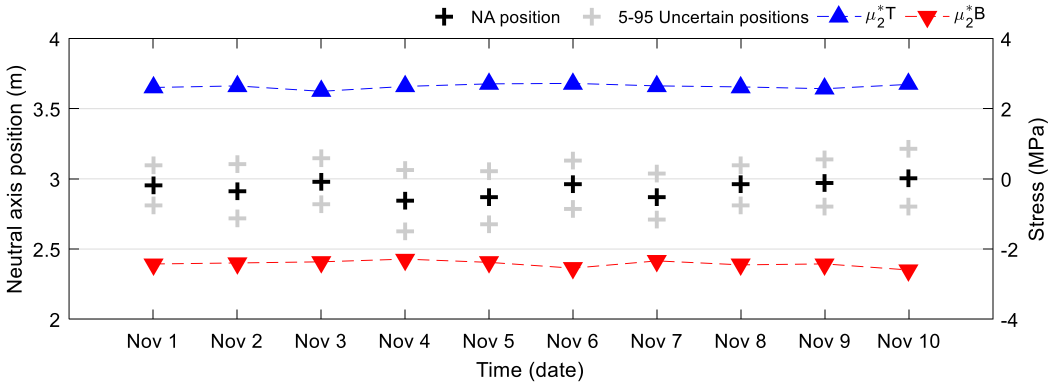

b) the 2nd neutral axis position induced by highway traffic

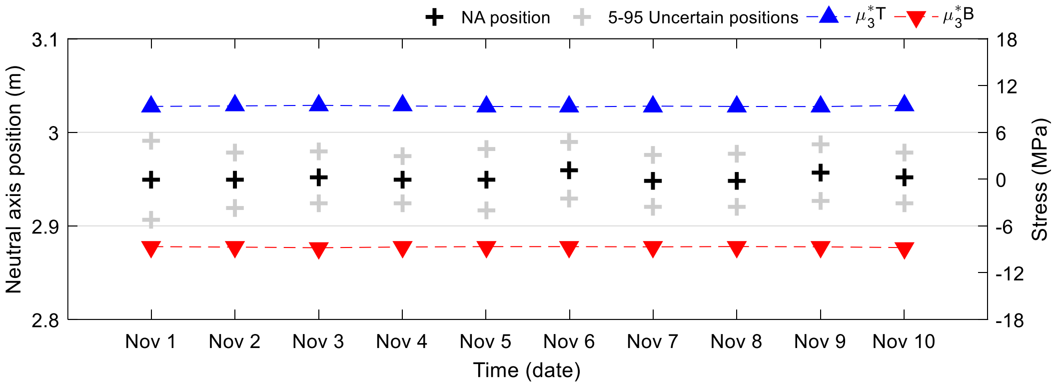

c) the 3rd neutral axis position induced by railway traffic

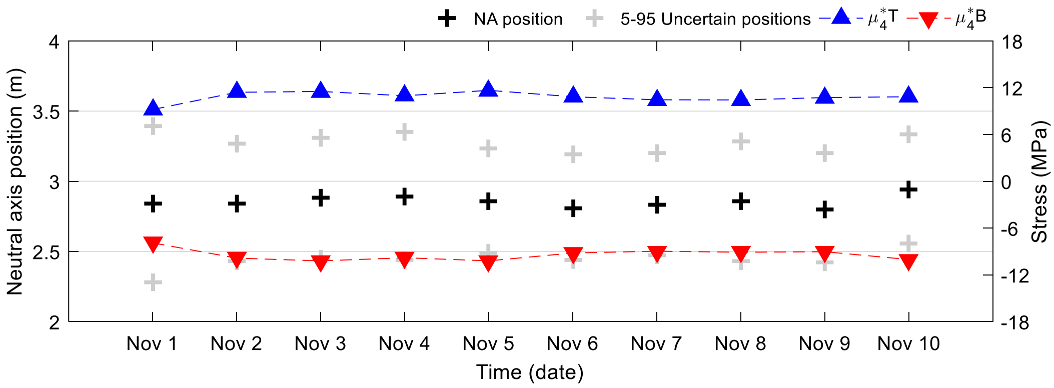

d) the 4th neutral axis position jointly induced by highway and railway

Figure 4.15 Daily neutral axis positions for north truss based on simulation

4.5 DAMAGE DETECTION OF BRIDGE DECK USING NEUTRAL AXIS BASED INDEXES

This section demonstrates the neutral axis based damage detection of bridge deck under stochastic traffic condition. Two damage indexes, i.e. the neutral axis change ratio and the cumulative neutral axis change ratio, are developed. Single-damage and multiple-damage cases are investigated to verify the effectiveness of the proposed method.

4.5.1 NA Change Ratio and Cumulative NA Change Ratio

For healthy condition of the Tsing Ma Bridge, the neutral axis of a monitoring cross section is expected to remain steady with limited intrinsic variation under stochastic traffic flow. As soon as the damage occurs at the nearby component, the neutral axis as a cross-sectional property will have apparent shift from the original position. Thereby, the relative difference between the initial neutral axis position corresponding to healthy condition and the new neutral axis position corresponding to damaged condition can be formulated as a damage index to indicate the presence of damage. Hence, the initial neutral axis position of the intact structure, which is now refer to the baseline neutral axis position, should be first determined.

The identified neutral axis positions based on the Bayesian FGM approach are themselves uncertain variables due to the presence of parametric uncertainty. With consecutive estimations of the neutral axis positions from the heathy bridge condition, the neutral axis positions can be updated in a Bayesian manner to seek for the baseline model. It is practical to presume that the jth neutral axis position obeys the Gaussian distribution $\varphi_j \sim N(\mu_{\varphi_j}, \sigma_{\varphi_j}^2)$. The Bayesian updating of the jth neutral axis position can be implemented as

$$p(\varphi_{j,\text{pred}}|\varphi_j) = \iint p\left(\varphi_{j,\text{pred}}\left|\mu_{\varphi_j}, \sigma^2_{\varphi_j}, \varphi_j\right.\right) p(\mu_{\varphi_j}, \sigma^2_{\varphi_j}|\varphi_j)\mathrm{d}\mu_{\varphi_j}\mathrm{d}\sigma^2_{\varphi_j} \tag{4.13}$$

where $\varphi_{j,\text{pred}}$ is called the predictive distribution of the neutral axis position based on the previous observations of φ_j, and $p(\mu_{\varphi_j}, \sigma^2_{\varphi_j}|\varphi_j)$ is the joint posterior distribution of the Gaussian parameters which has the form of

$$p\left(\mu_{\varphi_j}, \sigma^2_{\varphi_j}|\varphi_j\right) \propto p(\varphi_j\left|\mu_{\varphi_j}, \sigma^2_{\varphi_j}\right.)p(\mu_{\varphi_j}, \sigma^2_{\varphi_j}) \tag{4.14}$$

Once the conjugate normal-inverse-chi-squared prior is employed for the joint prior of μ_{φ_j} and $\sigma^2_{\varphi_j}$, the Bayesian updating based on Equations (4.13) and (4.14) can be manipulated in an explicit way. As illustrated in Table 4.10, the neutral axis positions during ten consecutive days from November 1 to 10, 2005 are utilised to construct the baseline model. The neutral axis positions $\boldsymbol{\varphi}$ are updated in a daily basis. The baseline neutral axis positions are listed in Table 4.11. In the Bayesian paradigm, the up-to-date baseline neutral axis positions can be available as long as new monitoring data are continuously fed in.

Table 4.10 Datasets for verification of neutral axis based damage detection method

Date	1	2	3	4	5	6	7	8	9	10
Condition	Baseline									
Date	13	14	15	16	17	18	19	20	21	22
Condition	Intact									
Date	23	24	25	26	27	28	29	30		
Condition	Single damage			Multiple damages						

Note: Dates are on November 2005.

A comparison between the baseline neutral axis positions and the neutral axis positions with respect to unknown structural condition can be made to indicate the damage occurrence. The neutral axis (NA) change ratio $\boldsymbol{\delta} = \{\delta_1, \cdots, \delta_J\}$ is formulated as

$$\delta_j = G^{-1} \sum_{g=1}^{G} \frac{\varphi_j^{(g)} - \bar{\varphi}_{j,\text{Baseline}}}{\bar{\varphi}_{j,\text{Baseline}}} \quad (j = 1, \cdots, J; g = 1, \cdots, G) \tag{4.15}$$

where δ_j is the averaged change ratio of the jth neutral axis position; $\varphi_j^{(g)}$ is the samples of the jth neutral axis position evaluated by Equation (4.8); and $\bar{\varphi}_{j,\text{Baseline}}$ is the mean value of the jth baseline neutral axis position as given in Table 4.11. Note that the NA change ratio δ_j has either positive or negative values: the positive change ratio indicates the upward movement of the neutral axis; whereas the negative represents the downward movement of the neutral axis.

Table 4.11 Baseline neutral axis positions for north truss

Comp.	Neutral axis position (m)		
	Mean	SD	Category
No.1	2.954	0.072	Highway-induced
No.2	2.930	0.123	
No.3	2.952	0.018	Railway-induced
No.4	2.857	0.250	Jointly induced by highway and railway

The identified neutral axis positions would exhibit intrinsic variability due to the multi-lane stochastic traffic under normal bridge operation. The directions of traffic-induced shifting of the neutral axis position are highly uncertain. However, the damage-induced moving direction of all the identified neutral axes is exclusive with either being upward or downward that depends on the change of cross-sectional property with respect to the damaged component. Hence, the neutral axis positions should have identical moving direction given the same damage scenario. Based on the proposed NA change ratio, the cumulative NA change ratio η can be further formulated as

$$\eta = \sum_{j=1}^{J} \delta_j \quad (j = 1, \cdots, J) \tag{4.16}$$

where δ_j is the jth change ratio of the neutral axis position. The cumulative NA change ratio is the linear summation over all the neutral axis change ratios, which results in greater index value when each of δ_j has identical positive or negative sign.

To validate the sensitivity of the proposed damage indexes, different damage extent at the diagonal strut adjacent to the monitoring cross section as depicted in Figure 4.16 are simulated by reducing the element stiffness to 75%, 50%, 25%, 1% of the original value, respectively. Figure 4.17 gives the calculated damage indexes for each damage extent and healthy condition. It is undetectable for 25% and 50% damage extent since no evident change of damage indexes has been found. For the 75% damage extent, noticeable downward shifts of the 1st, 2nd and 4th neutral axes are found with the cumulative NA change ratio of -2.3%. However, it is still questionable to raise a damage alert. For the 99% damage extent, the NA change ratio has synchronous negative values for all neutral axes and the cumulative NA change ratio reaches about -10%. In this regard, the presence of damage near the monitoring section can be confirmed with a good confidence level. Based on the above studies, the proposed method can confidently identify a damage with extent greater than 90% for a structural component. Similar detection accuracy for the Tsing Ma Bridge was also obtained by Chen et al. (2014), where an influence line based damage detection method was applied.

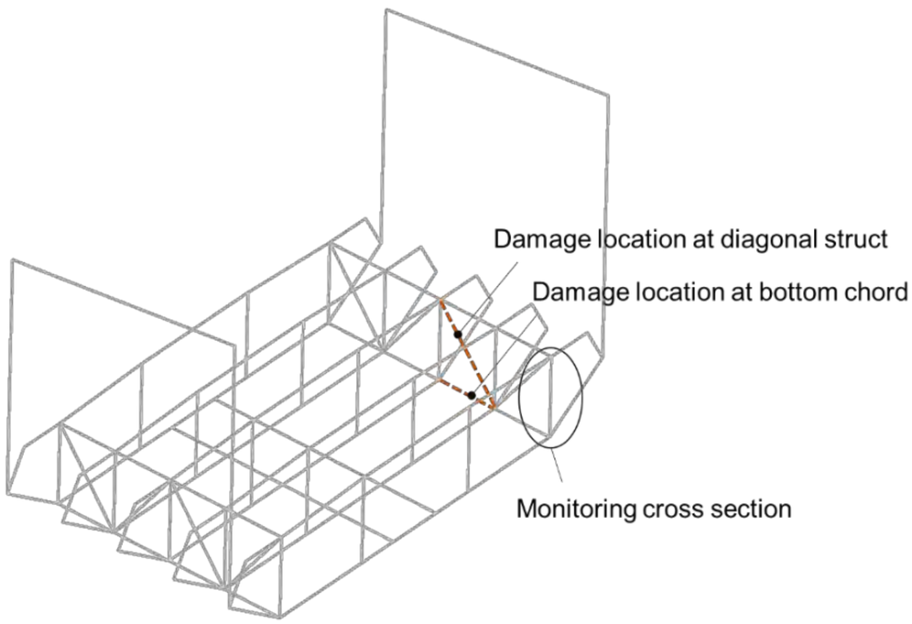

Figure 4.16 Damage scenarios on the bridge deck

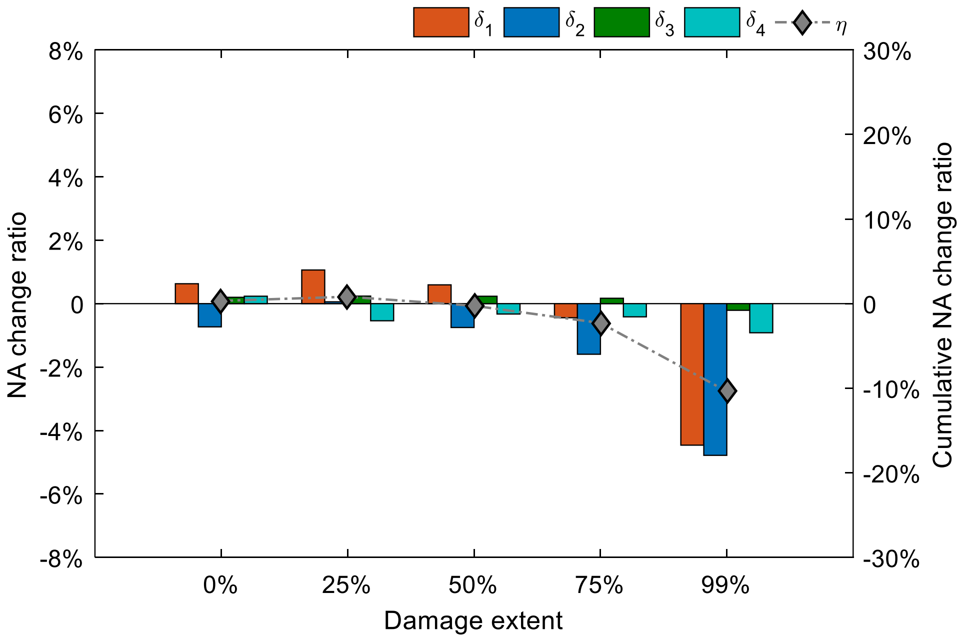

Figure 4.17 Calculated damage indexes for different structural condition

4.5.2 Case Study: Single Damage

The proposed neutral axis based damage detection method is further validated through numerical studies by considering single and multiple damages. As shown in Table 4.10, it is first assumed that the bridge deck is under the healthy status from November 13 to 20. For the single-damage case, the diagonal strut adjacent to the monitoring cross section as depicted in Figure 4.16 is assumed to be damaged by reducing its cross-sectional area to 1% of the original value, and it is presumed to occur since the date of November 21.

It finds that there exists both positive and negative values of the daily NA change ratio for most of the days under healthy status of the bridge as shown in Figure 4.18(a). As expected, the cumulative NA change ratio fluctuates around the zero value within these days, implying the intrinsic variation of the neutral axis under in-service traffic operation. Though tracking the change of the neutral axis positions, it signals a high possibility that the bridge deck is under heathy condition from November 13 to 20.

Negative values of the daily NA change ratio become predominant since the date of November 21 when single damage of the diagonal strut is introduced as shown in Figure 4.18(b). The highway-induced 1st and 2nd neutral axes have continuous significant downward movements during those days. The railway-induced 3rd neutral axis shifts downwards as well but with much shorter distance. The 4th neutral axis jointly induced by railway and highway, however, has both upward and downward movements in those days. Reasons for this phenomenon are two folds: (1) the railway-induced neutral axis position change is less sensitive to the damage of diagonal strut; and (2) the identified 4th neutral axis position is of the greatest uncertainty as revealed in Figure 4.10 and Figure 4.15. Consequently, it is observed the cumulative NA change ratio has negative values at -11.0% on average during these days. A damage occurrence alert can be issued based on the evident shifts of the neutral axis.

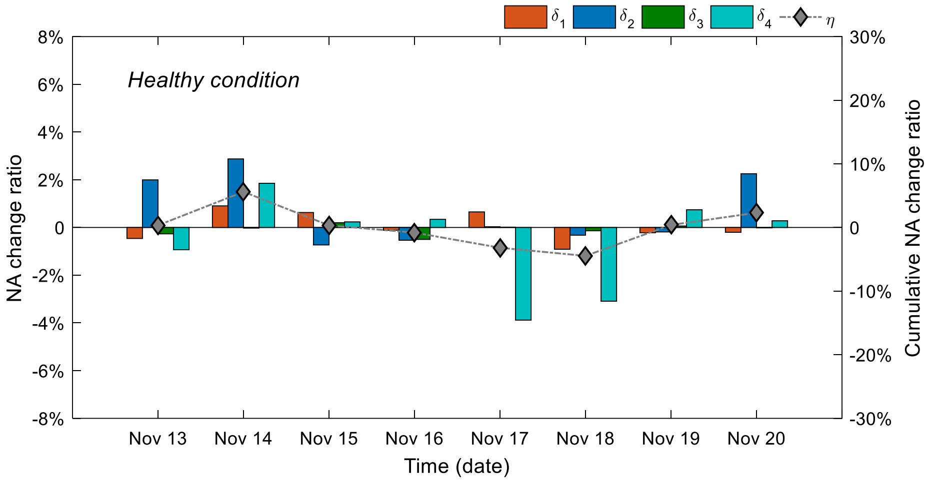

a) damage indexes under healthy condition

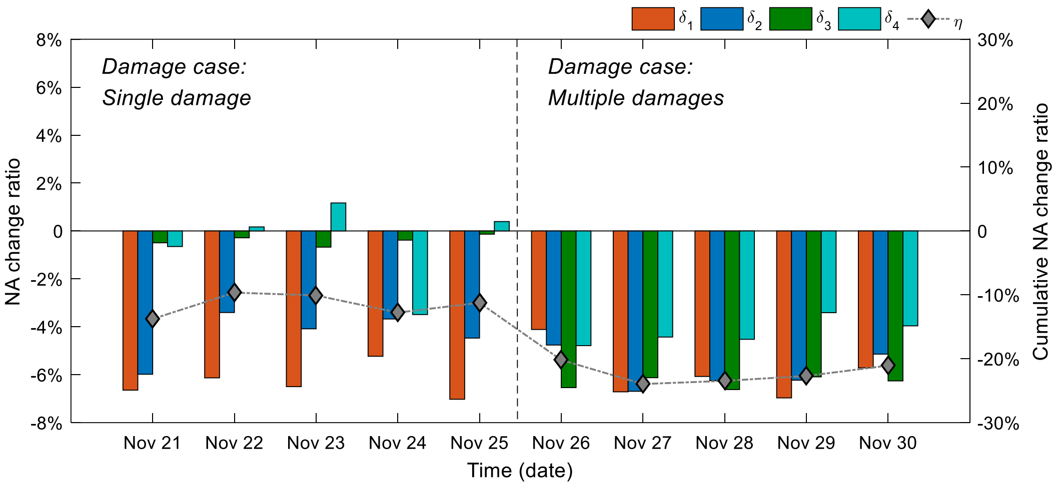

b) damage indexes under two damage cases

Figure 4.18 Detection of damage using neutral axis based indexes

4.5.3 Case Study: Multiple Damages

For the multiple-damage case, both the diagonal strut and the bottom chord adjacent to the monitoring cross section are assumed to be severely damaged. The cross-sectional areas of both elements are reduced to 1% of the original values. This damage scenario is presumed to occur since the date of November 26.

As plotted in Figure 4.18(b), the NA change ratio continuously holds large negative values since November 26, implying the synchronous downward movements of the neutral axis positions as multiple damages are introduced. Table 4.12 lists the maximum and minimum values of the two types of damage indexes under different structural conditions. The railway-induced 3rd neutral axis significantly moves downwards with nearly six times greater than the single-damage induced shift. It seems the railway-induced neutral axis position change is more sensitive to the damage of bottom chord. Negative change ratios of the 2nd and 4th neutral axes are noticeably greater than that of single-damage case as well. The upward movement of the 4th neutral axis is not observed under multiple damages. Nevertheless, the highway-induced 1st neutral axis has similar change ratio in either the single- or multiple-damage cases. The synchronous downward movements of the neutral axis positions raise alert that damages are existed. As the damage accumulates, the cumulative NA change ratio is almost two times greater than that of single-damage case. It further indicates the cumulative NA change ratio has the potential to be a damage severity indicator. However, possible false negative error of damage detection may occur when neutral axis change is offset, for example, if the neutral axis shift induced by structural member A is upward while the shift induced by structural member B is downward. More damage locations and components should be considered in order to develop a classification table for all nearby structural members according to different damage-induced NA shift directions.

Table 4.12 Maximum and minimum values of damage indexes for different structural condition

Structural condition		NA change ratio				Cumulative NA change ratio
		δ_1	δ_2	δ_3	δ_4	η
Intact	Max	0.9%	2.9%	0.2%	1.9%	5.6%
	Min	-0.9%	-0.7%	-0.5%	-3.9%	-4.5%
Single damage	Max	-5.2%	-3.4%	-0.1%	1.2%	-9.7%
	Min	-7.0%	-6.0%	-0.7%	-3.5%	-13.8%
Multiple damages	Max	-4.1%	-4.8%	-6.1%	-3.4%	-20.2%
	Min	-7.0%	-6.7%	-6.6%	-4.8%	-24.0%

The cumulative NA change ratio η under healthy condition provides the information about the intrinsic variability of the neutral axis position. Through the Bayesian updating of daily samples of η, the underlying distribution of η with respect to the healthy condition can be obtained as shown in Figure 4.19. It is of high possibility that η falls within the interval $[\mu - 2\sigma, \mu + 2\sigma]$ for the healthy condition. A fairly large deviance of η from the mean value can indicate the occurrence of damage. As such, positive and negative thresholds of η for detecting damage can be formulated as $\eta_H^- = \mu - 2\sigma$ and $\eta_H^+ = \mu + 2\sigma$, respectively. Note that μ and σ are updated mean and standard deviation for η, respectively. The probability of damage P_D can be calculated as

$$P_D = 1 - P(\eta_H^- < \eta_u < \eta_H^+) \tag{4.17}$$

where η_u is the cumulative NA change ratio for an unknown state. By using Equation (4.17), the probabilities of damage with respect to healthy condition, single-damage condition and multiple-damage condition are 2.4%, 37.6% and 51.7%, respectively.

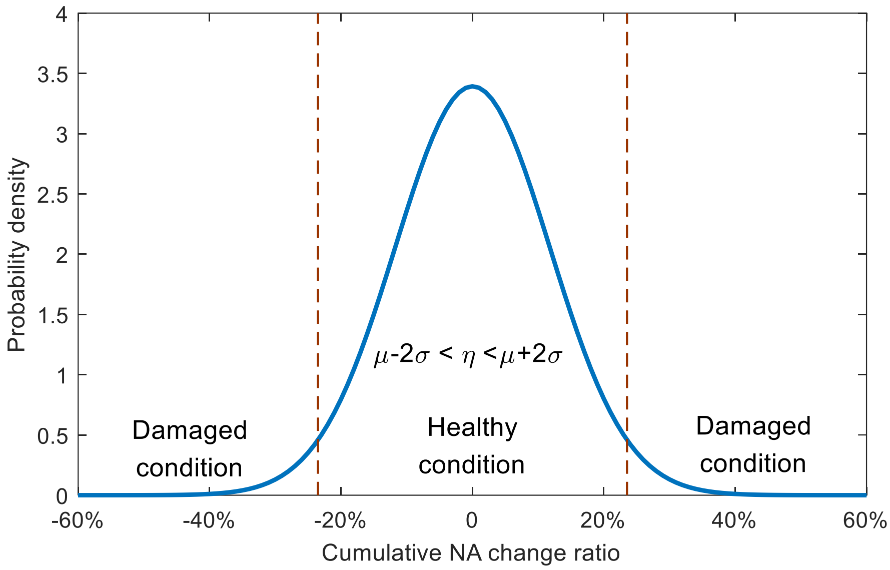

Figure 4.19 Determination of structural condition based on cumulative NA change ratio

4.6 SUMMARY

An ultimate goal of structural health monitoring is the timely detection of possible aging or damage signs in an in-service structure by using the measurement data. This chapter develops a neutral axis based damage detection method for the Tsing Ma Bridge under operational traffic condition. Sensitivity analysis based on bridge FEM is first carried out to investigate the variation of neutral axis position under deterministic moving loads on multiple traffic lanes. In-service multilevel stress responses are utilised to identify the neutral axis positions under stochastic traffic loads by means of the parametric Bayesian mixture model. Two damage indexes, i.e. the NA change ratio and cumulative NA change ratio, are proposed to indicate the presence of damage. Case studies with single and multiple damages are investigated to verify the effectiveness of the new method. Several important findings are summarised as follows.

(1) Traffic-induced neutral axis position is insensitive to the change of loading magnitudes

but heavily depends on the traffic lane in use. Stochastic highway and railway traffic on multiple lanes generate varying neutral axis position for a designated cross section over a given time period. Neutral axis position can only be adopted as a damage sensitive feature with the associated uncertainty being properly quantified.

(2) The proposed neutral axis position identification method based on the parametric Bayesian mixture model is able to accurately predict the mean values and associated uncertain ranges of each neutral axis. The identified neutral axis positions of healthy bridge condition keep relative stable under stochastic traffic loads.

(3) The influence line tool in conjunction with on-site traffic load data are able to construct the time history of stress responses for the Tsing Ma Bridge with adequate precision. Simulation-based neutral axis positions are of high similarity to the results based on monitoring in terms of the trend and uncertain range.

(4) Results of case studies show that damage of local component could be confidently detected by synchronous shifts of neutral axes of the neighbouring cross section. The cumulative NA change ratio triggers more convincible detection alerts when damage happens under operational traffic condition. It has the potential to be a damage severity indicator.

CHAPTER 5
NONPARAMETRIC BAYESIAN MIXTURE MODEL

5.1 INTRODUCTION

In Chapter 3, the parametric Bayesian mixture model along with Markov chain Monte Carlo-based posterior simulation technique is proposed to handle the multimodal structural responses with consideration of parametric uncertainty. The parametric model directly interprets the unknown data via inference on the relevant model parameters (e.g. component means, variances, and mixing weights). One of the limitations inherent in this process is that the number of mixture components of the parametric model is assumed to be a predefined deterministic value, which is equivalent to pose restrictive constraints on the model complexity. Although the Bayes factor-based model order selection procedure is preliminary proposed in Chapter 3 to address this critical issue, it is still impractical to compare all possible candidate models and the corresponding computation demand is prohibitive (Neal, 2000; Teh, 2011). This chapter presents a class of more flexible mixture models based on the nonparametric Bayesian approach, in which the number of mixture components can be directly estimated and automatically adapts to the unknown data structure. It further allows one to simultaneously incorporate both model order and parametric uncertainties inherent in the modelling process. The proposed nonparametric Bayesian mixture model stands as an improvement over the parametric counterpart.

When applying traditional parametric models to observed data, one potentially has made certain assumptions about the data-generating mechanism. For instance, assuming samples are drawn from a distribution family indexed with a set of finite-dimensional parameters. These probabilistic assumptions, if not be properly testified, could be unrealistic for the observed data such as structural health monitoring data, causing possible bias in model interpretation. The nonparametric (or semiparametric) approach has attracted long-term attention in both theoretical and practical aspects as it provides a framework that one can avoid arbitrary and possibly unverifiable assumptions inherent in parametric approach (Ghosal and Van der Vaart, 2017). Typically, the nonparametric approach abandons some specific parametric assumptions through building models over an infinite-dimensional parameter space. Thus, the dimension of model parameters is allowed to change with data size, avoiding possible over- or under-fitting. A simple example of the nonparametric approach would be the Parzen window method to density estimation, which centres a Gaussian density at each observation (i.e. one mean parameter per observation).

Motivating by the coherent and unified framework of the Bayesian theory, the nonparametric Bayesian approach arose in the 1970s and it paves a way to consider nonparametric models under the Bayesian framework. The Bayesian approach to nonparametric problems was introduced in the pioneer work of Ferguson (1973) and further refined by the works including Antoniak (1974), Ferguson (1983) and Lo (1984). The Dirichlet process mixture (DPM) model is one of the most widely discussed model in Bayesian nonparametrics. Differ from conventional parametric model, the DPM model is such a nonparametric Bayesian model that defined on an infinite-dimensional parameter space (infinite number of components) and uses only a finite subset of the available parameters (effective components) to represent the model. Hence, the model order as measured by the effective number of components can freely adapt to the unknown data structure. In this way, the number of components in mixture model is no longer a deterministic value but a random variable that can be directly inferred from the data. One can bypass the mixture model order selection issue, which is usually fraught with technical difficulties. More importantly, the model order uncertainty in the mixture model can be assessed in the meantime. Quantification of both model order and parametric uncertainties of multimodal structural responses can then be pursued. In the past two decades, the DPM model has been successfully applied to a variety of fields such as machine learning (Orbanz and Teh, 2010), image segmentation (Orbanz and Buhmann, 2008), document clustering (Huang et al., 2012), chemical mechanical planarization (Liu et al., 2017), reliability analysis (Mokhtarian et al., 2013) and SHM (Rogers et al., 2019).

The theoretical framework of the nonparametric Bayesian mixture model is presented in this chapter. A comprehensive comparison on the performance of the parametric and nonparametric approaches is further discussed. The layout of this chapter is organized as follows. Section 5.2 introduces the model framework of the nonparametric Bayesian approach, in particular, the Dirichlet process mixture model. The collapsed Gibbs sampler is devised to pursue the posterior mixture density samples. A quantitative diagnosis strategy is proposed to assess the convergence of the simulation. Section 5.3 demonstrates a numerical example, where the nonparametric Bayesian approach is tested through modelling on a trimodal data set. A comparison study on the performance of the parametric and nonparametric Bayesian approaches is presented in Section 5.4, where several key issues, including model complexity, goodness-of-fit, uncertainty characterization and computational demands, are carefully investigated.

5.2 MODEL FRAMEWORK

5.2.1 Dirichlet Process Prior

Thinking of the nonparametric models in the Bayesian manner, one first need to assign prior distributions for all model parameters, which now are on the infinite-dimensional parameter space. Unlike putting conventional prior distributions on individual parameters of a parametric model as shown in Chapter 3, infinite dimensional parameters usually constitute functions or measures, requiring workable prior distributions for functions or measures rather than random variables. The Dirichlet process (DP) first introduced in Ferguson (1973) is arguably the most widely adopted nonparametric prior and later it became the building block in Bayesian nonparametrics. In this section, we begin with the definition and key properties of the Dirichlet process, which are essential to derive the DPM model.

5.2.1.1 Dirichlet process

The Dirichlet process is a stochastic process whose sample paths are probability measures with probability one (Teh, 2011). Samples from DP can be regarded as random distributions with certain Dirichlet properties, thus one can loosely view DP as a distribution over distributions.

Formally, a random distribution G is distributed according to DP with the following formation

$$G \sim DP(\alpha, G_0) \tag{5.1}$$

where DP is parameterized by a positive concentration parameter α and a base measure G_0. The role of these two parameters playing in DP is analogous to the mean and variance in Gaussian distribution: the base measure G_0 is the expectation of G, i.e. $G_0(\cdot) = E[G(\cdot)]$, while the concentration parameter α reflects the diffusion of G about G_0. A key feature of DP is that a distribution drawn from DP is always discrete with probability one, regardless of whether the base measure G_0 is continuous or discrete. The Dirichlet properties of DP indicates that for any finite measurable partition $A_1, \cdots, A_r$ of the probability space Θ, the vector $(G(A_1), \cdots, G(A_r))$ is random and obey to the Dirichlet distribution

$$(G(A_1), \cdots, G(A_r)) \sim Dir(\alpha G_0(A_1), \cdots, \alpha G_0(A_r)) \tag{5.2}$$

Recall that the Dirichlet distribution is used as prior for mixing weights in finite Gaussian mixture (FGM) model, the DP extends the Dirichlet properties to infinite-dimensional setting. Because G is a distribution, we can also draw samples from G itself and later we shall see the Gaussian kernel parameters θ (mean and variance) are exactly drawn from G in our nonparametric DPM model. Suppose $\theta_1, \cdots, \theta_n$ be a sequence of independent samples from G and for any finite measurable partition $A_1, \cdots, A_r$, the posterior distribution of the vector $(G(A_1), \cdots, G(A_r))$ is still Dirichlet distributed

$$\big(G(A_1), \cdots, G(A_r)\big) | \theta_1, \cdots, \theta_n \sim Dir(\alpha G_0(A_1) + n_1, \cdots, \alpha G_0(A_r) + n_r) \tag{5.3}$$

where n_k is the number of observed θ_i's in the partition of A_k $(k = 1, \cdots, r)$. The posterior distribution of G conditional on $\theta_1, \cdots, \theta_n$ is again a DP with updated concentration parameter and base measure

$$G|\theta_1, \cdots, \theta_n \sim DP(\alpha + n, \frac{\alpha}{n+\alpha} G_0 + \frac{n}{n+\alpha} \frac{\sum_{i=1}^{n} \delta_{\theta_i}}{n}) \tag{5.4}$$

where δ_{θ_i} is the Dirac measure (a degenerate distribution with point masses) located at atom θ_i. Note that the posterior (updated) base measure has a form of weighted average over the prior base measure G_0 and the empirical distribution $\frac{\sum_{i=1}^{n} \delta_{\theta_i}}{n}$ of θ, indicating that there is a probability proportional to n that the posterior G is affected by the observations, while it holds the probability proportional to α that the posterior G remains in G_0. Thus, the concentration parameter α again describes the probability mass associated with the prior: as $\alpha \to \infty$, we have $G \to G_0$ pointwise since G is always discrete.

The posterior base measure is also the predictive distribution of θ_{n+1} given $\theta_1, \cdots, \theta_n$, hence we have the Blackwell-MacQueen urn scheme

$$\theta_{n+1}|\theta_1, \cdots, \theta_n \sim \frac{1}{n+\alpha} (\alpha G_0 + \sum_{i=1}^{n} \delta_{\theta_i}) \tag{5.5}$$

where the random G has been marginalized out. The clustering property of the DP is directly revealed by Equation (5.5): it allows positive probability to next sample θ_{n+1} that can be re-located to previous samples $\theta_1, \cdots, \theta_n$. In other words, if we have a sequence of draws $\theta_1, \theta_2, \cdots \sim G$ and $G \sim DP(\alpha, G_0)$, then there would exist repeated values of θ_i's, leading to groups (clusters) of θ_i's that take on the same values.

Because of the exchangeability of the sequence $\theta_1, \cdots, \theta_n$, any arbitrary θ_i $(i = 1, \cdots, n)$ can be regarded as the last observation in the sequence. Let $\theta_1^*, \cdots, \theta_J^*$ $(J \ll n)$ be the unique values among $\theta_1, \cdots, \theta_n$, then a set of θ_i's with identical values θ_j^* $(j = 1, \cdots, J)$ can be regarded as a group. The clustering property of DP can be rewritten as

$$\theta_i | \boldsymbol{\theta}_{-i} \sim \frac{1}{n-1+\alpha} (\alpha G_0 + \sum\nolimits_{j=1}^{J} n_{-i,j} \delta_{\theta_j^*}) \tag{5.6}$$

where $\boldsymbol{\theta}_{-i}$ is the subset of $\{\theta_1, \cdots, \theta_n\}$ without taking account of θ_i, and $n_{-i,j}$ is the number of θ_h's $(h \neq i)$ in the cluster associated with θ_j^*. As implied by Equation (5.6), accumulation of samples tends to occur in 'big' cluster associated with larger number of samples since the probability of drawing θ_i conditional on any other sequence is proportional to the cluster size $n_{-i,j}$. This is a rich-get-richer phenomenon, where 'big' clusters grow bigger faster (Teh, 2011).

5.2.1.2 Chinese restaurant process

As the sequence $\theta_1, \cdots, \theta_n$ is random in nature, the clustering property of DP leads to an infinite random partition of the index set $\{1, \cdots, n\}$ of θ, within which θ_i's have identical values. The distribution over the infinite random partitions is called the Chinese restaurant process (CRP) due to a delicate metaphor. Consider a restaurant with infinitely many tables and a sequence of customers waiting outside. The first customer enters and sits on the first table, followed by the second customer sits in the first table with probability of $\frac{1}{1+\alpha}$ or choose a new table with probability of $\frac{\alpha}{1+\alpha}$. The customers continue to join the restaurant with the following generalization: the i th customer either chooses an occupied table j with probability proportional to the number of customers already sitting there, or sits on a new unoccupied table with probability proportional to α. Customers sitting in the same table share one dish together. At any time point of this process, the allocation of customers to tables defines a random partition. A graphical illustration of the CRP is given in Figure 5.1. Given the observations, the CRP is a useful representation for the DPM model where customers represent the indexes associated with observations, tables represent the components, and dishes represent the component parameters. This will be further detailed in the following discussion.

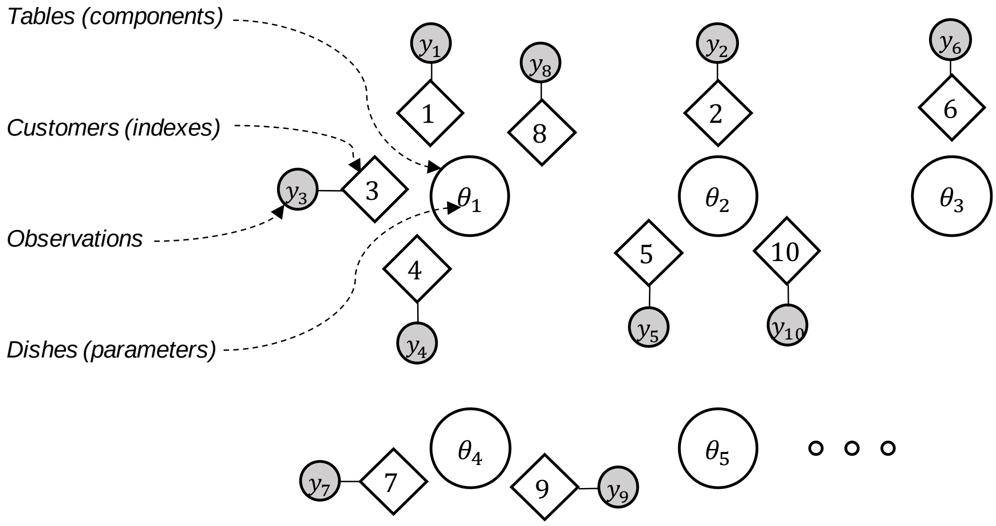

Figure 5.1 The Chinese restaurant process (Gershman and Blei, 2012)

Formally, we have the following conditional probability governing the CRP. Let $z_i = j$ be the allocation to jth table of the ith customer. The samples from CRP can be sequentially drawn from

$$\Pr(z_i = j|\mathbf{z}_{-i}) = \begin{cases} \dfrac{n_{-i,j}}{n-1+\alpha}, if\ j\ is\ an\ occupied\ table \\ \dfrac{\alpha}{n-1+\alpha}, if\ j\ is\ a\ new\ table \end{cases} \tag{5.7}$$

where $\mathbf{z}_{-i}$ is the allocations of $n-1$ customers excluding the ith customer. The parameter

α here implies that the larger value α has, the more likely the next customer will choose a new table, while the more tables will be occupied by customers during the process.

5.2.1.3 Stick-breaking construction

As revealed by Equation (5.5), samples drawn from a DP are composed of a weighted sum of point masses. The explicit realization of DP is achieved through the so-called stick-breaking construction

$$
\begin{aligned}
G &= \sum_{j=1}^{\infty} \omega_j \delta_{\theta_j^*} \\
\omega_j &= \beta_j \prod_{l=1}^{j-1} (1-\beta_l) \\
\beta_j &\sim Beta(1,\alpha) \\
\theta_j^* &\sim G_0
\end{aligned}
\tag{5.8}
$$

where ω_j is the probability mass (weight) at atom θ_j^* satisfying $\sum_{j=1}^{\infty} \omega_j = 1$. The procedure of stick-breaking is illustrated in Figure 5.2. Suppose we have a stick of unit length, which represent the total probability to be assigned to all the atoms. The stick is first randomly cut off with a length of $\beta_1 \sim Beta(1,\alpha)$, and we assign this $\omega_1 = \beta_1$ probability mass to the first randomly generated atom $\theta_1^* \sim G_0$. Then the remaining $(1-\beta_1)$ length of the stick is again cut off with the portion of $\beta_2 \sim Beta(1,\alpha)$, and we assign the probability mass of $\omega_2 = \beta_2(1-\beta_1)$ to the next atom $\theta_2^* \sim G_0$. The process continues so that the stick is divided into infinite number of segments with each segment length representing weighted point mass. The infinite sum of weighted point masses constitutes the discrete random measure G, which is indeed DP-distributed. The stick-breaking construction over ω is conveniently written as

$\omega \sim GEM(\alpha)$ (Sethuraman, 1994). As plotted in Figure 5.2, the parameter α controls the distributional shape of the beta distribution, where the larger value of α the smaller value of $\beta \sim Beta(1, \alpha)$ will be generated, hence the stick will be eventually divided into more segments. The parameter α contained in the stick-breaking construction here is functionally the same as in CRP.

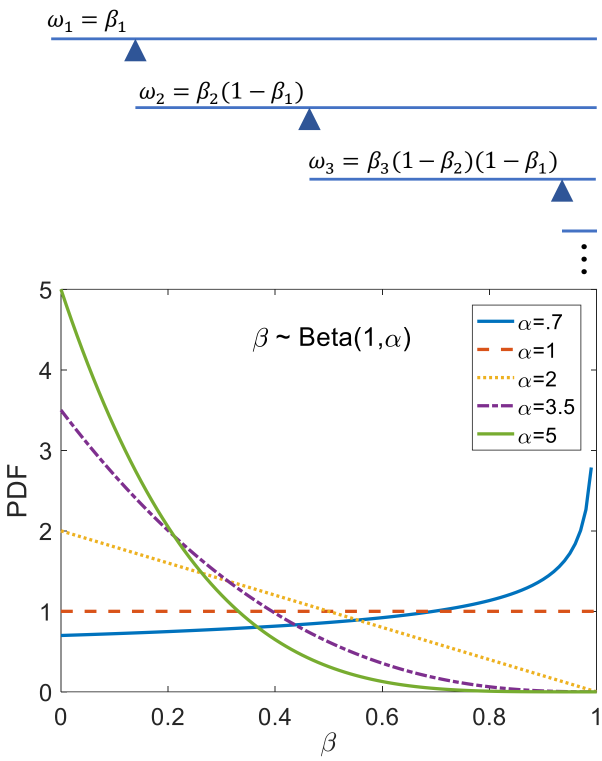

Figure 5.2 Stick-breaking construction and the beta distribution

5.2.2 Dirichlet Process Mixture Model

The direct implement of DP as a prior distribution is often infeasible since the random distributions drawn from DP are of discreteness which do not have density functions. From the perspective of nonparametric density estimation, one can solve the awkward discreteness by means of kernel technique: smooth over the DP draws with a continuous parametric density function. In general, the Bayesian nonparametric density estimation of a random variable Y

can be defined as (Gelman et al., 2014)

$$p(y) = \int K(y|\theta)\mathrm{d}G(\theta) \tag{5.9}$$

where $K(y|\theta)$ is a kernel density indexed by θ and $G \sim DP(\alpha, G_0)$. Due to the cluster property of DP, the nonparametric density defined in this way is equivalent to a mixture model with infinite number of components

$$p(y) = \sum_{j=1}^{\infty} \omega_j K(y|\theta_j^*) \tag{5.10}$$

where $\omega \sim GEM(\alpha)$ is generated from the DP stick-breaking construction. This nonparametric Bayesian mixture model is also referred to the Dirichlet process mixture (DPM) model. Sampling from the DPM model can be conducted through the following hierarchical structure

$$\begin{gathered} y_i \sim K(\cdot\,|\theta_i) \\ \theta_i \sim G \\ G \sim DP(\alpha, G_0) \end{gathered} \tag{5.11}$$

where y_i's are the observations of Y and θ_i's are the corresponding latent parameters ($i = 1, \cdots, n$) drawn from G. In this study, the Gaussian kernel is adopted in nonparametric density estimation, hence we have $\theta_i = (\mu_i, \sigma_i^2)$. The base measure G_0 is chosen to be the normal-inverse-chi-squared distribution which is conjugate to the Gaussian kernel. This conjugacy has been introduced in Chapter 3 and will not be detailed here. The conjugate setting is commonly used in DPM model and it allows direct sampling from the conditional distributions which brings computation convenience for the posterior inference of the DPM model.

With the stick-breaking construction, the DPM model can be rewritten using a similar form as the finite mixture model, in which the number of components is unbounded now. Together with Equations (5.8) and (5.11), we have the equivalent expression for DPM model

$$\begin{aligned} &\omega|\alpha \sim GEM(\alpha) && \theta_j^* \sim NIC(\xi_j, \kappa_j, \nu_j, s_j^2) \\ &z_i \sim Mult(\omega) && y_i \big| z_i, \theta_j^* \sim N(\theta_{z_i}^*) \end{aligned} \tag{5.12}$$

where ω is the mixing weight, z_i is the component indicator, $\theta_j^* = (\mu_j^*, \sigma_j^{2*})$ is the parameter of Gaussian component $N(\theta_j^*)$, and NIC is the normal-inverse-chi-squared prior over component parameters with hyperparameters $\{\xi_j, \kappa_j, \nu_j, s_j^2\}$. The stick-breaking representation reveals that the mixing weight ω decreases exponentially quickly, thus only a limited number of components are used in DPM model a priori. Generally, the DPM model is a mixture model with varying number of components - the model complexity can automatically adapt to the observation data. This is an essential difference with the FGM model where the number of components is a predetermined fixed value.

Direct evaluation of the posterior DPM model is computationally prohibitive because of the unbounded parameter dimension and the inherent complexity of the posterior (Escobar and West, 1995). In practice, it is common to perform approximate inference using Markov chain Monte Carlo methods to tackle this issue. Specifically, the Gibbs sampler is well suited for the posterior computation since the DP's Blackwell-MacQueen urn scheme of Equation (5.5) provides a well-defined full conditional posterior distribution for the model parameter θ. Combining with the Gaussian likelihood, the conditional posterior of $\theta_i|\boldsymbol{\theta}_{-i}$ of the DPM model with single observation y_i can be derived as

$$\theta_i|\boldsymbol{\theta}_{-i}, y_i \sim b\alpha q_0 H(\theta_i|y_i) + b\sum_{j\neq i} q_j \delta_{\theta_j^*}$$

$$\text{with } H(\theta_i|y_i) \propto G_0(\theta_i)N(y_i|\theta_i),$$

$$q_0 = \int G_0(\theta)N(y_i|\theta)\mathrm{d}\theta, \tag{5.13}$$

$$q_j = N(y_i|\theta_j^*), \text{ and}$$

$$b = \left(\alpha q_0 + \sum\nolimits_{j\neq i} N(y_i|\theta_j^*)\right)^{-1}$$

where H is the posterior of θ_i with prior of G_0, q_0 is the marginal likelihood of y_i, q_j is the Gaussian likelihood evaluated at y_i, and b is the normalizing constant that makes the above probability sum to one. Similarly, this conditional probability states that a new sample of θ_i is either identical to any other values of $\theta_j, (j \neq i)$ with probability proportional to q_j or is drawn from H with probability proportional to αq_0. With the conjugacy of prior G_0 and Gaussian kernel $N(\cdot|\theta)$, all terms are analytically tractable such that the conditional posterior of $\theta_i|\theta_{-i}, y_i$ can be directly sampled through Equation (5.13).

Although the implementation of Gibbs sampler based on the Blackwell-MacQueen urn scheme is straightforward, it tends to poor mixing and low efficacy as one may need to change parameter value θ for each observation y during every Gibbs run. To avoid the inefficiency of direct sampling of parameter θ, the collapsed Gibbs sampler (also known as marginal Gibbs sampler) as introduced in Neal (2000) is adopted for posterior inference of the DPM model in this study.

5.2.3 Posterior Simulation Using Collapsed Gibbs Sampler

The collapsed Gibbs sampler is devised in a back-to-front way that one may temporarily waive the sampling of the component parameter θ while drawing component indicator z for each observation y first. It is a feasible way since the conjugate setting allows the θ to be integrated out and the conditional probability of z is analytically available. Due to the clustering property of DP, in every Gibbs run, the y_i's that have same component indicator z_i are probabilistically grouped together as a cluster, in which they share the identical component parameter together. Obviously, sampling component parameter for observations that belong to the same cluster is more efficient than sampling individual parameters for each observation.

5.2.3.1 Conditional posterior of z

To begin with, we derive the conditional posterior probability of z by using the Bayes' theorem. The CRP representation of the random allocation of observations now plays a role as the prior for z in defining the conditional posterior distribution, since we do not have any observation (not yet combining the likelihood of y) so that z follows the CPR random partition. The posterior of z conditional on all other parameters and observations can be derived as

$$\begin{aligned}
&P(z_i = j|\boldsymbol{z}_{-i}, \boldsymbol{y}) \\
&\propto P(z_i = j|\boldsymbol{z}_{-i})\, p(\boldsymbol{y}|z_i = j, \boldsymbol{z}_{-i}) \\
&= P(z_i = j|\boldsymbol{z}_{-i})\, p(y_i|\boldsymbol{y}_{-i}, z_i = j, \boldsymbol{z}_{-i})\, p(\boldsymbol{y}_{-i}|z_i = j, \boldsymbol{z}_{-i}) \\
&\propto P(z_i = j|\boldsymbol{z}_{-i})\, p\big(y_i\big|\boldsymbol{y}_{-i,j}\big)
\end{aligned} \tag{5.14}$$

where $\boldsymbol{y}_{-i}$ is the subset of $\{y_1, \cdots, y_n\}$ without taking account of y_i, and $\boldsymbol{y}_{-i,j}$ is the set of observations that belong to the j th component but excluding y_i. Note that the term $p(\boldsymbol{y}_{-i}|z_i = j, \boldsymbol{z}_{-i}) = p(\boldsymbol{y}_{-i}|\boldsymbol{z}_{-i})$ is the normalized constant that can be neglected. The first term of Equation (5.14) is the prior of z_i which is readily obtained by CRP representation of Equation (5.7). The second term is the predictive distribution of y_i given other observations which is exactly the Student's T distribution with updated hyperparameters $\{\xi_j^*, \kappa_j^*, \nu_j^*, s_j^{2*}\}$

$$
\begin{aligned}
p(y_i|\boldsymbol{y}_{-i,j}) &= \int p(y_i|\theta_j^*)p(\theta_j^*|\boldsymbol{y}_{-i,j})\mathrm{d}\theta \\
&= T_{\nu_j^*}(y_i|\xi_j^*, (1+\kappa_j^*)s_j^{2*}/\kappa_j^*) \\
&\text{with } \nu_j^* = \nu_j + n_{-i,j}, \\
&\kappa_j^* = \kappa_j + n_{-i,j}, \\
&\xi_j^* = \tfrac{\kappa_j \xi_j + n_{-i,j}\bar{y}_{-i,j}}{\kappa_j + n_{-i,j}}, \text{ and} \\
s_j^{2*} &= \frac{1}{\nu_j + n_{-i,j}}\left(\nu_j s_j^2 + \sum_{h\in j, h\neq i}(y_h - \bar{y}_{-i,j})^2 \right. \\
&\qquad \left. + \frac{\kappa_j n_{-i,j}}{\kappa_j + n_{-i,j}}(\bar{y}_{-i,j} - \xi_j)^2\right)
\end{aligned}
\tag{5.15}
$$

where $n_{-i,j}$ and $\bar{y}_{-i,j}$ are the number of samples and sample mean of the set $\boldsymbol{y}_{-i,j}$, respectively. Substituting of Equations (5.7) and (5.15) into Equation (5.14), we have the conditional posterior probabilities of z_i for collapsed Gibbs sampler with model parameter θ integrated out

$$
\begin{aligned}
&P(z_i = j|\boldsymbol{z}_{-i}, \boldsymbol{y}) \\
&\quad = \begin{cases} \dfrac{n_{-i,j}}{n-1+\alpha} T_{\nu_j^*}\left(y_i|\xi_j^*, (1+\kappa_j^*)s_j^{2*}/\kappa_j^*\right), for\ j \leq J \\[2ex] \dfrac{\alpha}{n-1+\alpha} T_{\nu_j}\left(y_i|\xi_j, (1+\kappa_j)s_j^2/\kappa_j\right), if\ j = J+1 \end{cases}
\end{aligned}
\tag{5.16}
$$

Note that the predictive distribution of y_i now has two different expressions:

- Posterior predictive distribution: for $z_i = j\ (j \leq J)$ is an existing component with $\boldsymbol{y}_{-i,j}$ being the observations, the predictive distribution is the Student's T distribution with updated hyperparameters and then evaluated at y_i;
- Prior predictive distribution: if $z_i = J + 1$ is a new component given no observations (i.e. $\boldsymbol{y}_{-i,j} = \emptyset$), the predictive distribution is again the Student's T distribution but with prior hyperparameters and then evaluated at y_i.

Therefore, the DPM model can be interpreted as a mixture model consisting of J existing components $N(\cdot\,|\theta_j^*)$ and an $J + 1$ empty component for creation of new clusters.

Recall the FGM model in Chapter 3, the model order in terms of number of components J needs to be predetermined before estimating the parameters. Changing model order thus requires repeating estimation on many more finite mixture models with different value of J. By contrast, the flexibility characteristic of the DPM model is that a new component will be created and is allowed to either grow up or fade away during the Gibbs iterations. The effective number of components varies to a certain degree and thus it is a probabilistic value rather than a constant. The effective number of components can eventually be estimated from the data. Note that the DPM model may be regarded as a full Bayesian approach that all the unknown parameters contained in the model are treated as random variables and they are automatically inferred from the data.

5.2.3.2 Conditional posterior of $\boldsymbol{\theta}$

Sampling for the component parameter of θ_j^* can be implemented when given the allocation of observations. The conditional posterior distribution of θ_j^* is derived by the Bayes' theorem

$$p\left(\theta_j^* \middle| \boldsymbol{y}_j, \boldsymbol{z}\right) \propto G_0(\theta_j^*) \prod_{h \in j} N(y_h | \theta_j^*) \tag{5.17}$$

where $\boldsymbol{y}_j$ is the observations that belongs to the jth component. The conditional posterior distribution is indeed the normal-inverse-chi-squared distribution due to the conjugate setting. The marginal distributions of μ_j and σ_j^2 have explicit sampling form

$$\begin{gathered} \sigma_j^2 \middle| \boldsymbol{y}_j, \mathbf{z} \sim InvC(v_j^*, s_j^{2*}) \\ \text{with } v_j^* = v_j + n_j \text{ and} \\ s_j^{2*} = \frac{1}{v_j + n_j}\left(v_j s_j^2 + \sum_{h \in j}(y_h - \bar{y}_j)^2 + \frac{\kappa_j n_j}{\kappa_j + n_j}(\bar{y}_j - \xi_j)^2\right) \end{gathered} \tag{5.18}$$

and

$$\begin{gathered} \mu_j \middle| \sigma_j^2, \boldsymbol{y}_j, \mathbf{z} \sim N(\xi_j^*, \sigma_j^2 / \kappa_j^*) \\ \text{with } \xi_j^* = \frac{\kappa_j \xi_j + n_j \bar{y}_j}{\kappa_j + n_j} \text{ and} \\ \kappa_j^* = \kappa_j + n_j \end{gathered} \tag{5.19}$$

where n_j and $\bar{y}_j$ are the number of samples and sample mean of the set $\boldsymbol{y}_j$, respectively. Note that the marginal sampling distributions of component parameters of Equations (5.18) and (5.19) are closely resemble to that of FGM model since both of them adopts the conjugate setting.

5.2.3.3 Posterior mixture density samples

Repeating the sampling process for T times, the collapsed Gibbs sampler generates a series sequences of model parameters which includes the component parameters θ and the number of components J. After discarding the early samples, here refer to burn-in samples B, the rest of $G = T - B$ samples can be used to approximate the true model parameters. However, a technical difficulty will be soon encountered in summarizing the posterior model parameters: since the number of component J can vary to a degree during Gibbs run, the dimension of model parameters is not fixed now. It makes the posterior summarizing almost unattainable because the component parameters are not well-defined along the simulated sequences. To summarize the Bayesian estimation of the DPM model, instead, we evaluate the mixture densities $p^{(t)}(y)$ and provide posterior statistic metrics based on these simulated mixture density samples. For $t = (G + 1){:}T$, the mixture density samples of the DPM model can be formulated as (Gelman et al., 2014)

$$p^{(t)}(y) = \sum_{j=1}^{J^{(t)}} \left(\frac{n_j^{(t)}}{n+\alpha}\right) N\left(y \middle| \theta_j^{*(t)}\right) + \left(\frac{\alpha}{n+\alpha}\right) \int N(y|\theta) G_0(\theta) \mathrm{d}\theta \tag{5.20}$$

where the term $\int N(y|\theta) G_0(\theta) \mathrm{d}\theta$ representing a new component that can be computed according to Equation (5.15) with $\boldsymbol{y}_{-i,j} = \emptyset$. Note that the mixing weights in mixture density are not simulated but evaluated as follows: $\omega_j = \frac{n_j}{n+\alpha}$ $(j \leq J)$ for existing components while $\omega_{J+1} = \frac{\alpha}{n+\alpha}$ for new component. Technically, a tolerance value $\omega_{J+1} < 0.001$ is set for the collapsed Gibbs sampler to stop the random partition process. The nonparametric Bayesian approach is implemented in a way that directly draws posterior mixture density samples with varying number of components, rather than to draw individual mixture parameters in each Gibbs runs.

5.2.4 Quantitative Convergence Diagnosis

As mentioned in Chapter 3, simulation-based inference such as MCMC techniques requires monitoring of convergence of the Markov chains to the target distribution. Through simultaneously running several parallel chains from dispersed starting points, the mixing and stationarity of the chains can be assessed by analysis of between-chain variance and within-chain variance of the random variable being monitored (e.g., model parameters). The potential scale reduction factor (PSRF) can be evaluated and treated as a quantitative convergence criterion. This is the diagnosis strategy proposed by Gelman and Rubin (1992) which is used in Chapter 3 for the FGM model. For the convergence assessment of collapsed Gibbs sampler for DPM model, we adopted the diagnosis strategy proposed by Brooks and Giudici (2000), an extended version of the method of Gelman and Rubin (1992), to assess the convergence of chains with consideration of the variation not only between chains but also between models.

The phenomenon of trans-dimensional parameter space in Gibbs runs again brings challenge to convergence diagnosis. Note that direct monitoring of convergence of the natural model parameters is no longer a feasible way since in each Gibbs run the parameters are not well-defined. Based on the simulated posterior mixture density samples, Brooks and Giudici (2000) suggests to monitor the model deviance which retains a coherent interpretation throughout the simulation. The model deviance ϕ is defined as

$$\phi = -2\ln(p(y)) \tag{5.21}$$

where $p(y)$ is the mixture density sample evaluated by Equation (5.20). Hereafter, we track the deviance ϕ instead of the model parameters through Gibbs run to assess the convergence. Moreover, since the mixture density samples switch among different model orders along the simulation, we now need to also monitor the within-model variance and the between-model variance to ensure the chains are well mixed within models and between models. Note that within-model analysis means we focus on the density samples with the same model order, while between-model analysis represents the analysis of density samples with varying model order. Suppose we separately run L chains for inference of DPM model and we then have L chains of ϕ_l. Let $\phi_l^{(t)}$ denotes the value in chain l at iteration t, the total variance of ϕ under target distribution can be estimated by

$$V = \frac{1}{LT-1}\sum_{l=1}^{L}\sum_{t=1}^{T}(\phi_l^{(t)} - \bar{\phi})^2 \tag{5.22}$$

Suppose M possible models are visited in all the chains during the iteration, and define a counting function

$$I_l(t,m) = \begin{cases} 1 & if\ chain\ l\ is\ in\ model\ m\ at\ iteration\ t \\ 0 & else \end{cases} \tag{5.23}$$

where $l = 1, \cdots, L$, $t = 1, \cdots, T$ and $m = 1, \cdots, M$. Let K_{lm} denotes the number of times that model m is visited in chain l, that is

$$K_{lm} = \sum_{t=1}^{T} I_l(t,m) \tag{5.24}$$

Correspondingly, let $\phi_{lm}^{(k)}$ represents the kth observation of $\phi_l^{(t)}$ that belongs to model m within chain l, and $k = 1, \cdots, K_{lm}$. Then we can have the following different types of variance estimates of ϕ

$$W_c = \frac{1}{L} \sum_{l=1}^{L} \sum_{m=1}^{M} \sum_{k=1}^{K_{lm}} \frac{(\phi_{lm}^{(k)} - \bar{\phi}_l)^2}{MK_l - 1} \tag{5.25}$$

$$W_m = \frac{1}{M} \sum_{l=1}^{L} \sum_{m=1}^{M} \sum_{k=1}^{K_{lm}} \frac{(\phi_{lm}^{(k)} - \bar{\phi}_m)^2}{LK_m - 1} \tag{5.26}$$

$$W_m W_c = \frac{1}{LM} \sum_{l=1}^{L} \sum_{m=1}^{M} \sum_{k=1}^{K_{lm}} \frac{(\phi_{lm}^{(k)} - \bar{\phi}_{lm})^2}{K_{lm} - 1} \tag{5.27}$$

$$B_m = \sum_{m=1}^{M} \frac{(\bar{\phi}_m - \bar{\phi})^2}{M - 1} \tag{5.28}$$

$$B_m W_c = \sum_{l=1}^{L} \sum_{m=1}^{M} \frac{(\bar{\phi}_{lm} - \bar{\phi}_l)^2}{L(M - 1)} \tag{5.29}$$

where

$$K_l = \textstyle\sum_{m=1}^{M} K_{lm} \;\text{ and }\; K_m = \sum_{l=1}^{L} K_{lm}$$

and the sequence means are taken as

$$\bar{\phi}_m = \frac{1}{K_m} \sum_{l=1}^{L} \sum_{k=1}^{K_{lm}} \phi_{lm}^{(k)}$$

$$\bar{\phi}_l = \frac{1}{K_l} \sum_{m=1}^{M} \sum_{k=1}^{K_{lm}} \phi_{lm}^{(k)}$$

$$\bar{\phi}_{lm} = \frac{1}{K_{lm}} \sum_{k=1}^{K_{lm}} \phi_{lm}^{(k)}$$

$$\bar{\phi} = \frac{1}{LT}\sum_{l=1}^{L}\sum_{m=1}^{M}\sum_{k=1}^{K_{lm}}\phi_{lm}^{(k)}$$

For sufficient iteration T, if all chains are converged to the same target distribution, then both V and W_c should well approximate the total variance of ϕ, and both W_m and $W_m W_c$ should well approximate the within-model variance of ϕ, and both B_m and $B_m W_c$ should well approximate the between-model variance of ϕ. Each pairs of these variance estimates would be close to each other as the iteration continues. To quantitatively assess the convergence, we propose to monitor the potential scale reduction factors (PSRF) R of total variance, within-model variance and between-model variance

$$R_{tot} = \sqrt{\frac{T-1}{T} + \frac{V}{TW_c}} \tag{5.30}$$

$$R_W = \sqrt{\frac{T-1}{T} + \frac{W_m}{TW_m W_c}} \tag{5.31}$$

$$R_B = \sqrt{\frac{T-1}{T} + \frac{B_m}{TB_m W_c}} \tag{5.32}$$

Note that all PSRFs should approach to 1 after sufficient iterations, indicating the chains are stationary and well mixed between and within models. In this study, the convergence monitoring is performed by simulating two parallel chains (i.e. $L = 2$) for ϕ and the convergence is reached when all PSFRs satisfy $|R-1| \leq 10^{-4}$. By monitoring the PSRFs, a quantitative convergence assessment can be achieved with which the burn-in period and the total iteration times can be further determined.

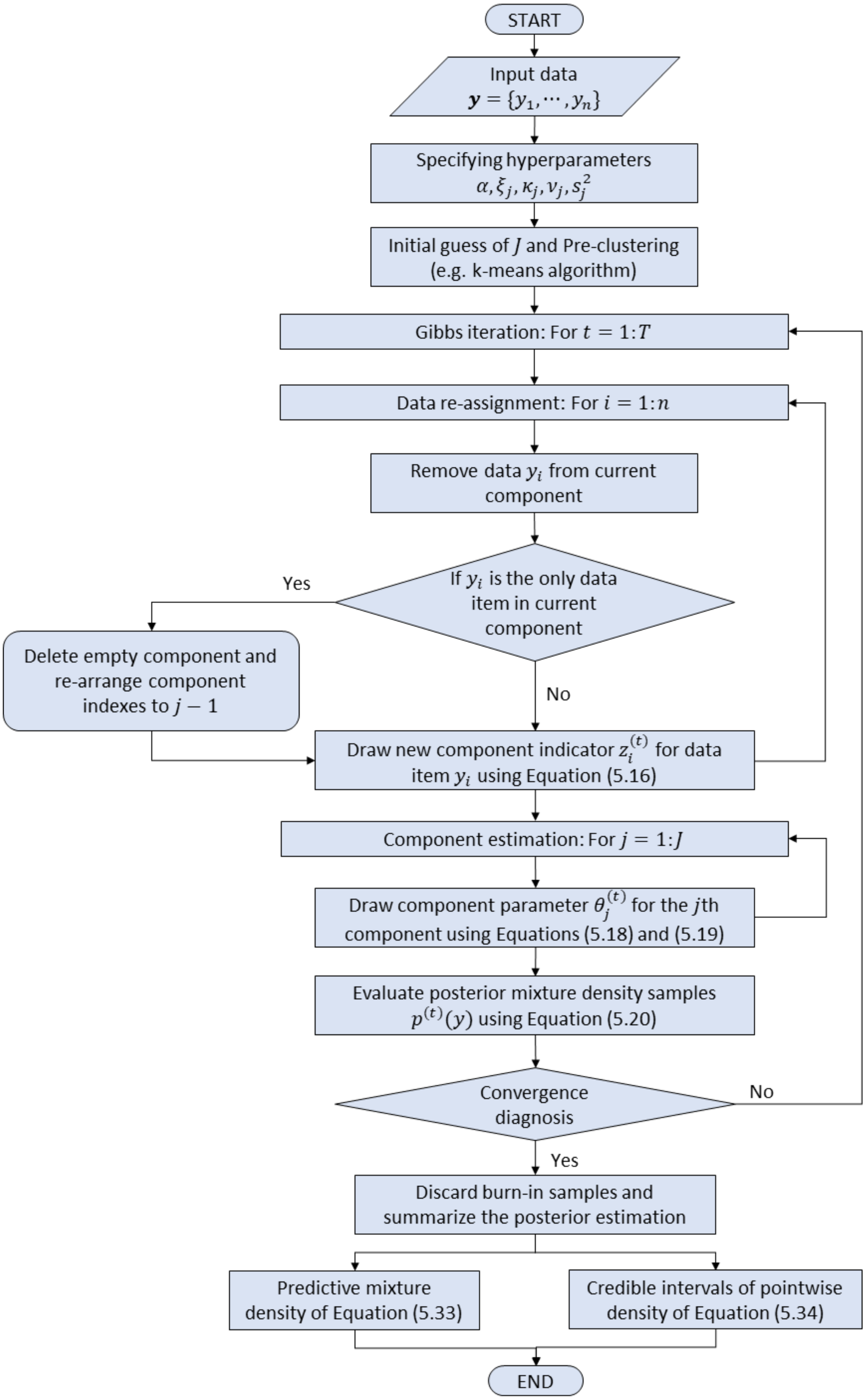

Figure 5.3 The nonparametric Bayesian approach based on DPM model

5.2.5 Predictive Mixture Density

Through the collapsed Gibbs sampler and the quantitative convergence diagnosis strategy, a sequence of posterior mixture density samples can be readily obtained after the burn-in period. Recall that in Chapter 3, the Bayesian estimation of the FGM model is provided in terms of the posterior model parameters. Now, we summarize the nonparametric Bayesian estimation of the DPM model via manipulating the posterior mixture density samples. The predictive mixture density of the DPM model is estimated as the mean function of posterior mixture density samples

$$p(\tilde{y}|\boldsymbol{y}) = G^{-1} \sum_{t=G+1}^{T} p^{(t)}(y) \tag{5.33}$$

This is a continuous nonparametric density function that averaging over the trans-dimensional parameter space, which represents the most plausible mixture density estimation given the observational data. Note that in FGM model, the predictive mixture density has a parametric form of weighed sum, and its function is constructed based on the posterior sample means of the model parameters.

Intuitively, the variability of the posterior mixture density samples reveals the uncertainty about the estimation of DPM model. Two levels of uncertainty, the model order and parametric uncertainties, contribute to the total variability of the posterior samples. Quantification of both model order and parametric uncertainties can then be achieved through characterizing the total variability of the posterior mixture density samples. This can be done by evaluating, for example, the upper and lower credible bounds of the pointwise density. Suppose we evaluate the pointwise density at y^*, and let P denotes the sequence of density values evaluated based on posterior mixture density samples $P = \{p^{(G+1)}(y^*), \cdots, p^{(T)}(y^*)\}$, then the 5-95 credible interval of the pointwise density is

$$[P_{0.05}, P_{0.95}] \tag{5.34}$$

The Bayesian estimation on the DPM model can be summarized in terms of the predictive mixture density and the associated credible interval of pointwise density. The flowchart of nonparametric Bayesian approach is summarized in Figure 5.3.

5.3 NUMERICAL VERIFICATION

5.3.1 Estimation of Trimodal Data Set

To verify the effectiveness for modelling the heterogeneous data, the proposed nonparametric Bayesian approach is first verified through the estimation of the trimodal data set. Diffuse priors are selected for mixture parameters with hyperparameters setting to $\nu_j = 2$, $s_j^2 = var(y) \times \nu_j$, $\xi_j = mean(y)$ and $\kappa_j = 1$ for all components. The DP concentration parameter is set to $\alpha = 1$ for a common choice.

In the absence of any experience of iteration times needed for convergence of the Markov chains, we suggest running the collapsed Gibbs sampler as long as possible so that the chains can reach stationary and mix properly. In this study, we choose to set to $T = 10000$ iterations with $L = 2$ parallel chains. Figure 5.4 provides typical Gibbs runs in terms of mixture density samples from the initial stage to final stage of the simulation. At the initial stage, some outliers of the mixture density samples with quite different distributional shapes are found, which are the early draws of the simulation. This is reasonable since the model parameters drawn at the beginning of simulation are too far from the target distributions. After some iterations, as in middle stage, the mixture density samples quickly become similar distributional shapes with each other. No outliers of mixture density samples are found afterwards. At the final stage, the mixture density samples vibrate within a constant range, indicating that the variability of the model parameters is under a low level.

The quantitative convergence diagnosis strategy is further applied to check the convergence of the simulation and help to determine the burn-in period. We first evaluate the monitoring variable ϕ using Equation (5.21). The trace plots of ϕ in Figure 5.5 show that the values of ϕ fluctuate within a limited range after the early iterations. A similar pattern is also found in FGM model, but the monitoring variables are the natural model parameters themselves. With the collection of ϕ, the PSRFs of total variance, within-model variance and between-model variance of ϕ can be checked.

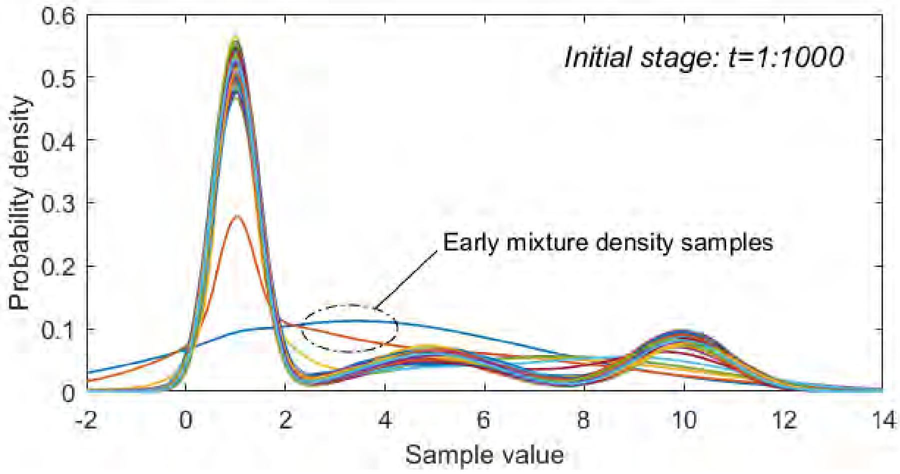

a) Initial stage of the simulation

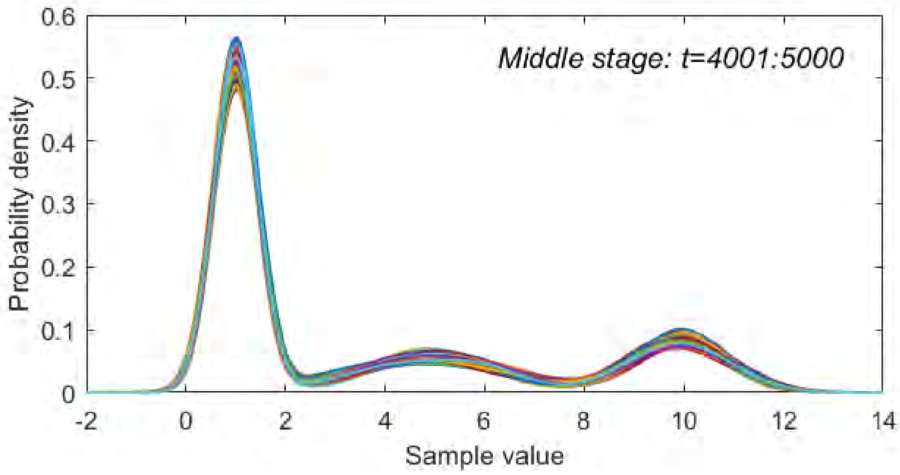

b) Middle stage of the simulation

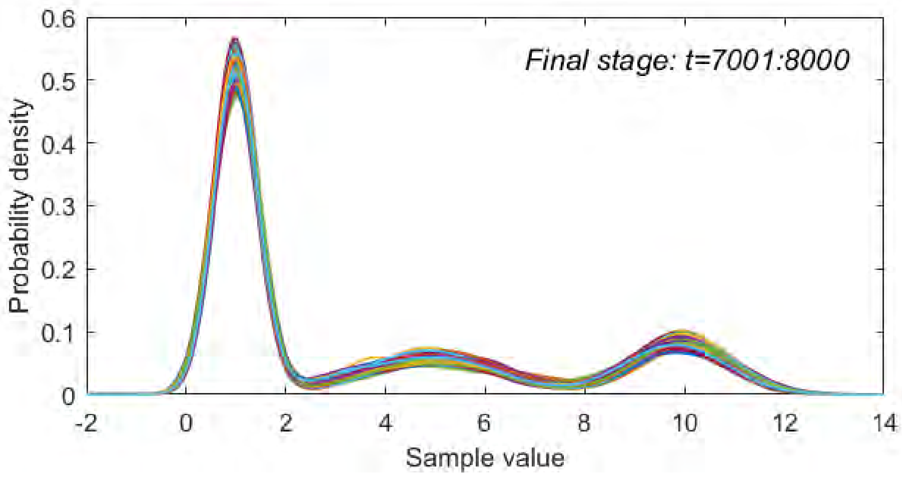

c) Final stage of the simulation

Figure 5.4 Evolution of the mixture density samples during the Gibbs iterations

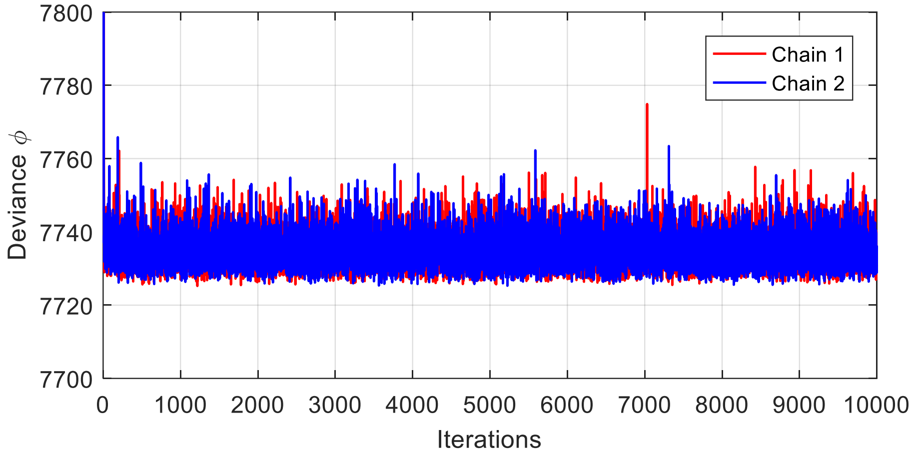

Figure 5.5 Trace plots of model deviance ϕ

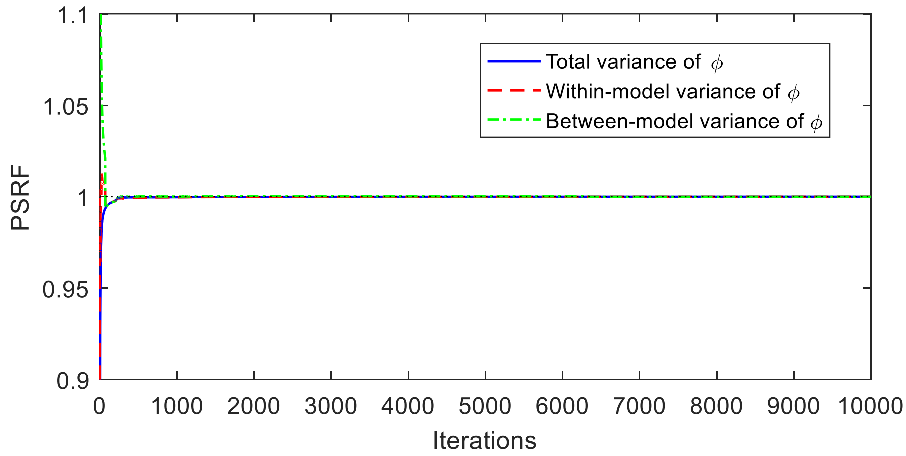

a) an overall view

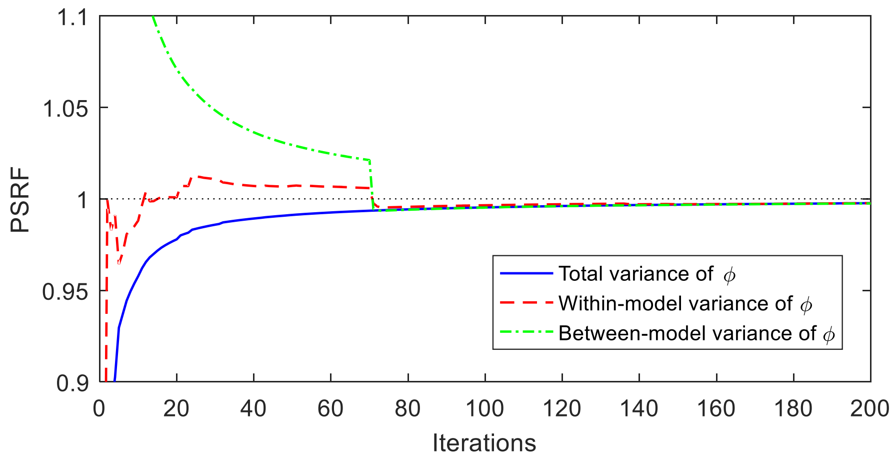

b) a zoom view of initial iterations

Figure 5.6 Quantitative convergence diagnosis based on potential scale reduction factor R

As shown in Figure 5.6, the curves of PSRF are all quickly approach to 1 through a few of iterations. The values of PSRF then remain steady around 1, which indicates that the chains of ϕ are stationary and well mixed. With the plots of PSRF, the convergence of the simulation can be confirmed. Table 5.1 gives the convergence metric based on PSRF. For the total variance and within-model variance, it takes about 3000 times of iterations to reach the convergence, while for the between-model variance, a fewer number of 858 steps are needed. Therefore, we determine the burn-in period $B = 4000$ for the subsequent analysis as a conservative choice. The rest of $G = T - B = 6000$ posterior mixture density samples are used to summarize the nonparametric Bayesian estimation.

Table 5.1 Convergence diagnosis metric for trimodal data set

Total variance of ϕ	Within-model variance of ϕ	Between-model variance of ϕ
Gibbs iterations needed to reach convergence $\|R-1\| \leq 10^{-4}$		
2617	2999	858

Based on the posterior mixture density samples, the predictive mixture density is estimated as the mean function of the samples using Equation (5.33), and the credible intervals of pointwise density are evaluated by using Equation (5.34). The estimated predictive mixture density and the associated 5-95 credible intervals are plotted in Figure 5.7. A good fitting of the predictive PDF with the empirical density is achieved through the nonparametric Bayesian approach. It is evident that the DPM model is capable of modelling multimodal data structure with satisfactory accuracy. The upper and lower uncertain bounds of pointwise density are both smooth curves, laying symmetrically in the two sides of the predictive PDF curve. Through the nonparametric approach, the variability of the estimated PDF due to both model order and parametric uncertainties is fully characterized by the uncertain bounds.

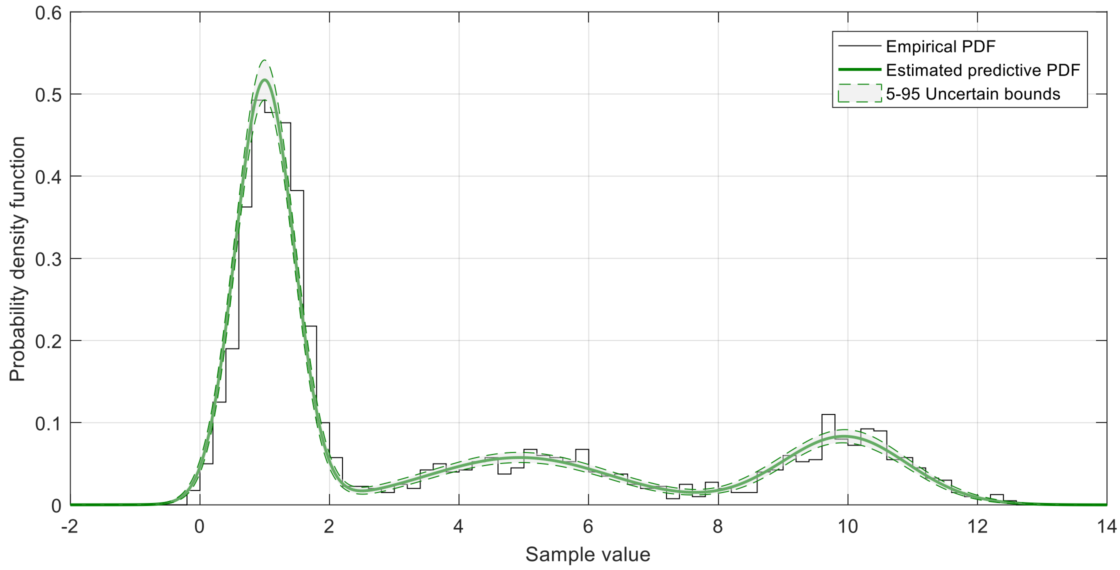

Figure 5.7 Estimated predictive mixture density and associated uncertain bounds for trimodal data set

5.3.2 Estimation of Benchmark Data Set

A benchmark data set as introduced in Celeux et al. (2006) and McGrory and Titterington (2007) is selected to further verify the effectiveness of the proposed parametric and nonparametric approaches. The underlying distribution model of the benchmark data set is a four-component Gaussian mixture

$$\begin{gathered} 0.26\mathcal{N}(-1.5, 0.5^2) + 0.288\mathcal{N}(0, 0.2^2) + 0.171\mathcal{N}(2.2, 3.4^2) \\ + 0.281\mathcal{N}(3.3, 0.5^2) \end{gathered} \tag{5.35}$$

As described in Celeux et al. (2006) and McGrory and Titterington (2007), posterior inferences have been evaluated by the Markov chain Monte Carlo (MCMC) approximation method and the variational approximation method, respectively. Parametric and nonparametric Bayesian approaches are used to estimate the mixture models. Posterior means given in the references and estimated by the parametric approach are listed in Table 5.2 for comparison. It is shown that the results of the parametric approach are close to the results given in the two references, indicating a good agreement among different algorithms. A comparison with the true values shows that the estimations by McGrory and Titterington (2007) and the parametric approach have better accuracy than that by Celeux et al. (2006). The PDFs of the estimated mixture models are shown in Figure 5.8, where all the fittings are able to well characterize the benchmark data set. It is found that the nonparametric approach has the best goodness-of-fit to the data histogram.

Table 5.2 Comparison on posterior estimations of benchmark data set

Comp.	Parameter μ	Parameter σ^2	Parameter ω
		True	
No. 1	-1.500	0.250	0.260
No. 2	0.000	0.040	0.288
No. 3	2.200	11.560	0.171
No. 4	3.300	0.250	0.281
		Parametric approach	
No. 1	-1.536	0.302	0.242
No. 2	-0.027	0.106	0.313
No. 3	2.126	14.237	0.109
No. 4	3.268	0.381	0.336
		Celeux et al. (2006)	
No. 1	-1.350	0.130	0.210
No. 2	-0.080	0.110	0.340
No. 3	3.120	7.040	0.140
No. 4	3.460	0.380	0.310
		McGrory and Titterington (2007)	
No. 1	-1.490	0.194	0.206
No. 2	0.005	0.022	0.251
No. 3	1.360	10.890	0.296
No. 4	3.380	0.292	0.247

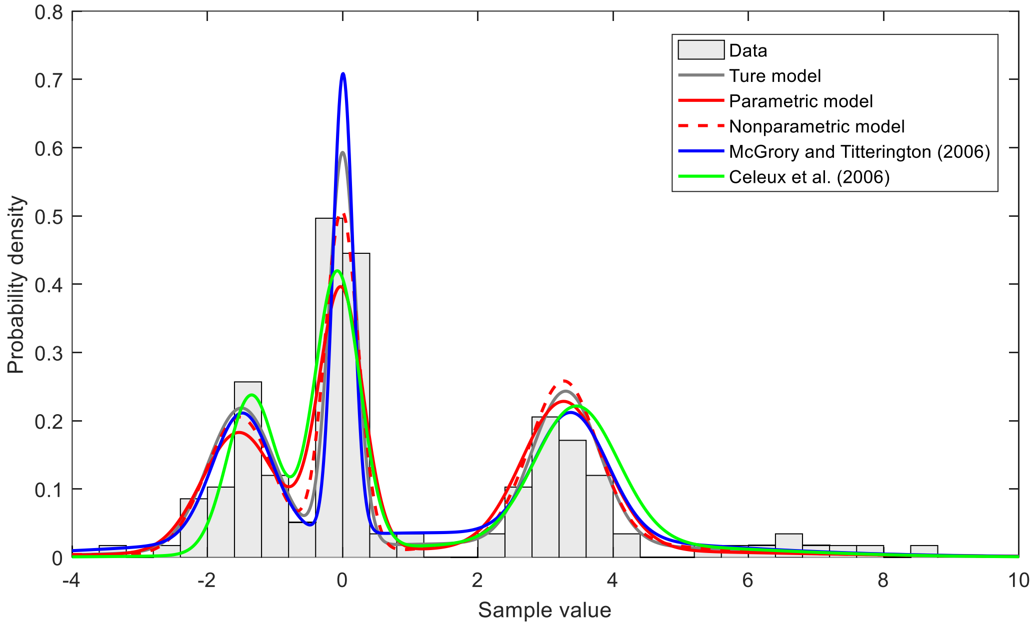

Figure 5.8 Comparison on PDF fittings of benchmark data set

5.4 COMPARISON ON PEFORMANCE OF PARAMETRIC AND NONPARAMETRIC APPROACHES

The nonparametric Bayesian approach based on DPM model has been exemplified by using the trimodal data set, proving the effectiveness in modelling heterogeneous data structure. The DPM model stands as an improvement in terms of automatic model complexity adaptation over the FGM model as introduced in Chapter 3. In this section, we compare the overall performance of the parametric and nonparametric Bayesian approach in terms of some key aspects: model complexity, goodness-of-fit, uncertainty characterization and computational demands. Note that the comparison is demonstrated based on the results of the trimodal data set.

5.4.1 Model Complexity

The number of components for the FGM model is a fixed value during the simulation. The optimal model order is determined by comparing several candidate models using the Bayes factor. In Chapter 3, the results of Bayes factor support that the optimal number of components is $J = 3$ for trimodal data set. This is identical to the true value of number of components of the test data set. The DPM model, however, allows the value of number of components to be random variable, which varies through the simulation. Figure 5.9 gives the plots of effective number of components through the iteration for the DPM model. After the burn-in period, the effective number of components has a relatively large variation, with the value ranging from $J = 4$ to $J = 14$. The histogram on the right panel summarizes the samples of J after the burn-in period, which has an approximate symmetric distribution with the most frequent occurrence of component number being $J = 6$. Apart from that, model order of $J = 5$ and $J = 7$ are also frequently encountered. Surprisingly, the true number of components $J = 3$ never emerges through the iteration.

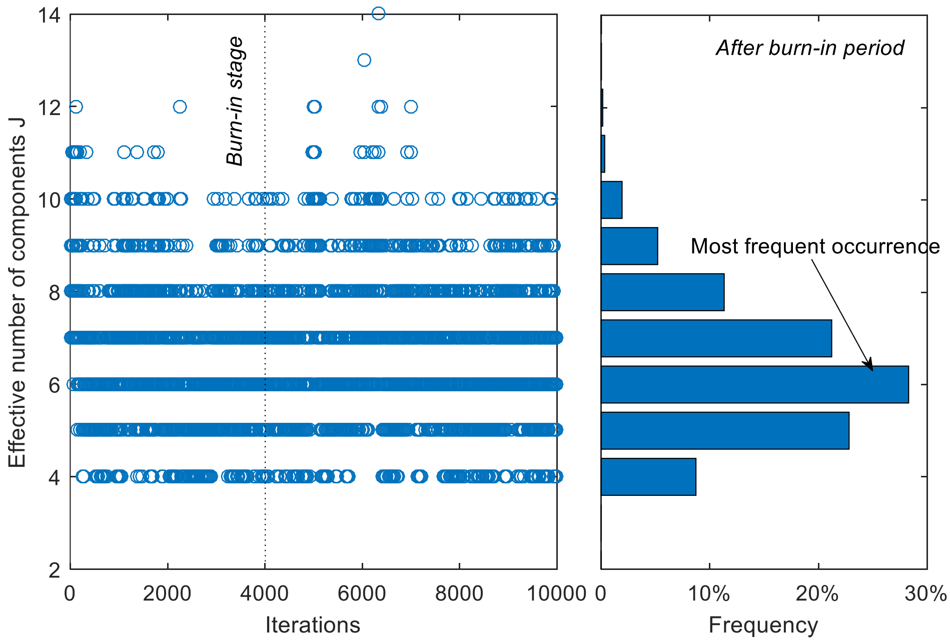

Figure 5.9 Effective number of components during the MCMC simulation

Although direct comparison between the optimal model order of the FGM model and the most frequent occurrence model order of the DPM model is somewhat inappropriate, it provides insight into the constitution of the estimated predictive density. Note that the predictive mixture density of the DPM model is a mean density function, averaging the posterior mixture density samples with orders of $J = 4$ to $J = 14$. In the case of trimodal data, the above analysis imply that the nonparametric approach tends to fit the data with larger number of components, while the parametric approach happens to find the true model order using the Bayes factor strategy.

5.4.2 Goodness-of-Fit

The predictive mixture density estimated by parametric and nonparametric approach have already been visually compared to the empirical data density. Both two estimated curves have good fitting with the empirical one as shown in Figure 5.10. A fairly large difference is found at the first mode of the mixture densities, where the DPM model reaches a higher density value at that mode. To make quantitative comparison on the goodness-of-fit of the predictive mixture density of two approaches, we perform the Kolmogorov-Smirnov test (K-S test) for two estimated models. The log-likelihood values are evaluated as well for reference.

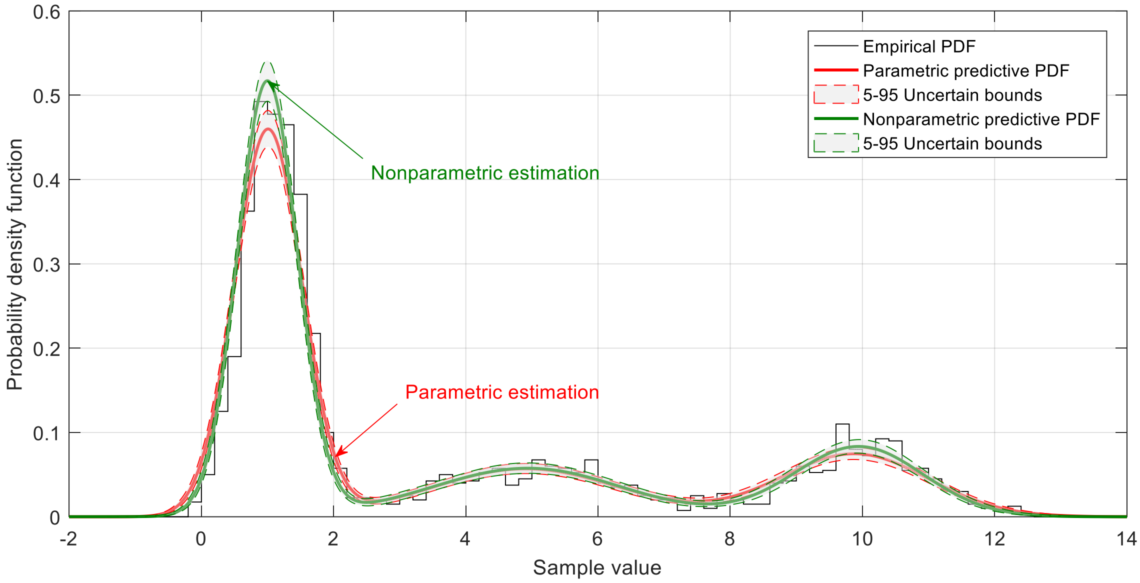

a) Predictive PDFs and associated uncertain bounds

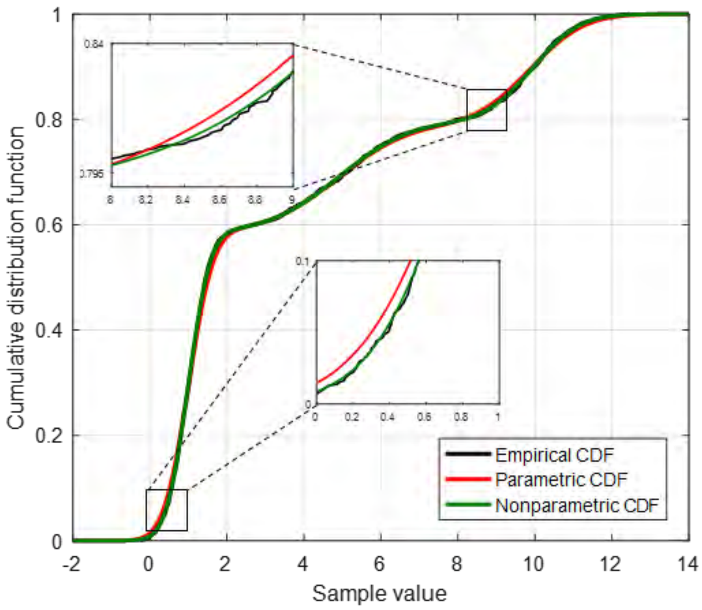

b) CDFs

Figure 5.10 Comparison on the PDFs and CDFs for the parametric and nonparametric approaches

5.4.2.1 Kolmogorov-Smirnov test

The K-S test serves as a statistical tool to determine the goodness-of-fit of the test sample with a reference theoretical probability distribution (Massey Jr, 1951). The K-S statistic D_n measures the maximum distance between the empirical cumulative distribution function $S_n(x)$

and the theoretical cumulative distribution function $F(x)$ of the test sample

$$D_n = sup_x |S_n(x) - F(x)| \tag{5.36}$$

where sup is the supremum of the set of distances. If the test sample comes from the theoretical distribution, i.e. $S_n(x)$ is close enough to $F(x)$, then D_n converges to 0 almost surely with the sample size $n \to \infty$. The cumulative distributions for FGM model and DPM model are plotted together with a comparison to the empirical cumulative distribution of the trimodal data set in Figure 5.10. Two estimated CDFs are closely attached to the empirical CDF with an overall view. However, a detailed view shows that the nonparametric CDF performs better than then parametric one.

The K-S test at significance level of 0.05 is independently performed for two theoretical models with the null hypotheses being that the test sample is drawn from the theoretical distributions. As presented in Table 5.3, both the K-S test results support (fail to reject) the null hypotheses. That is to say the trimodal data set can be regarded as samples drawn from either the parametric or nonparametric distribution. The P-value of the K-S test is further evaluated as an indicator of how strong we may reject the null hypothesis. Note that the lower P-value is, the stronger we may reject the null hypothesis. Thus, the P-value can serve as a criterion for assessing the goodness-of-fit of the model. It finds that the P-value of DPM model is noticeable higher than that of FGM model, indicating a superior fitting quality is achieved by the nonparametric approach.

Table 5.3 Comparison on the overall performance for the parametric and nonparametric approaches

		Parametric approach	Nonparametric approach
		Model complexity	
Number of components		3	6
Type		Optimal	Most frequent occurrence
Method		Bayes factor	DPM
		Goodness-of-fit	
K-S test		Fail to reject null hypothesis	Fail to reject null hypothesis
P-value of K-S test		0.2141	0.9053
Log-likelihood		-3.8843e+03	-3.8673e+03
		Uncertainty characterization	
KL divergence	Maximum	0.7969	1.0015
	Minimum	0.0129	0.0153
	Mean (SD)	0.1861 (0.0929)	0.2547 (0.1105)
		Computational demands	
Simulation time (hour)	MCMC	0.16	1.66
	Model order selection	4.47	-
	Total	4.63	1.66

5.4.2.2 Log-likelihood value

The likelihood value is a function of model parameters given the observational data. Maximizing the likelihood function yields the best estimation of model parameters in frequentist approach. In fact, the evaluation of likelihood is also the popular mean to determine the goodness-of-fit of the model, in which higher likelihood favors better fitting. Computing the log-likelihood value for the FGM model with observed data is straightforward since we have the Bayesian estimation of model parameters. In DPM model, we calculate the average log-likelihood value as

$$\ln p(\boldsymbol{y}|\boldsymbol{\Theta}) = G^{-1} \sum_{t=G+1}^{T} \sum_{i=1}^{N} \ln p^{(t)}(y_i) \tag{5.37}$$

where $\mathbf{\Theta}$ denotes the model parameters, and $p^{(t)}(\cdot)$ is the posterior mixture density sample of Equation (5.20). Table 5.3 presents the log-likelihood values for two approaches given the trimodal data set. It shows the DPM model obtains a higher log-likelihood value than the FGM model, which means the nonparametric PDF owns a better fitting. This is a consistent result with the K-S test. Evidences of K-S test and log-likelihood evaluation support that the nonparametric Bayesian approach has a better performance than the parametric counterpart in terms of model goodness-of-fit.

5.4.3 Uncertainty Characterization

The Bayesian paradigm provides a dedicated framework for statistical modelling of unknown data, in particular, the ability of characterizing different levels of uncertainty in model interpretation. The Bayesian analysis produces the most plausible estimation as well as an assessment on its accuracy. In practice, the modelling uncertainty is commonly expressed as the variability or probable interval for the location of the parameter value. The broader the probable interval, the higher level of uncertainty will be made about the parameter value. For the parametric approach, we obtain the most plausible mixture parameters and the associated credible intervals by summarizing the posterior parameter samples. Since the model order is assumed to be fixed, the variability of the posterior parameter values only conveys the parametric uncertainty.

A critical advantage of nonparametric Bayesian approach compared to the parametric counterpart is the capability to simultaneously incorporate uncertainty at two levels: parametric and model order uncertainties. The model order is treated as an unknown random variable in the DPM model, which automatically adapts the observation data. Then the variability of the posterior mixture density samples carries the information of both parametric and model order uncertainties. Data interpretation through the nonparametric Bayesian methods eventually brings more robust estimation, since the inference is performed under the consideration of both parametric and model order uncertainties.

Intuitively, we may have an initial guess that the 'degree of uncertainty' of the DPM estimation should be larger than that of the FGM estimation. To further prove this, we propose to use the relative entropy as a measure of uncertainty to compare the uncertainty characterization capability between the two approaches. The concept of relative entropy, also known as Kullback-Leibler (KL) divergence, is popular in information theory, where it serves as a measure of the average additional amount of information needed to transmit when an alternative distribution Q is used to approximate the true distribution P (Bishop, 2006)

$$D_{KL}(P\|Q) = \int P(x)\ln\left(\frac{P(x)}{Q(x)}\right)\mathrm{d}x \tag{5.38}$$

Note that the KL divergence satisfies $D_{KL}(P\|Q) \geq 0$ with equality if and only if $P = Q$, and it is not a symmetrical quantity, i.e. $D_{KL}(P\|Q) \neq D_{KL}(Q\|P)$. In fact, the KL divergence can be also interpreted as a dissimilarity measure between the two distributions P and Q, hence it is a proper measure to quantify the variability of the posterior mixture density samples. The KL divergence between the predictive mixture density $\tilde{p}$ and the posterior mixture density sample $p^{(t)}$ is evaluated by

$$D_{KL}\left(\tilde{p}\|p^{(t)}\right) = \int \tilde{p}(y)\ln\left(\frac{\tilde{p}(y)}{p^{(t)}(y)}\right)\mathrm{d}y$$
$$\approx \sum_{y} \tilde{p}(y)\ln\left(\frac{\tilde{p}(y)}{p^{(t)}(y)}\right)\Delta y \tag{5.39}$$

where the integral can be approximated by summing up the integrand evaluated at equally spacing grid Δy. Evaluation of the KL divergence for each posterior mixture density samples, say $t = G + 1{:}T$, we obtain a collection of values of $D_{KL}\left(\tilde{p}\|p^{(t)}\right)$.

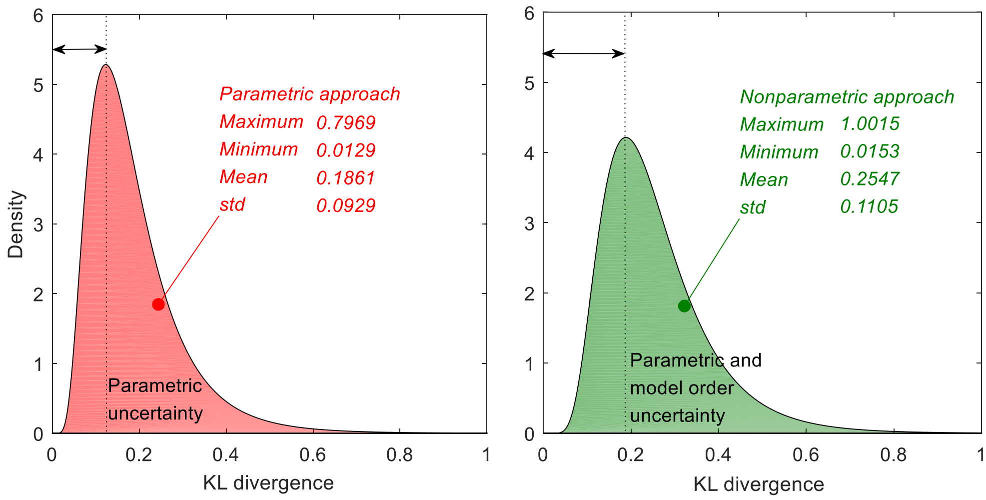

Figure 5.11 Comparison on the relative entropy for parametric and nonparametric approaches

The KL divergence are evaluated for two approaches as shown in Figure 5.11. It is not surprised to see the values of KL divergence are random distributed (approximate log-normal type), since they are calculated based on $\tilde{p}$ and $p^{(t)}$ which are stochastic functions in nature. The KL divergence of DPM model has the larger mean and standard deviation values than that of FGM model, implying that an overall larger dissimilarity is found between $\tilde{p}$ and $p^{(t)}$ of DPM model. In other words, a broader class of mixture density estimation is obtained using the nonparametric approach with the consideration of both parametric and model order uncertainties. Characterizing by the KL divergence, the degree of uncertainty of DPM estimation is larger than that of FGM model, which verifies our initial guess.

5.4.4 Computational Demands

A larger amount of computational time is usually required for Bayesian analysis, especially using the MCMC-based simulation for posterior inference. Lowering the computational demands and developing efficient algorithms are of great importance to the analysts. The time consumption of performing the parametric and nonparametric modelling is listed in Table 5.3 for comparison. Note that the simulation is implemented by MATLAB on a workstation with Intel Xeon CPU E5-1620 v3, 16 GB (RAM). It took about 4.63 hours to fully complete the inference on the FGM model, in which 0.16 hours (3%) was needed for MCMC simulation and 4.47 hours (97%) for model order selection. A large proportion of the computational demands are mainly due to the step of model order selection for the parametric approach. However, this model selection step is completely avoided for the nonparametric approach. A relative shorter computational time is achieved by the DPM model with a total of 1.66 hours required. Therefore, by automatically inferring the model order, the nonparametric approach has a more efficient computational performance than the parametric counterpart when dealing with the multimodal data.

5.5 SUMMARY

This chapter presents the Dirichlet process mixture model based on the nonparametric Bayesian approach for heterogeneous monitoring data, aiming to jointly consider the parametric and model order uncertainties. Through inferring on the infinite-dimensional parameter space, the nonparametric Bayesian approach allows the model complexity to automatically adapts to the observed data, leading to a full Bayesian analysis on the mixture model. Inference on the DPM thus provides both estimation on model parameters and model order, resulting to a robust model estimation. The effectiveness of the nonparametric approach is verified through the demonstration on modelling the trimodal data set and the benchmark data set. The comparison study gives insight into the performance of two approaches. The DPM model stands as an improvement over the FGM model in terms of better goodness-of-fit with lower computational demands. Quantification of the parametric and model order uncertainties are simultaneously achieved through the nonparametric modelling process. In Chapter 6, the proposed new approach is applied to characterize the multimodal structural responses acquired from the Tsing Ma Bridge for reliability-based assessment.

CHAPTER 6
RELIABILITY-BASED ASSESSMENT OF BRIDGE DECK CONSIDERING MODELLING UNCERTAINTIES

6.1 INTRODUCTION

Two classes of Bayesian probabilistic model, namely the parametric and nonparametric Bayesian mixture models, are proposed in Chapters 3 and 5 respectively, which are capable of (1) accommodating heterogeneous data structure with multiple sub-populations, and (2) characterizing the parametric and model order uncertainties arising from interpreting the observational data. Markov chain Monte Carlo-based algorithms are employed for the posterior inference of the mixture models. This chapter demonstrates the application of Bayesian mixture models to reliability assessment of the bridge deck of the suspension Tsing Ma Bridge (TMB) under multi-load condition with consideration of the impacts from modelling uncertainties.

Many uncertainty sources are invariably around the concerns of bridge condition assessment. Two broad categories of uncertainty are commonly accepted in terms of their intrinsic nature: aleatory uncertainty and epistemic uncertainty (Der Kiureghian, 1989; Zhang and Mahadevan, 2000; Igusa et al., 2002; Der Kiureghian, 2008; Der Kiureghian and Ditlevsen, 2009; Ellingwood and Kinali, 2009). The randomness of physical variables associated with structural resistance or external loadings, which is usually irreducible, is regarded as the type of aleatory uncertainty. Probability distributions are often employed to depict the aleatory uncertainty. While the type of epistemic uncertainty, which is potentially reducible, includes but not limited to imperfect model formulation, statistical uncertainty and measurement error. The emergence of epistemic uncertainty is mainly due to insufficient of real-world observed data or inability of precisely acquiring information. The classification of uncertainty sources with their examples in the field of bridge condition evaluation are listed in Figure 6.1.

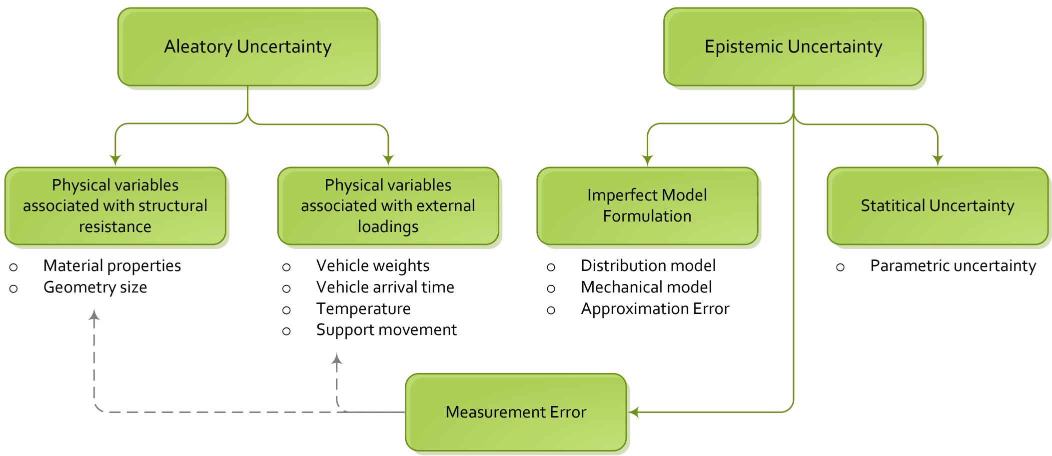

Figure 6.1 Uncertainty sources in bridge condition assessment

The classical reliability theory provides a rational mean to account for the inherent randomness, i.e. the aleatory uncertainty, associated with capacities and demands of the structure. When site-specific measurement data collected by structural health monitoring (SHM) system are fed in, the authentic resistance and loadings of the in-service bridge can be available with their intrinsic randomness being largely quantified. A probabilistic evaluation of the current serviceability or safety of the bridge system or its sub-component (often in terms of failure probability or reliability index) can be achieved using reliability principles. Research on integrating monitoring data with reliability analysis for condition assessment of in-service structures has been an active field in the past decades (Bhattacharya et al., 2005; Catbas et al., 2008; Hosser et al., 2008; Liu et al., 2009b; Ni et al., 2010; Li et al., 2012a; Li et al., 2012b; Xia et al., 2012a). However, most of the aforementioned studies only focus on how to address the inherent variability of the basic random variables based on field measurement data acquired from SHM system.

The epistemic uncertainty, another significant uncertain factor as stated previously, has been merely considered in the process of reliability-based bridge condition assessment so far. For example, the use of imprecise distribution models for the basic random variables and the statistical uncertainty arising from parameter estimation. In the case of reliability assessment of the TMB using field measurement data, there are two major kinds of epistemic uncertainty: (1) model order uncertainty, i.e. the determination of number of mixture components for modelling the multimodal response, and (2) parametric uncertainty, i.e. the variability in mixture parameter estimation due to the limited volume of monitoring data. To simplify the terminology, hereafter we use ‘modelling uncertainties’ to involve these two types of epistemic uncertainty since they stem from identifying proper probability distribution model for modelling the structural response. In contrast to fundamental randomness of the loadings and resistance, influence of the modelling uncertainties on estimation of failure probability or reliability index is yet a less explored area.

The proposed Bayesian mixture modelling approaches offer a novel solution to take account for the modelling uncertainties by means of reliability principles. The layout of this chapter is organized as follows. The structural health monitoring system instrumented on the TMB is first introduced in Section 5.2. Statistical analysis of the monitoring stress response on the longitudinal truss is given in Section 5.3. Multimodal peak stresses are extracted from the live load-induced stress response after eliminating the temperature effect. Section 5.4 provides the estimation of multimodal load effect by using the Bayesian mixture models. In Section 5.5, a conditional reliability index is proposed based on the first-order reliability method. Influence of uncertain mixture parameters on the reliability estimate is investigated. Reliability-based assessment of the bridge deck under modelling uncertainties is demonstrated.

6.2 INSTRUMENTED TSING MA BRIDGE

A case study on reliability assessment of the bridge deck of the Tsing Ma Bridge under modelling uncertainties by making use of long-term monitoring data is carried out in this chapter. The structural features of this suspension bridge and the long-term structural health monitoring system instrumented on the bridge are first introduced in this section.

6.2.1 Bridge Configuration

The Tsing Ma Bridge is a long suspension bridge with a main span of 1377 m and an overall length of 2.2 km, which connects the Hong Kong International Airport in Lantau Island with the urban area of Kowloon (refer to Figure 6.2). The main span crosses the strait between the Tsing Yi Island and the Ma Wan Island with two H-portal-type reinforce concrete towers, i.e. the Tsing Yi tower and the Ma Wan tower, founded on shallow water near these two islands.

The bridge has a double-level truss-stiffening box-shape steel deck - a hybrid structural configuration that mainly consists of Vierendeel cross frames, longitudinal trusses, orthotropic deck plates, and plane bracing system (refer to Figure 6.3). The upper level of the bridge deck has a dual three-lane highway while two airport railway lines and two emergency carriageways are laid on the lower level within the bridge deck. The streamline bridge deck runs through the longitudinal direction, connecting the Ma Wan abutment and Tsing Yi abutment. Fixed hinge bearings are used to support the bridge deck at Ma Wan abutment with only allowance of rotation other than the displacement of the deck; whereas an expansion joint is placed at Tsing Yi abutment to release the longitudinal displacement of the deck under temperature variation.

The two main suspension cables, which are composed of parallel galvanized steel wires, are accommodated by the four saddles located at the top of the towers. The suspenders, each of which is assembled by two pairs of wire ropes, are arranged with an 18 m-interval layout along the longitudinal direction, lifting the long-span steel bridge deck. Two gravity-type main anchorages are respectively placed at the Tsing Yi side and Ma Wan side to fix the main cables.

Since the opening to public in 1997, the bridge carries the busiest diurnal highway and railway traffic volume in between the airport and city centre and serves as one of the most essential links in the transportation network of Hong Kong.

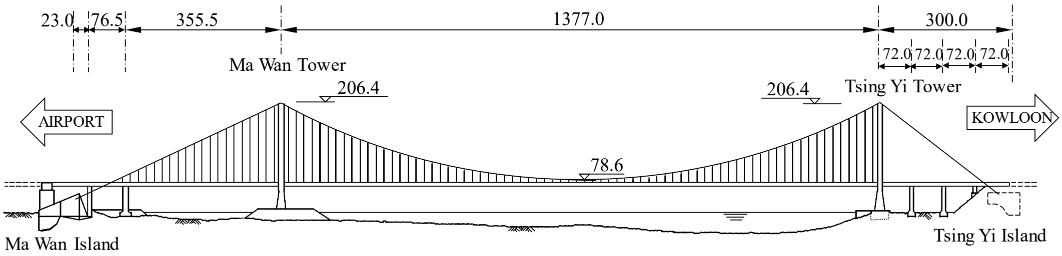

Figure 6.2 Layout of the Tsing Ma Bridge (unit: m)

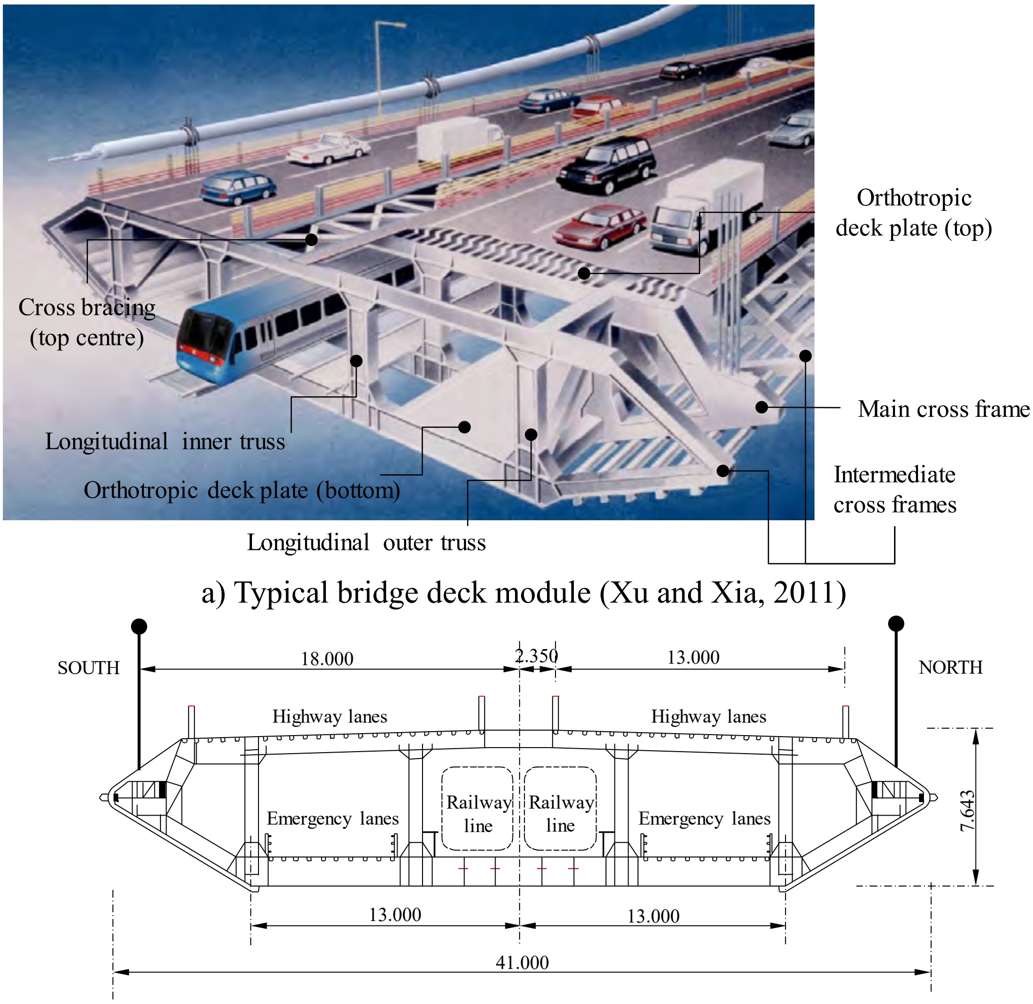

a) Typical bridge deck module (Xu and Xia, 2011)

b) Typical deck cross section

Figure 6.3 Configuration of the bridge deck at main span (unit: m)

6.2.2 SHM System of Tsing Ma Bridge

With the awareness of the significance of the Tsing Ma Bridge, a state-of-the-art long-term structural health monitoring system was deployed and managed by the Highways Department of the Hong Kong SAR Government to monitor and evaluate the serviceability and safety of the entire structure (Wong, 2004). The sensory system forms the key module of the architecture of the SHM system, which measures a comprehensive group of physical quantities ranging from the environmental/traffic loadings to local/global structural responses. As shown in Figure 6.4, a total of 282 sensors were deployed at the critical locations on the bridge, including anemometers, servo-type accelerometers, temperature sensors, dynamic strain gauges, global positioning systems, displacement transducers, level sensing stations, dynamic weigh-in-motion stations (Ni et al., 2011a).

As structural strain is a local deformation phenomenon associated with loading and material strength, monitoring of strain reflects the structural behaviour of the critical bridge component under applying loads. Sudden variation of strain pattern could be related to possible abnormalities of the bridge structure. Due to the maturity and relatively low cost of the strain sensing techniques, in-service monitoring of strain response has been most widely involved in SHM practices. As to heath monitoring of the TMB, a total of 110 weldable foil-type strain gauges were installed at three deck cross sections, i.e. CH23488.00 (chainage) near the middle of Ma Wan side span, CH23623.00 at the Ma Wan tower, and CH24662.50 near the 3/4 of main span, as shown in Figure 6.5.

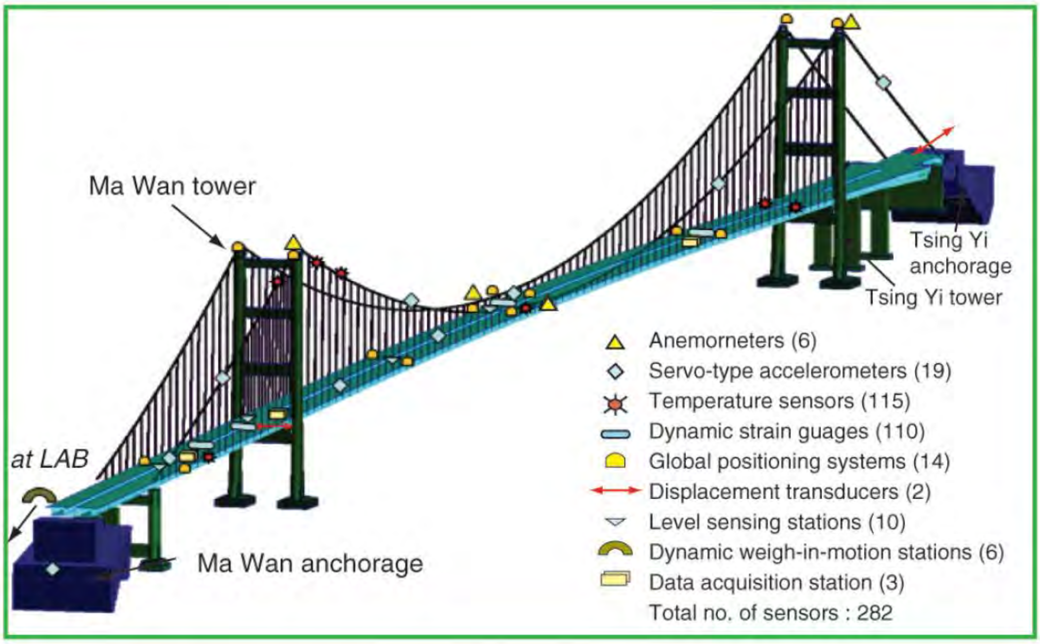

Figure 6.4 Sensor placement of structural health monitoring system for the Tsing Ma Bridge (Ni et al., 2011a)

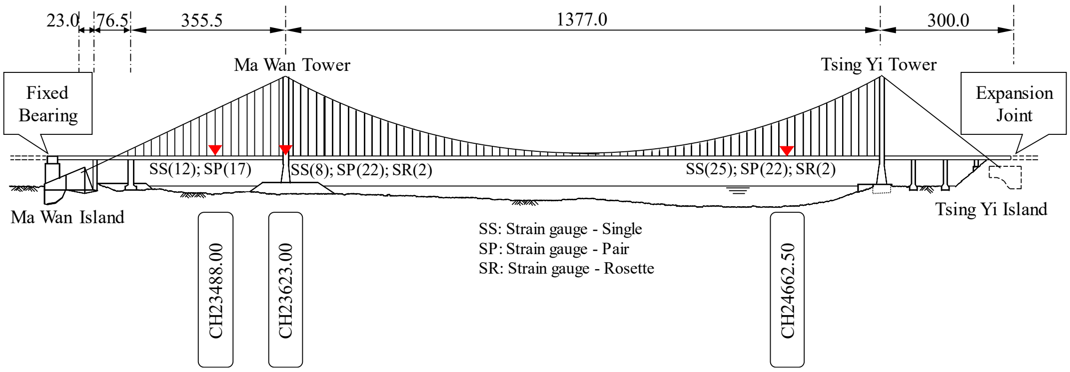

Figure 6.5 Strain monitoring of the Tsing Ma Bridge (unit: m)

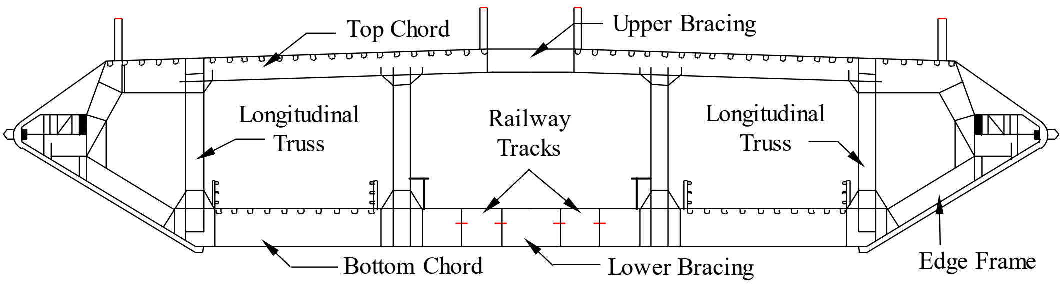

a) main cross frame

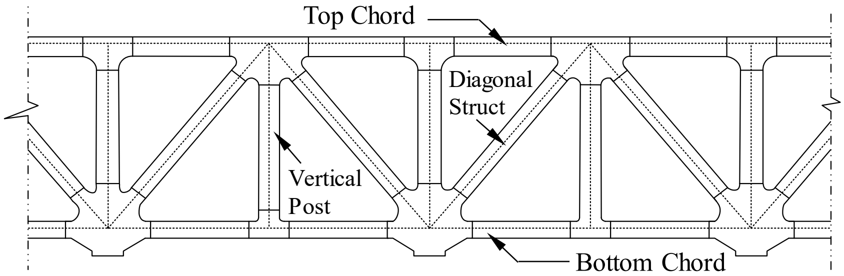

b) longitudinal truss

Figure 6.6 Critical elements of the bridge deck with strain monitoring at the main span

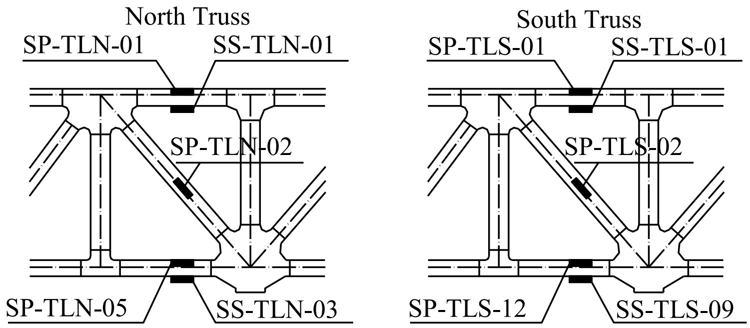

a) elevation view

b) cross-sectional view

Figure 6.7 Deployment of strain gauges on the longitudinal trusses

The strain monitoring deck section at main span (CH24662.50) is given with details Figure 6.6. To fully understand the structural behaviour under varying loads, three types of strain gauges, i.e. single, pair and rosette sensors, were deployed on the critical elements of (1) the main cross frame (top chords, bottom chords and edge frames), (2) the north and south longitudinal trusses (top chords, diagonal struts and bottom chords), (3) the railway tracks, and (4) the plane bracing system. Sampling rate of sensors should be properly selected to allow accurate reproduction and processing of original waveforms of the measurands, especially for high frequency components. Suppose the running speed of vehicles and trains on the bridge are 120 km/h and 100 km/h, respectively, and the length of a typical monitoring bridge deck is 4.5 m. The estimated frequency of vehicle- and train-induced peak responses are 7.4 Hz and 6.2 Hz, respectively. The Nyquist criterion requires that the sampling rate should be more than twice the highest frequency component of the original signals. Hence, a sampling rate of 51.2 Hz is set to 51.2 Hz for all sensors.

Load-carrying components are of high importance to long-span bridges. As for the TMB, the longitudinal trusses provide the major vertical bending stiffness of the bridge deck for accommodating both highway and railway loads. According to the bridge rating system based on criticality and vulnerability analysis, a priority should be given to regular inspection of the members of longitudinal trusses (Wong, 2006). In viewing this, long-term performance of the longitudinal trusses is the main focus of this study. A group of strain gauges, tagged as SPTLN01, SSTLN01, SPTLN02, SPTLN05 and SSTLN03 at north side, and SPTLS01, SSTLS01, SPTLS02, SPTLS12 and SSTLS09 at south side, have been attached on the top chord, diagonal strut, and bottom chord of the longitudinal trusses as depicted in Figure 6.7. One-year consecutive dynamic strain measurement data under routine operation of the bridge are collected from these sensors for subsequent reliability analysis.

6.3 STATISTICAL ANALYSIS OF STRESS RESPONSE UNDER MULTI-LOAD CONDITION

Monitoring stress responses of the longitudinal truss under the normal operation of the TMB are analysed in this section. Temperature-induced strain is firstly separated from the raw signal since most of it is released by the movement of expansion joint and contributes little to the stress due to live loads. Peak stresses are then extracted from the stress time histories to formulate the representative live load effect. Histograms of peak stress show the unique feature of multimodal load effect under routine operation of the bridge.

6.3.1 Raw Strain Signal of the Tsing Ma Bridge

Structural performance under extreme loads such as impact, gust, earthquake is no doubt a critical aspect for safety evaluation of a bridge. For the TMB, it has been reported that the safety reserve of bridge deck under typhoon condition has noticeable decrease as compared to normal operational condition (Xia et al., 2012a). Monitoring-based approach is able to reveal the actual condition of a bridge under extreme loads. The focus of this study is the long-term structural performance as well as the effects of modelling uncertainties on reliability assessment. Hence, the extreme loadings are not specifically investigated.

During the normal operation of the TMB, road vehicles run through the highway lanes on the upper deck while railway vehicles are operated on the tracks inside the lower deck. In addition, the TMB is subject to wind loads such as monsoon as the bridge site is in a wind-prone area of Hong Kong. Consequently, the monitored in-service strain responses of the longitudinal trusses are the combined effect of multiple loads, including highway traffic, railway traffic, wind and temperature. Figure 6.8 gives 24-hour raw strain signals of top chord, diagonal strut and bottom chord on the north (longitudinal) truss acquired from sensors SPTLN01, SPTLN02 and SSTLN03. The positive strain denotes compression, whereas the negative strain denotes tension. Noted that initial strain caused by dead load cannot be measured since the strain gauges were installed on the monitoring sections after completion of the bridge construction.

As shown in Figure 6.8, there are coexistence of low- and high-frequency strain components in the raw signals. A low-frequency strain component with cyclical amplitude over 24-hour time period is first observed. It reveals the longitudinal truss undergoes a process of expansion and compression along the longitudinal direction in a daily manner. By using a wavelet-based decomposition method, the low-frequency strain is first extracted from the total strain, which is demonstrated to be the temperature-induced strain.

Generally, the expansion joint placed at Tsing Yi abutment is expected to release the movement of the deck due to temperature variation. Displacement time history at the expansion joint should well represent the daily thermal effect on the bridge deck. A uniform ambient temperature field with overall temperature rising and dropping is assumed in this study. It is found that there is a consistent pattern between the extracted low-frequency strain and the displacement-derived strain at the expansion joint over 24-hour time period, therefore, it reasonably infers that the low-frequency strain component corresponds to the thermal effect on longitudinal truss due to daily ambient temperature variation (Ni et al., 2011b).

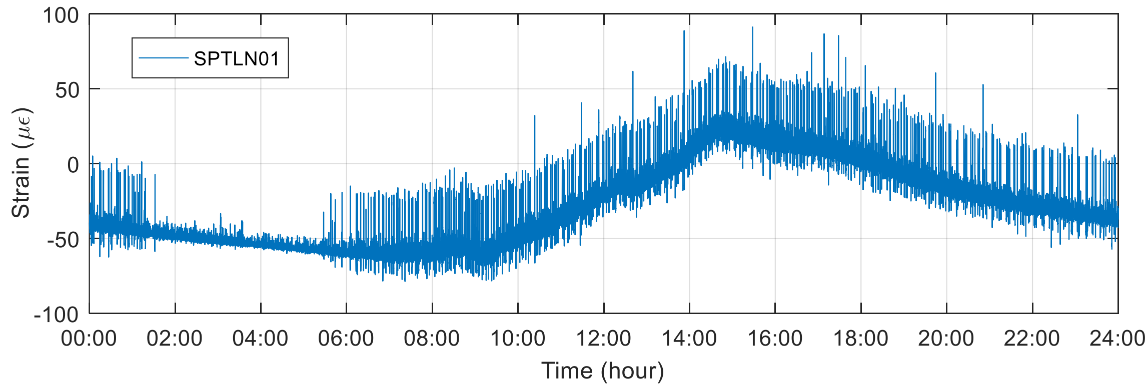

a) top chord

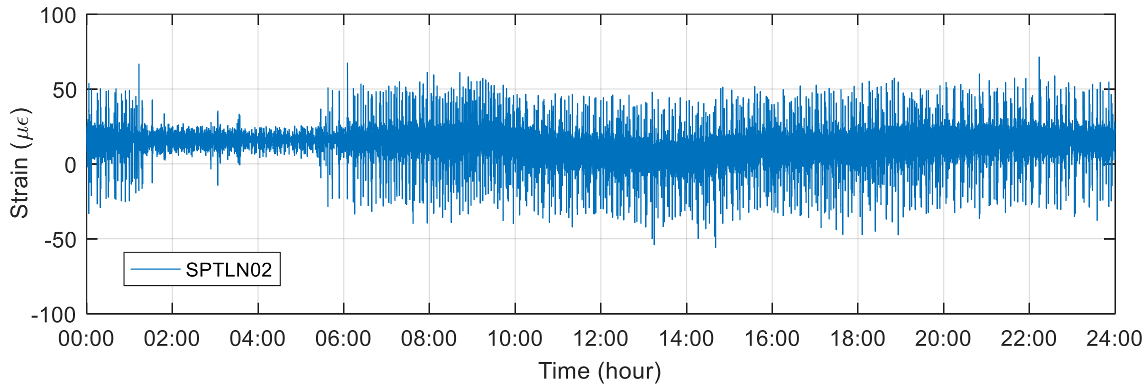

b) diagonal strut

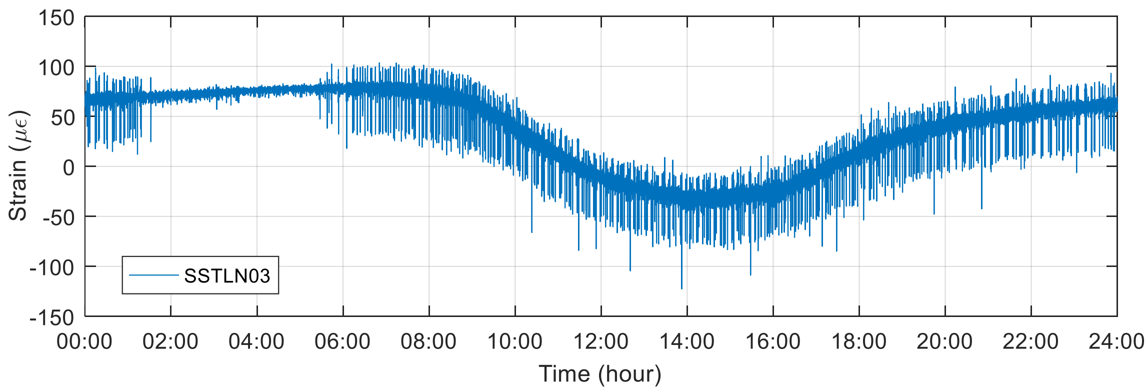

c) bottom chord

Figure 6.8 Raw strain signals of north truss (January 2, 2006)

High-frequency components in the strain signals are expected to be the results due to live load effects from road vehicles, railway trains and wind. According to the schedule of airport railway lines, the railway trains normally ceases to service during 2:00 to 5:00 a.m. everyday. As a result, lower magnitude of the monitoring strain responses is observed for all truss members around the specific period. Consequently, a mixed multi-component stochastic signal is observed for the raw strain measurements, indicating the combined effect of multiple loads experienced by the truss.

It is noteworthy that events of two trains meeting from opposite direction near the monitoring cross section can be considered as unfavourable loading events for the bridge. According to the traffic monitoring data, approximately two meeting events occur within each hour. Apart from generating greater bending moment for the bridge deck, there may be cases of large twisting moments during the passaging of two trains, which have impacts on serviceability of the bridge. However, existing strain sensors deployed on the monitoring cross section, which are normally used to measure the deformation along the longitudinal direction, may not be able to capture such a twisting moment. Additionally, train loads during a meeting event cannot be accurately identified by using the current strain-based conversion technique. These issues pose a barrier to precisely consider the twisting moment within the developed framework.

6.3.2 Elimination of Temperature-Induced Strain

Physical mechanisms of the temperature and the live loads (i.e. vehicle, train, and wind) acting on a bridge are fundamentally different. However, they are captured simultaneously in the monitoring signal. It is necessary to eliminate the temperature effect from the raw signal because live load effects may be distorted or contaminated by the temperature effect at any instance. More importantly, although the amplitude of the cyclical variation is somewhat large, the temperature-induced strain contributes little to the stress because most of it is released by the movement of the bridge deck at the expansion joint. Hence, the temperature-induced strain as absorbed by the expansion joint is excluded from the total strain for the live load characterization. Effects of highway, railway and normal wind are jointly considered in the mixture model for subsequent reliability analysis.

In order to eliminate the temperature effect from the raw mixed signals, a wavelet-based multi-component decomposition method is adopted here to obtain the live load effect arising from highway traffic, railway traffic and wind (Ni et al., 2011b). Wavelet multiresolution analysis enables the decomposition of the signal into multiple layers with different resolution scales in a perfect reconstruction sense. Figure 6.9 demonstrates the decomposition of the total strain on the top chord of the north truss, where the live load-induced strain is successfully extracted from the mixed signal after separating the trend ingredient of temperature effect.

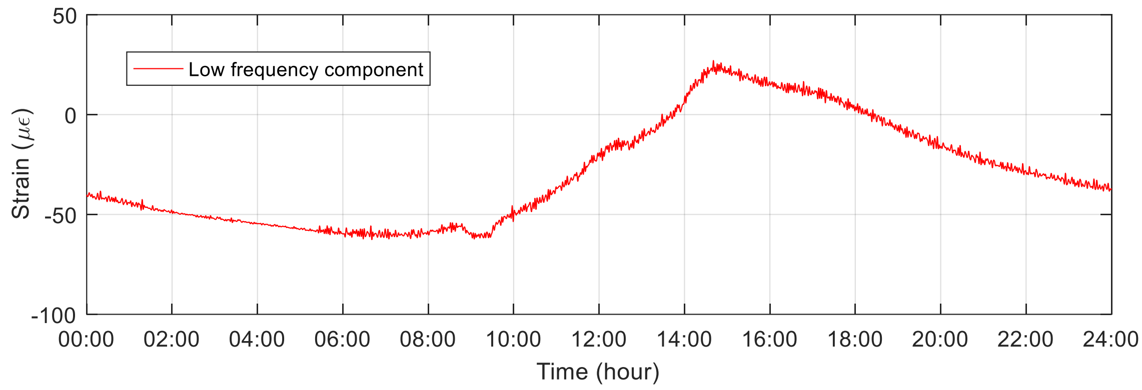

a) temperature trend in measured total strain

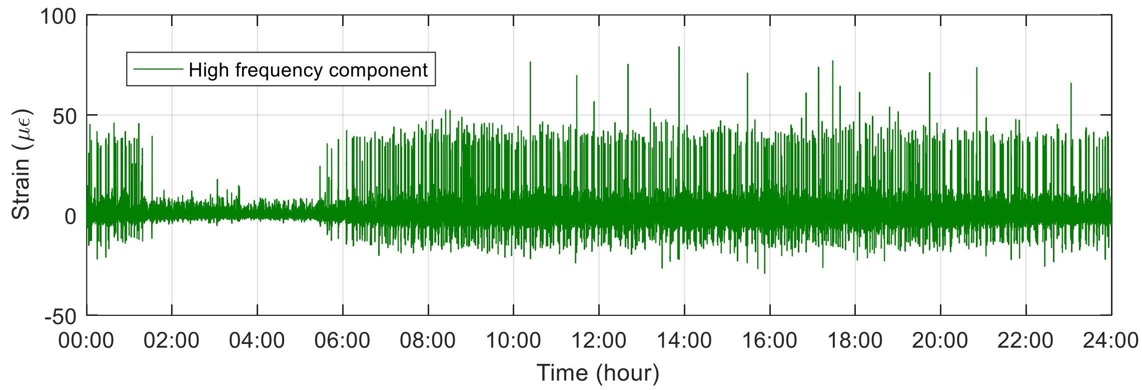

b) live load-induced strain after elimination of temperature effect

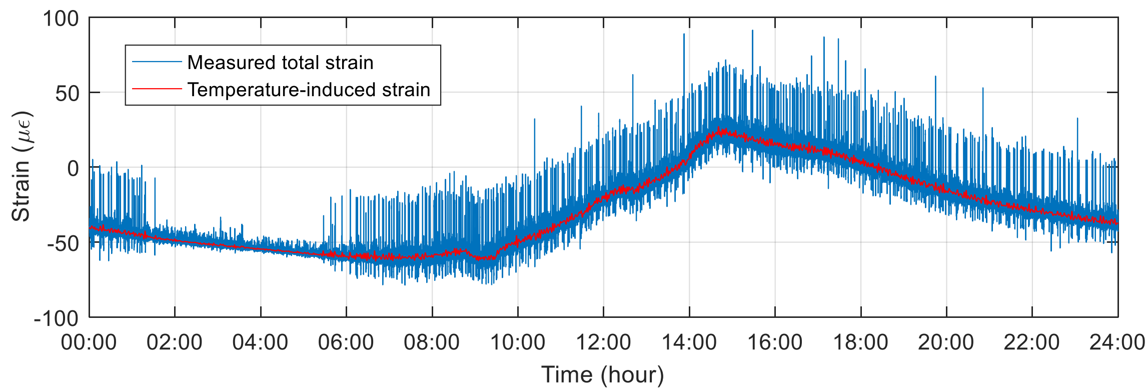

c) measured total strain

Figure 6.9 Decomposition of strain signal using wavelet multiresolution analysis

6.3.3 Multimodal Stress Response

Without loss of generality, strain measurements are hereafter converted to stress values by multiplying the elastic modulus E of steel with the fact that structural members are in elastic stage under normal bridge operation. Figure 6.10 provides a detailed plot of the stress time histories acquired from top chord, diagonal strut, and bottom chord of the north truss due to live loads in a 30-min temporal scale format. It can be observed that stress responses fluctuate rapidly with peaks and valleys in a short time period. Specifically, the stress responses at top and bottom chords evolve in time with almost the same amplitude but opposite directions, indicating flexural bending behaviour of the longitudinal truss under traffic loadings. Whereas, the diagonal strut mainly experiences axial tensile and compressive stress with identical amplitude under traffic loadings.

Peak locations (also valley locations) of the stress responses among the three time history plots are almost coincided with each other, indicating the truss members are subject to identical load events at the same moments. A comparison between the traffic arrival time and the occurrence of stress peaks shows that most of the peak values with larger amplitude are due to the trains running through the monitoring section, while the peak values with smaller amplitude are mainly caused by the passage of highway traffic. Peak response captures the actual stress level experienced by the deck truss under the normal operation of the bridge, thus it serves as a good measure for the safety reserve of truss members. As illustrated in Figure 6.10, the peak stress values are then extracted from the stress time histories by using an automatic peak counting method to construct the representative live load effects. Two principles are considered in the peak counting method. Firstly, the algorithm automatically searches the highest peak by ignoring other peaks within a prespecified distance, and the procedure is repeated for the highest remaining peak and iterates until it runs out of peak to consider. A minimum peak-to-peak distance is specified as 1000 data points in this study. Secondly, the peak values below the resolution of the strain gauge are filtered out. The resolution for a given sensor is estimated as peak-to-valley amplitude of the stress response when traffic loading is far from the monitoring section. For example, the resolution of sensor SPTLN01 is estimated as 0.4 MPa according to the stress signal so that peak values under 0.4 MPa are discarded. The automatic peak counting strategy performs well in processing the large amount of traffic-induced stress data with most of the peak stresses, rather than the spikes due to measurement noise, that needs to be taken into consideration are effectively identified.

To reduce the influence of daily traffic variation on the estimation of live load effect, the peak stresses acquired from deck trusses are processed in a monthly manner in this study. Figure 6.11 gives scatter plots of one-month peak stress responses from the top chord, diagonal strut and bottom chord of the north truss. Two subgroups of the peak stresses are clearly observed in each plot, which mainly corresponds to the two loading conditions of highway traffic and railway traffic. Note that the wind load acting on the bridge is a non-stationary process, the wind-induced effect may cause the in-between values among the peak stresses. Figure 6.12 further provides the histograms of one-month peak stress responses. Through checking the monthly stress responses of top chord, diagonal strut and bottom chord, it is found that the data acquired in the year of 2006 are of satisfactory quality as shown in Appendix since data missing and shifting are rarely seen and the stress histograms have consistent patterns over the year. They are used as the main database in this study.

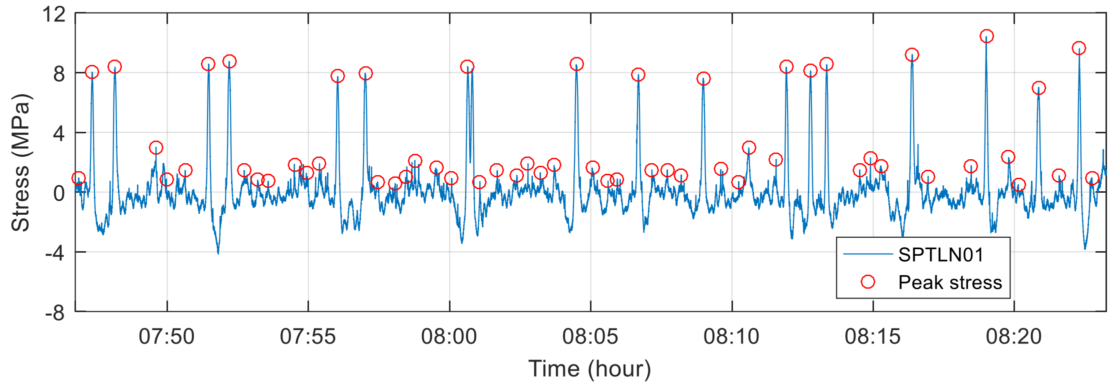

a) top chord

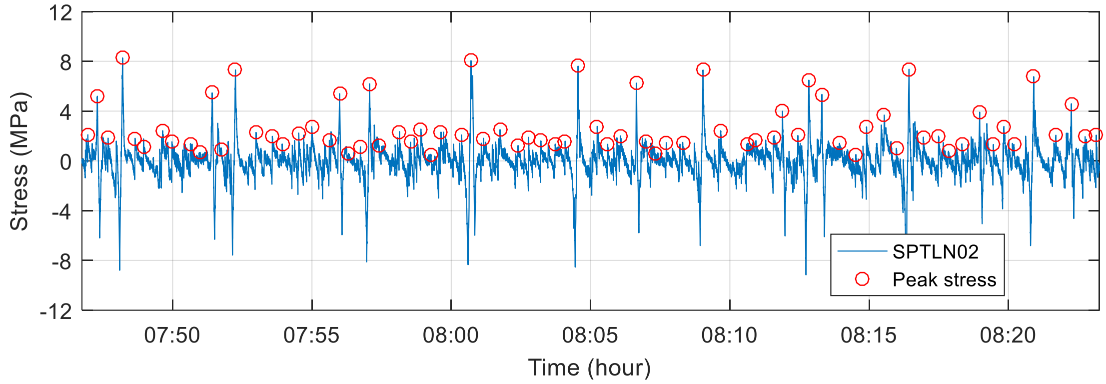

b) diagonal strut

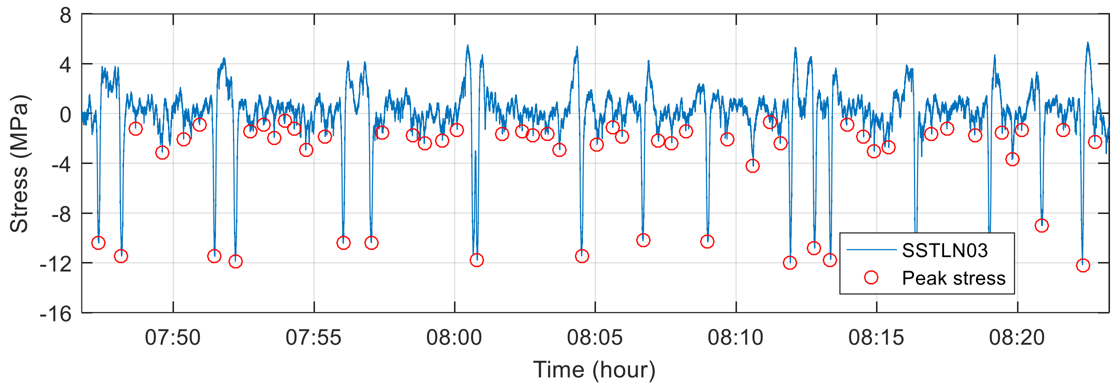

c) bottom chord

Figure 6.10 Stress responses and identified peak stresses in 30-min temporal scale (January 15, 2006)

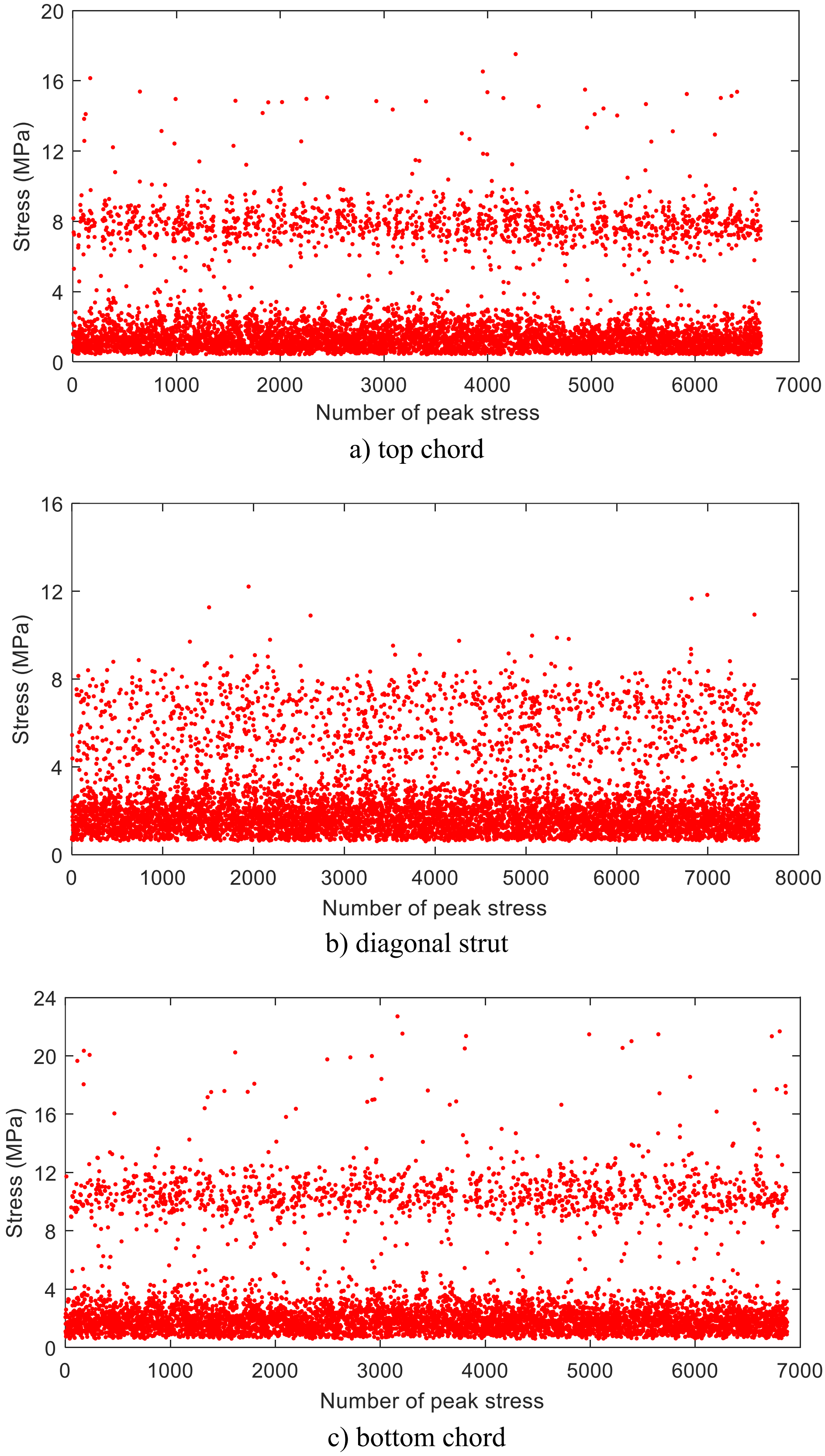

Figure 6.11 Extracted peak stresses (January 2006)

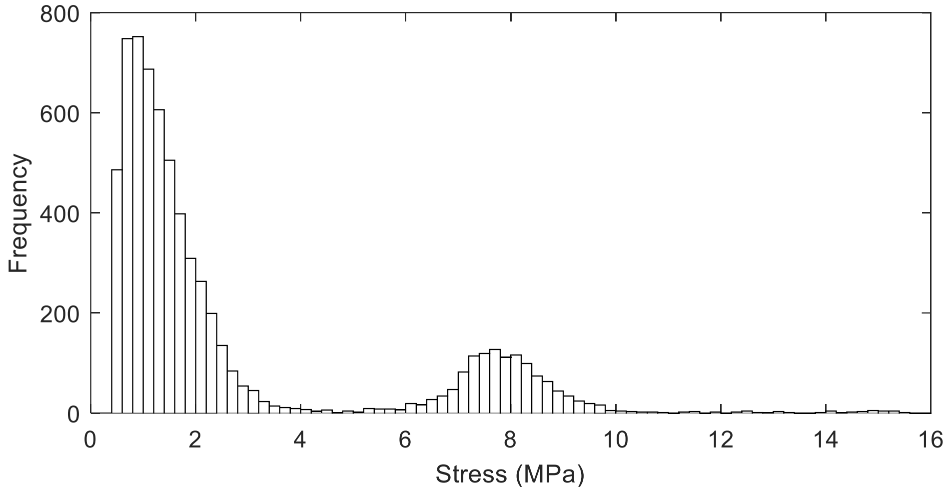

a) top chord

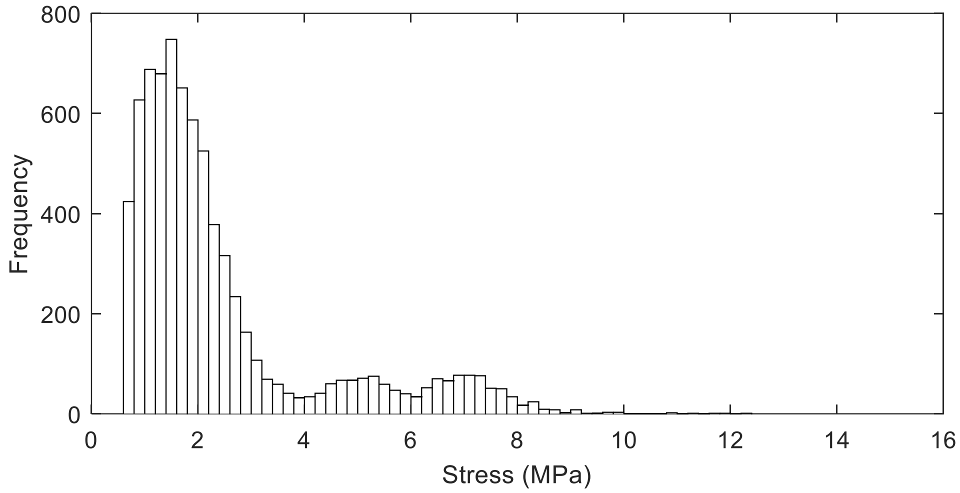

b) diagonal strut

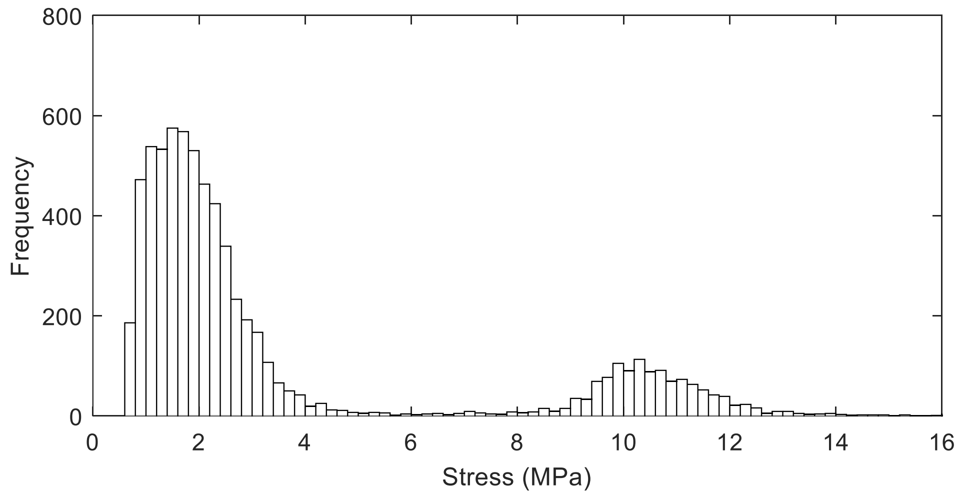

c) bottom chord

Figure 6.12 Histograms of peak stress (January 2006)

Due to the combined effect of highway traffic, railway traffic, and wind loads, the peak stresses are randomly distributed but mostly centralised to several stress levels, exhibiting the multimodal response feature. Estimation of the distribution model for multimodal load effect inevitably introduces additional modelling uncertainties such as the parametric and model order uncertainties. The proposed Bayesian mixture models are employed in the following section to address the estimation of multimodal stress response as well as quantifying the modelling uncertainties.

6.4 ESTIMATION OF MULTIMODAL LOAD EFFECT USING BAYESIAN MIXTURE MODELS

Estimation of the distribution model for the multimodal stress response is carried out in this section using the two proposed Bayesian mixture modelling approaches respectively. The model order uncertainty and parametric uncertainty are explicitly addressed under the Bayesian framework. Both parametric and nonparametric mixture PDFs of the multimodal load effect are estimated for the subsequent reliability analysis.

6.4.1 Parametric Estimation

With the consideration of parametric uncertainty, the parametric Bayesian mixture model, specifically the finite Gaussian mixture (FGM) model as proposed in Chapter 3, is first employed to estimate the multimodal load effect.

6.4.1.1 Selection of optimal model order

Multiple peaks are clearly displayed in the stress histograms as shown in Figure 6.12, but the exact number of peaks remains unknown. For FGM model, it is improper to specify the model order (i.e. number of components) by subjective visual inspection as it could lead to inadequate model estimation. The Bayes factor-based model order selection method as introduced in Chapter 3 is used here to find the optimal number of components of the FGM model for accommodating the multimodal load effect.

A group of FGM models with number of components ranging from one to ten, i.e. $J = 1$ to 10, are proposed as the candidate models. The log marginal likelihood (LML) as given in Equation (3.27) is evaluated for each candidate model. Note that comparison with LML values of each candidate model is equivalent to the comparison of pair-wised Bayes factor of the candidate models.

Another two commonly used model selection criteria, i.e. the Akaike Information Criterion (AIC) and the Bayesian information Criterion (BIC), are evaluated for each candidate model as well to compare with the results obtained from Bayes factor approach. These two criteria award goodness-of-fit of the model while penalise high model complexity. The optimal model order is selected by minimizing the AIC or BIC value as follows

$$AIC = -2\ln p(y|\mathbf{\Theta}) + 2P \tag{6.1}$$

$$BIC = -2\ln p(y|\mathbf{\Theta}) + P\ln N \tag{6.2}$$

where y are observations, $\mathbf{\Theta}$ are the mixture parameters, $\ln p(y|\mathbf{\Theta})$ is the log likelihood function of the mixture model, $P = 3 \times J$ is the number of mixture parameters, and N is the number of observations. To make the LML comparable with AIC and BIC, negative log marginal likelihood (NLML) is defined by simply transforming Equation (3.27) to its negative expression

$$NLML = -\ln p(y|\boldsymbol{\Theta}^{\star}) - \ln p(\boldsymbol{\Theta}^{\star}) + \ln p(\boldsymbol{\Theta}^{\star}|y) \tag{6.3}$$

where $\boldsymbol{\Theta}^{\star}$ are the posterior mean values of the mixture parameters. Consistently, minimizing NLML gives the optimal number of components.

The optimal model orders for the multimodal stress response at top chord, diagonal strut and bottom chord of the deck truss are identified using the three model selection criteria. Figure 6.13 gives the results of ten candidate models evaluated for the top chord, in which NLML has the overall minimum value at $J = 4$, indicating the optimal model order is uniquely identified as four by the Bayes factor approach. In contrast, both AIC and BIC criteria reach the minimum values at $J = 5$, suggesting a different model selection result. Table 6.1 summarizes the results of optimal model order identified by the three different criteria. The AIC and BIC criteria advise to use higher order complex mixture models for the multimodal stress response, whereas the Bayes factor approach prefers mixture model with less components. However, the model order identified for the diagonal strut is the same when using three different criteria. With respect to each truss element, all the three criteria suggest that higher order complex mixture models are needed for accommodating the multimodal stress responses of top and bottom chords than that of diagonal strut. It indicates the mixture pattern of live load effect, even under the identical multi-load condition, could vary significantly among different truss elements. The optimal model orders as identified by the Bayes factor approach are adopted for the subsequent mixture parameter estimation.

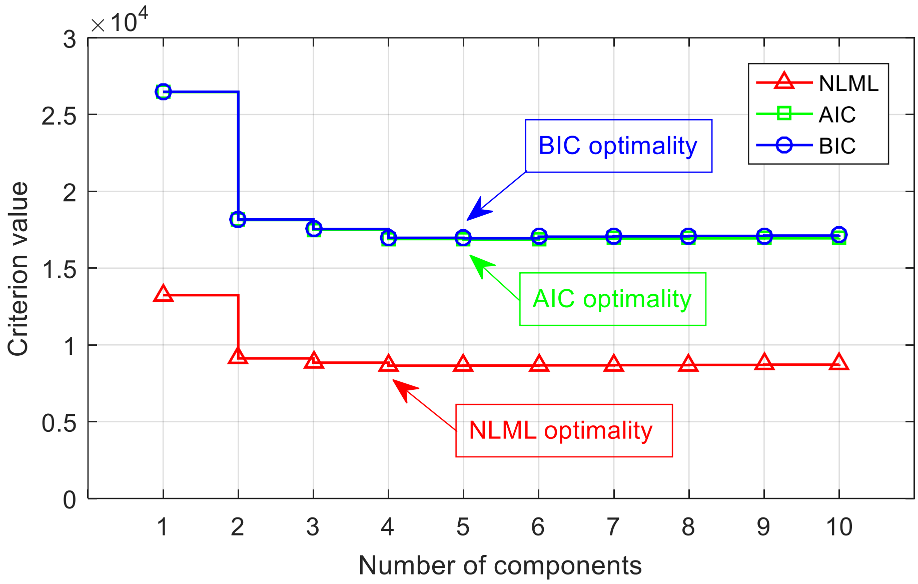

Figure 6.13 Determination of optimal model orders for FGM model of top chord using three different criteria

Table 6.1 Identified optimal model orders for FGM model using three different criteria

Locations	Optimal model order		
	Bayes factor	AIC	BIC
Top chord	4	5	5
Diagonal strut	3	3	3
Bottom chord	4	5	4

6.4.1.2 Estimation of parameters and predictive mixture PDF

Given the optimal model order, posterior samples of mixture parameters are obtained by using the Gibbs sampler as introduced in Chapter 3. A quick convergence of the Gibbs iteration is reached for all the simulations. The sample mean of the posterior mixture parameter is served as the estimation of multimodal stress response, which reflects the average load effect experienced by the truss. The 5-95 credible interval (CI) of the posterior mixture parameter is used to represent the parametric uncertainty arising from statistical inference of the multimodal data. Table 6.2 provides the posterior estimation of the multimodal stress response of the top chord, diagonal strut and bottom chord of the truss.

Table 6.2 FGM estimation of the multimodal stress response of north truss (January 2006)

Comp.	Parameter μ			Parameter σ^2			Parameter ω			Stress level
	5%	Mean	95%	5%	Mean	95%	5%	Mean	95%	
Top chord										
No. 1	0.952	0.972	0.992	0.110	0.119	0.128	0.449	0.474	0.499	I
No. 2	1.784	1.832	1.882	0.357	0.387	0.419	0.299	0.323	0.347	
No. 3	7.775	7.820	7.865	0.602	0.663	0.728	0.161	0.170	0.178	II
No. 4	7.285	7.896	8.519	12.730	15.595	19.016	0.027	0.034	0.041	III
Diagonal strut										
No. 1	1.145	1.174	1.204	0.097	0.108	0.120	0.319	0.350	0.382	I
No. 2	1.971	2.014	2.060	0.300	0.324	0.348	0.427	0.460	0.490	
No. 3	5.661	5.771	5.877	2.393	2.631	2.894	0.182	0.191	0.199	II
Bottom chord										
No. 1	1.493	1.539	1.585	0.246	0.272	0.301	0.476	0.523	0.570	I
No. 2	2.399	2.492	2.596	0.588	0.651	0.720	0.234	0.280	0.326	
No. 3	10.424	10.480	10.537	0.886	0.981	1.083	0.149	0.157	0.166	II
No. 4	9.757	10.396	11.058	19.872	24.008	28.773	0.033	0.039	0.046	III

Note: The order of components is ranked according to (1) the ascending order of μ; and (2) the last component with the maximum σ^2.

Multiple stress levels are clearly identified for the north truss. Taking the results for top chord as an example, it is shown that approximately 80% of the total peak stresses are allocated to the 1st and 2nd components with relatively small component means, say around 1.0 to 1.8 MPa. These two components represent the first level (level I) stress which can be interpreted as the load effect of superposition of highway traffic and wind load. The 3rd component occupies approximately 17% of the total peak stresses with larger component means about 7.8 MPa and relatively small component variance. It is the second level (level II) stress which can be regarded as the combined effect of railway traffic and wind load. The 4th component takes only about 3% of the total peak stresses with the greatest component variance. It is the third level (level III) stress that can be the representative of the superposition effect of highway traffic, railway traffic and wind load.

Within a certain long period, say one month, the wind speed and direction near the TMB can be quite different. Wind effect on the bridge, as compared with traffic-induced effect, is far more undetermined, causing sparse and dispersed peak stress values. Mixture models equipped with sufficient number of components are able to characterize the wind-induced peak stresses. The estimated FGM models with optimal model order facilitate the interpretation of multi-load effect. Similar findings of stress levels are also existed in the estimated FGM models for diagonal strut and bottom chord.

Given the posterior FGM estimation, the predictive PDFs and associated 5-95 uncertain bounds of the multimodal load effect for top chord, diagonal strut and bottom chord are constructed as depicted in Figure 6.16. The predictive PDFs fit well with the histograms of multimodal stress response for all three truss members. The upper and lower uncertain bounds are both continuous curves, laying symmetrically on the two sides of the predictive PDF curve. The uncertain bounds unveil the variability in PDF estimation of the FGM model due to parametric uncertainty.

6.4.2 Nonparametric Estimation

With the consideration of both model order and parametric uncertainties, the nonparametric

Bayesian mixture model, specifically the Dirichlet process mixture (DPM) model as introduced in Chapter 5, is utilised to estimate the multimodal load effect.

6.4.2.1 Varying model order

The model order in the DPM model is a random variable that is allowed to vary throughout the iteration of the collapsed Gibbs sampler. In other words, multiple model orders could appear along with the iteration. Figure 6.14 gives the variation of number of components during the collapsed Gibbs iteration for modelling the multimodal load effect of the top chord. It is observed that the model order has a relatively large variation, ranging from $J = 2$ to $J = 14$, throughout the iteration. Early samples of model order with rather small number of components are unable to represent the multimodality in the data, which tells that the iteration is not yet converged. The right panel provides the histogram of samples of J after the burn-in stage. Four predominant model orders, namely $J = 7$ to $J = 10$, are found from the histogram which take over 90% of occurrence times during the iteration. In particular, the model order of $J = 8$ is recognised as the most frequently occurring order (mode of model order) that used for DPM modelling.

Estimations of model order for the three truss members are summarised in Figure 6.15, in which $J = 8$, $J = 7$, and $J = 8$ are identified as the most frequently occurring model orders of top chord, diagonal strut and bottom chord, respectively. Note that the observed most frequently occurring model orders have overall larger values than the optimal model order identified in parametric approach as shown in Table 6.3. It is found that, in contrast to the FGM model, the

DPM model tends to fit the multimodal stress response with larger number of components, which is coincident with the results of comparison study given in Chapter 5. In addition, the most frequently occurring model order observed for diagonal strut is lower than that of top and bottom chords, which is again consistent with the results of FGM model. Inference through both FGM and DPM models indicates that the mixture pattern of live load effect could vary significantly among different structural elements even under the identical multi-load condition. From an engineering point of view, the high model order is needed if the stress responses are widely spread due to heavy vehicular and train loads.

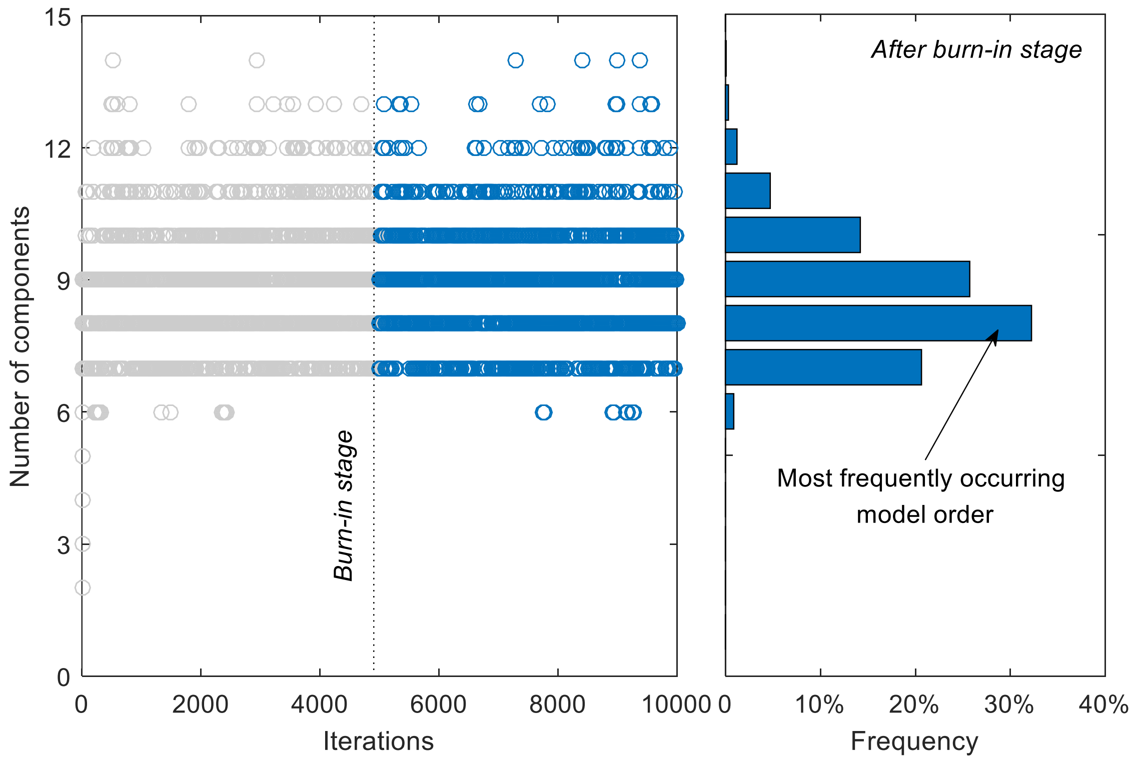

Figure 6.14 Varying model orders during the collapsed Gibbs iteration

Table 6.3 Identified model orders using parametric and nonparametric approaches

Locations	Model order	
	FGM (Optimal)	DPM (Most frequently occurring)
Top chord	4	8
Diagonal strut	3	7
Bottom chord	4	8

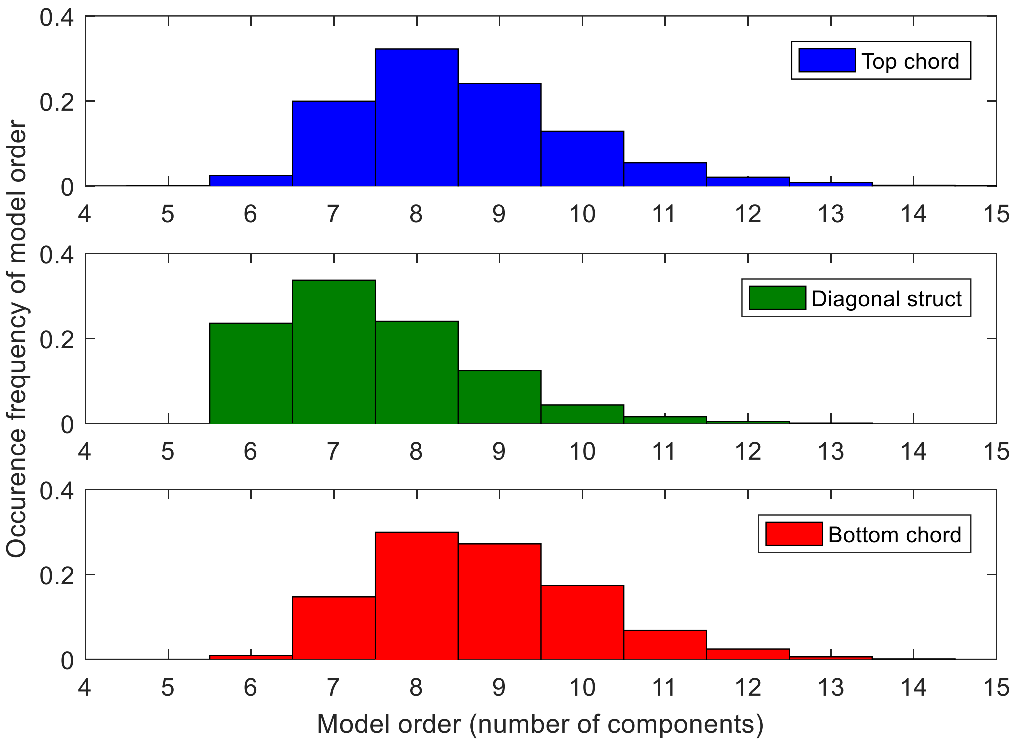

Figure 6.15 Occurrence frequency of model orders for DPM model

6.4.2.2 Estimation of predictive mixture PDF

Using the quantitative convergence diagnosis strategy proposed in Chapter 4, the convergence of the collapsed Gibbs iteration is checked for all simulations. A satisfactory convergence speed is achieved for most of the cases. The posterior mixture density samples are obtained after discarding the burn-in samples. As depicted in Figure 6.16, the predictive PDFs and associated

5-95 uncertain bounds of the multimodal load effect for top chord, diagonal strut and bottom chord are constructed by using the posterior mixture density samples. A good fitting is observed for the histograms of multimodal stress response with the predictive PDFs for all three truss members. The upper and lower uncertain bounds are both continuous curves, laying symmetrically on the two sides of the predictive PDF curve. The uncertain bounds unveil the variability in PDF estimation of the DPM model due to model order and parametric uncertainties.

As shown in Figure 6.16, both parametric and nonparametric PDFs and associated uncertain bounds are plotted together to make a direct comparison. More complicated mixture distributional shapes are observed for the DPM models for accommodating the multimodal stress response of three truss members. The K-S test and log-likelihood value are further evaluated to quantitatively compare the goodness-of-fit of the parametric and nonparametric PDFs. As given in Table 6.4, higher values of the P-value and log-likelihood of the DPM models are achieved for all truss members, which strongly favours that the nonparametric approach owns a better performance than the parametric counterpart with respect to PDF fitting. Note that the same remark is made for better nonparametric PDF fitting with the artificial data set in Chapter 5.

One-year parametric and nonparametric mixture PDFs and associated uncertain bounds of the multimodal load effect are estimated respectively and they are used for the subsequent reliability analysis.

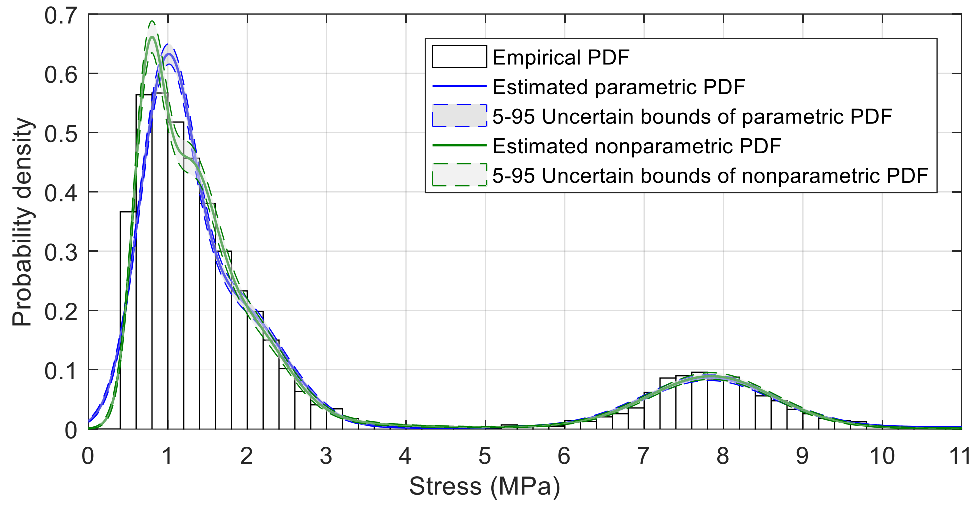

a) top chord

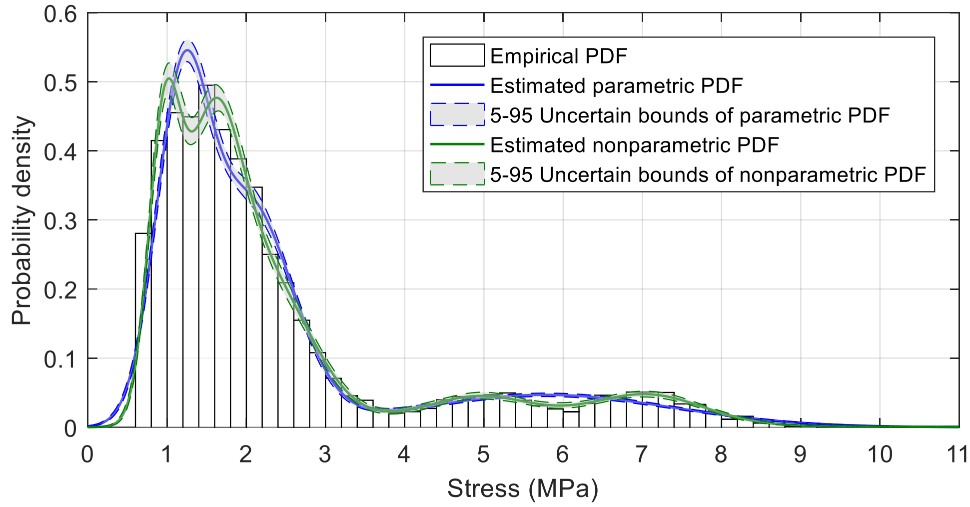

b) diagonal strut

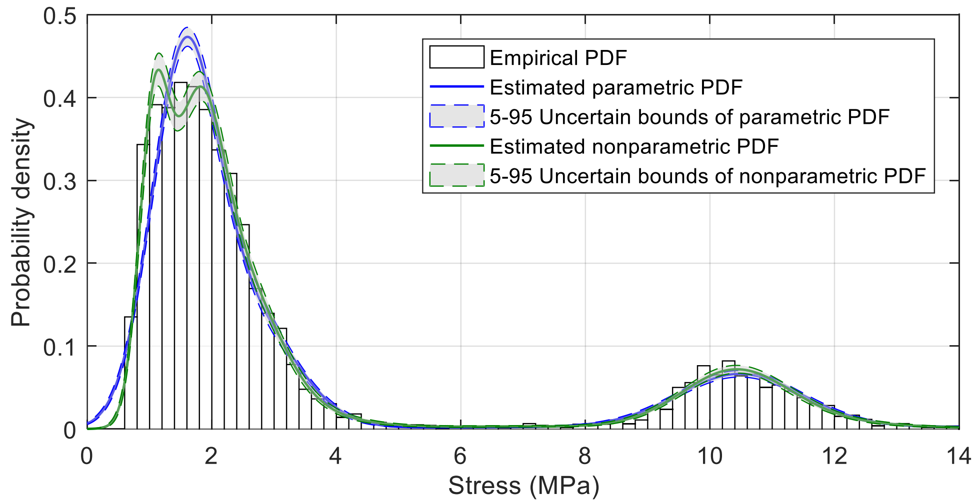

c) bottom chord

Figure 6.16 Estimated parametric and nonparametric PDFs with uncertain bounds for multimodal stress response of north truss (January 2006)

Table 6.4 Goodness-of-fit of parametric and nonparametric approaches

Locations	FGM	DPM
	P-value of K-S test	
Top chord	1.050e-06	**7.730e-02**
Diagonal strut	1.500e-03	**1.488e-01**
Bottom chord	5.974e-04	**6.933e-01**
	Log-likelihood	
Top chord	-9.963e+03	**-9.777e+03**
Diagonal strut	-1.152e+04	**-1.135e+04**
Bottom chord	-1.195e+04	**-1.176e+04**

Note: Higher values of P-value and log-likelihood favour better fitting.

6.5 RELIABILITY ASSESSMENT OF BRIDGE DECK UNDER MODELLING UNCERTAINTIES

Reliability assessment of the deck truss using the estimated Bayesian mixture models is carried out in this section. Based on the first-order reliability method (FORM), a conditional reliability index is formulated to take into account the variability of PDF estimation due to model order and parametric uncertainties. Sensitivity analysis is conducted to investigate the influence of uncertain mixture parameters on the reliability estimate. A demonstration of mitigating the uncertain reliability estimate is given by increasing the sample size of peak stress. The conditional reliability estimate is updated in a month-by-month manner to render a more accurate assessment result of the deck truss during the monitoring period.

6.5.1 FORM and Conditional Reliability Index

For reliability assessment based on monitoring data, it is convenient to compare the structural resistance R and the monitored load effect S to measure the structural safety. The performance function can be formulated as (Frangopol et al., 2008; Melchers and Beck, 2017)

$$g(\mathbf{X}, \mathbf{\Theta}) = R - S \tag{6.4}$$

where $\mathbf{X} = \{R, S\}$ is the resistance and load effect vector and $g(\mathbf{X}, \mathbf{\Theta}) < 0$ represents the failure state. To consider the modelling uncertainties, the model parameter vector $\mathbf{\Theta} = \{\boldsymbol{\theta}_R, \boldsymbol{\theta}_S\}$ associated with R and S is incorporated in the performance function. The failure probability $P_f(\mathbf{\Theta})$ under modelling uncertainties can be defined as

$$P_f(\mathbf{\Theta}) = \Pr(g(\mathbf{X}, \mathbf{\Theta}) < 0) = \int_{g<0} p_R(r; \boldsymbol{\theta}_R) p_S(s; \boldsymbol{\theta}_S) \mathrm{d}r\mathrm{d}s \tag{6.5}$$

where p_R and p_S are the probability distribution for R and S, respectively. Now, the monitored multi-load effect is represented by mixture PDF, the failure probability can be further derived as

$$\begin{aligned} P_f(\mathbf{\Theta}) &= \int_{g<0} p_R(r; \boldsymbol{\theta}_R) \left(\sum_{j=1}^{J} \omega_{S_j} p_{S_j} \left(s; \boldsymbol{\theta}_{S_j} \right) \right) \mathrm{d}r\mathrm{d}s \\ &= \sum_{j=1}^{J} \left(\omega_{S_j} \int_{g_j<0} p_R(r; \boldsymbol{\theta}_R) p_{S_j}(s; \boldsymbol{\theta}_{S_j}) \mathrm{d}r\mathrm{d}s \right) \end{aligned} \tag{6.6}$$

where $p_S = \sum \omega_{S_j} p_{S_j}$ is the mixture PDF with p_{S_j} being the jth component density, and $\bigcup_{j=1}^{J} g_j = g$ is the failure domain. Providing that p_R and p_{S_j} are normally distributed, the failure probability can be estimated by the first-order reliability method (FORM) as

$$P_f(\mathbf{\Theta}) \approx \sum_{j=1}^{J} \omega_{S_j} \Phi \left(-\beta_j(\boldsymbol{\theta}_R, \boldsymbol{\theta}_{S_j}) \right) \tag{6.7}$$

where $\beta_j(\boldsymbol{\theta}_R, \boldsymbol{\theta}_{S_j}) = \left(\mu_R - \mu_{S_j}\right) / \left(\sigma_R^2 + \sigma_{S_j}^2\right)^{1/2}$ is the reliability estimate associated with the jth mixture component, $\boldsymbol{\theta}_R = \{\mu_R, \sigma_R^2\}$ is mean and variance of R, and $\boldsymbol{\theta}_{S_j} = \{\mu_{S_j}, \sigma_{S_j}^2\}$ is the jth component mean and component variance of S. Thus, the reliability index with the consideration of modelling uncertainties, which termed as conditional reliability index $\beta(\boldsymbol{\Theta})$, can be defined as

$$\beta(\boldsymbol{\Theta}) = -\Phi^{-1}(P_f(\boldsymbol{\Theta})) \tag{6.8}$$

where Φ^{-1} is the inverse cumulative probability density of standard normal distribution. Equation (6.8) unveils that the conditional reliability index is a function of model parameter $\boldsymbol{\Theta}$, which implies the estimate of reliability index can be itself random variable due to the uncertain nature of $\boldsymbol{\Theta}$. In other words, not only the aleatory uncertainty (i.e. the intrinsic variability of resistance or load effect) but also the epistemic uncertainty (i.e. the inaccuracy inherent in model order selection and parameter estimation) has the impact on estimation of the structural reliability (Der Kiureghian, 2008; Der Kiureghian and Ditlevsen, 2009).

According to the design documents of the TMB, the maximum allowable stress for truss member under live loads in serviceability limit state was specified as 60 MPa (Wong, 2007). A coefficient of variation $\gamma = 0.075$ is adopted for this study (Chatterjee, 2008; Frangopol et al., 2008). These statistics are served as the probability descriptors of resistance R, which yield a mean value $\mu_R = 60$ MPa and a standard deviation $\sigma_R = \gamma\mu_R = 4.5$ MPa for assessment. Given the estimated mixture models of the multi-load effect, random samples of the conditional reliability index can be obtained as

$$\beta^{(g)} = -\Phi^{-1}\left(\sum_{j=1}^{J} \omega_{S_j}^{(g)} \Phi\left(-\frac{\mu_R - \mu_{S_j}^{(g)}}{\sqrt{\sigma_R^2 + \sigma_{S_j}^{2(g)}}}\right)\right) \tag{6.9}$$

where $\omega_{S_j}^{(g)}$, $\mu_{S_j}^{(g)}$ and $\sigma_{S_j}^{2(g)}$ $(g = 1, \cdots, G)$ are posterior samples of mixture parameters from the Gibbs iteration. Note that model order J shall be drawn from the iteration for evaluating the conditional reliability index when load effect is represented by the DPM model. Equation (6.9) provides a general expression to calculate the conditional reliability index by either using the FGM model or the DPM model.

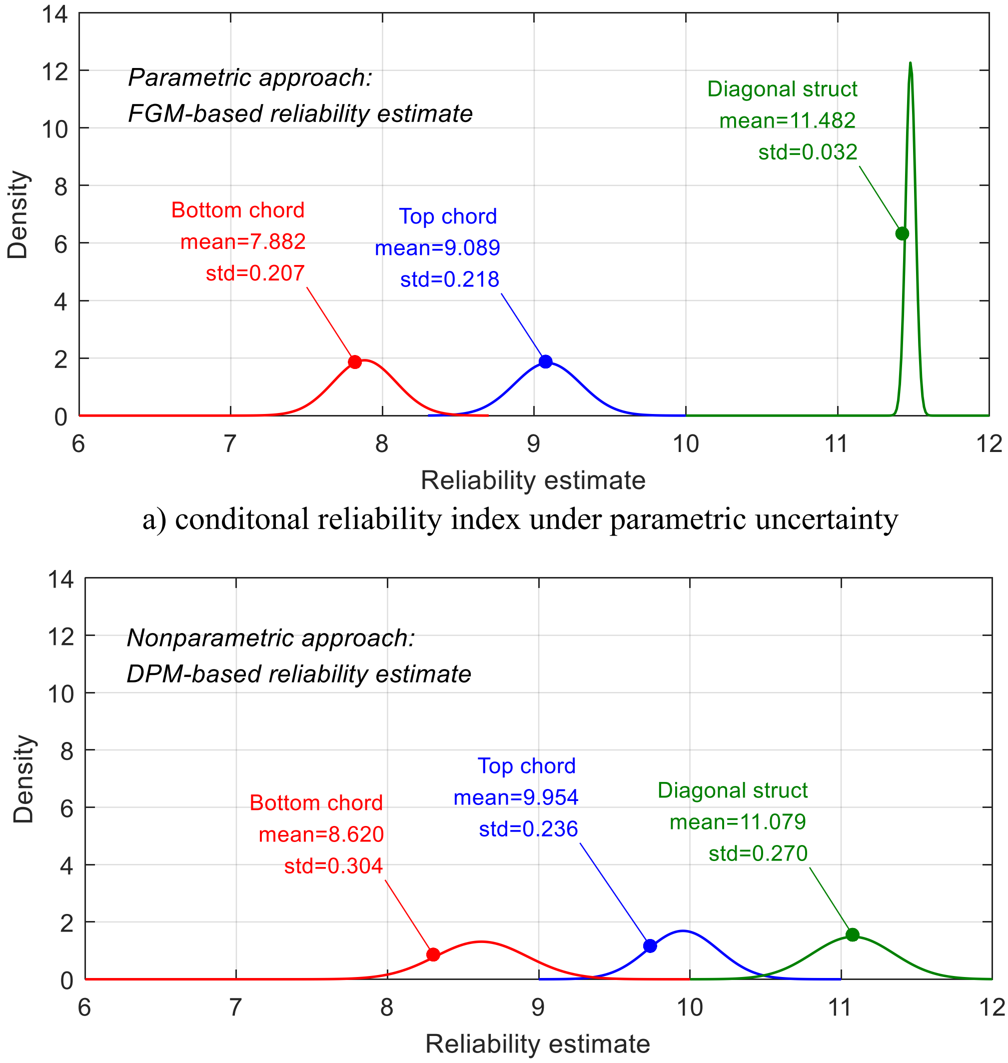

a) conditonal reliability index under parametric uncertainty

b) conditional reliability index under model order and parametric uncertainties

Figure 6.17 Conditional reliability index under modelling uncertainties for deck truss

Reliability assessment of the truss members under modelling uncertainties is demonstrated in Figure 6.17. As expected, the samples of conditional reliability index $\beta^{(g)}$ for each truss member are randomly distributed with different locations but similar scales (except for FGM-based reliability samples of diagonal strut). Sample mean and sample standard deviation of $\beta^{(g)}$ are evaluated for each truss member. The mean value of $\beta^{(g)}$ represents the average safety level for each truss member, while the standard deviation of $\beta^{(g)}$ measures the variation associated with this safety level due to modelling uncertainties. Table 6.5 lists the mean values and standard deviations of the conditional reliability index for each truss member in the year of 2006.

It is observed that the diagonal strut has an overall highest mean value, followed by the top chord, while the bottom chord owns the lowest mean value of the conditional reliability index. These findings agree well with the fact that the diagonal strut experiences overall smaller live load effect than the top and bottom chords as revealed from the estimated mixture PDFs. Note that assessment results by using either FGM or DPM model are not contradictory with each other. With respect to individual truss member, however, the calculated mean values by using each model are slightly different. It finds that the FGM-based analysis yields relative lower reliability for top and bottom chords, while it provides higher reliability for diagonal strut as compared to the DPM-based analysis.

Table 6.5 Estimation of conditional reliability index for deck truss

Position	Month	FGM-based reliability estimate		DPM-based reliability estimate	
		Mean	SD	Mean	SD
Top chord	Jan	9.089	0.218	9.954	0.236
	Feb	8.667	0.370	9.926	0.272
	Mar	8.483	0.573	9.797	0.375
	Apr	9.173	0.308	9.942	0.314
	May	9.371	0.266	9.818	0.343
	Jun	9.200	0.241	10.061	0.262
	Jul	9.176	0.245	9.861	0.301
	Aug	8.730	0.299	9.853	0.271
	Sep	8.925	0.275	10.161	0.163
	Oct	9.268	0.234	10.191	0.181
	Nov	9.337	0.211	9.679	0.348
	Dec	9.039	0.254	9.931	0.220
Diagonal strut	Jan	11.482	0.032	11.079	0.270
	Feb	11.425	0.045	11.065	0.276
	Mar	11.509	0.071	11.636	0.153
	Apr	11.562	0.036	11.137	0.319
	May	11.447	0.044	11.072	0.264
	Jun	11.446	0.041	10.857	0.357
	Jul	11.371	0.038	10.642	0.382
	Aug	11.461	0.035	11.150	0.318
	Sep	11.470	0.036	11.016	0.297
	Oct	11.435	0.038	10.799	0.321
	Nov	11.434	0.038	10.848	0.282
	Dec	11.457	0.035	11.394	0.190
Bottom chord	Jan	7.882	0.207	8.620	0.304
	Feb	7.289	0.419	8.631	0.322
	Mar	6.621	0.678	7.854	0.608
	Apr	8.201	0.344	8.882	0.330
	May	7.865	0.324	8.808	0.341
	Jun	7.596	0.319	8.980	0.232
	Jul	7.629	0.323	8.554	0.398
	Aug	7.560	0.269	8.333	0.357
	Sep	7.292	0.259	8.889	0.166
	Oct	8.027	0.252	8.877	0.302
	Nov	7.627	0.233	8.028	0.353
	Dec	7.543	0.299	8.120	0.433

6.5.2 Sensitivity Analysis of Uncertain Parameters

Uncertainty associated with the reliability estimate as measured by the standard deviation is of significance to the assessment. As shown in Table 6.5, it finds out the DPM-based analysis yields a similar degree of uncertainty of reliability estimates for the top chord, diagonal strut and bottom chord since the standard deviations are within a certain level. Nevertheless, the FGM-based analysis gives a relative lower degree of uncertainty of reliability estimate for the diagonal strut with much smaller values of standard deviation as compared to that of top and bottom chords. To figure out this, the investigation with respect to the influence of uncertain mixture parameters on the reliability estimate is carried out.

To analyse the sensitivity of a specific type of uncertain mixture parameter, we fix the other parameters by substituting their mean values in Equation (6.9) and compute the conditional reliability index accordingly. Three cases are considered here: (1) uncertain component means μ; (2) uncertain component variances σ^2; and (3) uncertain mixing weight ω. These three cases are compared with the case that all mixture parameters are uncertain in the reliability estimate which is exactly the results given in Figure 6.17. Influence of different types of uncertain mixture parameter on the reliability estimate is showed in Figure 6.18 with the boxplot being the range of reliability estimate under each case. In contrast to parameters μ and ω, the uncertain σ^2 leads to the greatest variation of the reliability estimate, which is almost the same level as the case that all mixture parameters are uncertain. It can be inferred that the uncertainty associated with reliability estimate is primarily affected by the variation of component variance σ^2.

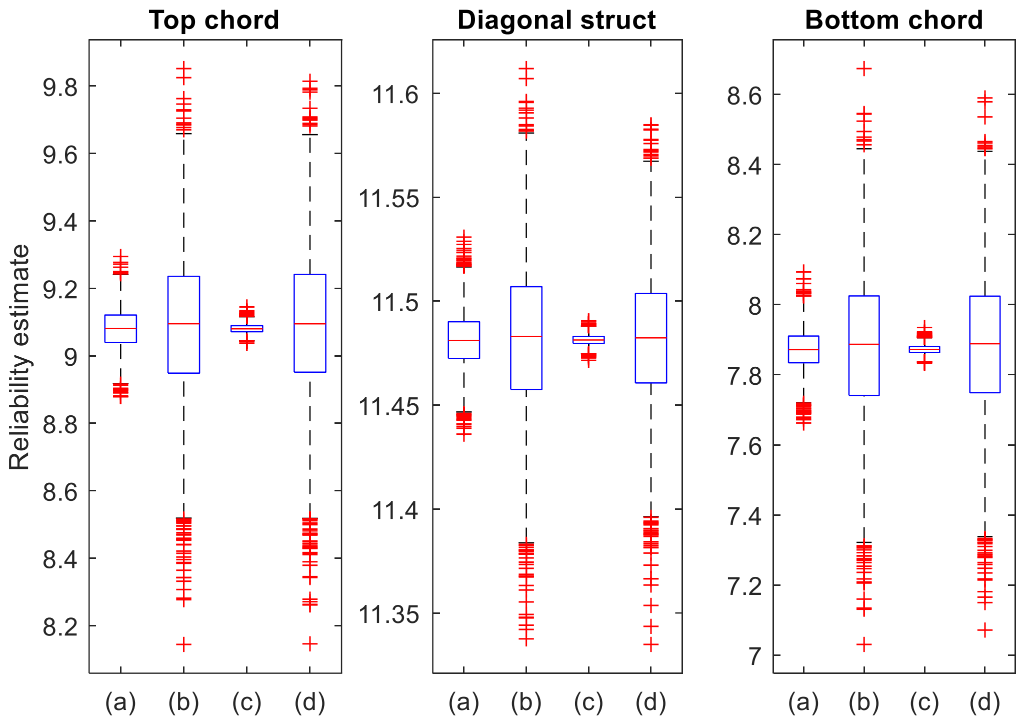

Figure 6.18 Influence of uncertain mixture parameters on reliability estimate: (a) uncertain μ; (b) uncertain σ^2; (c) uncertain ω; and (d) all uncertain

To further study the influence of individual uncertain component variance on the reliability estimate, another four cases are considered: (1) uncertain σ_1^2; (2) uncertain σ_2^2; (3) uncertain σ_3^2; and (4) uncertain σ_4^2 (for top and bottom chords). These four cases are compared with the case that all component variances are uncertain. As shown in Figure 6.19, it is observed that the uncertainty of reliability estimate is mainly due to the specific component variance that owns largest variation. In fact, as for top or bottom chord, it is found that there exists a small portion of peak stresses assigned to the 4th (or the 3rd) component, causing larger variation in the corresponding parameter estimation (larger 95% CIs of parameters). It consequently leads to a greater level of uncertainty (larger standard deviation) on the reliability estimate for top and bottom chords. However, this phenomenon is not evident for the estimated mixture model of diagonal strut.

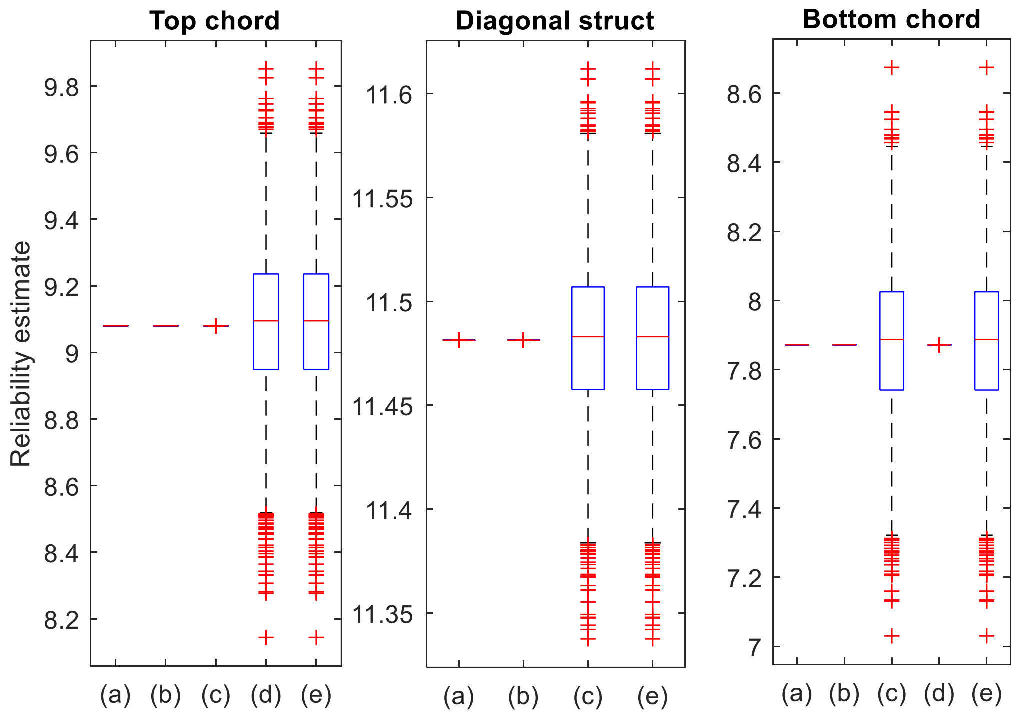

Figure 6.19 Influence of uncertain component variance on reliability estimate: (a) uncertain σ_1^2; (b) uncertain σ_2^2; (c) uncertain σ_3^2; (d) uncertain σ_4^2; and (e) all uncertain

6.5.3 Uncertainty Mitigation

Does the extent of uncertainty associated with the reliability estimate can be narrowed down? It has been reported that the epistemic uncertainty in reliability analysis can be possibly reduced by collecting additional observational data (Der Kiureghian, 2008). In the assessment of deck truss, we give illustrative examples to verify the statement.

Figure 6.20 shows the relationship between sample size of peak stress responses and the estimated reliability bounds. Through adjusting the peak counting strategy, i.e. increasing the sample size of the monthly representative peak stresses, an evident mitigation of the uncertainty of conditional reliability index is realized for both FGM-based and DPM-based analysis. Besides, the mean value has a slightly upward trend with the increase of sample size. It is seen that if monitoring data are insufficient, for example, when the sample size is less than 4000 as shown in Figure 6.20, the reliability estimates fluctuate with large uncertain bounds, yielding a misleading assessment to the structural performance. From the management authority's point of view, if the estimated uncertainty of reliability is unacceptable for decision-making, cost-effective actions should be taken to collect additional information to assist the bridge assessment. A compromise should be made between the cost of collecting additional data and the acceptability of uncertain level for the assessment.

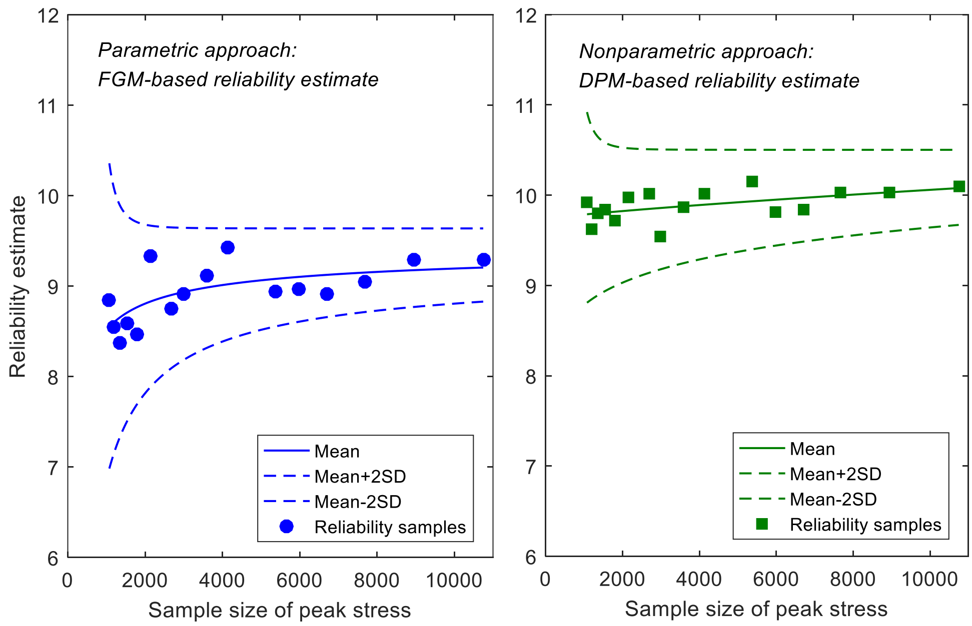

Figure 6.20 Relationship between sample size of peak stress and uncertainty of reliability estimate

Note that the DPM-based analysis is less sensitive to the change of sample size as against the FGM-based analysis as shown in Figure 6.20. The DPM-based reliability estimate retains relatively stable even when the monitoring data are insufficient. It attributes to the fact that the

DPM model with varying model order can avoid possible over- or under-fitting when there is lack of samples. However, the FGM model may suffer from this issue.

6.5.4 Continuous Reliability Updating

With continuous monitoring data, the conditional reliability index $\beta(\boldsymbol{\Theta})$ can be regularly updated to refine a more convincible assessment result for a given reference period. Assuming the samples of reliability estimate conform to the normal distribution $\beta \sim N(\mu_\beta, \sigma_\beta^2)$, a month-by-month reliability updating can be implemented by using the Bayesian theory

$$p(\beta_{\text{pred}}|\beta) = \iint p(\beta_{\text{pred}}|\mu_\beta, \sigma_\beta^2, \beta) p(\mu_\beta, \sigma_\beta^2|\beta)\, \mathrm{d}\mu_\beta \mathrm{d}\sigma_\beta^2 \tag{6.10}$$

where β_{pred} is defined as the predictive reliability index after obtaining monthly samples of conditional reliability index $\beta(\boldsymbol{\Theta})$, and $p(\mu_\beta, \sigma_\beta^2|\beta)$ is the posterior distribution of parameter which has the form of

$$p(\mu_\beta, \sigma_\beta^2|\beta) \propto p(\beta|\mu_\beta, \sigma_\beta^2) p(\mu_\beta, \sigma_\beta^2) \tag{6.11}$$

Assuming the normal-inverse-chi-squared prior for μ_β and σ_β^2, the Bayesian updating for conditional reliability index can be implemented in an explicit way (Gelman et al., 2014).

Figure 6.21 gives an example of the one-month reliability updating for the top chord. The predictive reliability index β_{pred} of February is obtained through updating the β_{pred} of January with newly obtained conditional reliability samples of February using Equations (6.10) and (6.11). Consequently, the assessment result based on the predictive reliability index is more convincible since it already incorporates both the information from January and February.

Following the same manner, month-by-month updating is implemented to pursue the assessment for a period of one-year for the top chord as illustrated in Figure 6.22. Note that there was a possible suspension of strain monitoring from February to March this year, which causes an insufficient number of peak stresses during this period as shown Figure 6.23. As recalled from the discussion about the relationship between sample size and reliability estimate, it is not surprising to see the lack of monitoring peak stress has noticeable impacts on the reliability updating as the mean values of β_{pred} drop and the standard deviations increase. In particular, this unexpected event has a great influence on the FGM-based analysis.

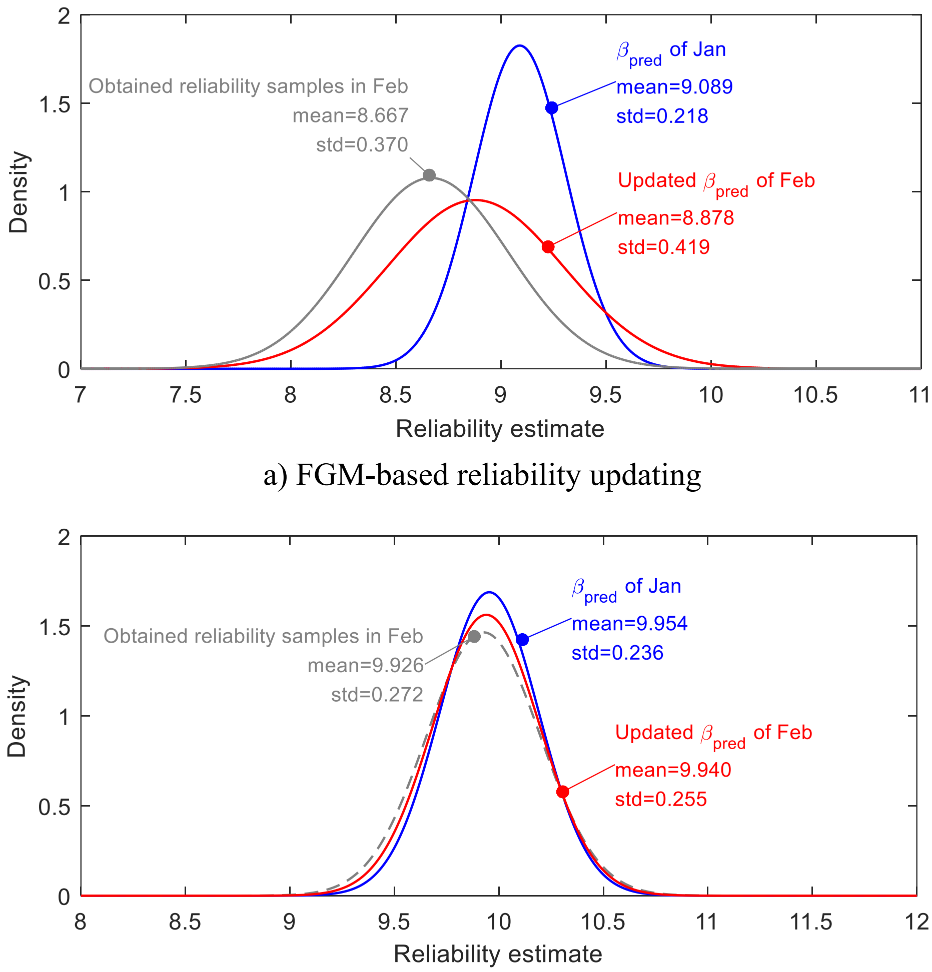

a) FGM-based reliability updating

b) DPM-based reliability updating

Figure 6.21 One-month reliability updating for top chord

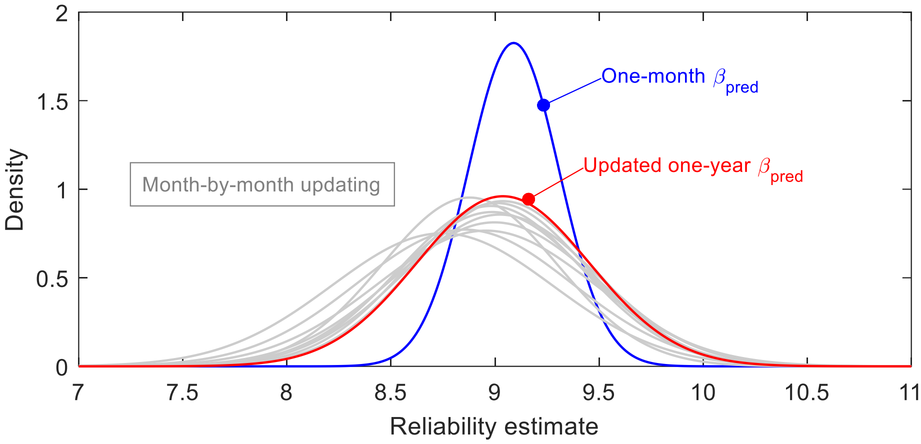

a) FGM-based reliability updating

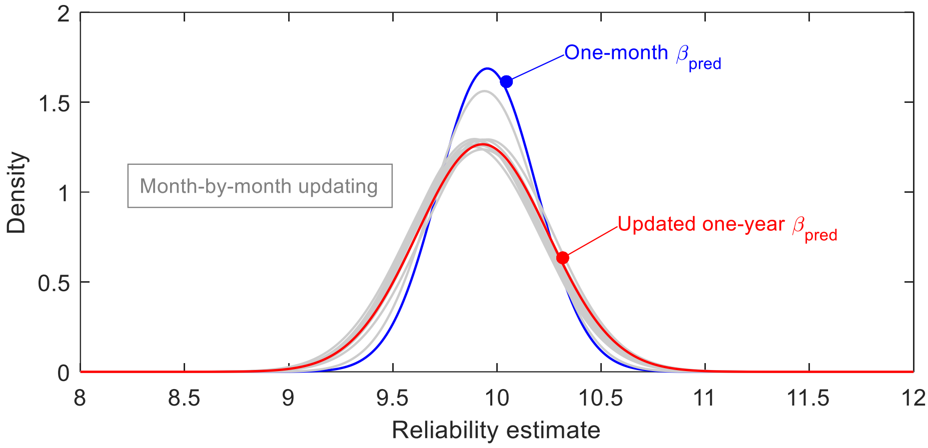

b) DPM-based reliability updating

Figure 6.22 One-year reliability updating for top chord

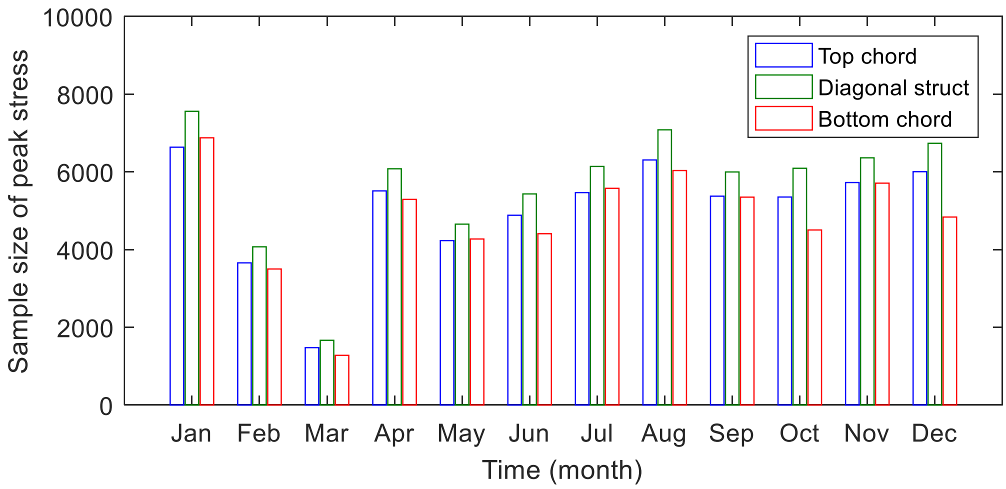

Figure 6.23 Sample size of peak stress used for reliability updating

One-year predictive reliability profiles of the deck truss are portrayed in Figure 6.24. According to the curves of mean value of the reliability estimate, the diagonal strut has the highest safety reserve, followed by the top chord, whereas the bottom chord owns the lowest safety reserve under the routine operation of the TMB. For the past one year, the predictive reliability profiles evolve over time with no sudden changes, indicating the deck truss is of satisfactory performance under the multi-load condition. Note that regular inspection is recommended for the bottom chord.

Uncertain bounds associated with the predictive reliability index give additional meaningful information for further decision making. For instance, the enlarged reliability bounds on February and March give a hint that additional manual inspection information might be needed to determine the structural behaviour during that specific period. From a practical point of view, bridge owners and engineers would first concern with the mean value of the reliability estimate to guarantee the good status of the structure; what follows is that an acceptable uncertain range on the reliability estimate would be preferred as it provides an extra confidence level to the assessment.

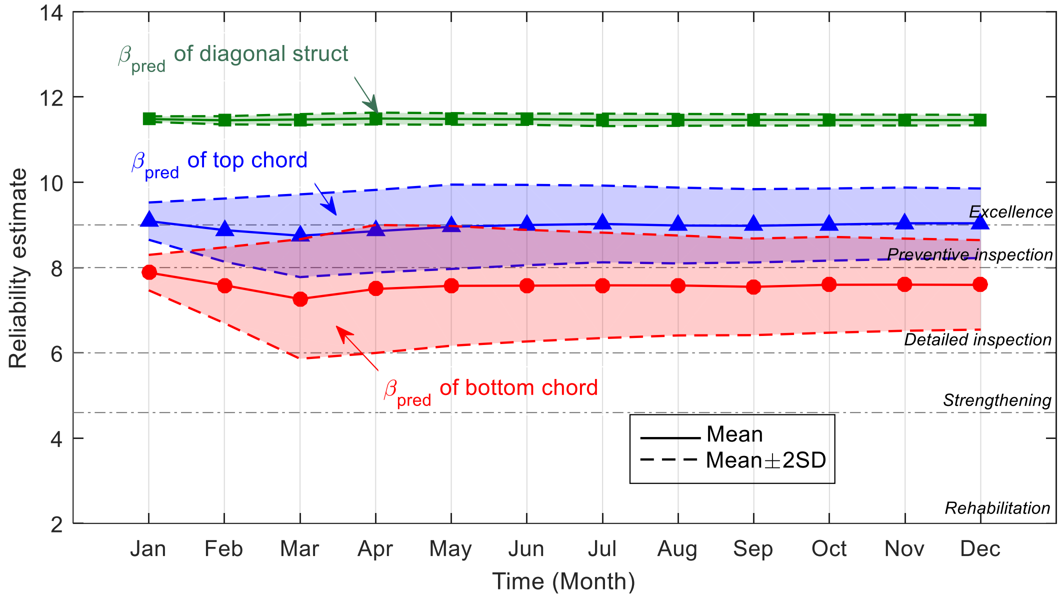

a) predictive reliability profile under parametric uncertainty

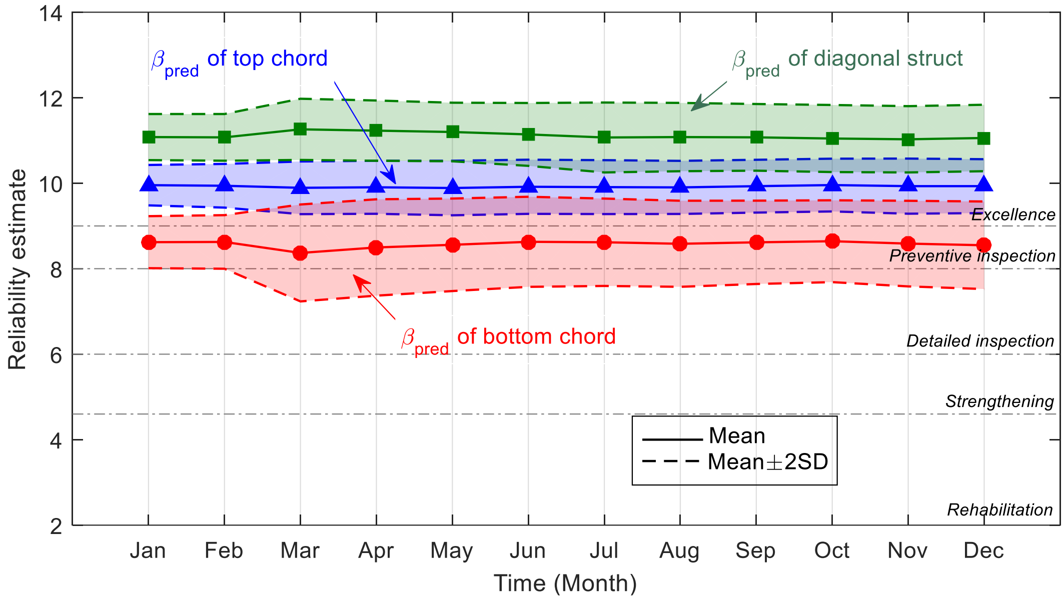

b) predictive reliability profile under model order and parametric uncertainties

Figure 6.24 Predictive reliability profiles under modelling uncertainties for deck truss

6.6 SUMMARY

Quantifying multi-level uncertainties in bridge condition assessment is of great desire. This chapter presents the application of Bayesian mixture models to reliability assessment of the long-span suspension bridge with consideration of the impacts from modelling uncertainties. A new conditional reliability index based on the FORM is formulated to account for modelling uncertainties arising from interpretation of the multimodal load effect. With consecutive monitoring data, the conditional reliability index is updated in a month-by-month manner to realise a more convincible assessment result. The key findings are summarised as follows.

(1) Through statistical analysis of the monitoring stress response, it is found that the peak stress of deck truss under multi-load condition has typical multimodal data characteristics, which are adequately captured by the Bayesian mixture models. Multiple stress levels, which stems from combined effect of highway traffic, railway traffic, and wind loads, are well discriminated and quantitatively identified by the mixture models.

(2) With the consideration of modelling uncertainties, the estimate of conditional reliability index is no longer a fixed value but a random variable that affected by the uncertain model parameters. Sensitivity analysis shows that variation of the estimated component variance has the dominated effect on the uncertainty of FGM-based reliability estimate. It further finds out that the reliability bounds can be mitigated by increasing the sample size of peak stress. There should be a balance between the cost of collecting additional monitoring data and the acceptability of uncertainty level of the assessment.

(3) Assessment results of the truss members from either FGM-based or DPM-based reliability analysis are consistent with each other, indicating both approaches are suitable for bridge reliability analysis under multi-load condition. Nevertheless, the DPM-based analysis outperforms the FGM-based counterpart in terms of less sensitive to the variation of

parameter estimation and sample size of the peak stress.

(4) Predictive reliability profiles over the monitoring period indicate that the deck truss is of satisfactory performance under the routine operation of the TMB. Regular inspection is recommended for the bottom chord. A clearer vision on the safety risk can be learnt by the management authorities through reporting not only the average structural reliability but also the extra associated uncertain level.

CHAPTER 7
CONCLUSIONS AND RECOMMENDATIONS

7.1 CONCLUSIONS

In-service long-span bridges are normally subject to multiple types of loadings such as highway traffic, railway traffic, wind and their combinations, resulting in heterogeneous and multimodal data characteristics. SHM-based methodology to assessment of the long-span bridge enables the quantification of substantial uncertainties in modelling the load effects, leading to a robust and predictive health measure of the structural condition. The thesis develops two classes of Bayesian mixture models for condition evaluation of the suspension Tsing Ma Bridge by making use of its long-term monitoring data with the capability to (1) accommodate multimodal structural responses due to multi-load, and (2) explicitly quantify the modelling uncertainties inherent in the monitoring data.

The thesis first develops the parametric Bayesian mixture model, i.e. the finite Gaussian mixture (FGM) model, to deal with the multimodal data with consideration of parametric uncertainty. The Gibbs sampler is devised to approximate the joint posterior of the mixture parameters with a quantitative convergence diagnosis strategy being used. Optimal model order is determined by a Bayes factor based approach. Numerical studies based on artificial data sets exemplify that the FGM model can adequately characterise the multimodal data in terms of fairly small model errors with promising convergence speed. Given the posterior samples obtained from the Gibbs simulation, the most plausible mixture parameters are conveniently obtained with associated uncertain bounds being explicitly quantified under the Bayesian framework. Damage detection of the Tsing Ma Bridge by making use of neutral axis position information is the goal pursued in this thesis. The sensitivities of changing loading distances, loading magnitudes, and traffic lanes on locating the neutral axis positions of a designated cross section are verified through a numerical study based on bridge FEM. Neutral axis positions under multi-lane stochastic traffic loads are identified using parametric Bayesian mixture model based on monitoring and simulated stress responses respectively. Postulated single- and multiple-damage cases on the bridge deck are effectively detected by the proposed two damage indexes based on neutral axis change. The nonparametric Bayesian mixture model, i.e. the Dirichlet process mixture (DPM) model, is subsequently developed to allow the model complexity automatically adapts to the observational data with the capability to jointly consider the parametric and model order uncertainties. To avoid low efficiency of direct sampling from the conditional posteriors, the collapsed Gibbs sampler is devised to pursue the posterior mixture density samples. An extended version of the quantitative convergence diagnosis strategy is proposed to assess the convergence of simulations. Given the posterior mixture density samples, quantification of both parametric and model order uncertainties is satisfactorily achieved through the nonparametric approach. With two Bayesian models at hand, the long-term reliability assessment of the Tsing Ma Bridge under modelling uncertainties is performed in this research. After the statistical analysis of raw signals, it finds out that stress responses under the combined effect of multi-load have typical multimodal data characteristics, which are adequately captured by either two Bayesian mixture models. Multiple stress levels, which stems from multiple loadings of highway traffic, railway traffic, wind and their combinations, are well discriminated and quantitatively identified by the mixture models. A new conditional reliability index is formulated based on first-order reliability method to account for the aleatory and epistemic uncertainties from multimodal stress responses. A sensitivity analysis of uncertain mixture parameters on reliability estimate is given. With consecutive monitoring data, the reliability index is updated in a month-by-month manner to refine a more convincible assessment result.

The important results and significant findings throughout the thesis are summarised as follows.

(1) Two classes of Bayesian mixture models along with the Markov chain Monte Carlo based inference tools developed in the thesis are well suited to characterise heterogeneous monitoring data with multimodality in viewing of accurate model fittings and fast convergence speed. Numerical studies suggest that the nonparametric model outperforms the parametric model in terms of better goodness-of-fit with lower computational demands. More importantly, the nonparametric approach stands as an improvement over the parametric counterpart that joint consideration of parametric and model order uncertainties can be achieved.

(2) Through statistical analysis of the monitoring raw signals, it is found that the peak stresses of the deck truss under multi-load have typical multimodal data characteristics, which are adequately captured by the Bayesian mixture models. Multiple stress levels, which stems

from combined effect of highway traffic, railway traffic, and wind loads, are well discriminated and quantitatively identified by the mixture models.

(3) Traffic-induced neutral axis position is insensitive to the change of loading magnitudes but heavily depends on the traffic lane in use. Stochastic highway and railway traffic on multiple lanes usually generate varying neutral axis position for a designated cross section over a given time period. Neutral axis position can only be adopted as a damage sensitive feature with its associated uncertainty being properly quantified. The proposed neutral axis position identification method based on the parametric Bayesian mixture model is able to accurately predict the mean values and associated uncertain ranges of the neutral axis position due to different traffic types. The identified neutral axis positions of the Tsing Ma Bridge based on monitoring stress responses keep relative stable under stochastic traffic loads.

(4) Simulation-based neutral axis positions over a time period are of high similarity to the results based on monitoring in terms of the daily trend of mean values and uncertain ranges. Results of case studies show that damage of local component could be detected by synchronous shifts of neutral axis (NA) change ratio of the neighbouring cross section. The cumulative NA change ratio triggers more convincible detection alerts under operational traffic condition when multiple damages occurred on the bridge deck. It has the potential to be a damage severity indicator.

(5) In the presence of modelling uncertainties, the estimate of conditional reliability index is no longer a fixed value but a random variable that affected by the uncertain mixture

parameters of the load effects. Sensitivity analysis shows that variability of the component variance has the dominated effect on the uncertainty range of FGM-based reliability estimate. It further finds out that the reliability bounds can be mitigated by increasing the sample size of peak stress. There should be a balance between the cost of collecting additional monitoring data and the acceptability of uncertainty level of the assessment.

(6) One-year reliability indexes of the truss members computed by either FGM-based or DPM-based analysis are consistent with each other, indicating both approaches are suitable for bridge reliability analysis under multi-load condition. Nevertheless, the DPM-based analysis outperforms the FGM-based counterpart in terms of less sensitive to the variation of parameter estimation and sample size of the peak stress. This is a desired property in SHM practice where monitoring data are sometimes unavailable due to malfunction of the system.

(7) Predictive reliability profiles over the one-year monitoring period indicate that the longitudinal truss is of satisfactory performance under the routine operation of the Tsing Ma Bridge. Regular inspection is recommended for the bottom chord where the reliability is lower. A clear vision on the safety risk can be learnt by management authorities through reporting not only the average structural reliability but also the extra associated uncertain level.

7.2 RECOMMENDATIONS

The present thesis covers two key topics, i.e. damage detection and reliability analysis, for current practice of monitoring-based condition assessment of long-span bridges under modelling uncertainties. Although some progress has been achieved in the finished studies, it is beneficial to discuss some remaining important issues that merit further research.

(1) Gaussian component/kernel density is employed in the Bayesian mixture models to realise analytical forms of full conditional posteriors for efficient MCMC simulations using Gibbs/collapsed Gibbs samplers. It is desired to develop other workable kernels such as lognormal, Weibull, Gumbel for mixture models in order to achieve more generalised settings. The Metropolis-Hastings sampler or variational Bayesian algorithms can be devised to pursue the mixture parameter estimation.

(2) The proposed damage detection method based on neutral axis position is able to detect local damage of the bridge deck under stochastic highway and railway traffic. However, wind load is a significant factor for normal operation of long-span bridge located in coastal region. Wind effect on bridges, which causes three-dimensional vibration of the bridge deck, will pose difficulties for accurate prediction of the neutral axis position. It is preferable to verify the feasibility of neutral axis based damage detection method under windy condition. Determination of a threshold of maximum wind speed to the success of damage detection is needed.

(3) Application scope of the proposed damage detection method will be extended if successful separation of wind-induced stress response from the monitoring signals can be achieved. A predictive model of the wind-induced stress response can be established by using the measured wind speed and direction on the bridge.

(4) More damage scenarios and different damage location should be properly considered. It is preferable to give a classification table for nearby structural members according to different damage-induced neutral axis shift directions. Sensitivity and reliability of the damage detection results should be evaluated in a quantitative way.

(5) Deterioration models of structural resistance and the associated uncertainties have not been fully considered in the present monitoring-based reliability assessment scheme. It is beneficial to conduct experimental study on long-term performance of steel or concrete structural members in order to learn the deterioration behaviours. Time-dependent reliability analysis can be realised by integrating the deterioration information in a coherent Bayesian framework.

REFERENCES

AASHTO. (2011). *The Manual for Bridge Evaluation*. Washington DC.

Aktan, A. E., Farhey, D. N., Brown, D. L., Dalal, V., Helmicki, A. J., Hunt, V. J., and Shelley, S. J. (1996). Condition assessment for bridge management. *Journal of Infrastructure Systems,* 2(3), 108-117.

Aktan, A. E., Farhey, D. N., Helmicki, A. J., Brown, D. L., Hunt, V. J., Lee, K.-L., and Levi, A. (1997). Structural identification for condition assessment: experimental arts. *Journal of Structural Engineering,* 123(12), 1674-1684.

Alvandi, A., and Cremona, C. (2006). Assessment of vibration-based damage identification techniques. *Journal of sound and vibration,* 292(1), 179-202.

Andersen, E. Y., and Pedersen, L. (1994). Structural monitoring of the Great Belt East Bridge. *Strait crossings,* 94, 189-195.

Antoniak, C. E. (1974). Mixtures of Dirichlet processes with applications to Bayesian nonparametric problems. *The annals of statistics,* 2(6), 1152-1174.

ASCE. (2017). *2017 Infrastructure Report Card*. Retrieved from https://www.infrastructurereportcard.org/cat-item/bridges/

Au, S. K. (2011). Fast Bayesian FFT method for ambient modal identification with separated modes. *Journal of Engineering Mechanics,* 137(3), 214-226.

Au, S. K., and Beck, J. L. (1999). A new adaptive importance sampling scheme for reliability calculations. *Structural Safety,* 21(2), 135-158.

Au, S. K., and Beck, J. L. (2001). Estimation of small failure probabilities in high dimensions by subset simulation. *Probabilistic engineering mechanics,* 16(4), 263-277.

Auld, B. A., and Moulder, J. C. (1999). Review of advances in quantitative eddy current nondestructive evaluation. *Journal of Nondestructive evaluation,* 18(1), 3-36.

Bagavathiappan, S., Lahiri, B. B., Saravanan, T., Philip, J., and Jayakumar, T. (2013). Infrared thermography for condition monitoring - a review. *Infrared Physics & Technology,* 60, 35-55.

Barrish, R. A., Grimmelsman, K. A., and Aktan, A. E. (2000). Instrumented monitoring of the Commodore Barry Bridge. *Proceedings of the Nondestructive Evaluation of Highways,* *Utilities, and Pipelines IV*, U.S.

Beck, J. L., and Au, S. K. (2002). Bayesian updating of structural models and reliability using Markov chain Monte Carlo simulation. *Journal of Engineering Mechanics,* 128(4), 380-391.

Beck, J. L., and Katafygiotis, L. S. (1998). Updating models and their uncertainties. I: Bayesian statistical framework. *Journal of Engineering Mechanics,* 124(4), 455-461.

Bhattacharya, B., Li, D., Chajes, M., and Hastings, J. (2005). Reliability-based load and resistance factor rating using in-service data. *Journal of Bridge Engineering,* 10(5), 530-543.

Bishop, C. M. (2006). *Pattern Recognition and Machine Learning*. New York: Springer.

Brooks, S. P., and Giudici, P. (2000). Markov chain Monte Carlo convergence assessment via two-way analysis of variance. *Journal of computational and graphical statistics,* 9(2), 266-285.

Brownjohn, J. M. W. (2007). Structural health monitoring of civil infrastructure. *Philosophical Transactions of the Royal Society A: Mathematical, Physical and Engineering Sciences,* 365(1851), 589-622.

Carden, E. P., and Fanning, P. (2004). Vibration based condition monitoring: a review. *Structural Health Monitoring,* 3(4), 355-377.

Cardini, A. J., and DeWolf, J. T. (2009). Long-term structural health monitoring of a multi-girder steel composite bridge using strain data. *Structural Health Monitoring,* 8(1), 47-58.

Catbas, F. N., and Aktan, A. E. (2002). Condition and damage assessment: issues and some promising indices. *Journal of Structural Engineering,* 128(8), 1026-1036.

Catbas, F. N., Susoy, M., and Frangopol, D. M. (2008). Structural health monitoring and reliability estimation: long span truss bridge application with environmental monitoring data. *Engineering Structures,* 30(9), 2347-2359.

Celeux, G., Forbes, F., Robert, C. P., and Titterington, D. M. (2006). Deviance information criteria for missing data models. *Bayesian analysis,* 1(4), 651-673.

Chakraborty, S., and DeWolf, J. T. (2006). Development and implementation of a continuous strain monitoring system on a multi-girder composite steel bridge. *Journal of Bridge Engineering,* 11(6), 753-762.

Chatterjee, S. (2008). *The Design of Modern Steel Bridges*. Oxford: Blackwell Science.

Chen, S. Z., Wu, G., and Feng, D. C. (2019). Damage detection of highway bridges based on long-gauge strain response under stochastic traffic flow. *Mechanical Systems and Signal Processing,* 127, 551-572.

Chen, Z. W., Cai, Q. L., and Li, J. (2016). Stress influence line identification of long suspension bridges installed with structural health monitoring systems. *International Journal of Structural Stability and Dynamics,* 16(04), 1640023.

Chen, Z. W., Zhu, S., Xu, Y. L., Li, Q., and Cai, Q. L. (2014). Damage detection in long suspension bridges using stress influence lines. *Journal of Bridge Engineering,* 20(3), 05014013.

Chib, S. (1995). Marginal likelihood from the Gibbs output. *Journal of the american statistical association,* 90(432), 1313-1321.

China Daily. (2019). 2 MTR trains collide in HK during system trial run. *China Daily*. Retrieved from https://www.chinadailyhk.com/articles/220/122/206/1552872858125.html?newsId=64912

Dempster, A. P., Laird, N. M., and Rubin, D. B. (1977). Maximum likelihood from incomplete data via the EM algorithm. *Journal of the Royal Statistical Society: series B (statistical methodology),* 39(1), 1-38.

Der Kiureghian, A. (1989). Measures of structural safety under imperfect states of knowledge. *Journal of Structural Engineering,* 115(5), 1119-1140.

Der Kiureghian, A. (1991). Bayesian analysis of model uncertainty in structural reliability. In *Reliability and Optimization of Structural Systems' 90* (pp. 211-221): Springer.

Der Kiureghian, A. (2008). Analysis of structural reliability under parameter uncertainties. *Probabilistic engineering mechanics,* 23(4), 351-358.

Der Kiureghian, A., and Ditlevsen, O. (2009). Aleatory or epistemic? Does it matter? *Structural Safety,* 31(2), 105-112.

Deraemaeker, A., Reynders, E., De Roeck, G., and Kullaa, J. (2008). Vibration-based structural health monitoring using output-only measurements under changing environment. *Mechanical Systems and Signal Processing,* 22(1), 34-56.

Diebolt, J., and Robert, C. P. (1994). Estimation of finite mixture distributions through Bayesian sampling. *Journal of the Royal Statistical Society: series B (statistical methodology),* 56(2), 363-375.

Doebling, S. W., Farrar, C. R., and Prime, M. B. (1998). A summary review of vibration-based damage identification methods. *Shock and vibration digest,* 30(2), 91-105.

Drinkwater, B. W., and Wilcox, P. D. (2006). Ultrasonic arrays for non-destructive evaluation: A review. *NDT & e International,* 39(7), 525-541.

Elhelbawey, M., Fu, C. C., Sahin, M., and Schelling, D. R. (1999). Determination of slab participation from weigh-in-motion bridge testing. *Journal of Bridge Engineering,* 4(3), 165-173.

Ellingwood, B. R. (1996). Reliability-based condition assessment and LRFD for existing structures. *Structural Safety,* 18(2), 67-80.

Ellingwood, B. R., and Kinali, K. (2009). Quantifying and communicating uncertainty in seismic risk assessment. *Structural Safety,* 31(2), 179-187.

Enevoldsen, I. (2011). Practical implementation of probability based assessment methods for bridges. *Structure and Infrastructure Engineering,* 7(7-8), 535-549.

Enright, B., and OBrien, E. J. (2013). Monte Carlo simulation of extreme traffic loading on short and medium span bridges. *Structure and Infrastructure Engineering,* 9(12), 1267-1282.

Enright, M. P., and Frangopol, D. M. (1998). Service-life prediction of deteriorating concrete bridges. *Journal of Structural Engineering,* 124(3), 309-317.

Enright, M. P., and Frangopol, D. M. (1999a). Condition prediction of deteriorating concrete bridges using Bayesian updating. *Journal of Structural Engineering,* 125(10), 1118-1125.

Enright, M. P., and Frangopol, D. M. (1999b). Reliability-based condition assessment of deteriorating concrete bridges considering load redistribution. *Structural Safety,* 21(2), 159-195.

Escobar, M. D., and West, M. (1995). Bayesian density estimation and inference using mixtures. *Journal of the american statistical association,* 90(430), 577-588.

Fan, W., and Qiao, P. (2011). Vibration-based damage identification methods: a review and comparative study. *Structural Health Monitoring,* 10(1), 83-111.

Farhidzadeh, A., Salamone, S., and Singla, P. (2013). A probabilistic approach for damage identification and crack mode classification in reinforced concrete structures. *Journal of Intelligent Material Systems and Structures,* 24(14), 1722-1735.

Farrar, C. R., Baker, W., Bell, T., Cone, K., Darling, T., Duffey, T., Eklund, A., and Migliori, A. (1994). *Dynamic Characterization and Damage Detection in the I-40 Bridge over the Rio Grande*. Retrieved from New Mexcico:

Farrar, C. R., Doebling, S. W., and Nix, D. A. (2001). Vibration-based structural damage identification. *Philosophical Transactions of the Royal Society A: Mathematical, Physical and Engineering Sciences,* 359(1778), 131-149.

Ferguson, T. S. (1973). A Bayesian analysis of some nonparametric problems. *The annals of statistics,* 1(2), 209-230.

Ferguson, T. S. (1983). Bayesian density estimation by mixtures of normal distributions. In Rizvi, M. H., Rustagi, J. S., and Siegmund, D. (Eds.), *Recent Advances in Statistics* (pp. 287-302): Academic Press.

FHWA. (2012). *Bridge Inspector's Reference Manual*. Washington DC.

Figueiredo, E., Radu, L., Worden, K., and Farrar, C. R. (2014). A Bayesian approach based on a Markov-chain Monte Carlo method for damage detection under unknown sources of variability. *Engineering Structures,* 80, 1-10.

Frangopol, D. M., Strauss, A., and Kim, S. (2008). Bridge reliability assessment based on monitoring. *Journal of Bridge Engineering,* 13(3), 258-270.

Frühwirth-Schnatter, S. (2006). *Finite Mixture and Markov Switching Models*. New York: Springer Science & Business Media.

Fujino, Y., and Siringoringo, D. M. (2011). Bridge monitoring in Japan: the needs and strategies. *Structure and Infrastructure Engineering,* 7(7-8), 597-611.

Garbatov, Y., and Soares, C. G. (2002). Bayesian updating in the reliability assessment of maintained floating structures. *Journal of Offshore Mechanics and Arctic Engineering,* 124(3), 139-145.

Gelman, A., Carlin, J. B., Stern, H. S., Dunson, D. B., Vehtari, A., and Rubin, D. B. (2014). *Bayesian Data Analysis* (third ed.). New York: CRC Press.

Gelman, A., and Rubin, D. B. (1992). Inference from iterative simulation using multiple sequences. *Statistical Science,* 7(4), 457-472.

Gershman, S. J., and Blei, D. M. (2012). A tutorial on Bayesian nonparametric models. *Journal of Mathematical Psychology,* 56(1), 1-12.

Ghosal, S., and Van der Vaart, A. (2017). *Fundamentals of Nonparametric Bayesian Inference*. Cambridge: Cambridge University Press.

Goller, B., and Schueller, G. I. (2011). Investigation of model uncertainties in Bayesian structural model updating. *Journal of sound and vibration,* 330(25), 6122-6136.

He, W. Y., Ren, W. X., and Zhu, S. (2017). Damage detection of beam structures using quasi-static moving load induced displacement response. *Engineering Structures,* 145, 70-82.

Heylen, W., Lammens, S., and Sas, P. (1997). *Modal Analysis Theory and Testing* (Vol. 200). Leuven, Belgium: Katholieke Universiteit Leuven.

Hjelmstad, K. D., and Shin, S. (1997). Damage detection and assessment of structures from static response. *Journal of Engineering Mechanics,* 123(6), 568-576.

Hosser, D., Klinzmann, C., and Schnetgöke, R. (2008). A framework for reliability-based system assessment based on structural health monitoring. *Structure and Infrastructure Engineering,* 4(4), 271-285.

Hua, X. G., Ni, Y. Q., Chen, Z. Q., and Ko, J. M. (2009). Structural damage detection of cable-stayed bridges using changes in cable forces and model updating. *Journal of Structural Engineering,* 135(9), 1093-1106.

Huang, R., Yu, G., Wang, Z., Zhang, J., and Shi, L. (2012). Dirichlet process mixture model for document clustering with feature partition. *IEEE Transactions on knowledge and data engineering,* 25(8), 1748-1759.

ICE. (2018). *State of the Nation 2018: Infrastructure Investment*. Retrieved from https://www.ice.org.uk/news-and-insight/the-infrastructure-blog/october-2018/state-of-the-nation-2018-investment

Igusa, T., Buonopane, S. G., and Ellingwood, B. R. (2002). Bayesian analysis of uncertainty for structural engineering applications. *Structural Safety,* 24(2), 165-186.

Imai, K., and Frangopol, D. M. (2001). Reliability-based assessment of suspension bridges: application to the Innoshima Bridge. *Journal of Bridge Engineering,* 6(6), 398-411.

Kashima, S., Yanaka, Y., Suzuki, S., and Mori, K. (2001). Monitoring the Akashi Kaikyo Bridge: first experiences. *Structural engineering international,* 11(2), 120-123.

Katafygiotis, L. S., and Beck, J. L. (1998). Updating models and their uncertainties. II: model identifiability. *Journal of Engineering Mechanics,* 124(4), 463-467.

Katafygiotis, L. S., Papadimitriou, C., and Lam, H. F. (1998). A probabilistic approach to structural model updating. *Soil Dynamics and Earthquake Engineering,* 17(7), 495-507.

Ko, J. M., and Ni, Y. Q. (2005). Technology developments in structural health monitoring of large-scale bridges. *Engineering Structures,* 27(12), 1715-1725.

Koo, K.-Y., Brownjohn, J. M. W., List, D., and Cole, R. (2013). Structural health monitoring of the Tamar suspension bridge. *Structural Control and Health Monitoring,* 20(4), 609-625.

Lam, H. F., Peng, H. Y., and Au, S. K. (2014). Development of a practical algorithm for Bayesian model updating of a coupled slab system utilizing field test data. *Engineering*

Structures, 79, 182-194.

Lau, S., Lee, D., and Leung, C. (2015). Barge that struck and sparked traffic chaos on key bridge linking to Hong Kong airport 'breached height limits'. *South China Morning Post*. Retrieved from https://www.scmp.com/news/hong-kong/economy/article/1871482/hong-kong-traffic-chaos-tsing-ma-bridge-closes-leaving

Lavine, M., and West, M. (1992). A Bayesian method for classification and discrimination. *Canadian Journal of Statistics,* 20(4), 451-461.

Legislative Council of the HKSAR. (2015). Emergency closure of Kap Shui Mun Bridge [Press release]. Retrieved from https://www.info.gov.hk/gia/general/201511/11/P201511110551.htm

Li, H., Li, S. L., Ou, J. P., and Li, H. W. (2012a). Reliability assessment of cable-stayed bridges based on structural health monitoring techniques. *Structure and Infrastructure Engineering,* 8(9), 829-845.

Li, J., and Hao, H. (2015). Damage detection of shear connectors under moving loads with relative displacement measurements. *Mechanical Systems and Signal Processing,* 60, 124-150.

Li, J., and Hao, H. (2016). A review of recent research advances on structural health monitoring in Western Australia. *Structural Monitoring and Maintenance,* 3(1), 33-49.

Li, S., Zhu, S., Xu, Y. L., Chen, Z. W., and Li, H. (2012b). Long‐term condition assessment of suspenders under traffic loads based on structural monitoring system: application to the Tsing Ma Bridge. *Structural Control and Health Monitoring,* 19(1), 82-101.

Liu, J., Beyca, O. F., Rao, P. K., Kong, Z., and Bukkapatnam, S. T. S. (2017). Dirichlet process Gaussian mixture models for real-time monitoring and their application to chemical mechanical planarization. *IEEE Transactions on Automation Science and Engineering,* 14(1), 208-221.

Liu, M., Frangopol, D. M., and Kim, S. (2009a). Bridge safety evaluation based on monitored live load effects. *Journal of Bridge Engineering,* 14(4), 257-269.

Liu, M., Frangopol, D. M., and Kim, S. (2009b). Bridge system performance assessment from structural health monitoring: a case study. *Journal of Structural Engineering,* 135(6), 733-742.

Lo, A. Y. (1984). On a class of Bayesian nonparametric estimates: I. density estimates. *The annals of statistics,* 12(1), 351-357.

Mahadevan, S., Zhang, R. X., and Smith, N. (2001). Bayesian networks for system reliability reassessment. *Structural Safety,* 23(3), 231-251.

Maia, N., Silva, J., Almas, E., and Sampaio, R. (2003). Damage detection in structures: from mode shape to frequency response function methods. *Mechanical Systems and Signal Processing,* 17(3), 489-498.

Massey Jr, F. J. (1951). The Kolmogorov-Smirnov test for goodness of fit. *Journal of the american statistical association,* 46(253), 68-78.

McCann, D., and Forde, M. (2001). Review of NDT methods in the assessment of concrete and masonry structures. *NDT & e International,* 34(2), 71-84.

McGrory, C. A., and Titterington, D. (2007). Variational approximations in Bayesian model selection for finite mixture distributions. *Computational Statistics & Data Analysis,* 51(11), 5352-5367.

McLachlan, G., and Peel, D. (2000). *Finite Mixture Models*. New York: John Wiley & Sons.

Melchers, R. E., and Beck, A. T. (2017). *Structural Reliability Analysis and Prediction* (3rd ed.). Hoboken: John Wiley & Sons.

Messervey, T. B., Frangopol, D. M., and Casciati, S. (2011). Application of the statistics of extremes to the reliability assessment and performance prediction of monitored highway bridges. *Structure and Infrastructure Engineering,* 7(1-2), 87-99.

Ministry of Transport of the People's Republic of China. (2011). *Specification for Inspection and Evaluation of Load-bearing Capacity of Highway Bridges*. Beijing.

Mokhtarian, P., Namazi-Rad, M.-R., Ho, T. K., and Suesse, T. (2013). Bayesian nonparametric reliability analysis for a railway system at component level. *Proceedings of the IEEE International Conference on Intelligent Rail Transportation (ICIRT)*, Beijing, China.

Mori, Y., and Ellingwood, B. R. (1993). Reliability-based service-life assessment of aging concrete structures. *Journal of Structural Engineering,* 119(5), 1600-1621.

Nair, K. K., and Kiremidjian, A. S. (2006). Time series based structural damage detection algorithm using Gaussian mixtures modeling. *Journal of Dynamic Systems, Measurement, and Control,* 129(3), 285-293.

Neal, R. M. (2000). Markov chain sampling methods for Dirichlet process mixture models. *Journal of computational and graphical statistics,* 9(2), 249-265.

Ni, Y. Q., and Chen, R. (2016). Bayesian approach for mixture modelling of stress response data. *Proceedings of the 2016 International Conference on Advances in Structural Monitoring and Maintenance*, Jeju, Korea.

Ni, Y. Q., Wong, K. Y., and Xia, Y. (2011a). Health checks through landmark bridges to sky-high structures. *Advances in Structural Engineering,* 14(1), 103-119.

Ni, Y. Q., Xia, H. W., Wong, K. Y., and Ko, J. M. (2011b). In-service condition assessment of bridge deck using long-term monitoring data of strain response. *Journal of Bridge Engineering,* 17(6), 876-885.

Ni, Y. Q., Xia, H. W., and Ye, X. W. (2012). Neutral-axis position based damage detection of bridge deck using strain measurement: numerical and experimental verifications. *Proceedings of the 6th European Workshop on Structural Health Monitoring*, Dresden, Germany.

Ni, Y. Q., Xia, Y., Liao, W. Y., and Ko, J. M. (2009). Technology innovation in developing the structural health monitoring system for Guangzhou New TV Tower. *Structural Control and Health Monitoring,* 16(1), 73-98.

Ni, Y. Q., Ye, X. W., and Ko, J. M. (2010). Monitoring-based fatigue reliability assessment of steel bridges: analytical model and application. *Journal of Structural Engineering,* 136(12), 1563-1573.

Ni, Y. Q., Ye, X. W., and Ko, J. M. (2011c). Modeling of stress spectrum using long-term monitoring data and finite mixture distributions. *Journal of Engineering Mechanics,* 138(2), 175-183.

Nichols, J. M., Link, W. A., Murphy, K. D., and Olson, C. C. (2010). A Bayesian approach to identifying structural nonlinearity using free-decay response: application to damage detection in composites. *Journal of sound and vibration,* 329(15), 2995-3007.

Okasha, N. M., Frangopol, D. M., and Orcesi, A. D. (2012). Automated finite element updating using strain data for the lifetime reliability assessment of bridges. *Reliability Engineering & System Safety,* 99, 139-150.

Orbanz, P., and Buhmann, J. M. (2008). Nonparametric Bayesian image segmentation. *International Journal of Computer Vision,* 77(1-3), 25-45.

Orbanz, P., and Teh, Y. W. (2010). Bayesian nonparametric models. In Sammut, C. and Webb, G. I. (Eds.), *Encyclopedia of Machine Learning* (pp. 81-89). Boston, MA: Springer.

Ou, J. P., and Li, H. (2010). Structural health monitoring in mainland China: review and future trends. *Structural Health Monitoring,* 9(3), 219-231.

Pandey, A., and Biswas, M. (1994). Damage detection in structures using changes in flexibility. *Journal of sound and vibration,* 169(1), 3-17.

Papadimitriou, C., Beck, J. L., and Katafygiotis, L. S. (2001). Updating robust reliability using structural test data. *Probabilistic engineering mechanics,* 16(2), 103-113.

Park, B. J., Zhang, Y., and Lord, D. (2010). Bayesian mixture modeling approach to account for heterogeneity in speed data. *Transportation research part B: methodological,* 44(5), 662-673.

Peeters, B., and De Roeck, G. (2001). One-year monitoring of the Z24-Bridge: environmental effects versus damage events. *Earthquake engineering & structural dynamics,* 30(2), 149-171.

Pines, D., and Aktan, A. E. (2002). Status of structural health monitoring of long - span bridges in the United States. *Progress in Structural Engineering and materials,* 4(4), 372-380.

Qiu, L., Yuan, S. F., and Boller, C. (2017). An adaptive guided wave-Gaussian mixture model for damage monitoring under time-varying conditions: Validation in a full-scale aircraft fatigue test. *Structural Health Monitoring*, 1475921717692571.

Qiu, L., Yuan, S. F., Chang, F. K., Bao, Q., and Mei, H. F. (2014). On-line updating Gaussian mixture model for aircraft wing spar damage evaluation under time-varying boundary condition. *Smart Materials and Structures,* 23(12), 1-14.

Rafiq, M. I., Chryssanthopoulos, M. K., and Sathananthan, S. (2015). Bridge condition modelling and prediction using dynamic Bayesian belief networks. *Structure and Infrastructure Engineering,* 11(1), 38-50.

Richardson, S., and Green, P. J. (1997). On Bayesian analysis of mixtures with an unknown number of components (with discussion). *Journal of the Royal Statistical Society: series B (statistical methodology),* 59(4), 731-792.

Robert, C. P., and Casella, G. (1999). *Monte Carlo Statistical Methods*. New York: Springer-Verlag, New York.

Rogers, T. J., Worden, K., Fuentes, R., Dervilis, N., Tygesen, U. T., and Cross, E. (2019). A Bayesian non-parametric clustering approach for semi-supervised structural health monitoring. *Mechanical Systems and Signal Processing,* 119, 100-119.

Salawu, O. (1997). Detection of structural damage through changes in frequency: a review. *Engineering Structures,* 19(9), 718-723.

Sanayei, M., and Onipede, O. (1991). Damage assessment of structures using static test data. *AIAA Journal,* 29(7), 1174-1179.

Saydam, D., and Frangopol, D. M. (2013). Applicability of simple expressions for bridge system reliability assessment. *Computers & Structures,* 114, 59-71.

Sethuraman, J. (1994). A constructive definition of Dirichlet priors. *Statistica sinica*(4), 639-650.

Shi, Z., Law, S., and Zhang, L. (1998). Structural damage localization from modal strain energy change. *Journal of sound and vibration,* 218(5), 825-844.

Sigurdardottir, D. H., and Glisic, B. (2013). Neutral axis as damage sensitive feature. *Smart Materials and Structures,* 22(7), 075030.

Sigurdardottir, D. H., and Glisic, B. (2014). Detecting minute damage in beam-like structures using the neutral axis location. *Smart Materials and Structures,* 23(12), 125042.

Sigurdardottir, D. H., and Glisic, B. (2015). The neutral axis location for structural health monitoring: an overview. *Journal of Civil Structural Health Monitoring,* 5(5), 703-713.

Sohn, H. (2006). Effects of environmental and operational variability on structural health monitoring. *Philosophical Transactions of the Royal Society A: Mathematical, Physical and Engineering Sciences,* 365(1851), 539-560.

Sohn, H., Farrar, C. R., Hemez, F. M., Shunk, D. D., Stinemates, D. W., Nadler, B. R., and Czarnecki, J. J. (2003). *A Review of Structural Health Monitoring Literature: 1996–2001*. Retrieved from New Mexcico:

Sohn, H., and Law, K. H. (1997). A Bayesian probabilistic approach for structure damage detection. *Earthquake engineering & structural dynamics,* 26(12), 1259-1281.

Sohn, H., and Law, K. H. (2000). Bayesian probabilistic damage detection of a reinforced ‐ concrete bridge column. *Earthquake engineering & structural dynamics,* 29(8), 1131-1152.

Soman, R., Malinowski, P., and Ostachowicz, W. (2016). Bi ‐ axial neutral axis tracking for damage detection in wind ‐ turbine towers. *Wind Energy,* 19(4), 639-650.

Straub, D., and Der Kiureghian, A. (2010a). Bayesian network enhanced with structural reliability methods: application. *Journal of Engineering Mechanics,* 136(10), 1259-1270.

Straub, D., and Der Kiureghian, A. (2010b). Bayesian network enhanced with structural reliability methods: methodology. *Journal of Engineering Mechanics,* 136(10), 1248-1258.

Strauss, A., Frangopol, D. M., and Kim, S. (2008). Use of monitoring extreme data for the performance prediction of structures: Bayesian updating. *Engineering Structures,* 30(12), 3654-3666.

Teh, Y. W. (2011). Dirichlet process. In Sammut, C. and Webb, G. I. (Eds.), *Encyclopedia of Machine Learning* (pp. 280-287). Boston, MA: Springer.

The Highways Agency. (2017). *Design Manual for Roads and Bridges: Volume 3 Highway*

Structures: Inspection and Maintenance. London.

Tsang, D., Lam, J., and Yau, C. (2019). Hong Kong MTR, hit by train collision, suffers second setback as woman falls on tracks at Kowloon Tong. *South China Morning Post*. Retrieved from https://www.scmp.com/news/hong-kong/article/3002089/hong-kong-mtr-trains-collide-near-central-station

Turer, A., Levi, A., and Aktan, A. E. (1998). *Instrumentation, Proof-testing and Monitoring of Three Reinforced Concrete Deck-on-Steel Girder Bridges Prior to During, and After Superload*. Cincinnati: Cincinnati Infrastructure Institute.

Vanik, M. W., Beck, J. L., and Au, S. K. (2000). Bayesian probabilistic approach to structural health monitoring. *Journal of Engineering Mechanics,* 126(7), 738-745.

Wang, H., Li, A., Guo, T., and Tao, T. (2014). Establishment and application of the wind and structural health monitoring system for the Runyang Yangtze River Bridge. *Shock and Vibration,* 2014.

Wang, J. Y., Ko, J. M., and Ni, Y. Q. (2000). Modal sensitivity analysis of Tsing Ma Bridge for structural damage detection. *Proceedings of the SPIE 5th International Symposium on Nondestructive Evaluation and Health Monitoring of Aging Infrastructure*, Newport Beach, U.S.

Wong, K. Y. (2004). Instrumentation and health monitoring of cable - supported bridges. *Structural Control and Health Monitoring,* 11(2), 91-124.

Wong, K. Y. (2006). Criticality and vulnerability analyses of Tsing Ma Bridge. *Proceedings of the International Conference on Bridge Engineering - Challenges in the 21st Century*, Hong Kong.

Wong, K. Y. (2007). Stress and traffic loads monitoring of Tsing Ma Bridge. *Proceedings of the China Bridge Congress 2007*, Chongqing, China.

Xia, H. W., Ni, Y. Q., Wong, K. Y., and Ko, J. M. (2012a). Reliability-based condition assessment of in-service bridges using mixture distribution models. *Computers & Structures,* 106, 204-213.

Xia, H. W., Ni, Y. Q., and Ye, X. W. (2012b). Neutral-axis position based damage detection of bridge deck using strain measurement: formulation of a Kalman filter estimator. *Proceedings of the 6th European Workshop on Structural Health Monitoring*, Dresden, Germany.

Xia, Y., Chen, B., Weng, S., Ni, Y. Q., and Xu, Y. L. (2012c). Temperature effect on vibration properties of civil structures: a literature review and case studies. *Journal of Civil Structural Health Monitoring,* 2(1), 29-46.

Xia, Y., Wang, P., and Sun, L. (2018). Neutral axis based health monitoring and condition assessment techniques for concrete box girder bridges. *International Journal of Structural Stability and Dynamics,* 19(1), 1940015.

Xu, Y. L., and Xia, Y. (2011). *Structural Health Monitoring of Long-Span Suspension Bridges*. London: CRC Press.

Yuen, K. V. (2010). *Bayesian Methods for Structural Dynamics and Civil Engineering*. Singapore: John Wiley & Sons.

Yuen, K. V., and Mu, H. Q. (2015). Real‐time system identification: an algorithm for simultaneous model class selection and parametric identification. *Computer‐Aided Civil and Infrastructure Engineering,* 30(10), 785-801.

Yun, C.-B., Lee, J.-J., Kim, S.-K., and Kim, J.-W. (2003). Recent R&D activities on structural health monitoring for civil infra-structures in Korea. *KSCE Journal of Civil Engineering,* 7(6), 637-651.

Zaurin, R., and Catbas, F. N. (2009). Integration of computer imaging and sensor data for structural health monitoring of bridges. *Smart Materials and Structures,* 19(1), 015019.

Zhang, E. L., Feissel, P., and Antoni, J. (2011). A comprehensive Bayesian approach for model updating and quantification of modeling errors. *Probabilistic engineering mechanics,* 26(4), 550-560.

Zhang, R. X., and Mahadevan, S. (2000). Model uncertainty and Bayesian updating in reliability-based inspection. *Structural Safety,* 22(2), 145-160.

Zhao, L., and Shenton III, H. W. (2005). Structural damage detection using best approximated dead load redistribution. *Structural Health Monitoring,* 4(4), 319-339.

Zheng, R., and Ellingwood, B. R. (1998). Role of non-destructive evaluation in time-dependent reliability analysis. *Structural Safety,* 20(4), 325-339.

Zhu, B., and Frangopol, D. M. (2013). Reliability assessment of ship structures using Bayesian updating. *Engineering Structures,* 56, 1836-1847.

APPENDIX

Peak stress histograms of 2006: top chord

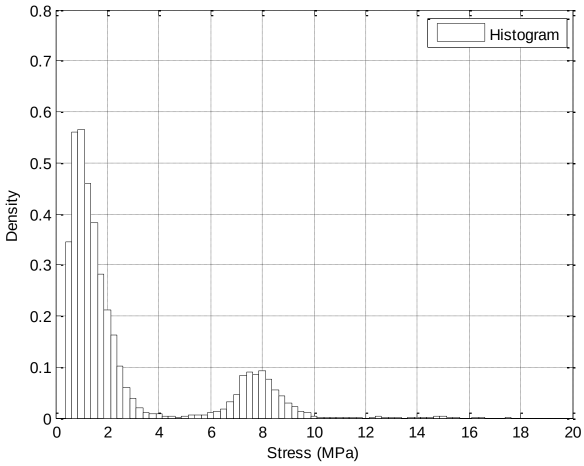

January

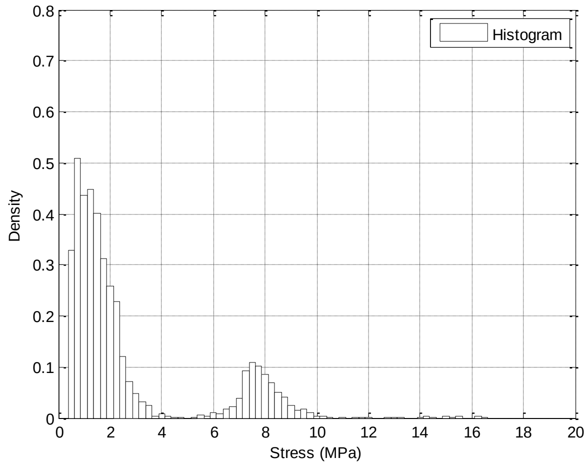

February

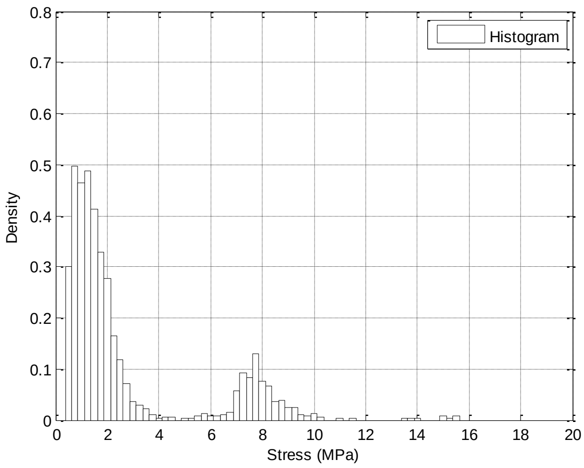

March

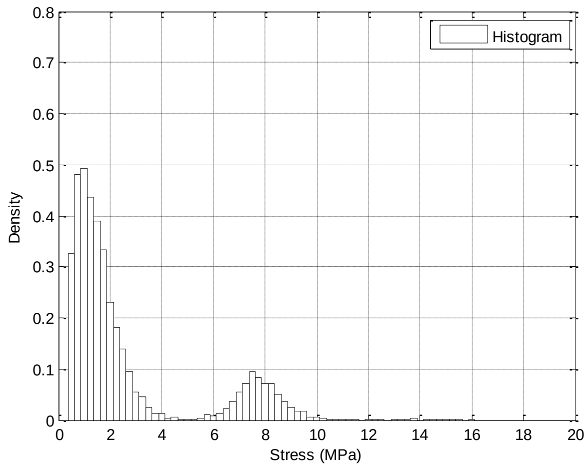

April

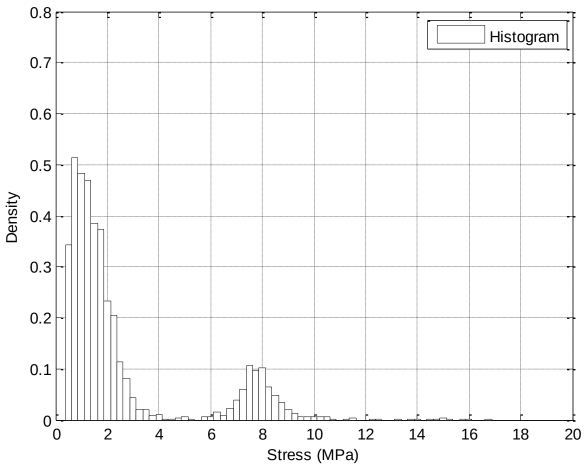

May

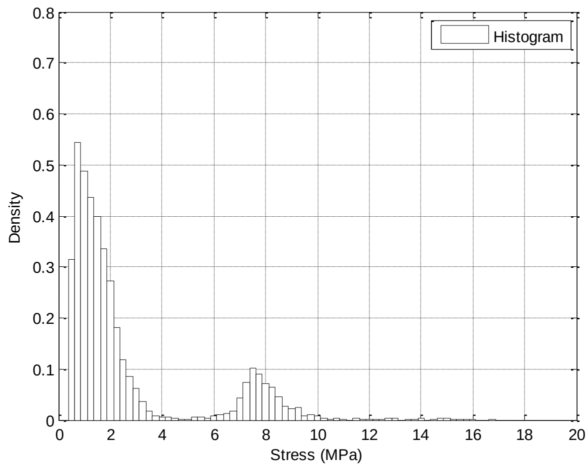

June

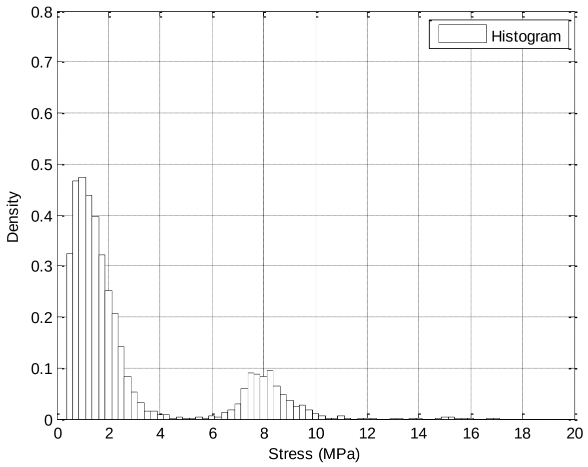

July

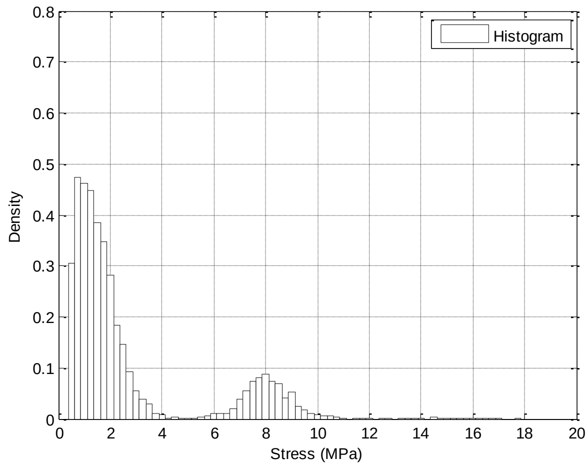

August

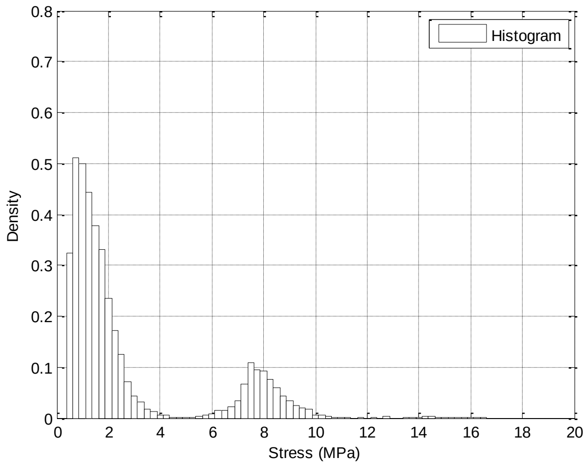

September

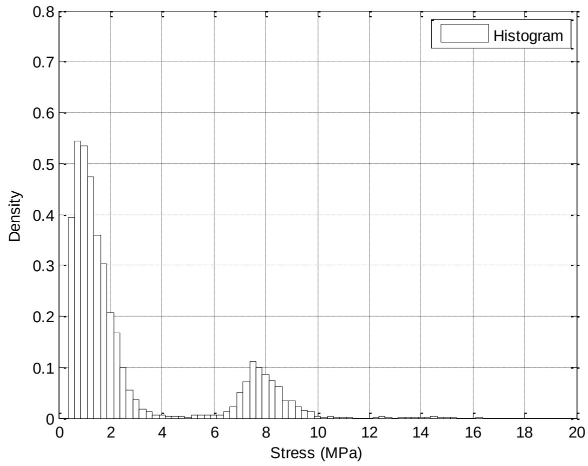

October

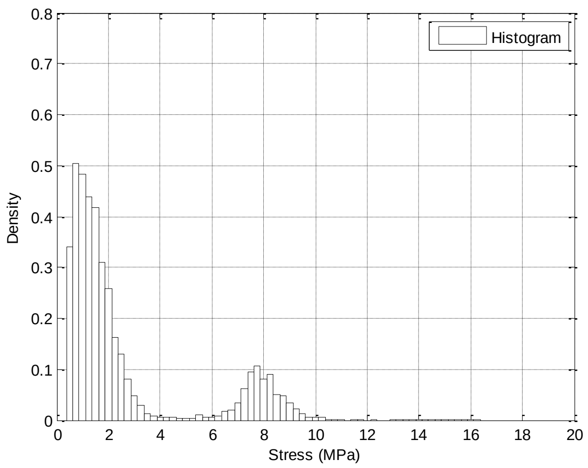

November

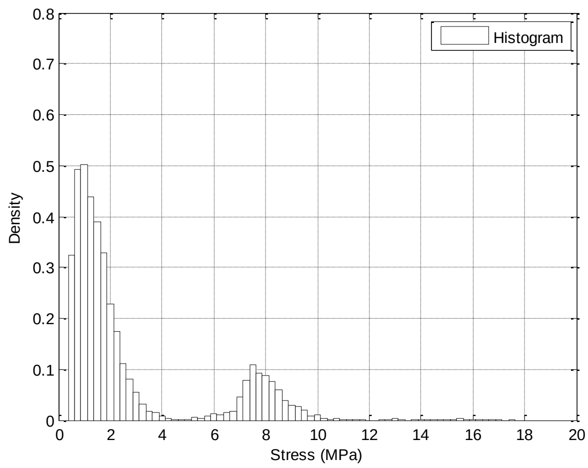

December

Peak stress histograms of 2006: diagonal strut

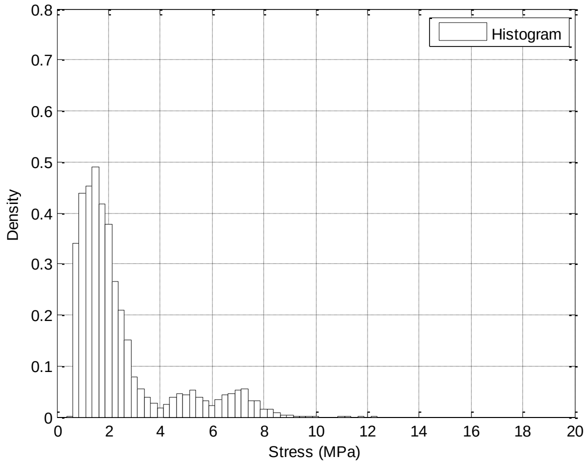

January

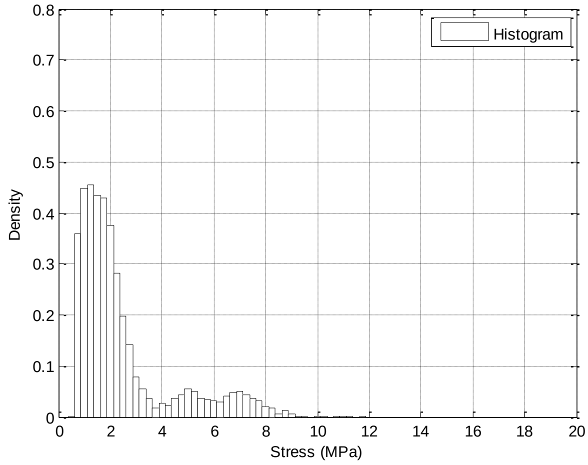

February

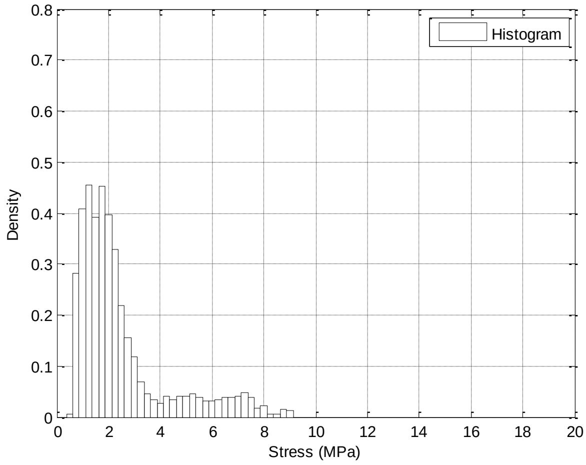

March

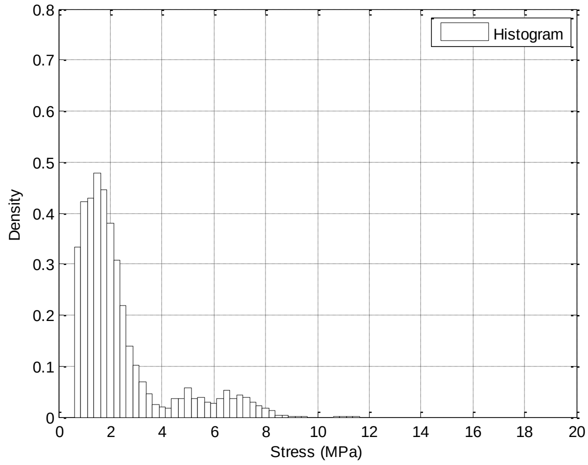

April

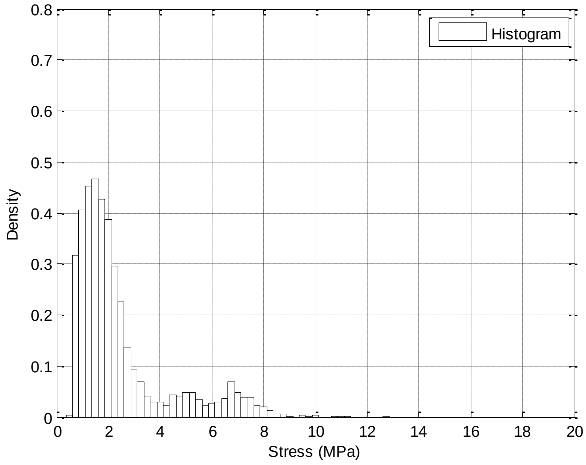

May

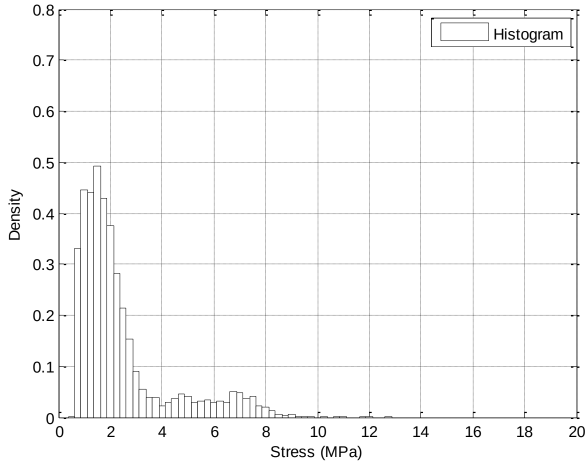

June

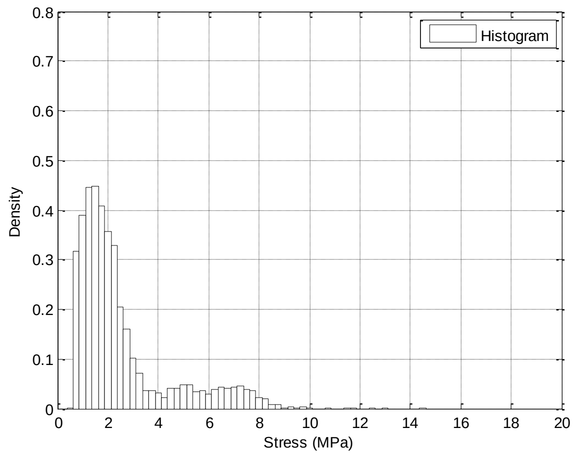

July

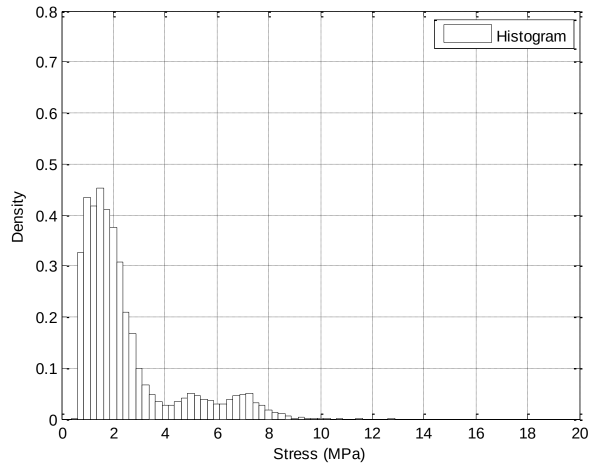

August

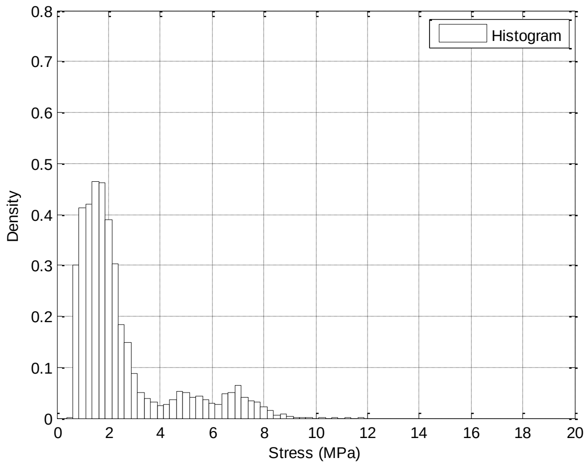

September

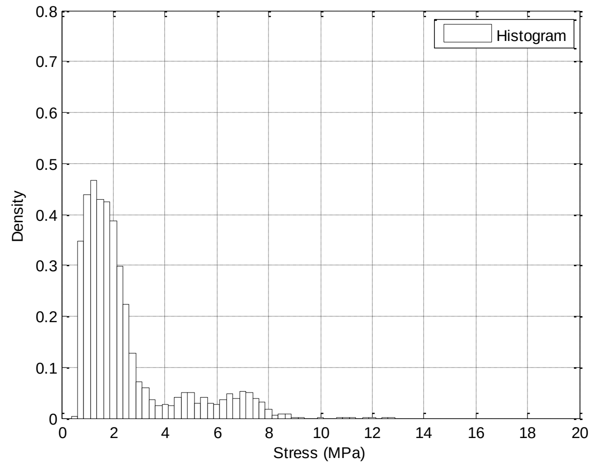

October

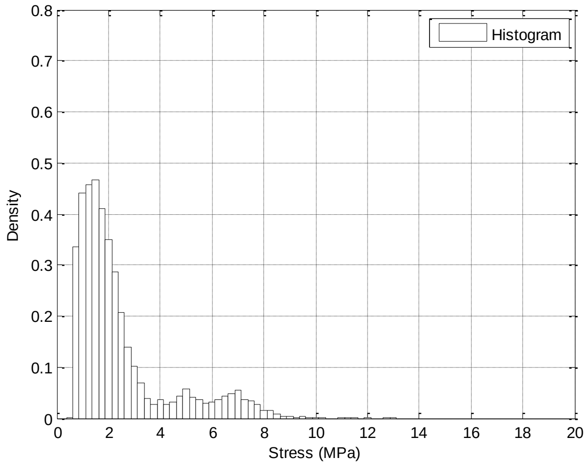

November

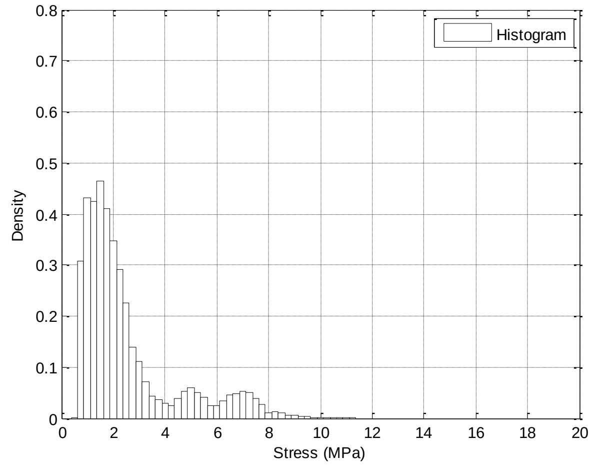

December

Peak stress histograms of 2006: bottom chord

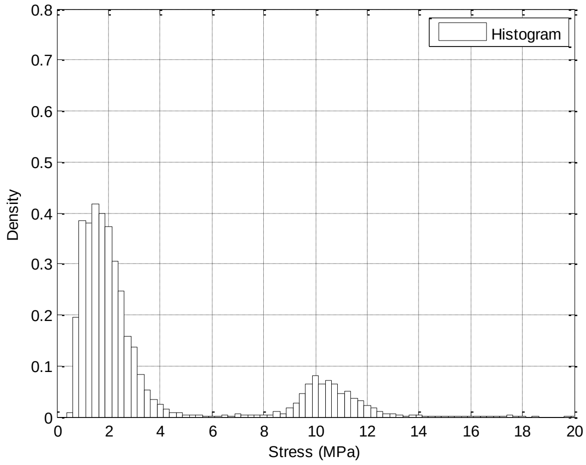

January

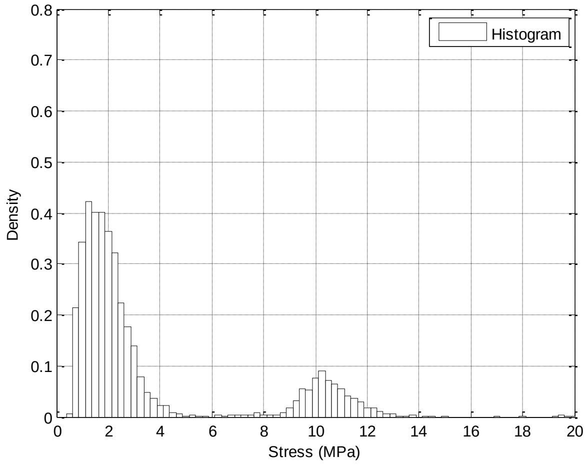

February

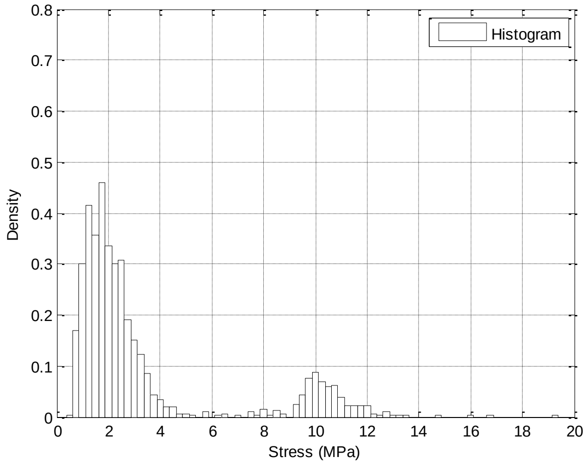

March

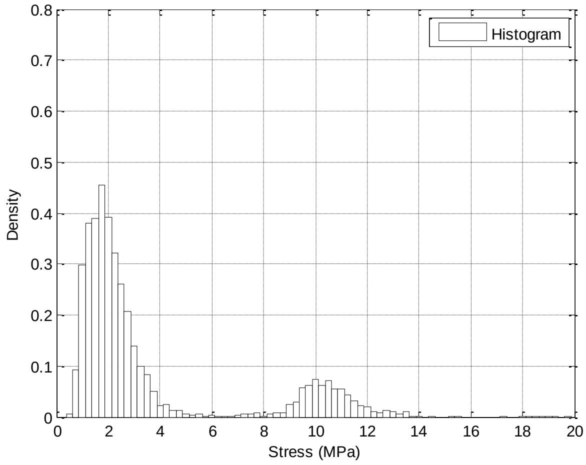

April

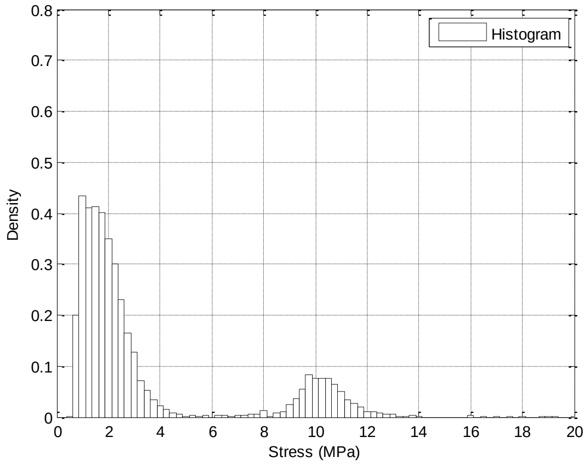

May

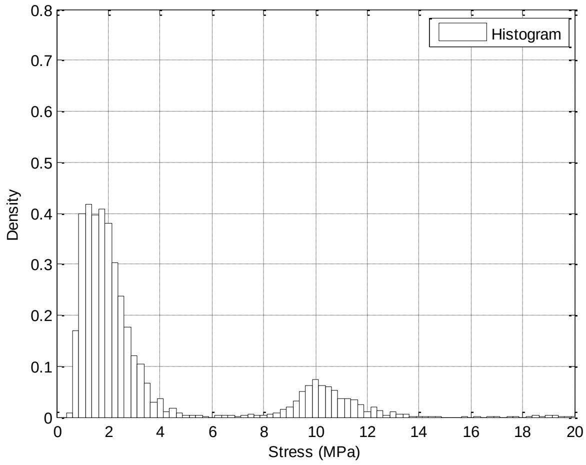

June

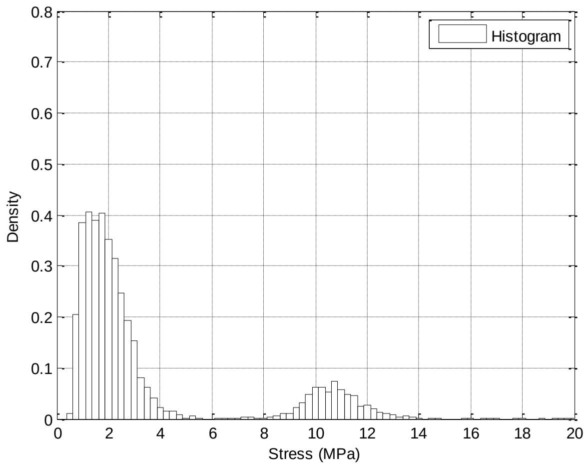

July

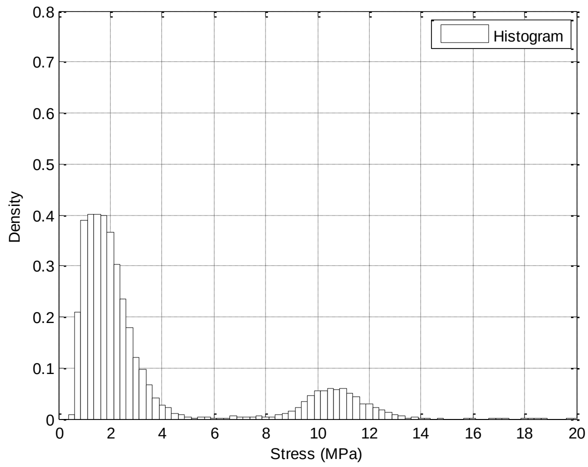

August

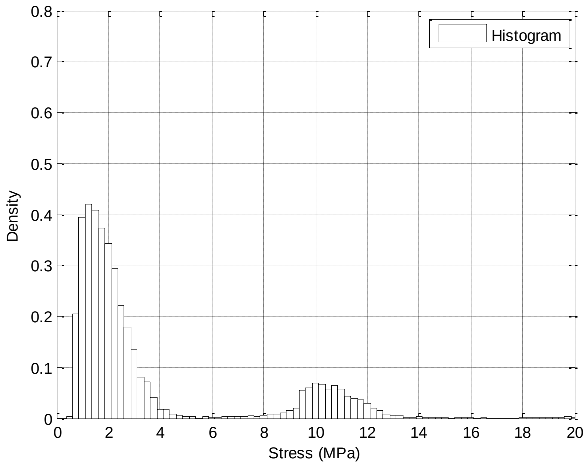

September

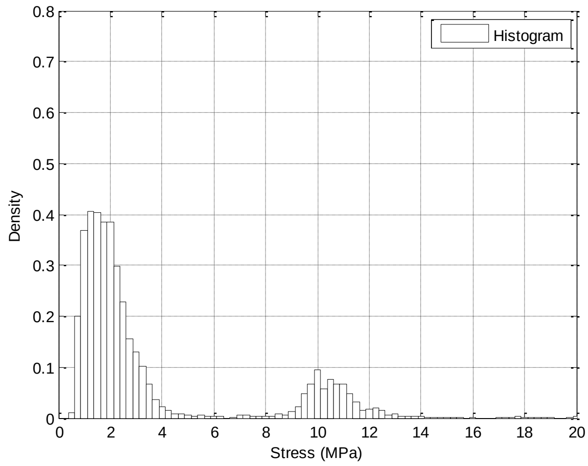

October

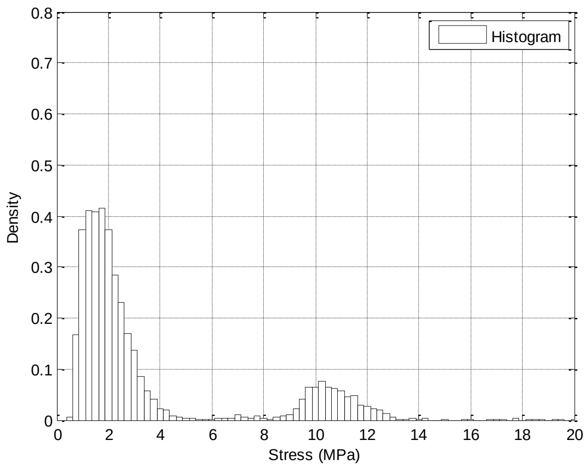

November

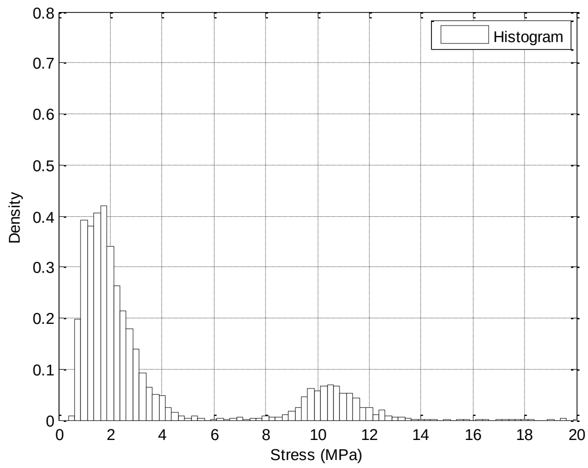

December